Novel Characterisation and Modelling Techniques for Spintronic Materials

Trinity College Dublin
Coláiste na Tríonóide, Baile Átha Cliath
The University of Dublin

JACK O'BRIEN
MAGNETISM AND SPIN ELECTRONICS GROUP
SCHOOL OF PHYSICS AND CRANN
TRINITY COLLEGE DUBLIN

A THESIS SUBMITTED TO THE UNIVERSITY OF DUBLIN, TRINITY COLLEGE IN
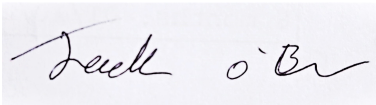PART-FULFILMENT OF THE REQUIREMENTS FOR THE DEGREE OF
Doctor of Philosophy

February 19, 2024

Declaration

I declare that this thesis has not been submitted as an exercise for a degree at this or any other university and it is entirely my own work.

I agree to deposit this thesis in the University's open access institutional repository or allow the Library to do so on my behalf, subject to Irish Copyright Legislation and Trinity College Library conditions of use and acknowledgement.

I consent to the examiner retaining a copy of the thesis beyond the examining period, should they so wish (EU GDPR May 2018).

Jack O'Brien

Summary

Spintronic materials have the potential to revolutionise certain aspects of information technology. Proposed applications include high-speed low-power MRAM (magnetic random access memory) for more efficient computers and on-chip THz magnetic oscillators for increased wireless data transmission speeds. An ideal material for spintronics is a zero-moment half-metal (ZMHM), which exhibits no stray magnetic field but simultaneously intrinsic spin-polarised conduction. The first ZMHM, Mn_2Ru_xGa, was discovered by the Magnetism and Spin-Electronics Group in Trinity College Dublin in 2014, with a vast body of work being undertaken in the last decade to develop and take advantage of the discovery. Initial efforts focused on optimisation of the stoichiometry of the material, thereby changing electronic density of states (DOS), a process referred to as Fermi-level engineering. The static and quasi-static properties of Mn_2Ru_xGa are currently quite well understood thanks to the efforts of those students who came before me, along with the interpretive talents of the senior researchers. Key properties such as spin-polarisation, magnetic moment per atom and the strength and direction of the magnetocrystalline anisotropy have been thoroughly investigated. With this foundation to build off, my focus has been to develop a complete "picture" of the system and its **dynamic** properties, a conceptual physical basis for all of the effects that we do observe or **wish** to observe. This encompasses both a mathematical simulation model for the dynamics as well as knowledge and control of the physical structure of the system and, importantly, how the two relate. The layout of this thesis reflects the goals outlined above.

In the first chapter, I give an extended introduction and motivation for the investigation of spintronics materials and why computational models and knowledge of the physical structure is so important.

In the second chapter, I discuss the computational models that I have helped to develop, with my supervisor. Our goal was, and is, the ability to simulate all the effects that interest us in a physically justifiable manner with as minimalistic a model as possible. Because of the enormous complexity, a suitable strategy is to divide and conquer different aspects of the final envisioned model, to this end our first model was a relatively simple, 1D,

classical spin dynamics model, which was nonetheless capable of simulating complex spin structures and interesting dynamics. We then went the opposite direction, calculating the static energy of a system with some quasi-particle of dynamic motion (a magnon or phonon) imposed, but with a realistic 3D lattice structure where interatomic interactions were distance-dependent. The final model encompasses both previous models and much more: Ehrenfest dynamics where the conduction electrons are modelled fully quantum mechanically and are coupled to the classical atomic spins of the first model and classical mobile nuclei.

In the third chapter, I focus on the structural characterisation of materials, primarily through crystal diffraction. I investigated variations on the quintessential Mn_2Ru_xGa in the name of optimisation as well as potential new materials. As mentioned, the electronic and magnetic properties depend on the electron wavefunction overlap, which in turn depends critically on the crystal lattice size and structure. Understanding not just the relationship between crystal structure and magnetic properties but also all the intervening steps is imperative to us.

In the fourth chapter, I detail the Mössbauer spectroscopy setup developed with my supervisor. This technique utilises the peculiarities of the nuclear energy levels of a naturally occurring isotope of iron, ^{57}Fe, to probe with startling sensitivity the local electromagnetic environment of said nuclei, thereby yielding information about the chemical bonding and magnetic orientation. The limitation to Fe-containing materials is unfortunate but we would be remiss not to take advantage of the technique simply because Mn-based materials appear to be more promising for ferrimagnetic spintronics at present. When opportunities arose to collaborate and provide unique measurements and data to fellow researchers, we were more than happy to act despite sometimes the tenuous links to "the dynamics of spintronic materials".

I finally conclude what I have accomplished in this work, build on the foundations of the work of previous students and with sufficient anchoring to allow those who come after to continue the construction of this grand picture we have envisioned.

Acknowledgements

First and foremost I would like to thank my supervisor Professor Plamen Stamenov for his support and guidance throughout my work. I think I can confidently say he is the most dedicated researcher I have met, spending countless hours experimenting, coding and writing while simultaneously dealing with the bureaucracy of professorship. Without his efforts, this thesis could not be.

I would like to thank Professor Coey and Group D for their support also. Dr. Venkatesan for practical help in the beginning, while I was getting oriented and familiar with the new processes of independent research. Dr. Gercsi for his computational support and his oiling of the Group D machine. Drs. Atcheson and Rode for their experimental guidance and theoretical brainstorming, as well as their efforts to help keep equipment running and the Group moving forward. Drs. Kumar, Teichert and Cronin for their contributions to the team.

A special thanks to my fellow students and office partners in general, in order of appearance: Stephen and Jane, Kat for both her research and social efforts, Akshara, Nigel, Ajay for his great help with PCAR measurements and being my mentor when I did a project with the Group as an undergrad student, Sruthy, Rui, Tim, Simon, Brian, Lucy, Zexiang and Orrie, thanks to each and every one. In particular I would like to thank Ross, who has been my "partner in crime" since the beginning, I could not have asked for a better COVID-buddy during **those** turbulent years to keep spirits high.

Thanks to R for her unwavering support during the final stretch, through both heartfelt encouragement and Michelin-star worthy food. Even with all the time sunk into writing, the last year has been one of the best I have experienced, here's to many more.

Last but not least (arguably most...) I thank my family for always being there when I needed them and giving me more than I ever deserved. Whether it is the peace of mind from having somewhere concrete to stay in Dublin at all times, or simply being there to talk to, I greatly appreciate all they have done for me.

Thank You

Contents

List of Publications

1. K. Siewierska, G. Atcheson, A. Jha, K. Esien, R. Smith, S. Lenne, N. Teichert, **J. O'Brien**, J. Coey, P. Stamenov, *et al.*, "Magnetic order and magnetotransport in half-metallic ferrimagnetic Mn_yRu_xGa thin films," *Physical Review B*, vol. 104, no. 6, p. 064414, 2021.
   doi: 10.1103/physrevb.104.064414.

2. Y. He, S. Lenne, Z. Gercsi, G. Atcheson, **J. O'Brien**, D. Fruchart, K. Rode, and J. Coey, "Noncollinear ferrimagnetism and anomalous hall effects in Mn_4N thin films," *Physical Review B*, vol. 106, no. 6, p. L060409, 2022.
   doi: 10.1103/physrevb.106.l060409.

3. **J. O'Brien**, H. Ahmadian Baghbaderani, F. O. Keller, N. Dempsey, L. H. Lewis and P. Stamenov, "Hardware, methodology and applications of 2^+D backscatter Mössbauer spectroscopy with simultaneous X-ray and γ-ray detection", *Measurement Science and Technology*, vol. 35, no. 2, p. 025503, 2023.
   doi: 10.1088/1361-6501/ad044b.

4. **J. O'Brien**, A. Naden, K. Siewierska, B. Ouladdiaf, J. M. D. Coey, K. Rode, P. Stamenov, and G. Atcheson, "Exchange-driven anomalous magnetism in epitaxial Mn_2Ru_xGa," *in prep*, 2023.

List of Figures

List of Tables

Chapter 1

Introduction

1.1 History and Context

Technological advancement has been dominated by innovations in semiconductor processes since the proliferation of the CMOS (complementary metal-oxide semiconductor) process in the early 1960s [1]. This process enabled high-speed, low-power transistors to be created and incorporated into ICs (integrated circuits) and the optimisation of these transistors was the task at hand for the next almost half-century. A very well-known statement regarding the development that followed was Moore's law [2], where Moore noted in 1965 that the number of transistors per IC doubled roughly every two years. This "law" translated directly into cost-per-performance decreases for decades before eventually slowing down. Moore's law slowed dramatically in the 2000s and has ceased to be valid since the 2010s, primarily because MOSFETs cannot physically be made any smaller. In the vertical direction the insulating gate dielectric is only a handful of monolayers thick and cannot decrease further due to electron tunnelling leakage currents, while in the planar direction the size is limited by the lithography process: as of 2014, the cutting-edge in extreme-UV lithography (in public knowledge) utilised a wavelength of $13.5\,\mathrm{nm}$, with maximum resolution being a similar size to the wavelength [3], with established commercial equipment reaching $< 20\,\mathrm{nm}$ in lateral size[1]. Similarly to transistors, the size and therefore areal density of magnetic recording bits also roughly doubled every two years in the late 20th

---

[1]Of course, the talk of "4 nm" nodes and similar by the companies such as Samsung and Intel is purely marketing propaganda with no connection whatsoever to the technologies in question, although the terms *would* be accurate had Moore's law continued.

century. This is perhaps unsurprising given both technologies depend on the deposition and small-scale control of thin films. Scaling has also stagnated when it comes to magnetic bits: when they fall below a certain size (dependent on the material properties), stray fields can no longer be made precise enough to individually control them and they become susceptible to thermal fluctuations. Occasionally, new breakthroughs occur, such as the addition of an exchange-coupled hard magnetic layer to improve stability [4]. More recently, the HAMR and MAMR (heat/microwave assisted magnetic recording) write heads have been developed, which allow the recorded magnetic bits to be natively very stiff, with their switching then being assisted by means of heat (using a surface-plasmon focused laser to heat locally) [5], or by a microwave field (thus exciting ferromagnetic resonance in the recording medium locally using a tiny spin-torque oscillator) [6].

Due to the eventual stagnation of these and other technologies, which have driven advancement in the information age, focus has increasingly shifted to searching for new technologies rather than improving old ones. For example, three very important fields which are intensively researched today include:

- **Quantum computing**, which seeks to harness the inherent probabilistic nature of quantum mechanics, where there are predicted uses in, for example, cryptography: creating unbreakable encryptions while breaking older ones. A leading candidate is single photon qubits [7] and it is a very illustrative example: if a standard optical beam splitter allows through 50% of a beam of light and deflects the other 50%, what happens if a single photon hits the splitter? It cannot be split so it must either be entirely transmitted or reflected with a certain probability of each occurring. Superconductivity is another promising mechanism to enable quantum qubits: entanglement and other quantum properties are clearly exhibited on a macroscopic scale in such materials [8] with the obvious caveat that non-ambient conditions are required[2]. Finally, there is a strong connection to magnetism: the exchange interaction is a common mechanism by which quantum qubits are entangled, such as in a gated array of single-electron quantum dots, where the gate voltage is used to control the degree of coupling [9].

---

[2]Unless the recent arχiv pre-prints are to be believed. Update as of the thesis corrections: the claims of superconductivity in these papers have indeed been shown to be incorrect

- **Battery technologies** are very important in the modern world with renewable energy such as solar seeing increased adoption, and fossil-fuel burning engines being phased out. Bigger, better, cheaper and cleaner batteries are needed to store renewable energy such as solar (which is only available during the day...) and enable electric motors to compete with their bi-stroke brethren.

- **Spintronics** is arguably the field which can continue the progress in IT without a drastic change of approach. While the charge and spin of electrons have long been harnessed in, for example, transistors and magnetic recording, respectively, their functionality is rarely combined and used together. The broad aim of spintronics is to harness that combined power. Phenomena which are quite mature and have already seen adoption in commercial devices include GMR and TMR (giant and tunnelling magnetoresistance) where the measured electrical resistance strongly depends on an external magnetic field, lending itself to use in magnetic field sensors or hard drive read heads. This is only the tip of the iceberg, however, and currently technologies based around spin-torque are being developed in applications such as MRAM (magnetic random-access memory) and SOT (spin-orbit torque) oscillators [10].

The latter of the above fields is the one which I find myself in. However, rather than commercial device development, we are more concerned with the fundamental material research, in particular the modelling and understanding of novel materials, which have the potential to satisfy some of the requirements of spintronics devices and hence enable the visions to be realised. Developing a complete picture of exactly **how** these novel materials work, **why** they exhibit the properties that they do, and **what** effects/phenomena can be realised as a result, is an imperative task where work must be backed by computation and experiment.

1.2 Basic Magnetism

It is worthwhile to recap some of the more fundamental aspects of magnetism before discussing more specific theory and experimental methods. Magnetic materials span a plethora of systems which exhibit varied manifestations of magnetism, in particular spon-

taneous magnetisation and the hysteretic and coercive effects that accompany it. Today, we know that magnetisation can be reduced to the angular momentum of electrons and to a lesser extent, nuclei, and this angular momentum obeys quantum mechanics. To understand the many varied effects of magnetism, it is wise to start with the quantum mechanics of the electron.

1.2.1 Magnetism of The Electron

1.2.1.1 Orbital and Spin Angular Momentum

Orbital angular momentum of electrons can be phenomenologically treated as due to their orbital motion around the nucleus. Electric current travelling in a loop causes a magnetic moment $|m| = IA$ where A is the area of the loop and the direction of $\vec{m}$ is determined by the cross product of the position and velocity vectors of the electron, or equivalently using the right hand rule: when giving a "thumbs up", if ones' fingers follow the path of the conventional current then the thumb points in the direction of $\vec{m}$. The same logic applies to single electrons with the caveat that they travel in the opposite direction of current as they are negatively charged particles. The current is charge per unit time $I = -\frac{e}{\tau} = -\frac{ev}{2\pi r}$, giving $\vec{m} = -\frac{e}{2}\vec{r} \times \vec{v}$ when multiplied by the area. Classical angular momentum tells us that $\vec{l} = m_e \vec{r} \times \vec{v}$ and so $\vec{m} = -(\frac{e}{2m_e})\vec{l} = \gamma\vec{l}$, where we define the gyromagnetic ratio $\gamma = -\frac{e}{2m_e}$, one of the more important proportionality constants in magnetism.

Of course, the classical picture of electrons whizzing around the nucleus following some ring-shaped path is not correct, that would require constant electromagnetic radiation to be produced due to the constant acceleration of the charged particle. Rather, electrons exist is *quantised* orbital states of the nucleus in their ground state. The orbital angular momentum is similarly quantised in units of $\hbar$ such that $m_z = \gamma m_l \hbar$ where the z axis is arbitrarily chosen as the quantisation axis and the orbital quantum number $m_l = 0, \pm 1, \pm 2...$ depends on the orbital state in question. This provides another fundamental unit, the Bohr magneton $\mu_B = \frac{e\hbar}{2m_e} \approx 9.274 \times 10^{-24}\,\mathrm{A\,m^2}$ [3], so that $m_z = -m_l \mu_B$.

---

[3] It is often convenient to express μ_B in other units: $\mu_B \approx 9.274 \times 10^{-24}\,\mathrm{J\,T^{-1}} \approx 0.0579\,\mathrm{meV\,T^{-1}}$

Spin angular momentum is a intrinsic property of electrons (and other fermions) which does not depend on some orbital state. It could be treated similarly as due to the spinning motion of the finite-volume electron but this is not as justifiable as the surface of the electron would need to break the speed of light to provide enough angular momentum. The spin moment has constant magnitude and can only be quantised by its direction $m_s = \pm 1/2$, importantly it cannot be zero, unlike the orbital moment. The gyromagnetic ratio for the spin angular momentum is *double* that for the orbital: $\vec{m} = -\frac{e}{m_e} m_s \vec{s}$. For consistency, the "g-factor" is introduced, equal to $g_l \approx 1$ for the orbital and $g_e \approx 2$ for the spin angular momenta so we can write $\vec{m} = -g \frac{e}{2m_e} m_s \vec{s}$. The g-factor is absorbed into the gyromagnetic ratio $\gamma = -g \frac{e}{2m_e}$.

Spin-orbit coupling describes how the spin and orbital angular momenta of an electron orbiting a nucleus combine to form the total $\vec{j}$, with the effective atomic g-factor then being determined by the Landé equation [11, §3.7]. It can be classically approximated again by assuming the electron is travelling around the nucleus, this time from the electrons reference frame. The nucleus orbits the electron with a resulting magnetic field due to the circulating current $|B_{so}| = \mu_0 \frac{I_n}{2r} = \mu_0 \frac{Zev}{4\pi r^2}$ which acts on the *spin* moment of the electron with energy $\varepsilon_{so} = -\mu_B B_{so}$. The appearance of the atomic number Z and the electron orbital radius r show that this interaction is greater for heavier elements and inner shell electrons.

Angular momentum is more properly described fully quantum mechanically using wave or matrix mechanics due to Schrödinger (and later Dirac) or Heisenberg respectively. It turns out that the three Cartesian components of the angular momentum vectors do not commute with one another but all commute with the total angular momentum.

$$[j_x, j_y] = i\hbar \varepsilon_{xyz} j_z, \qquad \left[\mathbf{j}^2, j_z \right] = 0,$$

where ε is the cyclic permutation operator and j_z is conventionally chosen as the Cartesian component to be measured along with $\mathbf{j}^2$. In quantum mechanics, observables can only be measured simultaneously if their operators commute so we cannot know all components of angular momentum, but we can know one component and the magnitude, typically again z is chosen as the quantisation axis along which we do know the angular momentum

projection. The end result is that we can describe angular momentum vector as being positioned on a cone of values around the z axis, where the planar projection of the vectors is not, and indeed *cannot* be, known.

The possible orbitals (eigenvectors) that an electron can occupy are defined as solutions to the Schrödinger (or Dirac as appropriate) equation $\mathcal{H}\varphi = \varepsilon\varphi$ where applying the Hamiltonian operator to the eigenvector yields the scalar energy (eigenvalue) of the vector. The Hamiltonian in question is

$$\mathcal{H} = -\frac{\hbar^2}{2m_e}\nabla - \frac{Ze^2}{4\pi\epsilon_0 r}$$

where ∇ is the spatial Laplace operator and the second term is the potential well from the nucleus due to the Coulomb interaction. Solutions are obtained by separating the radial and angular parts of the wave function and utilising the spherical harmonics, the known solutions to the Laplace equation in spherical coordinates. These harmonics form an *orthonormal basis* such that any function defined on the surface of a sphere can be expressed as a sum of them. In tandem with the radial part of the wave functions, this accounts for all of space. The correlation of the spherical harmonics to the structure of the magnetic quantum numbers is clear when examined, see Figure 1.1. The radial part of the solution for a spherical potential such as the nuclear Coulomb potential can be described by the product of Laguerre polynomials with an exponential decay [12, §3.7]. The radial part of the wavefunction for a given orbital is determined by the quantum numbers n and l while the angular part is determined by l and m_l. In general, the principal quantum number n determines the size of the orbital while l and m_l determine the shape and orientation respectively. The orbitals described so far are exact solutions to the Schrödinger equation for a one-electron atom, i.e. hydrogen, and their energy increases with increasing quantum numbers. For real atoms with many electrons, the electron-electron and spin-orbit interactions complicates things, in some cases causing anomalies in the energies of successive atomic orbitals.
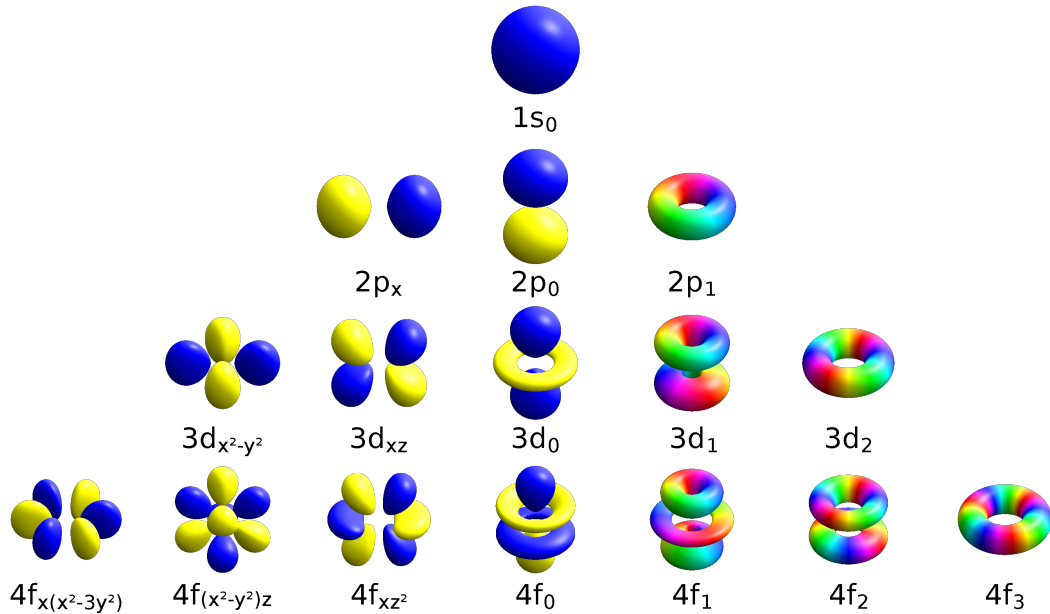
Figure 1.1: One-electron (hydrogenic) orbitals for $n = 5$, with $n - 1$ possible values for l, and $2l + 1$ possible values for m_l. For comparison, on the right are the complex-valued pure spherical harmonics with phase indicated by colour while the left shows the commonly used real superpositions. As the spherical harmonics form an orthonormal basis, any superposition of them can be used and real superpositions oriented with respect to the Cartesian axes are a useful choice as these will be eigenvectors of a Hamiltonian whose symmetry is determined by crystal structure. © Geek3 [13] / CC BY-SA 4.0

1.2.2 Many-Electron Atoms

Electrons are indistinguishable Fermions, meaning no two electrons can occupy the same quantum state, in contrast to bosons for which many can occupy an identical state. Practically, this means that electrons on the same atom (which can technically be found in the same position) must have different quantum numbers. In addition to the three numbers related to the orbitals, electrons can have positive or negative spin, signified by the quantum number $m_s = \pm\frac{1}{2}$. Thus two electrons can exist in any orbital. Taking ground-state iron as an example, there are 26 electrons to distribute among the orbitals. According to Hund's empirical rules, electrons fill orbitals with m_l taking precedence over m_s, the explanation being that electrons in the same orbital experience greater mutual repulsion from the Coulomb interaction so tend to fill different orbitals first [14, §4.2.0]. The electron configuration for free iron is $[Ar]3d^6 4s^2$, illustrated in Figure 1.2. In filled orbitals the magnetic quantum numbers, both orbital and spin, cancel out so that there is net

zero effect. For the $3d^6$ electrons of Fe, the quantum numbers are $m_l = -2, -1, 0, 1, 2, -1$ and $2m_s = 1, 1, 1, 1, 1, -1$, thus the atom as a whole has orbital angular momentum $\sum m_l = L = 2$ and spin angular momentum $\sum m_s = S = 2$. The total angular momentum is the vector sum of the orbital and spin components, Hund's third empirical rule describes how the two angular momenta couple: if the orbital is more than half-full $J = L + S$ and if it is less than half-full $J = L - S$, so that for ground-state iron $J = 4$. There are some quirks regarding the order in which electron orbitals are filled, the
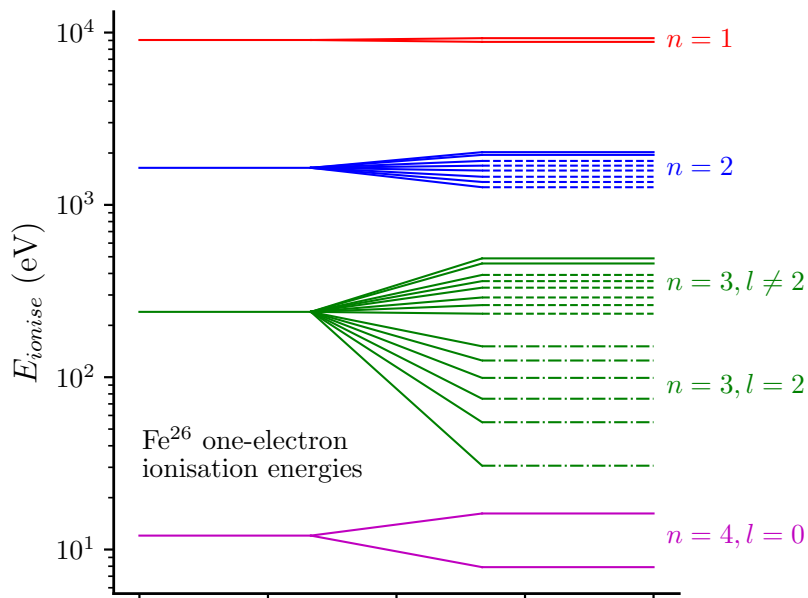
Figure 1.2: The successive ionisation energies of iron i.e. the energy required to remove the outermost electron of Fe, Fe^{1+}, Fe^{2+} and so on.

$[Ar]3d^6 4s^2$ ground state of iron being an example. The first oxidation is in fact $[Ar]3d^7$: when the first s electron is removed, the "bonus energy" from having a fully filled orbital is no longer relevant and energy is minimised by putting the lone remaining s electron into the d orbital.

1.2.3 Many-Atom Lattices

The total angular momentum J determines the magnetic moment of the atoms, but when atoms bind together to form materials, another layer of intrigue is added. The orbitals of adjacent bonding atoms tend to hybridise, altering their energy and occupation. In fact, the nature of bonding is to reduce the overall energy of a system, usually via the transfer or sharing of electrons between atoms such that the undesirable partially-filled

shells become filled, thus almost by definition, bonding tends to destroy the magnetism of atoms. Depending on the nature of the bonding (ionic, covalent, metallic), the details of the magnetism can vary wildly and are quite difficult to predict. One of the more popular methods of modelling the hybridised-orbital band structure of materials in magnetism is spin-resolved DFT (density functional theory) [15], which attempts to predict the energy and occupancy of all the hybrid orbitals of a material with the macroscopic properties being predicted from there. However, DFT involves many approximations and it cannot model the effect of finite temperature or crystalline disorder, and is very computationally intensive.

One standard way to model magnetisation is to take an extreme situation which can be predicted with come confidence and treat non-extreme materials as a linear combination of the extremes. Electrons in a material can be considered localised on their host atom, maintaining their atomic magnetisation, or delocalised throughout the material as in a metal with the Coulomb potential of the lattice being considered a perturbation. The electron wavefunctions in $4f$ orbitals and in the $3d$ orbitals of insulating ionic compounds are not involved in hybridisation, they are either buried far enough below other orbitals (such as $5s$ and $5p$) or undergo complete electron transfer, with the magnetism being the same as for a free atom in some oxidation state in the latter case. Usually, the lanthanide materials have localised magnetic electrons while the $3d$ metals have delocalised ones [14, §3.4].

1.2.3.1   The Crystal Field Interaction

Apart from orbital hybridisation, there are two further important phenomena that occur when magnetic atoms form a solid. These are due to the crystal field interaction, that is, the interaction of electrons on one atom with the Coulomb potentials of other nearby atoms in a crystal lattice. Three common lattice structures are shown in Figure 1.3. The non-spherical d and f orbitals, which are responsible for magnetisation, are affected by the crystal field potential. For the transition metals, the $3d$ orbitals are some of the outer ones along with the $4s$ orbitals and are relatively strongly affected by the neighbouring atoms' electrons. The crystal field potential usually has cubic symmetry, as in Figure 1.3, and this potential is added to the spherically symmetric Coulomb potential of the host
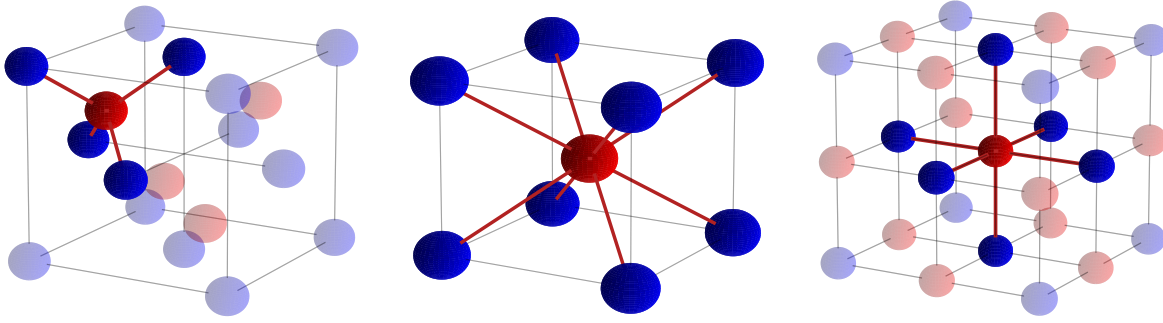
Figure 1.3: Zincblende, bcc and rocksalt lattice structures with nearest-neighbour coordination highlighted. All structures have cubic symmetry with 4, 8 and 6 nearest neighbours respectively. The element-wise interactions in Heusler alloys have the same symmetry as in zincblende structures while simple cubic lattices have the same nearest-neighbour symmetry as rocksalt.

nucleus. This results in the ring-like symmetry of the spherical harmonics which describe the orbitals being broken, as the pure spherical harmonics are not eigenstates of the combined nuclear and crystal field potentials. Linear combinations of the spherical harmonics with cubic symmetry can be found that are eigenstates of both potentials, resulting in the orbitals illustrated on the left hand side of Figure 1.1. The end result is that the orbital angular momentum of the electrons is quenched as the rings of charge density, which allowed the electrons to circulate in the xy plane, are disrupted. This means that for the transition metals, the atomic magnetisation is due only to the spin: $\max(m_z) \approx g_S S \mu_B$, where, to reiterate, $g_S \approx 2$ and $S = \sum m_s$ with $|m_s| = 1/2$. For free atoms of the same element $\max(m_z) \approx g_J J \mu_B$. This quenching does not apply to the lanthanide elements however, the magnetic $4f$ shell is more tightly bound to the host nucleus on average and does not feel the effect of potentials from other atoms in the crystal. For more detail and examples, see [14, §4.4].

1.2.4 Collective Magnetism

So far, we have discussed the origin of magnetism from an atomic perspective and how it evolves when multiple atoms come together to form materials. The main question now is how and why the magnetic moments associated with individual atoms often work together to yield macroscopic magnetic phenomena such as ferromagnetism and ferrimagnetism.

The force which causes the magnetic moments of unpaired electrons on adjacent atoms

to align parallel is the **exchange** force and it can be seen as an extension of the orbital hybridisation discussed above. Electrons are indistinguishable meaning that they can be **exchanged** without altering the energy of a system, in the common example of a hydrogen molecule with two nuclei and two electrons, this means that the electrons can swap atoms and orbit the molecule as a whole. This implies that the electrons can inhabit the same space, but from the Pauli exclusion principle electrons in the same place must have opposite spin. Quantum mechanically, we say that the **total** wavefunction for the two electrons must be antisymmetric meaning they can either have the same spin or be able to occupy the same space, but not both or neither. To give an idea of the maths; for the hydrogen molecule, the possible combined wavefunctions are:

$$\Psi_I = \phi_{asym}(1,2)\chi_{sym}(1,2) \qquad \Psi_{II} = \phi_{sym}(1,2)\chi_{asym}(1,2) \tag{1.1}$$

where ϕ and χ denote the spatial and spin parts of the wavefunction and $1,2$ refer to the two electrons. The spatial parts are equal to $\phi_{sym/asym} = \left(1/\sqrt{2}\right)(\varphi_1 \pm \varphi_2)$ where φ are the wavefunctions (eigenvectors of the Schrödinger equation) for the two individual electrons. The energies of the two possible total wavefunctions are evaluated using the Hamiltonian for the Schrödinger equation. The difference in these energies turns out to be equal to the exchange integral:

$$J = \int \varphi_1^*(\vec{r}') \, \varphi_2^*(\vec{r}) \, H(\vec{r},\vec{r}') \, \varphi_1(\vec{r}) \, \varphi_2(\vec{r}') \, \mathrm{d}r^3 \mathrm{d}r'^3 \tag{1.2}$$

where we note the position r is exchanged across the integral. The energy of the system is written as $\varepsilon = -2J\mathbf{s}_1 \cdot \mathbf{s}_2$ where J (henceforth the exchange integral rather than total angular momentum) is expressed in units of energy. The famous Heisenberg Hamiltonian generalises this equation describing the exchange between two electrons to describe exchange between arbitrary magnetic atoms. This leads to the Heisenberg model of materials where atoms are treated as singular composite spins, discussed in the following chapter.

$$\mathcal{H} = -J\vec{S}_1 \cdot \vec{S}_2$$

Properly, the spin vectors $\vec{S}$ should be quantum mechanical operators, but in the Heisenberg model of treating atoms as magnetic moments, they are effectively vectors.

We now understand the origin of this Hamiltonian: the exchange integral J is equal to the energy difference between total wavefunctions for two electrons with symmetric and antisymmetric spatial parts, while the dot product $\vec{S}_1 \cdot \vec{S}_2$ is 1 for parallel spins and 0 for anti-parallel, but also can be treated continuously where the dot product is proportional to the cosine of the angle between the two spin vectors. It is interesting to observe that the exchange interaction described here is analogous to Hund's third rule applied to adjacent atoms rather than different orbitals of the same atom. The electrons filling the d orbitals in an atom tend to align their spins first in orthogonal orbitals before occupying the same orbitals with opposing spins.

In general, the sign and magnitude of J dictates the type of magnetism exhibited by a material. Positive J lowers the energy for parallel spins (ferromagnetism), negative J lowers the energy for anti-parallel spins (antiferromagnetism) and small J is not able to overcome the thermal random vibrations by itself so the atomic spins essentially ignore each other (paramagnetism), until an external field is applied which works with the exchange to create a magnetic moment bigger than expected for independent atoms. Recall also that atoms with no unfilled orbitals have 0 net angular momentum and there are no unpaired spins to consider (non-magnetic). There is also diamagnetism wherein a material *opposes* an applied field, this is classically explained by Langevin [16] as the applied field reducing the effective current which leads to electrons' orbitals moment, thus effectively inducing a negative moment in the material relative to the applied field, an identical effect also occurs with conduction electrons. In fact all materials exhibit this diamagnetic effect but it is small and only really important for those that are non-magnetic. One situation where diamagnetism is encountered in my line of work is when measuring the moment of a magnetic thin film on a non-magnetic substrate: the huge relative volume of the substrate means its "small" diamagnetic response dominates the overall signal and must be subtracted.

Refer to Coey [14, §5.2] or Cullity & Graham [11, §4.3], along with your favourite introductory quantum mechanics textbook, for a more pedagogical introduction.

1.2.4.1   Distance-Dependence

We have seen that the magnitude and size of the exchange integral J largely determines the magnetic properties of a material, together with crystal structure. What then determines the value of J? In real materials with different types of atoms, each with many electrons which are localised and delocalised to different degrees, it is an immense challenge to try and conceive a method to determine the magnetic state from first principles. The Bethe-Slater curve shown in Figure 1.4 plots the value of the exchange integral J as a function of the ratio between the size of the atom r_a and the size of the d orbital r_{3d}. Physically, the Bethe-Slater curve makes a lot of sense. A smaller r_a/r_{3d} implies that the
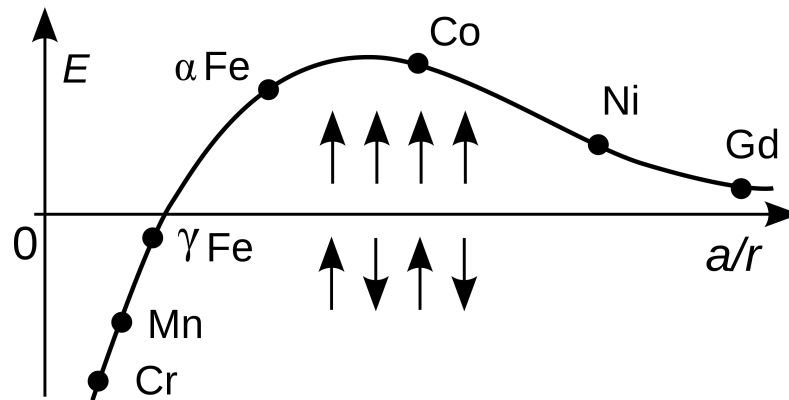
Figure 1.4: The Bether-Slater curve showing the value of the nearest-neighbour exchange integral as a function of the ratio of atomic radius to $3d$ (or $4f$) orbital radius. Not only are the ferromagnetic elements clearly outliers in the graph but their J values match up to their observed Curie temperatures. This curve, while obviously not capturing the full detailed physics of the interactions, reinforced the idea that orbital-overlap is crucial to exchange.
Zureks, CC0 License [17]

magnetic $3d$ orbitals extend relatively further from the host nucleus and interact more strongly with similar orbitals on adjacent atoms. For very small values as in Cr and Mn, the overlap is so much that the electrons must have opposing spin to satisfy the Pauli exclusion principle. For Fe, Co and Ni, there is significant overlap between the $3d$ orbitals of adjacent atoms such that the exchange integral is large but there is enough "room" for the electrons so they do not have to occupy the same quantum state and force J negative. Then for larger ratios the $3d$ orbitals are buried and do not interact with orbitals from other atoms. This curve gives a surprisingly accurate prediction of the type and strength

of exchange coupling, in particular it predicts that Mn exchange becomes ferromagnetic in compounds where the Mn atoms are further apart. The Bethe-Slater curve does not, however, account for exchange interactions between further than nearest-neighbour atoms, does not consider orbital hybridisation and does not consider the different interactions between different d orbitals with different shapes. The Bethe-Slater curve is discussed in the context of modern electronic structure theory, with orbital-resolved DOS (density of states) computed via DFT, by Cardias et al. [18].

1.2.4.2 Band Magnetism

Many of the arguments presented in the previous few sections implicitly assumed the magnetic electrons were localised, true for the $4f$ electrons and for insulation $3d$ compounds. For the $3d$ **metals**, this is not the case. The $3d$ and $4s$ electrons are both relatively far away from the host nuclei and engage in hybridisation and bonding with other atoms in solids. In this scenario it no longer makes sense to consider the individual orbitals but material-wide hybridised **bands** of electron density, a.k.a. the DOS. An excellent conceptual description of the formation of bands is given by Cullity & Graham [11, §4.4], in summary, when two similar atoms with an outer filled s shell come together, eventually the orbitals will begin to overlap. The electrons on the different atoms are not distinguishable and cannot occupy the same space by the Pauli exclusion principle so this causes the s orbitals to hybridise and form two new, energy-split levels. As the two new levels have **different** energy, the electrons can happily occupy them and satisfy Pauli's principle. If we consider say 10^{17} Fe atoms[4] in a metal where the outer orbitals strongly hybridise, then to satisfy Pauli exclusion the $3d$ and $4s$ orbitals will need to split into a **great** number of sub-levels to the extent that they effectively form a continuum in energy: a band. The width of the bands depends on the how many sub-levels are necessary, which depends on how many electrons have to "share" the same space, which depends on how close together the atoms are (the material's lattice parameter) and how far from the nucleus the atomic orbitals are (proportional to the nuclear charge). The s orbitals are further from the nucleus and form wider bands than the $3d$ orbitals, which often form sharp bands. In addition, since d orbitals can house 10 electrons compared to s bands' 2, the d bands have

---

[4]There are 1.061×10^{17} Fe atoms in a $50\,\text{nm} \times 5\,\text{mm} \times 5\,\text{mm}$ film.

a much greater density.

The equilibrium properties of metals depends on the position of the Fermi level in the DOS. The Fermi level is simply the energy up to which the DOS is populated by electrons. For a single atom, the Fermi energy is just the energy of the highest occupied orbital but for metals, it depends on the hybridisation of the orbitals into bands and the number of electrons in the orbitals which hybridise. Just as the exchange energy following from the Pauli exclusion principle leads to Hund's third rule and preferentially fills orbitals with a certain spin quantum number, it analogously shifts the spin-up and spin-down DOS relative to the Fermi level in metals. An example of some calculated spin-resolved DOS for the magnetic $3d$ metals are shown in Figure 1.5. In essence, for a metal to be
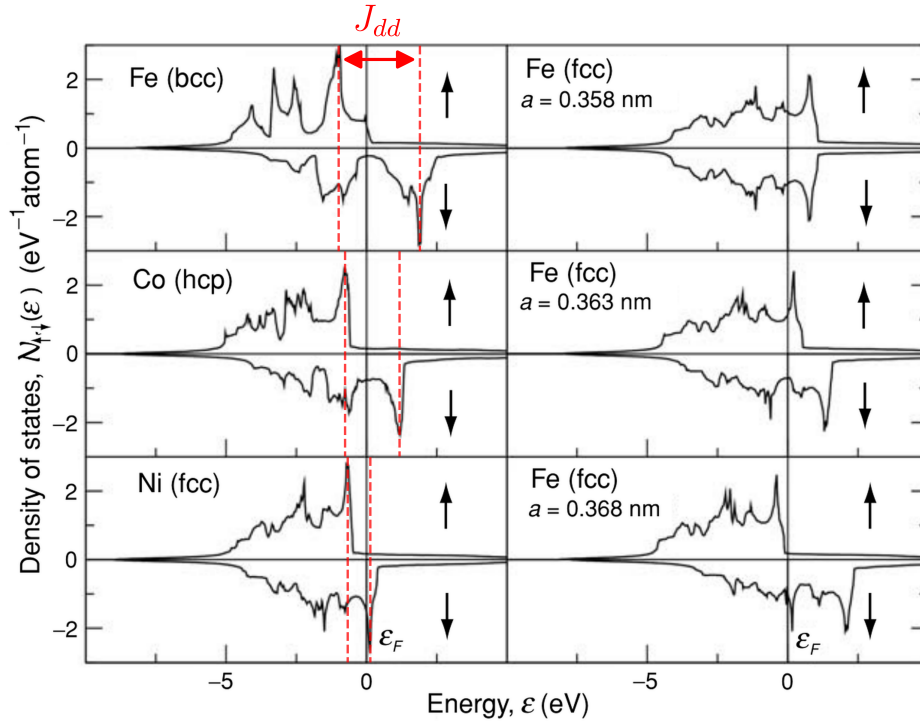
Figure 1.5: The spin-resolved DOS for the three elemental metals which are ferromagnetic at room temperature, with the effect of exchange-splitting denoted. Also shown are the calculated DOS for fcc γFe with three different assumed lattice parameters to show the immense sensitivity of the DOS to the interatomic spacing. (Calculations courtesy of Ivan Rungger, via Coey [14].)

ferromagnetic, there must be significant $3d$ (or $4f$) DOS both sides of the Fermi level but not too far apart, and the responsible atoms must be at the correct separation relative to their atomic number so that the exchange energy is sufficient to push electrons in one

spin band below the Fermi energy into the other spin-band above the Fermi energy. This is the case for Fe, Co and Ni in elemental form and the case for innumerable other mixed-elemental compounds. Note in Figure 1.5 that while Fe has the largest splitting of its bands, the splitting is not as "clean" as the other ferromagnetic metals, so Fe does not have the largest Curie temperature.

One of the initial great accomplishments of the band magnetism theory was the explanation of the magnetic moment per atom in the ferromagnetic metals. In free atoms, the moment must be an integer number of Bohr magnetons as the electrons occupy discrete energy levels, but when the orbitals are continuous bands of both $4s$ and $3d$ character, the spin imbalance can naturally be non-integer as the electrons of the entire material are shared between the bands which cross the Fermi energy. In modern times, DFT-calculated band structure has found increasing applications in spintronics where it can help explain the myriad of electron transport properties and anomalies which are intrinsically linked to the DOS and position of the Fermi surface.

The origins of the main magnetic interactions, namely exchange and the crystal field, have been introduced here for both "types" of magnetism: localised and delocalised. The effect of these interactions and many more are discussed in more detail in the following chapter, which concerns simulations, as they are introduced into our numerical atomistic dynamics simulation model.

1.3 Spin Electronics

I will give a brief introduction to spin electronics and a briefer introduction to some of the applications because many are discussed in more depth in later chapters where they are relevant.

1.3.1 Spin Polarisation

Spin-polarisation is a measure of the discrepancy between spin-up and spin-down states at the Fermi level. There are a number of different definitions depending on the application at hand: when considering electron tunnelling, the difference in DOS for up and down states is what matters; while for ballistic or diffusive electric current the DOS should be

scaled by the value or squared value of the Fermi velocity respectively [19, 20]:

$$P = \frac{N_\uparrow(E_F)\, v_{F\uparrow}^n - N_\downarrow(E_F)\, v_{F\downarrow}^n}{N_\uparrow(E_F)\, v_{F\uparrow}^n + N_\downarrow(E_F)\, v_{F\downarrow}^n} \tag{1.3}$$

where $\uparrow, \downarrow$ denotes the spin band, N is the DOS, E_F is the Fermi energy, v_F is the Fermi velocity and $n = 0, 1, 2$ for tunnelling, ballistic or diffusive transport respectively. We can see from the Figure 1.5 that the strong ferromagnetic metals Co and Ni have a significant spin-polarisation at the Fermi level. If a material is fully spin-polarised at the Fermi level ($P = 100\%$) it is referred to as a half-metal, this occurs when the hybridised $4s$ states are pushed above or below the Fermi surface and the $3d$ states are sufficiently spin-split by exchange so that only one spin has DOS at the Fermi energy. Half-metallicity is a very interesting property predicted in 1986 in the transition metal oxide CrO_2 [21] and first demonstrated via spin-resolved photo-emission spectroscopy (SR-PES) in a complex Mn perovskite material $La_{0.7}Sr_{0.3}MnO_3$ [22]. Different forms of half-metallicity are discussed by Coey et al. in the context of the discoveries of the late 80s and 90s [23]. Most materials which exhibit this phenomena are transition metal oxides or Heusler alloys.

1.3.2   Magneto-Transport

The key property of half-metals is that low-bias current (low, so that it only involves a small shift of the Fermi surface) only involves electrons of one spin and is a spin current as much as a charge current. This is naturally of great interest in the field of spintronics. The various magneto-resistance effects AMR, GMR and TMR (anisotropic, giant and tunnelling magneto-resistance) are all commercially useful effects in sensors and other such devices and can be traced back to the band-structure. TMR spin valves in particular have a diverging magnitude of effect when incorporating a half-metallic material: these involve the tunnelling of electrons from a magnetic material with fixed direction of magnetisation, across an insulating barrier, to a magnetic material with a magnetisation which can be changed. These conduction electrons pick up the polarisation direction of the fixed layer. When the two magnetic layers have parallel magnetisation, the resistance is lowest as the polarised conduction electrons have similarly polarised states in the free layer which they can occupy. If the free layer is a half-metal and has anti-parallel magnetisation compared

to the fixed layer, then the resistance will theoretically be infinite as there are **no** minority spin states at the Fermi level in the material. GMR and TMR stacks are discussed again in the simulations chapter.

1.3.3 Magnetic Precession

Something I have not yet mentioned is magnetic moment precession or magnetic resonance. An applied field exerts a torque on a magnetic moment perpendicular to their co-plane such that the magnetisation precesses about the field direction. In addition, real materials have a damping term that causes the motion to lose energy and the magnetisation to fall towards the applied field direction, a typical spiral motion is shown in Figure 1.6. The
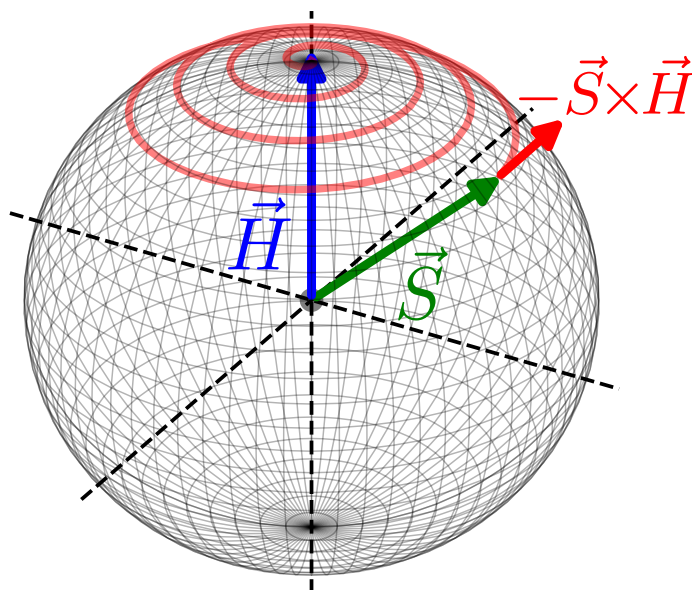
Figure 1.6: The spiral motion of a magnetic moment in an external field due to the torque and intrinsic material damping.

various magnetic interactions in a material, such as exchange and anisotropy, together yield an effective magnetic field, which acts on a given electronic or atomic magnetic moment. If the magnetic moment is not parallel to this field, a torque is exerted, resulting in precession. The frequency of precession depends on the strength of the effective field and thus the magnetic interactions. Kittel solved the equation of motion (discussed at length in the simulation chapter so I will not go into detail here) to obtain the natural resonance frequency using a mean-field approximation and assuming thin film geometry

for ferromagnets and antiferromagnets [24, 25]:

$$\omega_0 = \gamma\mu_0 \left(H_a - M_S\right) \qquad \omega_0 = \gamma\mu_0 \sqrt{H_a \left(H_a + 2H_{ex}\right)} \qquad (1.4)$$

where H_{ex} and H_a are the effective field due to the exchange and anisotropy, M_S is the saturation magnetisation of the material and γ is the gyromagnetic ratio with units of Hertz per Tesla; for free electrons $\gamma_e \approx 28\,\mathrm{GHz\,T^{-1}}$. The effective anisotropy field in the uniaxial (single easy axis) approximation is $H_a = 2K_u/M_S$. These results, while simple and approximate, give a very good idea as to how magnetic precession might occur in materials. H_a is typically of order $1\,\mathrm{T}$ and thus results in resonance frequencies in the 10s of GHz, however, if the saturation magnetisation can be made small while maintaining atomic magnetisation, the frequency can increase. H_{ex} is typically two orders of magnitude higher $\approx 100\,\mathrm{T}$, yielding resonance frequencies in the THz range.

Exchange-driven precession is thus one potential way to access the famed "THz gap"[5]. The frequency of oscillation itself is just one piece of the puzzle, how to excite and control the oscillation is another. Ideally, the oscillation will be optically or electronically controlled and should not be susceptible to the influence of external perturbations.

1.4 The Zero-Moment Half-Metal

One might envision an optimal spintronics material to have:

- A half-metallic band structure, wherein spin-currents are generated simply upon application of a voltage.

- Large intrinsic effective fields due to anisotropy (preferably uniaxial) and exchange.

- No stray field that could effect neighbouring devices in a small scale integrated chip, or be effected by external field.

Such a material is called a zero-moment half-metal (ZMHM) and is not a figment of imagination but a theoretically well-studied and even experimentally demonstrated material.

---

[5]Producing and detecting THz frequency electromagnetic radiation is notoriously difficult, lying in the region between those easily accessible using mature electronic and optical technologies [26]. Bridging the THz gap is an oft-quoted motivating factor in spintronics [27].

ZMHMs were first discussed and predicted by electronic structure calculations by van Leuken and de Groot in 1995 [28]. Many of the predicted materials were Heusler alloys, containing two transition metals and a p-block element, thus providing all the orbital states and unpaired electrons necessary, the difficulty being in growing these materials with the correct crystal structure to realise the effects. Many materials were predicted by DFT or more conceptual arguments to be ZMHMs in the proceeding years [29, 30] but without any success in actually fabricating the materials. The structures assumed in calculations were always unstable or the magnetic properties different in reality than in simulation because of some ignored effects or approximations. This is indeed one of the major downfalls of DFT and similar calculations, they **are** aggressive simplifications of the real, detailed picture and complete spin-polarisation or other binary predictions are often "smoothed-out" in reality for these typically high-entropy materials. Indeed, for the highly-structured, complex and continuous DOS of transition metal compounds to have a significantly large region in energy with absolutely no states for one spin orientation and a non-negligible amount of states for the other spin orientation, and for the Fermi energy to further fall in this region, requires a small miracle of band structure engineering.

With the technological advancement, increasing skill and endless work of scientific researchers in the field however, these miracles become possible. Modern crystal growth techniques, particularly in thin film form, are a far cry from those even 20 years ago. Especially, high-quality deposition facilities are more accessible than previously, with a large number of researchers worldwide being able to add their efforts. The first experimental demonstration of a ZMHM was the material Mn_2Ru_xGa (MRG) fabricated by the magnetism and spin electronics group in Trinity College Dublin in 2014 [31]. Prior to, and since, this discovery, MRG and other Mn-containing Heusler alloys have been thoroughly investigated by our group here in Trinity in a quest to understand, improve and optimise the material and its properties [32, 33, 34, 35, 36].

MRG is not an antiferromagnet but a ferrimagnet as the two antiferromagnetically coupled Mn sublattices lie on chemically inequivalent crystal sites, with Ga or Ru as nearest-neighbour elements respectively: this of course changes the orbitals' hybridisation and occupancy and thus the magnetic properties. The two sublattices exhibit different evolution of their respective magnetic moments as a function of temperature, pressure

and other external parameters. The differing evolution of the magnetisation of the two sublattices with temperature means that there will exist a temperature where the magnitudes of the moments of the two sublattices are equal and thus cancel each other out, resulting in zero net moment for the material, but without the symmetry constraints of a pure antiferromagnet. This "compensation temperature", as it is called, can also be tuned by changing the lattice parameters, composition etc. of the material; we saw earlier how sensitive the magnetic properties are to the crystal structure. This enables a great deal of control over the material properties.

One of the more interesting and unique properties predicted to be exhibited by MRG is current-driven THz-frequency self-oscillations [37, 38]. The low-power oscillating elements, when incorporated in devices with a power source and amplifier, would enable high-speed (albeit short-range due to the nature of electromagnetic radiation, suitable for intra-device or NFC communications) wireless communication at speeds currently unachievable. This is only possible because of the broken inversion symmetry in MRG, a product of its inverse Heusler alloy structure which is not possible in pure antiferromagnets. Thus this **subset** of ZMHMs, the compensated ferrimagnets, are more practically useful due to the spin-orbit coupling effects that can exist in the materials due to the lack of crystal inversion symmetry.

Mn_2Ru_xGa has also been shown to exhibit all-optical-switching (AOS), one of the only rare-Earth-free materials to show this phenomenon. Mn_2Ru_xGa shows deterministic toggle-switching on a sub-pico second timescale without other external stimuli apart from light [39, 40]. This type of non-equilibrium ultrafast dynamics involves multiple degrees of freedom and multiple quasi-particles (electrons, spins, phonons etc.) and understanding the details of energy and momentum transfer involved in this process is part of our motivation.

This harkens back to the common concept of a three-temperature model, where the spin, lattice and electron subsystems are treated as independent but coupled energy baths, this can be extended to a four-temperature model for systems with antiferromagnetically coupled spins. The dynamics of the system are governed by the empirical coupling constants between said baths. The simplicity of this model is its primary strength but for understanding and attempting to control some of the aforementioned more complicated

phenomena, microscopic formalisms of the empirical coupling constants are desired, i.e. the constants $G_{1,2}$ in Figure 1.7 will be replaced with equations from the relevant theories. For example, sd-exchange coupling between the spin and electron subsystems, with the spin and lattice subsystems coupled via magnetocrystalline anisotropy. A fully mi-
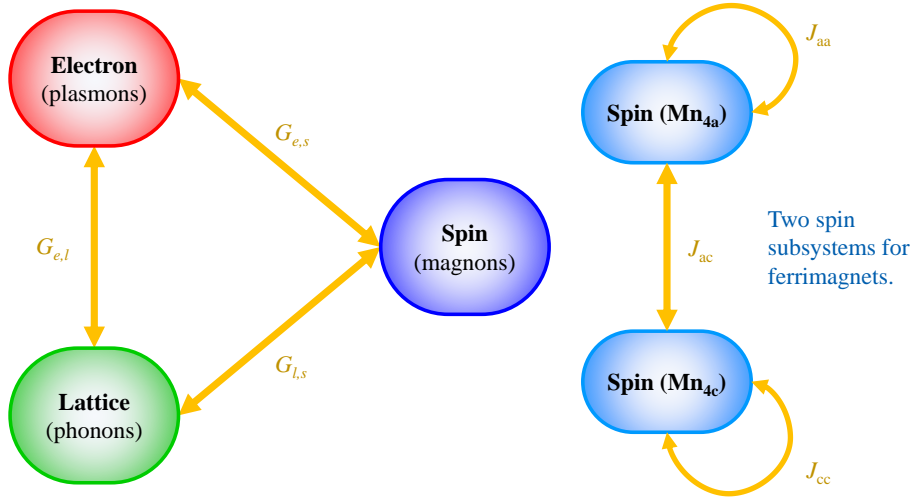
Figure 1.7: A diagrammatic representation of a four-temperature model for coupled subsystems. In a simulation, the dynamics of each would be simulated separately with the influence of the different subsystems on one another treated as external fields or potentials.

croscopic four-temperature model is a lofty goal to strive towards. In the simulations chapter, a comprehensive microscopic description of the dynamics of the spin subsystem is developed, with inclusion of the other subsystems beginning in the later parts of the chapter.

MRG is an extremely interesting and promising material which drove the development of our simulation model, the topic of the second chapter, and is the subject of the majority of the experiments in the third, structural characterisation, chapter. For this reason, it is introduced here, more details about the magnetisation and structure are discussed in the aforementioned chapters.

1.5 Techniques

Some more general techniques, not strictly limited to applications in spin electronics, that I have utilised over the years are Mössbauer spectroscopy and point-contact Andreev spectroscopy.

1.5.1 Mössbauer Spectroscopy

The Mössbauer effect is the ability of nuclei in solids to emit or absorb photons with effectively no recoil, due to the photon energy being low enough not to excite any phonons, and the crystallite which contains the nucleus recoiling as one mass. The recoil energy is reduced by a factor equal to the number of atoms in the crystallite, relative to a free nucleus emitting the same photon, becoming negligible. A radiative nuclear transition which exhibits this effect and has a suitably small bandwidth is capable of precisely probing the hyperfine shifts in nuclear energy levels due to changes in the chemical environment. Mössbauer spectroscopy is most often performed with ^{57}Fe which is a naturally occurring isotope of Fe with an abundance of 2.12%. This first nuclear energy level of this isotope has energy $E = 14.4\,\text{keV}$ with a half-life of $\tau_{1/2} \approx 100\,\text{ns}$. When excited the nuclei can decay via photon emission with a bandwidth of order $\Gamma \approx 5\,\text{neV}$, these photons can then be used to probe the hyperfine shifts in energy levels of other ^{57}Fe nuclei with resolution of order $E/\Gamma \approx 10^{12}$. The penetrative nature of γ-rays means sample can be investigated completely non-destructively and with no surface preparation necessary. As a nuclear probe, this technique is especially complementary to most electromagnetic radiation-based techniques which rely on interactions with the atomic electrons. This technique is an extremely useful and somewhat unique tool for investigating the local structural and magnetic properties of Fe in materials which contain this most famous of magnetic elements, the technique is discussed in great detail in the fourth chapter of this thesis, which is based on our methodology-themed paper recently published in IOP Measurement Science and Technology [41].

The technique was used to study a wide range of materials of interest in the field of spin electronics and general magnetism including $Co_xFe_yB_z$ amorphous ribbons used in high-speed switching power electronics and magneto-oscillators, thick films of the very strong magnet $Nd_2Fe_{14}B$ deposited using a new high-throughput sputtering technique, and tetragonal FeNi (tetrataenite) from meteoritic samples with potential to replace high-anisotropy rare-Earth containing magnets.

1.5.2 Point-Contact Andreev Spectroscopy

Another technique which is of great use and is extremely relevant in the field of spintronics is point-contact Andreev-reflection (PCAR). This is something I spent significant time on at the beginning of my doctoral research but since the start of the COVID pandemic, we have only been able to acquire the liquid He required to perform these measurements for less than a month of combined time and a negligible amount of new results were obtained.

PCAR utilises a superconducting point contact to measure the contact spin polarisation of a material [19]. The sample is mounted on a stage below a Nb (or similar superconductor) wire with a sharpened tip attached to a piezo stepper motor. The apparatus is inserted into a cryogenic chamber and cooled down below the superconducting temperature of Nb at $9.2\,\text{K}$, before the motor is used to lower the wire into the sample, hopefully puncturing any protective oxide layer which has formed. The conductance of the contact is then measured as a function of applied bias of order $\pm 20\,\text{mV}$.

How does this yield information on spin-polarisation? In superconductors, electrons do not travel alone but in Cooper pairs, which experience almost no electrical resistance [42]. These Cooper pairs consist of two electrons with opposite spin. Consider a normal-metal (NM) superconductor (SC) interface with a low-bias current applied. An electron will travel from the NM towards the SC interface and impinge. To conserve charge, momentum and spin, upon generation of a Cooper pair in the SC, an "electron hole" with opposite charge and momentum to the impinging electron is reflected from the interface in the NM. In this case, a charge of $2e$ is transferred across the interface and so the conductance is **doubled** relative to the baseline. The baseline is determined by either the high-bias or high-temperature ($> T_c$) conductance where superconductivity is destroyed. Now consider the NM is replaced by a fully spin-polarised half-metal (HM). When the electron impinges on the interface, there are no states of opposite spin in the HM and so spin cannot be conserved and no Cooper pair is generated: the conductance is completely suppressed. Thus by measuring the conductance of the SC point contact in this technique, the contact spin-polarisation can be obtained. I was personally not able to measure a significant amount of PCAR data from MRG samples or otherwise during my Ph.D. for the aforementioned reasons and I therefore do not devote any more time to the technique in this dissertation, for more information, refer to the thesis of Borisov [20] or the publications

of Soulen et al. [19] and Stamenov [43, 44]. In the future, PCAR measurements may become more popular here if the proposed plan to purchase a closed-loop system (utilising He gas and a compressor rather than liquid He) comes to fruition. This would make running the cryogenic chamber significantly cheaper and less prone to supply-chain issues but with the not-insignificant hurdle that $> €250{,}000$ capital investment is required up front. Proposals for a grant to enable this purchase are being submitted to funding calls when possible.

References

[1] F. Wanlass and C. Sah, "Nanowatt logic using field–effect metal–oxide semiconductor triodes," in *1963 IEEE International Solid–State Circuits Conference. Digest of Technical Papers*, vol. VI, pp. 32–33, 1963. [Cited on page 1]

[2] G. E. Moore, "Cramming more components onto integrated circuits," *Proceedings of the IEEE*, vol. 86, no. 1, pp. 82–85, 1998. [Cited on page 1]

[3] B. Wu and A. Kumar, "Extreme ultraviolet lithography and three dimensional integrated circuit–a review," *Applied Physics Reviews*, vol. 1, no. 1, 2014. [Cited on page 1]

[4] D. Suess, T. Schrefl, R. Dittrich, M. Kirschner, F. Dorfbauer, G. Hrkac, and J. Fidler, "Exchange spring recording media for areal densities up to 10 Tbit/in^2," *Journal of Magnetism and Magnetic Materials*, vol. 290, pp. 551–554, 2005. [Cited on page 2]

[5] M. H. Kryder, E. C. Gage, T. W. McDaniel, W. A. Challener, R. E. Rottmayer, G. Ju, Y.-T. Hsia, and M. F. Erden, "Heat assisted magnetic recording," *Proceedings of the IEEE*, vol. 96, no. 11, pp. 1810–1835, 2008. [Cited on page 2]

[6] K. Yoshida, M. Yokoe, Y. Ishikawa, and Y. Kanai, "Spin–torque oscillator with negative magnetic anisotropy materials for MAMR," *IEEE transactions on magnetics*, vol. 46, no. 6, pp. 2466–2469, 2010. [Cited on page 2]

[7] J. L. O'brien, "Optical quantum computing," *Science*, vol. 318, no. 5856, pp. 1567–1570, 2007. [Cited on page 2]

[8] J. Clarke and F. K. Wilhelm, "Superconducting quantum bits," *Nature*, vol. 453, no. 7198, pp. 1031–1042, 2008. [Cited on page 2]

[9] D. Loss and D. P. DiVincenzo, "Quantum computation with quantum dots," *Physical Review A*, vol. 57, no. 1, p. 120, 1998. [Cited on page 2]

[10] A. Hirohata, K. Yamada, Y. Nakatani, I.-L. Prejbeanu, B. Diény, P. Pirro, and B. Hillebrands, "Review on spintronics: principles and device applications," *Journal of Magnetism and Magnetic Materials*, vol. 509, p. 166711, 2020. [Cited on pages 3, 39, 45, and 46]

[11] B. D. Cullity and C. D. Graham, *Introduction to magnetic materials, Second Edition*. John Wiley & Sons, 2009. [Cited on pages 5, 12, and 14]

[12] J. J. Sakurai and J. Napolitano, *Modern quantum mechanics, second edition.* Addison–Wesley, 2011. [Cited on page 6]

[13] W. contributor: Geek3", "Atomic orbitals spdf m–eigenstates and superpositions.png," 2023. `https://commons.wikimedia.org/w/index.php?title=File:Atomic_orbitals_spdf_m-eigenstates_and_superpositions.png&oldid=806768761`, Accessed 2024–02–09. [Cited on pages x and 7]

[14] J. M. Coey, *Magnetism and magnetic materials.* Cambridge university press, 2010. [Cited on pages x, xii, 7, 9, 10, 12, 15, 32, 38, 40, 41, 42, 49, 56, 66, and 212]

[15] C. R. Jacob and M. Reiher, "Spin in density–functional theory," *International Journal of Quantum Chemistry*, vol. 112, no. 23, pp. 3661–3684, 2012. [Cited on page 9]

[16] P. Langevin, "Magnetism and electron theory," *Ann. chim. et phys.*, vol. 5, no. 8, pp. 68–125, 1905. English translation available from Wikisource. [Cited on page 12]

[17] W. contributor: Zureks, "Bethe–slater curve by zureks.svg," 2023. `https://commons.wikimedia.org/w/index.php?title=File:Bethe-Slater_curve_by_Zureks.svg&oldid=822518318`, Accessed 2024–02–09]. [Cited on pages x and 13]

[18] R. Cardias, A. Szilva, A. Bergman, I. D. Marco, M. Katsnelson, A. Lichtenstein, L. Nordström, A. Klautau, O. Eriksson, and Y. O. Kvashnin, "The Bethe–Slater curve revisited; new insights from electronic structure theory," *Scientific reports*, vol. 7, no. 1, p. 4058, 2017. [Cited on page 14]

[19] R. Soulen Jr, J. Byers, M. Osofsky, B. Nadgorny, T. Ambrose, S. Cheng, P. R. Broussard, C. Tanaka, J. Nowak, J. Moodera, *et al.*, "Measuring the spin–polarisation of a metal with a superconducting point contact," *science*, vol. 282, no. 5386, pp. 85–88, 1998. [Cited on pages 17, 24, and 25]

[20] K. Borisov, *Point–contact Andreev reflection and tunneling spectroscopy using high–field superconductors, topological insulators and compensated ferrrimagnets.* PhD thesis, Trinity College Dublin, 2017. [Cited on pages 17 and 24]

[21] K. Schwarz, "CrO_2 predicted as a half–metallic ferromagnet," *Journal of Physics F: Metal Physics*, vol. 16, no. 9, p. L211, 1986. [Cited on page 17]

[22] J.-H. Park, E. Vescovo, H.-J. Kim, C. Kwon, R. Ramesh, and T. Venkatesan, "Direct evidence for a half–metallic ferromagnet," *Nature*, vol. 392, no. 6678, pp. 794–796, 1998. [Cited on page 17]

[23] J. Coey and M. Venkatesan, "Half–metallic ferromagnetism: example of CrO_2," *Journal of Applied Physics*, vol. 91, no. 10, pp. 8345–8350, 2002. [Cited on page 17]

[24] C. Kittel, "On the theory of ferromagnetic resonance absorption," *Physical review*, vol. 73, no. 2, p. 155, 1948. [Cited on page 19]

[25] C. Kittel, "Theory of antiferromagnetic resonance," *Physical Review*, vol. 82, no. 4, p. 565, 1951. [Cited on page 19]

[26] R. Köhler, A. Tredicucci, F. Beltram, H. E. Beere, E. H. Linfield, A. G. Davies, D. A. Ritchie, R. C. Iotti, and F. Rossi, "Terahertz semiconductor–heterostructure laser," *Nature*, vol. 417, no. 6885, pp. 156–159, 2002. [Cited on page 19]

[27] Z. Feng, H. Qiu, D. Wang, C. Zhang, S. Sun, B. Jin, and W. Tan, "Spintronic terahertz emitter," *Journal of Applied Physics*, vol. 129, no. 1, 2021. [Cited on page 19]

[28] H. Van Leuken and R. De Groot, "Half–metallic antiferromagnets," *Physical review letters*, vol. 74, no. 7, p. 1171, 1995. [Cited on page 20]

[29] S. Wurmehl, H. C. Kandpal, G. H. Fecher, and C. Felser, "Valence electron rules for prediction of half–metallic compensated–ferrimagnetic behaviour of Heusler compounds with complete spin–polarisation," *Journal of Physics: Condensed Matter*, vol. 18, no. 27, p. 6171, 2006. [Cited on page 20]

[30] I. Galanakis, P. Mavropoulos, and P. H. Dederichs, "Electronic structure and Slater–Pauling behaviour in half–metallic Heusler alloys calculated from first principles," *Journal of Physics D: Applied Physics*, vol. 39, no. 5, p. 765, 2006. [Cited on page 20]

[31] H. Kurt, K. Rode, P. Stamenov, M. Venkatesan, Y.-C. Lau, E. Fonda, and J. Coey, "Cubic Mn_2Ga thin films: crossing the spin gap with ruthenium," *Physical review letters*, vol. 112, no. 2, p. 027201, 2014. [Cited on pages 20, 140, and 181]

[32] D. Betto, K. Rode, N. Thiyagarajah, Y.-C. Lau, K. Borisov, G. Atcheson, and Žic, Mario and Archer, Thomas and Stamenov, Plamen and Coey, JMD, "The zero–moment half–metal: how could it change spin electronics?," *AIP Advances*, vol. 6, no. 5, 2016. [Cited on pages 20 and 69]

[33] K. Borisov, D. Betto, Y.-C. Lau, C. Fowley, A. Titova, N. Thiyagarajah, G. Atcheson, J. Lindner, A. Deac, J. Coey, *et al.*, "Tunnelling magnetoresistance of the half–metallic compensated ferrimagnet Mn_2Ru_xGa," *Applied Physics Letters*, vol. 108, no. 19, 2016. [Cited on page 20]

[34] C. Fowley, K. Rode, Y.-C. Lau, N. Thiyagarajah, D. Betto, K. Borisov, G. Atcheson, E. Kampert, Z. Wang, Y. Yuan, *et al.*, "Magnetocrystalline anisotropy and exchange probed by high–field anomalous Hall effect in fully compensated half–metallic Mn_2Ru_xGa thin films," *Physical Review B*, vol. 98, no. 22, p. 220406, 2018. [Cited on pages 20 and 64]

[35] C. Banerjee, N. Teichert, K. Siewierska, Z. Gercsi, G. Atcheson, P. Stamenov, K. Rode, J. Coey, and J. Besbas, "Single pulse all–optical toggle switching of magnetization without gadolinium in the ferrimagnet Mn_2Ru_xGa," *Nature communications*, vol. 11, no. 1, p. 4444, 2020. [Cited on page 20]

[36] J. O'Brien, A. Naden, K. Siewierska, B. Ouladdiaf, J. M. D. Coey, K. Rode, P. Stamenov, and G. Atcheson, "Exchange–driven anomalous magnetism in epitaxial Mn_2Ru_xGa." in prep, 2023. [Cited on page 20]

[37] R. E. Troncoso, K. Rode, P. Stamenov, J. M. D. Coey, and A. Brataas, "Antiferromagnetic single–layer spin–orbit torque oscillators," *Physical Review B*, vol. 99, no. 5, p. 054433, 2019. [Cited on page 21]

[38] S. Lenne, Y.-C. Lau, A. Jha, G. Y. Atcheson, R. E. Troncoso, A. Brataas, J. Coey, P. Stamenov, and K. Rode, "Giant spin–orbit torque in a single ferrimagnetic metal layer," *arXiv preprint arXiv:1903.04432*, 2019. [Cited on pages 21 and 69]

[39] C. Banerjee, N. Teichert, K. Siewierska, Z. Gercsi, G. Atcheson, P. Stamenov, K. Rode, J. Coey, and J. Besbas, "Single pulse all–optical toggle switching of magnetization without gadolinium in the ferrimagnet Mn_2Ru_xGa," *Nature communications*, vol. 11, no. 1, p. 4444, 2020. [Cited on page 21]

[40] C. Banerjee, K. Rode, G. Atcheson, S. Lenne, P. Stamenov, J. Coey, and J. Besbas, "Ultra-fast double–pulse all–optical reswitching of a ferrimagnet," *Physical Review Letters*, vol. 126, no. 17, p. 177202, 2021. [Cited on page 21]

[41] J. O'Brien, H. A. Baghbaderani, F. O. Keller, N. Dempsey, L. H. Lewis, and P. Stamenov, "Backscatter mössbauer spectroscopy with simultaneous X–ray and γ–ray detection." in review, 2023. [Cited on page 23]

[42] L. N. Cooper, "Bound electron pairs in a degenerate Fermi gas," *Physical Review*, vol. 104, no. 4, p. 1189, 1956. [Cited on page 24]

[43] P. Stamenov and J. Coey, "Fermi level spin–polarization of polycrystalline thulium by point–contact Andreev reflection spectroscopy," *Journal of Applied Physics*, vol. 109, no. 7, 2011. [Cited on page 25]

[44] P. Stamenov, "Point–contact Andreev reflection from semimetallic bismuth: the roles of the minority carriers and the large spin–orbit coupling," *Journal of Applied Physics*, vol. 113, no. 17, 2013. [Cited on page 25]

Chapter 2

Atomistic Magnetics Simulations

2.1 Motivation

Observation is the basis of science and empirical evidence will always trump simulated results, however, simulations do and will always have a place in research. In particular, experiments which are very difficult or expensive and have well-developed theories, such as magnetic neutron scattering from polycrystalline thin films, are good candidates for confirmation via simulation. Simulations of physical equations provide a fast and inexpensive method to investigate phenomena and compare materials. From the invention and proliferation of computers through to the current information age, simulations and computations constitute an ever-increasing proportion of physics research and for good reason. Making a particular thin-film stack with the desired accuracy requires access to deposition and characterisation facilities typically costing millions, while experimental procedures often take months to optimise. On the other hand, in 2023 anyone with access to a computer can perform simulations and test variations of that same stack. A small workstation with excellent computation ability will cost in the tens of thousands, while access to large-scale supercomputer facilities for a limited time can be obtained for a modest fee. Of course, simulations **always** involve some approximation of physical reality, but the results obtained are nonetheless invaluable and in particular can help serve as a guide to experimental work. The speed and ease of exploring a vast amount of parameter space once the underlying equations are coded means a huge amount of results can be simulated and compared to observations to see which simulated microscopic event matches the ob-

served effect most closely, this is especially useful in the development of new materials to help understand the underlying mechanisms, see e.g. Barker et al. [1].

In materials science and especially magnetism, there are traditionally three distinct paradigms when it comes to simulations: macroscopic, microscopic and atomistic, with the newer atomistic approach becoming more popular in recent times with increasing computer power [2]:

- Macroscopic simulation deals with averages and so-called mean field models which makes it easy to simulate large volumes quickly, this is especially useful for things like magnetisation reversal and domain structure simulation of relatively simple materials [3, §7]. Of course, the typical materials in modern investigations are not at all simple and the focus on nanoscopic and quantum phenomena means macroscopic models are becoming less useful.

- The microscopic approach is essentially an extension to the macroscopic approach where the material parameters can vary spatially but the variation is confined to be smooth (or slow), such that it remains continuous and integrable. This framework allows the simulation of features down to the sub-micrometre (100s of nm) +range including the domain structure in many materials and shape effects.

- Atomistic simulations consider the interaction of magnetic moments on individual atoms in a material. This is obviously the most accurate approach as no averaging or assumptions are made which could obscure nanoscale effects that are observed in reality and is actually conceptually easier as the discrete interaction terms between individual magnetic dipoles are very simple[1]. The issue arises when one considers the sheer number of atoms which must individually be considered. A cube of Fe with side length $10\,\mathrm{nm}$ contains 85000 atoms. Due to the long range ($1/r$) of some magnetic effects including the demagnetisation field, the interaction of each atom with every other atom must be considered. If we then consider dynamics where the energy and fields must be computed for many thousands of time steps, the calculations quickly become prohibitive, but can still be performed on scales of 10s of nanometres and

---

[1]This is neglecting higher-order (quadrupole or octupole) expansions. This is a reasonable approximation for many systems, such as $3d$ transition metals, but not necessarily for more complicated alloys which may contain multiple $4f$ and $3d$ elements, where the shape of the electronic orbitals comes into play.

nanoseconds with modern supercomputers. The atomistic approach is the only truly justifiable approach when considering non-collinear or ferrimagnetic materials where the magnetisation is not continuous, or when considering ultra-fast processes [2, 4].

The frontier of magnetic simulations showcases startling parallels with the famous technological "THz Gap", which says there are no devices which operate efficiently at THz frequencies, roughly between the electronic and optical regimes. Magnetism has long been a proposed medium to bridge the gap, but perhaps not coincidentally, the simulation of THz phenomena is also less than trivial. True "deep-theory" approaches like DFT already take days to compute a small number of static atoms on a periodic grid at zero temperature and cannot be used for dynamics. Complex and cumbersome Hamiltonians which can accurately describe all the phenomena necessary for fast dynamics can generally only be propagated by numerical integration methods in time-dependent simulations for 100000s of steps (with size typically below $\Delta t = 0.01\,\text{fs}$) before the diverging build-up of errors due to the finite precision of computers and especially of methods such as FFTs [5]. So these types of microscopic dynamics simulations can go up to roughly $10^5 \times 0.01\,\text{fs} = 1\,\text{ps}$, i.e. a single period of a THz oscillation, which is not enough to gain an accurate picture. More simple simulations or manually normalising the results at each step can circumvent this problem, but are not ideal methods. The necessary continuity constraints of micromagnetic approaches also precludes effects that occur faster than high GHz speeds.

In this chapter, I will discuss existing simulation models and programs, before describing my own and discussing some specific results that were obtained and their significance.

2.1.1 Existing Magnetics Simulations Programs

I will briefly discuss a few of the most common and useful existing magnetic simulation frameworks/programs, how they are programmed, their intended strengths and their usefulness and shortcomings. In general, the equations solved are partial differential equations (PDEs) which describe the evolution of some property (in this case magnetisation) with time.

2.1.1.1 OOMMF

The Object Oriented Micro Magnetics Framework (OOMMF) was first released, by the US government backed NIST, in 1998 and has been one of the most widely used magnetics simulations programs since then [6]. OOMMF uses a finite-difference mesh to compute large volumes efficiently. Different meshing techniques and their strengths are discussed by Sjodin [7]. Meshing is the concept of dividing a large volume into a manageable number of cells or elements, or equivalently averaging over chunks of atoms, to enable simulation at a macroscopic scale. Finite-difference methods divide a volume into a grid of points and essentially perform a Taylor-expansion of the PDE at each point, generating finite-difference equations. This is a relatively easy method to implement and can be made more accurate by increasing the number of points in the grid and the order of the integrator, but does not deal well with complex geometries or non-uniform grids or parameters, which vary sharply in space or time. The program is written in C++ for efficiency, with a user interface written in the tk/tcl language. The main draw of this program is its robustness and maturity that come with development over multiple decades by a world-leading institution. It was somewhat dated in appearance and perhaps less accessible compared to other newer programs but there have been many extensions and interfaces written, such as a Python interface by Beg et al. [8]. In addition, OOMMF version 2.0 was released in beta in 2022 and represents a significant modernisation of the software.

2.1.1.2 MuMax3

MuMax3 is a newer framework for micromagnetic simulations which also uses the finite-difference discretisation method. The primary purpose of MuMax3 was to leverage the power of modern GPUs (graphics processing units) to speed up computation. The software is written in the GO and CUDA languages, the latter being specific to NVIDIA-brand GPU architecture [9]. For large-enough meshes, the use of GPUs can speed up calculations by an order of magnitude or more compared to CPUs, forming a kind of middle ground between typical PCs and supercomputer clusters but much closer to the price point of typical PCs. The software also has a web browser interface and, generally, an increased accessibility that one would associate with a newer software. The aforementioned update to OOMMF

may make the accessibility battle a lot closer.

2.1.1.3 VAMPIRE

The VAMPIRE software package is another new package which facilitates the atomistic simulation of magnetisation dynamics [10]. The program focuses both on efficiency (necessary for atomistic simulations) and accessibility, where the experiment to be simulated is defined by a number of commands written in an input file. It is written in C++ with a large but well-organised and well-commented code-base, which is a big positive, as one can quite easily find the bare code for any calculation of interest. This is the most actively developed project meaning it regularly changes and has features added. While there are numerous good ways to perform many basic experiments, there are still many features missing, partly as a result of the focus on accessibility: it was very simple to define a bcc, fcc or amorphous lattice using a built-in command but there was no easy way to define a custom unit cell structure in the past. When I briefly used VAMPIRE 4 in 2019 the documentation was rather poor as it had not caught up with development. Now with VAMPIRE 6, the number of commands and importantly their documentation appears to have greatly increased, making VAMPIRE a truly accessible and useful tool limited primarily by the intrinsic limits of atomistic simulations. VAMPIRE has found particular use for modelling small-size phenomena and ultra-fast demagnetisation, both of which are far easier to do with an atomistic approach [11, 12].

2.1.1.4 Others

There are, of course, many other downloadable programs and software for magnetics simulations, I have only discussed the (arguably) most popular ones here, which happen to be finite-difference and atomistic based. The excellent MuMax3 review [13] lists and references many others, including finite-element based programs. Finite-element solutions are generally less efficient and slower than finite-difference, but can be more useful for complex shaped materials as a uniform grid is not needed and resolution can be increased in specific areas and decreased elsewhere as needed.

A more recent development in micromagnetics is the Landau-Lifshitz-Bloch (LLB) equation, where the effect of temperature is intrinsically included in the derivation via the

Curie-Weiss equations, allowing for the length of the magnetic moment vectors to change [14]. This is therefore not a Heisenberg model where the lengths are constant. This method is now seeing some adoption in the canonical programs listed above as it brings micromagnetism a step closer to atomistic simulations whilst maintaining the performance advantage, at the cost of a significantly more complex underlying theory.

2.1.2 Greater Context of Simulations

It is beneficial to comment on the connection of the simulations described later in this chapter with other calculations, experiments and real-world materials. When considering input values for the parameters in the simulations, there are essentially two options which we follow: either choose values close to those observed in or calculated for real materials, or choose values so that simulations can be performed in the desired region of phase space without necessarily corresponding to a specific material, to verify model correctness for example.

Concerning magnetic parameters in MRG, namely exchange and anisotropy, a mixture of calculations and observations can help inform the values for input parameters. Anisotropy in particular can be derived from measurements of magneto-transport effects [15], while exchange is primarily directly calculated by *ab initio* methods (DFT) while being restrained by magnetisation or resonance measurements. Careful MFT (mean field theory) fitting of precise magnetisation data can help to determine the different exchange (inter and intra sublattice) parameters in MRG or similar materials [16]. Magnetisation measurements are particularly difficult for low moment materials however and high fields (¿ 50 T) are desired.

Regarding the input parameters for the electronic part of the Ehrenfest dynamics simulations in section 2.3, there is one particular method of fixing the values. Extensive DFT simulations have been performed on MRG over the years and it is known that the Δ_1 and Δ_5 hybridised bands are the most prominent at the Fermi level, for example see calculations of Stamenova on the related but simpler material Mn_3Ga [17]. Since we used a TB (tight-binding) model for the Ehrenfest dynamics, we can fit the TB model to the dispersions calculated by DFT, adjusting parameters to get a close match, thus the parameters for the electronic part of the simulations correspond to the real-life (or as close

as DFT can get) MRG material. Incidentally, one way to gain experimental insight into the electronic states at the Fermi level is PCAR measurements.

In terms of **outputs** from the ultrafast dynamics simulations, the main in-house comparative technique we have is TR-MOKE (time-resolved magneto-optical Kerr effect) which can be used in particular to measure demagnetisation. The main issue is that many of the simulations are based on the assumption of being close to the Fermi energy, while laser-induced thermal excitation relies on massively inflating the electronic temperature. "THz-in THz-out" experiments are the next step up but would require access to a FEL (free-electron laser), which are in high-demand.

With this commentary in mind, the rest of the chapter can proceed more clearly with more obvious context for the simulations described.

2.2 Atomistic Magnetic Simulation Model

All the popular existing software have their own ideal use cases but they all fall into the common trap of making specific niche simulations quite difficult or involved, in exchange for general accessibility and broad applicability to simple problems. For this reason it is not uncommon to write ones own software, which can do a very specific job adequately, while not being as efficient or nearly as widely applicable as a published software package. This is what I did, starting in earnest over the COVID lock-down in 2019. The code, which will described in the coming sections, was based on one initially written by my supervisor Prof. Stamenov, using the engineering software MathCad 15 [18]. This version of the intuitive and surprisingly performant software was first released in 2010 but as of 2021 is no longer supported[2]. I re-wrote and extended the code in Python, making it more generally accessible and adaptable with especially more input/output options.

2.2.1 Theory

The materials I and most of the spintronics group in Trinity are interested in are primarily ferrimagnetic materials. This class of materials, and the related antiferromagnets, obviously do not have spatially continuous magnetisation so atomistic simulations are an easy

---

[2]MathCad was originally released in 1986 and was one of the first live-editing interactive notebook interfaces for calculations

choice. In an atomistic model, the only interactions we have to consider are between pairs of spin vectors, which makes the physics quite simple.

An optimal balance between complexity and performance can be obtained using a classical Heisenberg model of the spins [19]. In this kind of model, the spins are treated as constant length vectors which can rotate freely in $3d$ Cartesian space. It is a very intuitive model which nonetheless captures many of the key physical aspects of spin dynamics. Physically, the Heisenberg model is applicable to localised spins, such as exist in insulating materials or the deep-lying $4f$ electrons of the rare-Earths. Generally, if the electrons which contribute to the magnetisation and conduction can be separated at least to first order, the Heisenberg Hamiltonian can be used. Exchange interactions between the localised magnetic electrons and mobile conduction electrons can be included via an $s - d$ model, where the letters refer to the energy sub-levels hosting the electrons. For materials with orbital hybridisation of the s and d bands, a tight binding model which explicitly includes site-hopping would be more appropriate. Treating the entire electronic band structure as a whole is the next level up, this is necessarily the most accurate model but for dynamics simulations is impractical. Different models and their applicability are discussed by Coey [3, §5.2,§5.3]. Generally, "electron", "spin" and "lattice" processes occur at different timescales (roughly $< 1\,\text{fs}$, $100\,\text{fs}$ and $> 1\,\text{ps}$ respectively) and can be considered independently. There are many instances where this is not the case, for instance some models for ultra-fast demagnetisation where the magnetisation lowers faster than the exchange interaction should allow. A different model that does not assume classical spins is necessary for proper modelling, such as the pd-band model of Töws and Pastor [20].

The classical Heisenberg model is by far the most common approach due to its simplicity, with most existing programs such as VAMPIRE using it by default. From here on, I use $\vec{S}$ and $\vec{H}$ to denote the atomic spin vector and perturbing field.

2.2.1.1   Equation of Motion

An equation of motion is needed so we can simulate the dynamics of the magnetic moments by numerical integration. A starting point is that the rate of change of the orientation of

the magnetic moment is directly proportional to the torque on it:

$$\frac{\partial \vec{S}}{\partial t} = \gamma \vec{\tau}$$

The torque on a magnetic moment in a magnetic field is simply $\vec{\tau} = \vec{S} \times \vec{H}$. In real-materials, there is also a damping term which tends to align the moment with the field. The damping is driven by quantum mechanical spin-lattice relaxation events and so is included phenomenologically in this classical model, defined as perpendicular to the precession via another cross product: $\vec{\tau} = \vec{S} \times \vec{S} \times \vec{H}$. The origin of the damping is the transferral of angular momentum from the localised spins to the lattice system via conduction electrons ($s-d$ scattering), this naturally depends on the resistivity and therefore the temperature, as well as just how localised the polarised electrons are ($3d$ versus $4f$) [21, §2.4.1]. The equation of motion was formulated by Landau and Lifshitz [22] and then the damping altered by Gilbert [23] to give the LLG equation:

$$\frac{\partial \vec{S}}{\partial t} = -\frac{\gamma_i}{1 + \alpha_i^2} \left[\vec{S}_i \times \vec{H}_i + \alpha_i \vec{S}_i \times \left(\vec{S}_i \times \vec{H}_i \right) \right], \qquad (2.1)$$

where i denotes a particular atom and γ and α are the atom-specific gyromagnetic ratio and damping parameters respectively, which can be temperature and frequency dependent. Numerical integration of this equation with a suitably small time step will yield the time evolution of the magnetic moments and is the key process in magneto dynamic simulations. The above form is a common one due to the relative ease of numerical integration [24]. The effective field $\vec{H}$ in the LLG equation has a number of terms, which depend on the Hamiltonian, for each atom through [4, §3].

$$\vec{H}_i = -\frac{1}{\mu_i} \frac{\partial \mathcal{H}_i}{\partial \vec{S}_i} \qquad (2.2)$$

Within the Heisenberg Hamiltonian, which described the energy of the system, there are many physical terms that can be included, depending on whether they are expected to be significant for a given material and experiment, for example:

$$\mathcal{H} = \mathcal{E}_{ex} + \mathcal{E}_{an} + \mathcal{E}_{Ze} + \mathcal{E}_{DM} + \mathcal{E}_{d},$$

where the five terms come from the direct exchange, the magnetocrystalline anisotropy, the Dzyaloshinsky-Moriya (antisymmetric superexchange) interaction, an external field and the demagnetising or dipole field, respectively. Now we need expressions for each of these energy terms to complete the model.

2.2.1.2 Hamiltonian Energy Terms

Exchange The most important magnetic interaction is of course the exchange interaction. It arises from the overlap of the wavefunctions of electrons and the Pauli exclusion principle, where the spin part of the wavefunction must have the opposite polarity (symmetric or antisymmetric) to the spatial part to satisfy that the total wavefunction be antisymmetric for the Fermionic electrons. The exchange interaction strength is proportional to the difference in energy between the symmetric and antisymmetric states, which depends on the spatial extent of the electron orbitals and generally on the details of the atomic energy levels. For complex realistic materials, the interactions become numerous and complicated, especially when orbital hybridisation is involved and it is best to empirically determine the strength of the exchange interaction [3, §5.2]. DFT and other tight-binding models which consider the entire electronic band structure can **estimate** the exchange strength between different pairs of atoms. Heisenberg's generalised equation simply relates the energy to the cosine of the angle between the **spin operators** of two atoms, or equivalently, their vector dot product, for a particular atom i:

$$\mathcal{E}_{ex,i} = -\sum_j J_{i,j} \left(\vec{S}_i \cdot \vec{S}_j \right), \tag{2.3}$$

where $J_{i,j}$ is the strength of exchange between atoms of type i and j and we sum over all other atoms in the system. Practically, exchange is a short-range interaction so the sum is only over nearby atoms, usually nearest and second-nearest neighbours, or extending to some specific cut-off distance.

Magnetocrystalline Anisotropy The $3d$ and $4f$ orbitals, that contain the unpaired electrons which lead to magnetism, are typically oblong in shape. In a typical crystal structure consisting of atoms on discrete positions, the orbitals of a central atom pointing in certain high-symmetry directions with respect to the surrounding ions and their orbitals

will be stabilised. Then, through spin-orbit coupling, the spin moment of the central atom gains preferred directions of orientations [3, §4.4]. Uniaxial anisotropy is the most interesting for the majority of applications due to its binary nature, with two low energy states and a barrier between them. This form of anisotropy will often suffice to model materials with a long axis such as many hexagonal materials, like Co, or tetragonal lattices. For the $3d$ elements, the magnetic electrons are in the outer shells, close to the surrounding ions, which create the crystal field. This is why the orbital moment is quenched for the $3d$ magnetic elements and why the crystal anisotropy is strong than for the rare-Earth elements. The latter have magnetic $4f$ shells, which are closer to the nucleus, with more shielding relative to the $3d$ electrons. Due to its crystal lattice origin, magnetocrystalline anisotropy can be described by an expansion in terms of the direction cosines of the crystal [3, §A.H]. Conventional forms of the uniaxial [25] and cubic [10] anisotropy used in calculations are given below. Note that only even terms are permitted by time-reversal symmetry and uniaxial anisotropy starts at second order, while cubic anisotropy starts at fourth.

$$
\begin{aligned}
\text{Uniaxial}: \quad & \mathcal{E}_{an,i} = -K_{u2,i}\left(\vec{S}_i \cdot \vec{e}_{k,i}\right)^2 - \frac{K_{u4,i}}{12}\left[35\left(\vec{S}_i \cdot \vec{e}_{k,i}\right)^4 - 30\left(\vec{S}_i \cdot \vec{e}_{k,i}\right)^2\right], \\
\text{Cubic}: \quad & \mathcal{E}_{an,i} = -\frac{1}{2}K_{c4,i}\left(S_{ix}^4 + S_{iy}^4 + S_{iz}^4\right) + K_{c6,i}\left(S_{ix}^2 S_{iy}^2 S_{iz}^2\right),
\end{aligned}
\tag{2.4}
$$

where K_i are the (empirically determined) anisotropy constant of various orders and $\vec{e}_k$ is the uniaxial anisotropy unit vector, for which the system energy is lowest when parallel with the spin moment. This form of anisotropy is local and so there is no summing over adjacent atoms.

Zeeman Interaction This is the most simple term in the Heisenberg Hamiltonian, simply equal to the energy of a magnetic dipole in an external field.

$$
\mathcal{E}_Z = -\mu_0 \vec{S}_i \cdot \vec{H}
\tag{2.5}
$$

A common convention is to assume the spin moment is in unit of Bohr magnetons μ_B, so the Hamiltonian remains with energy units.

Dzyaloshinsky-Moriya Interaction   The DMI is an antisymmetric exchange interaction first described by Dzyaloshinsky in 1957 [26]. After Anderson proposed a new theory for superexchange in 1959 [27], exchange between two cations mediated through a non-magnetic anion, Moriya was soon able to rigorously derive the DM interaction by including spin-orbit coupling (SOC) in Anderson's theory using a second order perturbation method [28]. The interaction is described by the simple formulae:

$$\mathcal{E}_{DM} = \vec{D}_{i,j} \cdot \left(\vec{S}_i \times \vec{S}_j \right) \qquad \vec{D}_{i,j} = -J_{DM} \left(\hat{r}_{ik} \times \hat{r}_{jk} \right), \tag{2.6}$$

and interestingly has lowest energy penalty when the two spins are aligned perpendicularly. This very interesting result implies that the DM interaction can stabilise non-collinear magnetic structures and indeed is the reason for the very small magnetic moments observed in some materials, which should otherwise be antiferromagnetic such as αFe_2O_3 [26]. In addition, DMI helps to stabilise chiral domain structures and skyrmions, which can lead to some interesting effects [29]. DMI is frequently encountered in the interfacial form, whereby the inversion symmetry is inherently broken by the interface and a heavy metal, such as Pt or W, with large SOC can populate the opposite side of the interface to the magnetic atoms, as illustrated in Figure 2.1.

Whether the spins cant towards or away from one another depends on the sign of J_{DM} and therefore on the heavy metal and magnetic element chosen [30]. The strength of this interaction, thanks to its SOC origins, is roughly two orders of magnitude less than the direct exchange [3, §5.2.1]. It is not always included in calculations but given the interest in chiral and topological effects in recent years, any simulation software would be remiss to exclude the effect.

Dipole (Demagnetising) Interaction   Perfectly aligned magnetic moments results in a large stray field and increased in free energy which is combated by the dipole field. The dipole field at an atom is the sum of the contributions from all other atoms, as usual:

$$\mathcal{H}_{d,i} = -\mu_0 \vec{S}_i \cdot \vec{H}_{d,i} \qquad \vec{H}_{d,i} = \frac{1}{4\pi} \sum_{j \neq i} \frac{3}{r_{ij}^3} \left[\left(\vec{S}_j \cdot \hat{r}_{ij} \right) \hat{r}_{ij} - \vec{S}_j \right] \tag{2.7}$$
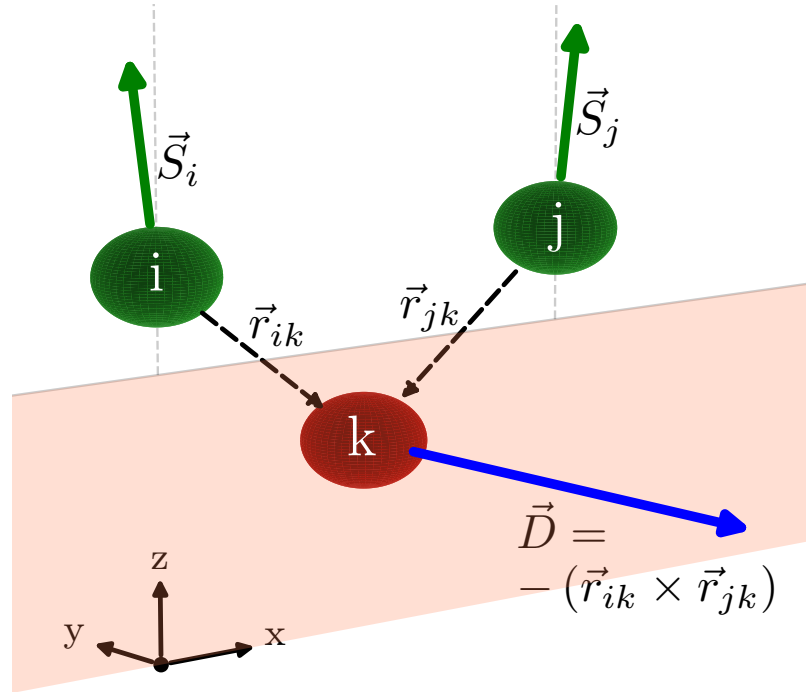
Figure 2.1: An illustration of interfacial DM interaction between two spins S_i and S_j, mediated by superexchange through an atom k with positive J_{DM}. The finite angle between the spins results in a non-zero cross-product and a reduction in energy via Equation 2.6. The signs are chosen by convention. Note that $\vec{S}_i \times \vec{S}_j$ is directed along the y-axis so $\vec{D}_{i,j} \cdot (\vec{S}_i \times \vec{S}_j)$ is negative and the energy is lowered, if J_{DM} was negative, the spins would be canted towards one another rather than away.

Contrary to the short-range (exponential) exchange and local anisotropy terms, the r^{-3} fall-off of the dipole interaction means it is long-range. This is not ideal as it means the contribution from every other atom must be considered for each atom, and is the slowest part of the calculation in atomistic simulations. Often, the authors of publications concern themselves with nanoparticles or antiferromagnets, where the dipole field is negligible, or use some micromagnetic approximation [4, §2].

2.2.1.3 Other Torques

Some effects are not related to an energy density and more readily included directly as torques to be added to Equation 2.1. These include the spin-torque terms which are due to currents flowing through the material. There is much interest in controlling magnetic moments and structures directly through currents as there is far greater scope for miniaturisation in devices compared to attempting to control the magnetisation via stray fields. After Manchon et al. [31, §II.A], a convenient way to include the torques in

the equation of motion is via:

$$\vec{T} = \tau_{FL}\vec{S} \times \vec{\xi} + \tau_{DL}\vec{S} \times \left(\vec{S} \times \vec{\xi}\right), \tag{2.8}$$

where FL and DL refer to the field-like and damping-like components of the torque, respectively. Field-like means it acts similar to an external field and tends to cause the moment to precess while the damping-like tends to align the moment with the field. This formula can be used to model most types of spin-torques, with the vector $\vec{\xi}$ depending on the microscopic origin of the torque. The near-identical form of this equation to the LLG equation is striking and not a coincidence. It is convenient to describe the spin-torque phenomena as a two-step process, first the polarisation of moving conduction electrons and second the effect of the local magnetic field produced by the conduction electrons on the localised magnetic electrons.

STT   The simplest current related torque is the spin-transfer-torque (STT) due to Slonczewski [32]. As the name suggests this involves the transfer of angular momentum from strong magnetic "reference" layer to another layer. The geometry is illustrated in Figure 2.2.

The geometry is identical to GMR (giant magneto-resistance) stacks because of the similar underlying physics. A conducting barrier must be used (as opposed to the tunnelling barriers which yield the largest MR) because an insulating spacer simply does not allow enough energy to transfer through to affect the free layers magnetisation. The combination of MR and current-based switching is finding commercial use in STT-based MRAM (magnetic random access memory) devices, wherein a small current can read the MR and a large current can reverse the free layer magnetisation via the STT.

SOT   A second class of spin-torques are the spin-orbit torques (SOT). With this fundamentally different phenomenon, the SOC plays a more direct role in polarising the conduction electrons and a second polarising magnetic layer is not required. Additionally, the SOT effects can be separated into those due to intrinsic and extrinsic SOC, the latter usually involving a heavy-metal layer. SHE (spin hall effect) and iSGE (inverse spin galvanic effect) are extrinsic effects due to spin-dependent scattering and broken symmetry
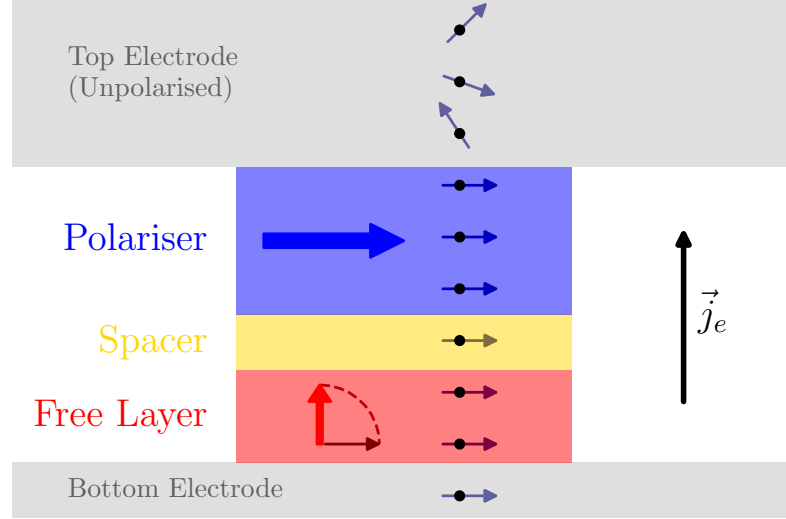
Figure 2.2: STT requires a CPP (current perpendicular to plane) geometry and a magnetic reference layer which is strongly pinned or damped to polarise the conduction electrons without itself being deflected. These polarised electrons then cross a (conducting) barrier and exert a torque on a second magnetic layer. The angular momentum is transferred simply by exchange in both magnetic layers, as the mechanism is the same, the reference layer must be more strongly pinned.

at an interface respectively. Intrinsic SOC can be provided by the Rashba and Dresselhaus effects, which are similar to iSGE but result directly from the broken inversion symmetry of the magnetic crystal [33].

The SHE is due to spin-dependent scattering of an electric current in a material with SOC, the up and down electrons are deflected transverse to the direction of current flow in opposite directions, resulting in a pure-spin current transverse to the electric current [21]. This can then be treated essentially the same way as STT, its just the origin of the polarisation that is different. Importantly, this effect is experimentally realised in a CIP (current in plane) geometry, which changes the practical picture for device applications. For example, in a switching device, the large switching current pulse has to be passed through the thin-film stack, which degrades the interfaces and limits the device lifetime. If the same device uses SOT switching, then only the reading current passes through the stack and there is essentially no degradation.

A magnetic crystal with a non-centrosymmetric space group can exhibit intrinsic SOC, resulting in a spin-current which exerts a torque on the magnetisation, through the Rashba
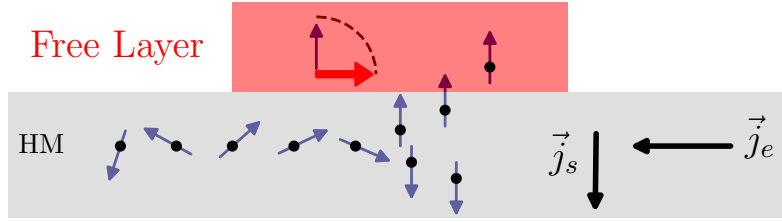
Figure 2.3: An SOT switching device, such as one shown here which utilises the SHE, has a CIP geometry. Crucially, this means that the large "write" current does not need to pass through the stack of delicate thin layers as in the STT case, thus improving longevity. The non-magnetic HM layer (W, Pt etc.) provides the SOC which creates the transverse spin-current.

or Dresselhaus effects [33]. Additionally, in strained thin films, which would otherwise be centrosymmetric, the entire volume can be non-centrosymmetric due to the changing lattice parameter. We saw earlier that the SOT can be considered as a magnetic field to determine its effect on the local magnetisation. I will not go into the detailed quantum mechanics of the SOC, but linear response theory says that the magnetic field can be related to the electric field by a tensor and following Neumann's symmetry principle, the tensors have to have the same symmetry as the crystal point group [21, §III.B]. The tensors can then be expanded in the direction of the magnetisation for each crystal point group, as has been done by Železný et al. [34]. If one knows the symmetry of their crystal, the SOT due to intrinsic SOC can be described using the matrices calculated by Železný et al., with the strength of the SOC usually determined experimentally, except for simple systems which can feasibly be calculated using DFT.

A last point of interest about SOT effects: in the linear response theory, since the effective field from the SOC can be expanded in terms of the local magnetic moments, a staggered local field can be generated on alternating atomic sites thanks to the broken inversion symmetry [35]. This allows for the control of antiferromagnetic and ferrimagnetic magnetic sublattices, which can not be influenced by a globally uniform field, whether that be an applied Oersted field or STT injected polarised current. This is probably the main reason for the current interest specifically in SOT devices.

Non-Adiabatic Spin-Torque A type of spin torque due to Zhang and Li is the non-adiabatic spin-torque due to current moving in a spatially varying magnetisation [36]. Conceptually this is a quite simple phenomenon again due to the exchange coupling between conduction electrons and local magnetisation. A conduction electron can be polarised by the local magnetisation at site 1, then move to site 2, and if site 2 has a different magnetisation than site 1, the conduction electron can exert a torque on said magnetisation, torquing it towards the direction of site 1. This means that, in a domain wall (DW) for example, moving electrons will tend to drag the DW along with them.
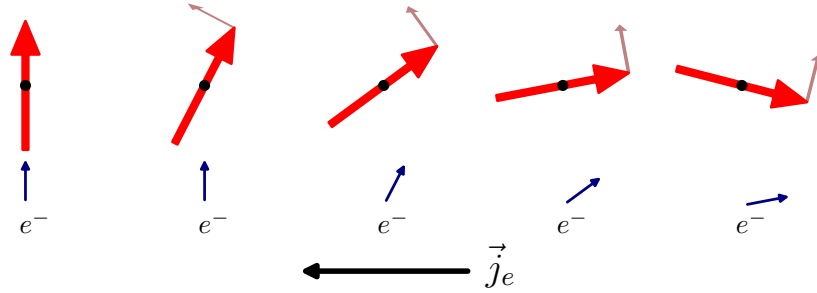
Figure 2.4: As the electrons move from left to right, they are polarised by each local magnetisation site they come too. In aligning to the magnetisation of each subsequent site, they exert a reactionary torque on that site towards the orientation of the previous site. This results in DW motion opposite to the direction of current flow (with the electrons).

The non-adiabatic torque can be included via an equation of the form:

$$\vec{T} = b_J \vec{S} \times \left[\vec{S} \times \left(\vec{j_e} \cdot \vec{\nabla} \right) \vec{M} \right] - c_J \vec{S} \times \left(\vec{j_e} \cdot \vec{\nabla} \right) \vec{M}, \tag{2.9}$$

which is then added directly to the LLG Equation 2.1. Note that this equation has the same form as the aforementioned torques but with the current density times the spatial derivative of magnetisation replacing the effective field. The magnitude of the effect (the terms b_J and c_J) depends on a number of material parameters, including the spin-current polarisation, the current density, the spin-flip relaxation time and the exchange relaxation time.

Temperature The effect of finite temperature is a difficult one to include. The LLB equation mentioned in subsubsection 2.1.1.4 includes finite temperature in a physically reasonable but complex way. The usual way of including temperature in atomistic simula-

tions is using Langevin dynamics and adding a temperature-dependent stochastic effective field, which then contributes to the torque in the LLG equation. This field is typically uncorrelated Gaussian white noise, to emulate the random effects of temperature fluctuations. However, it has been pointed out that the thermal fluctuations are correlated with the atomic properties at the atomic level due to the mutual interactions of the atomic, electronic and magnetic systems, and this has implications for ultra-fast processes that might occur at timescales of the order of the integration step $\Delta t < 1\,\mathrm{fs}$ [10]. In fact, using *coloured* noise rather than white noise can help to alleviate this problem, that is, biasing the Gaussian distribution towards lower or higher energy depending on the problem at hand [37]. We have chosen not to include these temperature effects in our model at the current time as we are not so interested in temperature dependent processes compared to phenomena that can be modelled with a $T = 0\,\mathrm{K}$ assumption, so the added complexity is not necessary. Later in the examples section, we show how a perturbing "energy pulse" can effectively be simulated directly through the applied field or current term.

2.2.1.4   Atoms

As mentioned, one of the primary reasons for choosing atomistic simulations is the ability to naturally simulate ferrimagnetic materials and high-frequency phenomena. Two (at least) distinct sublattices are required with different material parameters (magnetic moment, exchange and anisotropy strength, etc.). Physically this is trivial and the practical implementation will be discussed later.

The number of interaction included in the Hamiltonian and the cut-off distance chosen will dictate the number of parameters for each atom. For a simple simulation of two sublattices using only nearest-neighbour, first order uniaxial anisotropy and not including any current-dependent terms, there will be nine parameters: the nearest-neighbour exchange strength, anisotropy constant, DMI constant and magnetic moment for each sublattice and the inter-sublattice exchange constant. Hereafter I will use the example of the material MRG when discussing different terms, as this has been the main material of focus for my simulations. Recall that MRG is a Heusler alloy with anti-ferromagnetically coupled Mn atoms on the $4a$ and $4c$ Wyckoff positions, as these sites are chemically inequivalent, the magnitude of the magnetic moments are different, making this a ferrimagnetic material.

The subscripts a and c are used to denote the sublattice that specific material parameters apply to. For example, the nearest-neighbour inter-sublattice exchange constant is J_{ac} while the intra-sublattice second nearest-neighbour exchange would be J_{aa2} and J_{cc2}. The strength of the pair-wise exchange interactions in MRG were estimated by Siewierska et al. [38] using a mean-field model, they are of order $10\,\mathrm{K}$ and are used to emulate a "real material" in the following.

Initially, we simulated a 1D chain of fixed-position Heisenberg spins, to test the code and remove the need for optimisation. Extending to more dimensions of course massively slows down simulations. Material parameters were constant, making the simulation very simple but nonetheless allowing the investigation of different magnetic configurations for the atomic chain, thus providing a proof of concept.

A second iteration of the code calculates the exchange energy depending on the distance between atoms, using an oscillating potential reminiscent of the RKKY interaction [3, §5.2.2]. This is applicable to Mn atoms, the sign of whose exchange constant is strongly distance-dependent [39]. To make use of this distance-dependence exchange, the atomic positions can be allowed to change with an exponential restoring force similar to the Lennard-Jones potential [40] pushing them back into position. If the pairwise exchange between neighbouring atoms and the resulting effective fields are recalculated after every time step, then we can effectively simulate coupled magnon-phonon interactions, something which is very rarely attempted: generally the concept of "atoms" does not even exist in magnetic simulations, only the spins and their magnetic/electric interactions are considered. Additionally, including phonons in micromagnetic simulations where the material is averaged over substantial volumes is of course impossible. Of course, this greatly increases the calculation time and requires substantial optimisation of the code.

2.2.2 Implementation

2.2.2.1 Programming Language

The choice of how to implement the numerical simulations and in particular what programming language to use is not important in the initial proof-of-concept stage. When extending the model to larger simulations or including more long-range (including many

atoms) effects, the efficiency of computation becomes very important. Our simulation code was initially written using the engineering software MathCad 15 [18]. This is a very visual software whose GUI (graphical user interface) is reminiscent of a sheet of paper and is therefore quite accessible for those with engineering or physics backgrounds, who are not necessarily experienced programmers. In addition, many of the back-end algorithms are optimised *compiled* code and thus very fast [3]. While it has some advantages, MathCad is an old piece of software and the pen-and-paper style makes for limited options especially for data visualisation and input/output. For better control when exploring the very broad parameter space, better presentation of the results and much better accessibility, a Python [41] version of the code was also written.

Python is an interpreted language which is run in real time by the Python Interpreter. Code can be tested "on-the-fly", allowing for very quick and easy testing as one is writing. Python avoids the usual speed penalty of interpreted languages via a plethora of libraries which are imported and called by the interpreter. In particular, the NumPy (numerical Python) library [42] introduces vectorised arrays into Python: mathematical operations on or with these arrays is automatically delegated to highly-optimised compiled machine code, vastly speeding up computation time. Compiled extensions can also be manually written in languages such as C and called from within Python. Another comparatively rarely discussed benefit of NumPy is that code can be written in a format that closely resembles the mathematical form, thanks to the vectorisation, making the implementation of physical equations yet easier/more intuitive. For visualisation I use the package matplotlib [43], which is a powerful but user-friendly plotting interface which makes the production of vector (capable of infinite scaling) images trivial

More recently, to speed up computation and enable the extension of the code to more dimensions, a number of the heavy computation functions were written in the OpenCL language, an open-source standard for parallel computation [44]. This is a C-style language, wherein the written code is first compiled to a general intermediate format and a local compiler can detect the hardware capabilities of the current system and compile the intermediate code to execute across multiple available CPU and GPU cores simultaneously,

---

[3]Compiled code is written and then converted to low-level CPU instructions before being executed and is by far the fastest type of code. *Interpreted* code uses a large and heavy (in computation terms) software engine to interpret written code in real time and execute it, this is necessarily much slower but a lot easier to write and test.

allowing automatic and highly parallel computation on a plethora of platforms. Provided the code is written in a fashion which can be parallelised, this can allow for a speed-up of orders of magnitude. As an example, numerical integration cannot be parallelised as each step depends on the previous state and steps have to be performed one at a time, however, the numerous calculations within each step can be performed simultaneously across multiple available computing cores, be they on the CPU or GPU.

2.2.2.2 Integration

In order to propagate the dynamics of the system, the LLG partial differential equation (Equation 2.1) must be numerically integrated with a suitably small time-step. The various forms of numerical integration follow from the basic property of calculus that as one "zooms in" on a continuous function (reduces the range of the independent variable), the function will more closely approximate a linear one. This is equivalent to a first order Taylor expansion. The premise with propagation by integration is that the differential equation which specifies the derivative is complicated and not directly integrable so we choose a small enough step size and assume the function is approximately linear at the length scale and thus we can calculate the next point only having knowledge of the slope at the current point.

The most fundamental version of this is Euler integration, which is exactly the method stated above. Here I use the usual notation with the time step $h = \Delta t$ and the derivative function written as $\frac{dy}{dt} = f(y, t)$. The value of the function at every point in time can be iteratively determined using the unintegrable derivative function via:

$$y_{i+1} = y_i + hf(y_i, t_i)$$

where $t_{i+1} = t_i + h$. So long as the time step h is sufficiently small, this method should work for any continuous function, however, more complex algorithms can achieve better results.

There are many established algorithms but two of the main families are the Runge-Kutta (RK), or predictor-corrector, and Adams-Bashforth (AB), or linear multistep, methods. RK algorithms are single-step algorithms which use the derivative at multiple intermediate steps to minimise the local error due to truncation and obtain a better prediction

while the multistep algorithms rather remember the positions and derivatives at previous steps and use a linear combination of previous derivatives to predict the next step. An excellent overview of these algorithms can be found at their respective Wikipedia pages [45, 46]. Their applicability and implementation is discussed from a more practical point of view by Press et al. [47, §16]. I will describe the fourth order versions of both here:

Runge-Kutta 4	Adams-Bashforth 4
$f_0 = f(y_0, t_0)$	$f_0 = f(y_0, t_0)$
$y_1 = y_0 + f_0 \frac{h}{2}$	$y_1 = y_0 + f_0 h$
$f_1 = f(y_1, t_0 + h/2)$	$f_1 = f(y_1, t_0 + h)$
$y_2 = y_0 + f_1 \frac{h}{2}$	$y_2 = y_1 + (3f_1 - 1f_0) \frac{h}{2}$
$f_2 = f(y_2, t_0 + h/2)$	$f_2 = f(y_2, t_0 + 2h)$
$y_3 = y_0 + f_2 h$	$y_3 = y_2 + (23f_2 - 16f_1 + 5f_0) \frac{h}{12}$
$f_3 = f(y_3, t_0 + h)$	$f_3 = f(y_3, t_0 + 3h)$
$y_4 = y_0 + (f_0 + 2f_1 + 2f_2 + f_3) \frac{h}{6}$	$y_{i+1} = y_i + (55f_i - 59f_{i-1} + 37f_{i-2} - 9f_{i-4}) \frac{h}{24}$
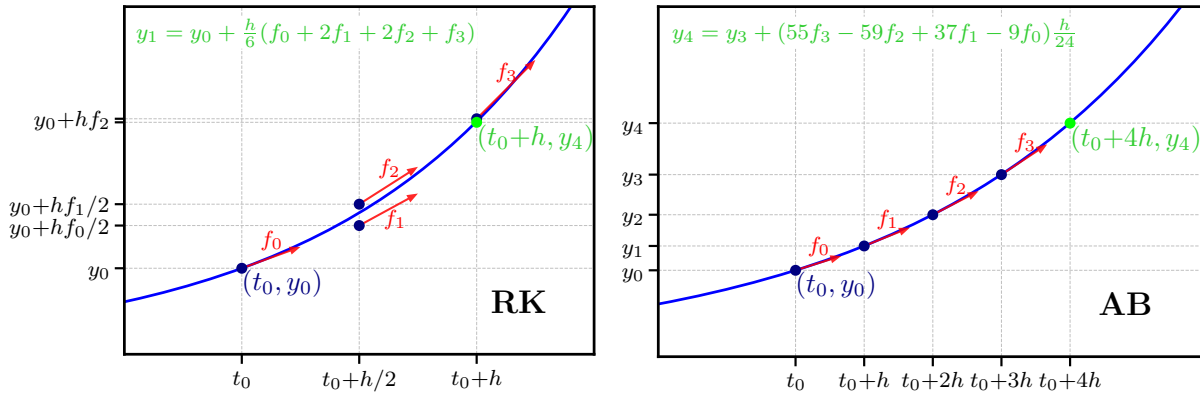
Figure 2.5: An example of numerically integrating the differential equation $\frac{dy}{dt} = y$ with $t_0 = 2$ and $y_0 = e^2$, using the two fourth order methods defined above. In order to cover the same range, the step h is four times smaller for the AB method. Note that the derivative needs to be evaluated four times per range. Both methods give an accurate answer despite the large step size here.

There are a number of practical differences between the methods, the AB method is a multistep method which uses linear combination of n previously calculated positions and derivatives to calculate the next step, for n^{th} order. This has the downside that the first few steps are not as accurately approximated as there are no previous derivatives to consider. After the initial stage, propagation is simple and done via one equation. In the classic RK

method as described above, each step is a function of a number of intermediate steps and calculations, the intermediate steps are discarded after the final step is obtained. One of the key benefits of this and other single-step methods is that *adaptive stepping* is trivial to implement. Adaptive stepping estimates the error in the previous step by finding the difference between methods of order n and $n-1$. If the error is small, the step size can be increased and vice versa, this can allow for far faster convergence of integral problems [47, §16.2]. Another advantage is that there is no need to save previous derivatives, in case memory efficiency is a large issue. Both methods are *explicit* in that the next position is calculated directly from previous or intermediate steps as opposed to solving a system of equations.

In addition to accuracy, the other key characteristic of numerical integration methods is the stability, which quantifies how fast error builds up due to small discrepancies, which might be due to very rapidly changing slope or simply floating point errors from the finite precision computer numbers. Both being fourth order, the two methods described above are again similar, the AB method can be more accurate for very smooth functions while the RK function is more adaptable. For my simulations, I tended to use the third or fourth order AB method as it was quite easy to implement and offered sufficient stability, as well as being faster as only one derivative is calculated per step. My Python code for a number of different order AB methods can be found on my GitHub [48]. It is worth noting that the VAMPIRE simulation software utilises the Heun's method, which is a second order RK method, which they decided offered an optimal trade-off of efficiency and accuracy [10, §4.3]. A short-but-sweet comparison of different numerical integration methods can be read courtesy of Fathoni et al. [49].

In the future, implementing the RK4 method with an adaptive step could prove useful. One can envisage this might be particularly suitable for simulating the time evolution of a system returning to equilibrium after an initial sharp perturbation, the rate of change of the system should steadily decrease and become more smooth over time, meaning larger steps could provide enough accuracy and therefore speed up the simulation of a given time period. An analogy be made with the finite element method in micromagnetics, where a material can be split into large or small regions as necessary to use computing power where it is needed the most.

A last point is that, when dealing with stochastic equations, such as the LLG equation with the random temperature field included, additional considerations are required to ensure convergence. Specifically, the magnitude of the spin must be conserved, this is most easily done simple by normalising the magnitude at each time step. Such a brute force method is rather inelegant, though effective, and utilising a more complicated *implicit* method would be mathematically preferable. Another point is that integration of an ODE with a stochastic element is non-trivial. The wide range of frequency components in a Gaussian random field can easily confuse adaptive-step algorithms with their noise. Technically, stochastic equations with white noise should not be integrated using conventional calculus but Itô calculus [50][51, §4], but usually this complicating factor is ignored, which is justifiable for short-time integration using small uniform step size. Regardless, as mentioned, we have not used the temperature dependent LLG equation so have not had to consider this point.

The first results reported here are all from a 1D chain of Heisenberg spins with fixed atomic positions. This simple one-dimensional analogue is easy to understand and visualise as well as being computationally very cheap, allowing a wide swathe of parameter space to be investigated relatively quickly. Despite the simplicity, many complex phenomena can be investigated in this 1D analogue. Another point in the favour of reduced-dimensional models is that modern technological devices are tending towards low dimensions as well: thin films layers can often be considered as effectively 2D, sometimes being a single monolayer thick, while nanowires constitute 1D systems and nanodots can be treated as 0D in some cases.

Regarding the Hamiltonian, the only terms that are included in **all** simulations are the nearest-neighbour inter-sublattice and intra-sublattice exchanges (J_{aa}, J_{cc} and J_{ac}), second order uniaxial anisotropy (K_a and K_c (The $u2$ subscript of Equation 2.4 is dropped in place of a ferrimagnetic sublattice denomination)), the DMI (J_{DMa} and J_{DMc}) and the applied field (B). Other terms that are included for a particular simulation are introduced when relevant. This 1D ferrimagnetic model can be easily visualised, see Figure 2.6. It is important to stress that the while the supposed physical layout of the atoms is 1D in this model, the spins are still $3d$ Heisenberg classical spins.

The relative strengths of the different terms can change depending on the material in
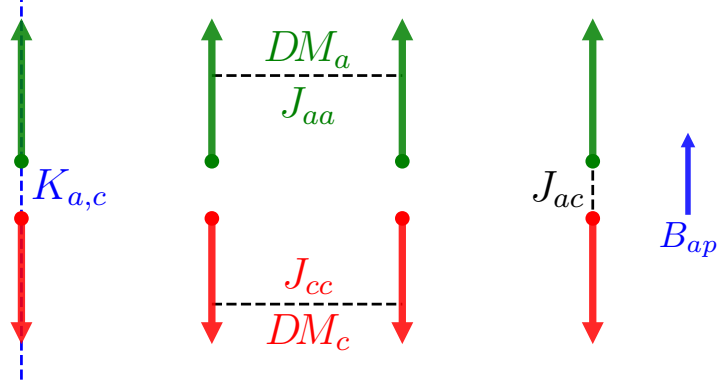
Figure 2.6: A diagram illustrating the default system, with interatomic interactions in red and green respectively, while the macroscopic interactions (which are the same for all atoms) are in blue. The usual way this is treated in the simulations is with the spin unit vectors of the two sublattices stored in two $N \times 3$ arrays where N is the number of atoms. This simplifies things as the first array index is then effectively the position of the atom.

question, but a comparative table is given below, with values for FePt from Strungaru et al. [52] and Mryasov et al. [53], GdFeCo alloys from Ostler et al. [54] and Evans et al. [4], and values for MRG from Siewierska et al. [38] or Fowley et al. [16]. Terms such as the **temperature field**, **STT** and indeed the **Zeeman** interaction of course depend on the size of the temperature, current and field respectively, but are generally similar in strength, at around $0.1 \, \text{meV}$.

Table 2.1: The relative strengths of some of the material-dependent interaction terms in the LLG Hamiltonian for an atomistic spin model. Strungaru et al. used a nearest neighbour model for FePt with the exchange raised to give the observed Curie temperature, so the exchange parameter is inflated due to containing higher-order terms. The huge anisotropy is thanks to the large spin-orbit coupling of the heavy metal Pt.

	FePt	GdFeCo	MRG
Exchange (intra-sublattice)	$42 \, \text{meV}$	$28.1 \, \text{meV}$	$2 \, \text{meV}$
Exchange (inter-sublattice)	*NA*	$-6 \, \text{meV}$	$-2.1 \, \text{meV}$
Anisotropy	$1.47 \, \text{meV}$	$0.05 \, \text{meV}$	$0.1 \, \text{meV}$
DMI	$0.05 \, \text{meV}$	$0.01 \, \text{meV}$	$< 0.01 \, \text{meV}$

Another bonus of the 1D layout is that by putting time on the second axis, the evolution of the system can be visualised in a 2D colour map, although to view all Cartesian

projections of the spin on both sublattices, a minimum of six plots would be required.

2.2.3 Skyrmion Simulations

Though not directly relevant to MRG, there is a huge amount of interest in chiral magnetism and effects in the present-day [55]. Chiral magnetic structures are often topologically protected, i.e. they sit in an energy minimum due to the geometric orientation of the spins. Chiral domain walls (DWs) and skyrmions [56] are the two quintessential examples of chiral magnetic structures, with DWs representing a 180° rotation of the local magnetisation while skyrmions represent a full 360° rotation.
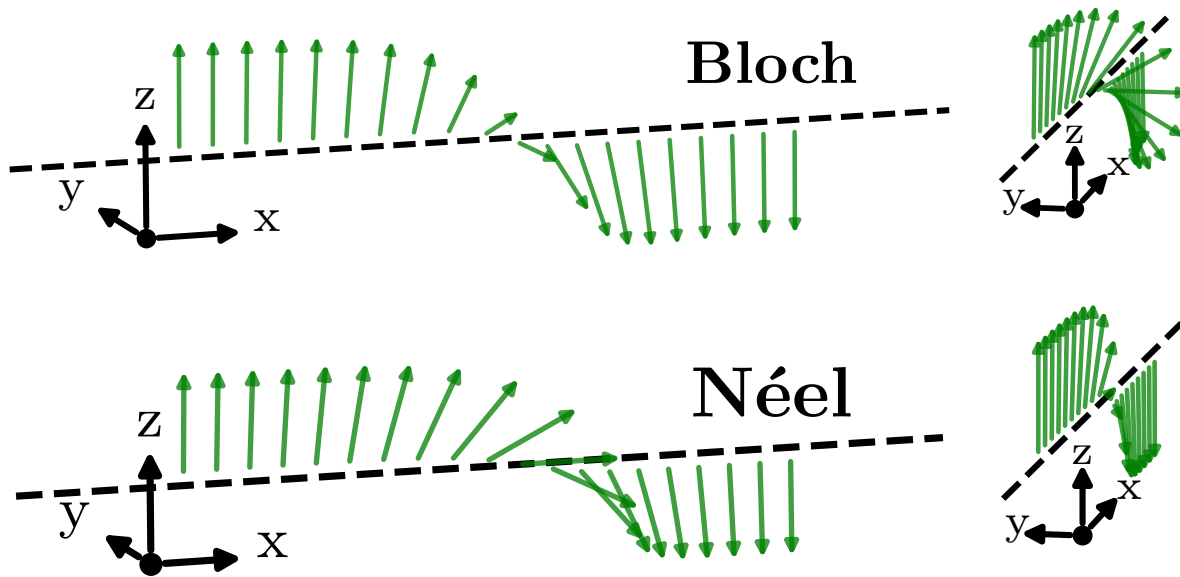
Figure 2.7: An illustration of Bloch (top) and Néel (bottom) magnetic DWs. If we assume the magnetisation is switching from up to down in the x direction, and the black dashed line is the x axis: in the Bloch wall, the magnetisation rotates around x while in a Néel wall, it rotates around y. See also figure 7.5 of Coey [3].

These configurations can more easily be observed by separately plotting the x, y and z projections as lines on a 1D graph:

Skyrmions can be thought of as two DWs stuck together, with the caveat that the DWs must have the same chirality. Their topologically protected nature comes from the fact that they cannot be annihilated via a continuous deformation of their host field, as per their original definition by their namesake Tony Skyrme [57] in the context of quantum field theory. This chirality is enforced by the aforementioned DMI, caused by SOC in
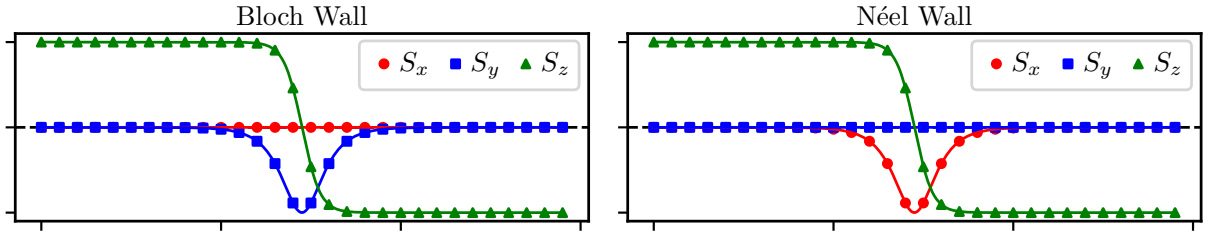
Figure 2.8: The Cartesian projections of typical Bloch (left) and Néel (right) magnetic DWs.

tandem broken inversion symmetry that is intrinsic to the crystal structure or due to an interface. For an excellent illustration of the four basic types of skyrmion (right-hand
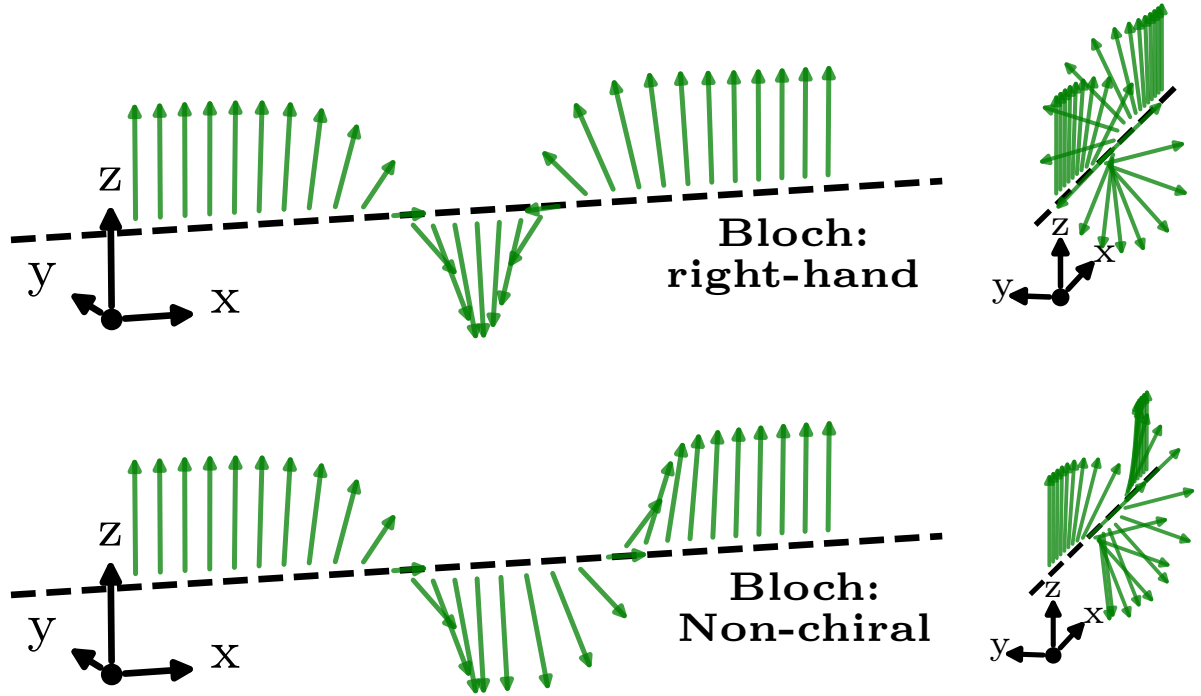
Figure 2.9: An example of a Bloch skyrmion with right handed chirality (top) and a joining of two DWs with different chirality (bottom). It is clear from the side-on view that in the non-chiral version, the magnetisation can be made uniform via rotation without crossing an energy barrier - there is no topological protection. In the skyrmion case, assuming the spins at the ends of the chains are fixed, the magnetisation can only be made uniform by rotating two neighbouring spins away from each other, resulting in a large exchange-driven energy barrier.

and left-hand chiral Bloch and Néel skyrmions) see figure 1 of Chen at al. [58].
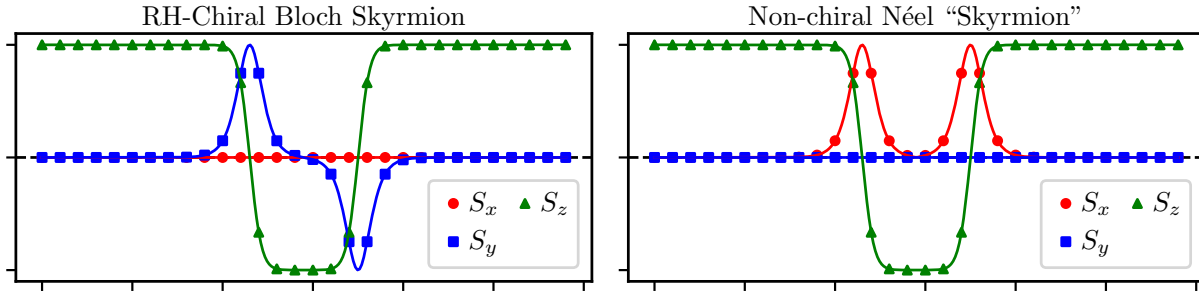
Figure 2.10: The Cartesian projections of right-hand chiral Bloch skyrmion (left), and non-chiral Néel (right) quasi-skyrmion.

2.2.3.1 Procedure

We wished to investigate the stability and size of skyrmions as a function of the material parameters within the framework of our model. The method we choose for this was to impose a skyrmionic state as an initial condition and then let the system evolve by numerically integrating. The x-axis is chosen as the direction in which the spins are placed and the z direction is the axis along which the spins are aligned (so the uniaxial anisotropy or applied field axis). For the Bloch skyrmions, the spins rotate around x through the yz plane, while for the Néel skyrmions, the spins rotate around y through the xz plane. The initial state was defined by the equation:

$$\vec{S}_i = \cos\left[\frac{\pi}{2}\tanh\left(\frac{i+r}{w}\right) - \frac{\pi}{2}\tanh\left(\frac{i-r}{w}\right)\right]\hat{e}_z + \sqrt{(1 - S_z^2)}\,\hat{e}_\sigma, \qquad (2.10)$$

where $\sigma = x$ or y, r is the skyrmion radius and w is the wall width. This is an approximation which is very close to the analytical solution computed by energy minimisation and since this is a dynamic simulation the true solution should be obtained over time in any case. For chirality, S_σ can be multiplied by a step function centred on the middle of the skyrmion to swap the sign on one side. The second sublattice is defined with slightly reduced magnitude and antiferromagnetic coupling as $S_c = -0.85S_a$. A 1D chain of atoms of length $N = 100$ was simulated for each sublattice, with the initial skyrmion diameter equal to 22 atoms. Both types of chiral skyrmion and also a non-chiral DW pair were tested.

Regarding the material parameters, we choose "average" values for the exchange similar to typical FM or AFM materials: $J_{aa} = 30.4\,\text{meV}$ and $J_{ac} = -20.27\,\text{meV}$. A large

anisotropy value of $K_{a,c} = 0.95\,\text{meV}$ was chosen (same for both sublattices), close to those observed in heavy-metal containing materials, and a very large DMI of $J_{DM} = 0.61\,\text{meV}$ was chosen. The latter two parameters were chosen to ensure the simulations were performed in the correct phase space that skyrmions might be stabilised, rather than corresponding to one specific material, values observed in real materials can be compared in Table 2.1. The Damping parameter α was set to unity (critical damping) as opposed to a realistic value to accelerate the relaxation to the equilibrium state, a realistic value (closer to $\alpha \approx 0.1$) is only needed when simulating a time-dependent phenomena. The time step was chosen to be $1\,\text{fs}$, again smaller is not needed as no fast dynamics are expected during relaxation. The time step can equivalently be set to 1 and the exchange constant 20 in the meV fs unit system (as opposed to SI: J s).

2.2.3.2 Results

Firstly it is interesting to consider the evolution of a pair of DWs with opposite chirality, what I have been referring to as a quasi-skyrmion. This spin configuration is not topologically protected and thus is not expected to be stable and indeed, this is what was observed.
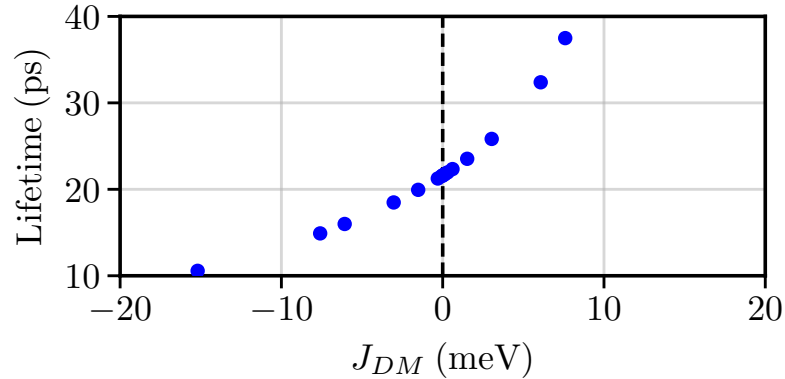
Figure 2.11: Time taken before skyrmion radius diverges in the relaxation simulation for non-chiral quasi-skyrmions. The fact that non-chiral spin configurations are not stable is a promising result for the model and the implementation of the various energy terms. The lifetime increases for increasing DMI strength and appears to start diverging (indicating stability) for large values, the values around $J_{DM} = 0$ are more realistic, as we know DMI is a spin-orbit correction to the exchange and should be orders of magnitude smaller.

Secondly, we tested Bloch and Néel skyrmions for a range of anisotropy and DMI

strengths to observe the equilibrium size after relaxation by integrating the LLG equation. The results are shown in a colour-map: The results are quite interesting: clearly,
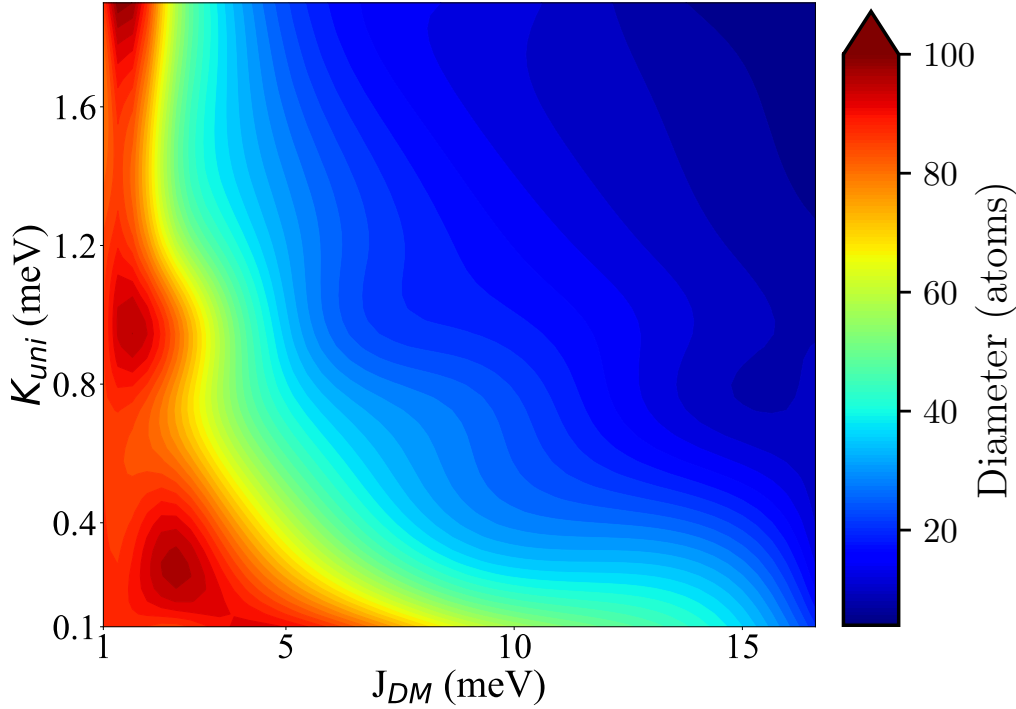
Figure 2.12: This colour diagram shows the equilibrium skyrmion diameter, the value of $2r$ obtained by fitting the final profile with Equation 2.10, for various values of J_{DM} and $K_{a,c}$. Equilibrium is deigned to have been reached when r and w no longer change significantly over roughly 100 time steps (only a few hundred steps are usually saved to save memory and post-processing time). The simulations performed resulted in an irregular grid of points being measured in this range and the "wobbles" in the colour-map are artefacts of the interpolation of the plotting software.

increasing DMI strength tends to reduce the equilibrium skyrmion size, there is a rather sharp threshold above which the skyrmion was stable over the length of the simulation. Below around $3\,\mathrm{meV}$, a stable skyrmion state was not found as the skyrmion increased to near the size of the lattice used. The DMI strength which facilitated stable skyrmionic configurations was an order of magnitude larger than the values observed in real materials, perhaps emphasising that a perfect 1D chain of spins, though useful to consider, is not always an accurate analogue to the real world. Larger values for the uniaxial anisotropy led to a greater area of stability in the phase space shown in Figure 2.12. The anisotropy did not have a huge effect on the skyrmion size except for small values less than $\approx 1\,\mathrm{meV}$.

At the upper end of the energy scale investigated, when the DMI constant is greater than roughly half the ferromagnetic exchange constant, the skyrmion is no longer stable

and collapses on itself on a fs timescale. This makes sense intuitively, as the favourable angle between adjacent spins increases with increasing DMI coupling constant, this canting becomes stronger than the anisotropy and the spins rotate away from the easy axis. At some point the ferromagnetic exchange will take over and a "spin-flop" will occur within the centre of the skyrmion, which only extends over a couple of atoms at very high DMI strength. Following collapse there were many residual oscillations or magnons (see subsection 2.2.4) propagating through the spin chain due to the energy released by the abrupt spin reordering.

Following Rohart and Thiaville [59], if we assume the magnetisation is confined in the xz plane, then the micromagnetic energy density for a 1D chain of atoms can be expressed as

$$E(\theta(x)) = \int_{x_A}^{x_B} \left[A \left(\frac{\partial \theta}{\partial x} \right)^2 - D \frac{\partial \theta}{\partial x} - K \cos^2 \theta \right] dx, \tag{2.11}$$

this equation is not considering a second sublattice, but since there were no external perturbation in in our investigation of the skyrmions and the lattice was assumed to be collinear, the results should still apply. From this equation we can see that the rate of rotation of the spins, equivalent to the sharpness of the skyrmion, is increased or decreased depending on the sign of the DMI, matching up with our intuitive picture.

Higher-Dimensional Lattice   The properties of skyrmions in a 2D lattice was considered by Wang et al. [60]. There is an additional energy term in that case due to the curvature of the DWs which form the rim of the skyrmion and the skyrmion diameter tends to **increase** with increasing DMI strength. As succinctly explained by Kim et al. [61], a primary function of the DMI is to lower the energy cost of DWs thus enabling the skyrmion to smooth out, there is no other consideration for the 1D case. However, in the 2D case, the area of the DW also increases for increasing skyrmion size even if the shape of a cross-section through the wall remains constant, an area (r^2) related effect which cannot occur in 1D. This is the reason for the discrepancy between the two dimensionalities.

The results we obtained using the LLG equation and an 1D atomistic approach are therefore consistent with results in literature, which are dominated by energy minimisation techniques in 2D and occasionally micromagnetics simulations using OOMMF or other standard software packages.

2.2.4   Magnon Simulations

Magnons are a collective excitation of a system of coupled spins. They can be thought of as quasiparticles which constitute localised, slightly out-of-phase, coherent rotation of neighbouring spins. They arise essentially because, due to the sinusoidal variation of the projection of the spin vector onto an axis as it rotates away from said axis, the energy penalty from the exchange interaction due to the misalignment of neighbouring spins is minimised by having a small misalignment spread across a number of spins instead of a large misalignment of one spin. Coupled with Larmor precession in the event of an effective field, this results in the coherent and slightly out-of-phase rotation of the spins. An illustrative example of a magnon in a 1D lattice of spins is shown in Figure 2.13. Here the wavelength of the magnon has a defined meaning, as illustrated by the red line.
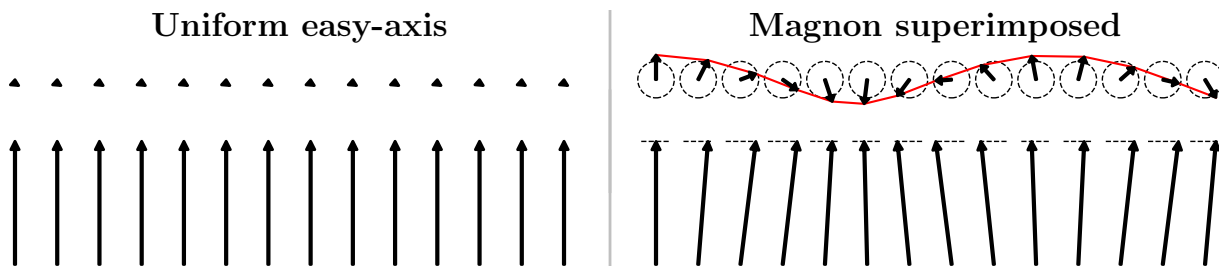
Figure 2.13: A 1D lattice of spins in an uniform spin state aligned along the vertical easy axis (left) and the same with a magnon mode (right), showing a top-down and side-on view of the spins. The magnitude of the canting away from the easy axis is exaggerated for clarity.

The frequency of the magnon describes how fast the spins oscillate around the circular path shown while the wavevector describes how close in phase adjacent spins are. The wavevector therefore determines how far from parallel alignment the adjacent spins are, meaning the energy of a basic magnon monotonically increases with increasing wavevector due to increased penalty from the exchange. For more complicated magnon modes in lower-symmetry directions, especially in non-cubic lattices, the dependence of the energy on the wavevector can be non-trivial.

One of the main promising features of ferrimagnetic spintronics materials is the potential for high-frequency dynamics. Conventional magnons occur when ferromagnetically aligned spins rotate about the applied or magnetocrystalline field with a very small misalignment between neighbouring spins. Antiferromagnets possess an additional mode

wherein the spins within each sublattice remain aligned but a finite angle appears between the spins in opposing sublattices such that they are no longer anti-parallel. In this case, the restoring force comes from the, usually very strong, inter-sublattice exchange (J_{ac}, which is always $\gg k_u$), which permits high energy (and therefore high frequency) oscillations. The two modes are visualised in Figure 2.14 in a macrospin approximation:
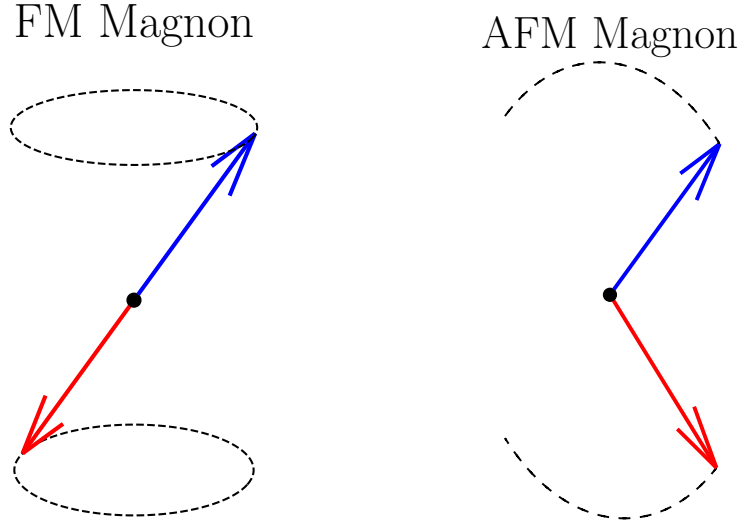
Figure 2.14: The ferromagnetic (FM) and antiferromagnetic (AFM) magnon modes available to a material with two anti-parallel spin sublattices, in a macrospin approximation. The magnitude of the oscillations is greatly exaggerated compared to reality. For the FM mode, the spins on the two sublattices precess in phase so they remain collinear at all times, while for the AFM mode, the spins precess out of phase

2.2.4.1 Procedure

The existence of oscillations after skyrmion collapse, mentioned in the previous section, boded well for the capability of the code to simulate magnons. In order to investigate the evolution of magnons in our 1D lattice, it is necessary to apply some perturbation. We accomplished this with an applied field pulse. In order to excite the widest range of magnons possible (energy and wavelength), the field pulse applied must be both spatially and temporally sharp, this way high energy and short wavelength magnons can be excited which will decay over time to lower energies and longer wavelengths. To force a turbulent initial state and ensure as many different magnon modes are occupied as possible, the field applied was also bipolar in space, mathematically, we define the field pulse as a DW with atomic-scale width. The field pulse thus defined contains a large range of Fourier compo-

nents extending up to high frequencies, the exact details of the pulse are not important as the purpose is simply to excite a large range of natural modes of the magnetic system. There is no direct physical analogue for such a sharp pulse, but, for example, SOT effects (which are proportional to the **local** magnetisation) can vary on a sub-unit-cell scale in AFM materials. Another method which works similarly well is to simply have the spins be randomly oriented in the initial state and allow relaxation from there, the effective fields and torques will be sufficiently huge, but the method of applying a field pulse to the uniform spin structure is a more realistic and elegant solution. The spatial and temporal profile of a typical applied field pulse are shown in Figure 2.15:
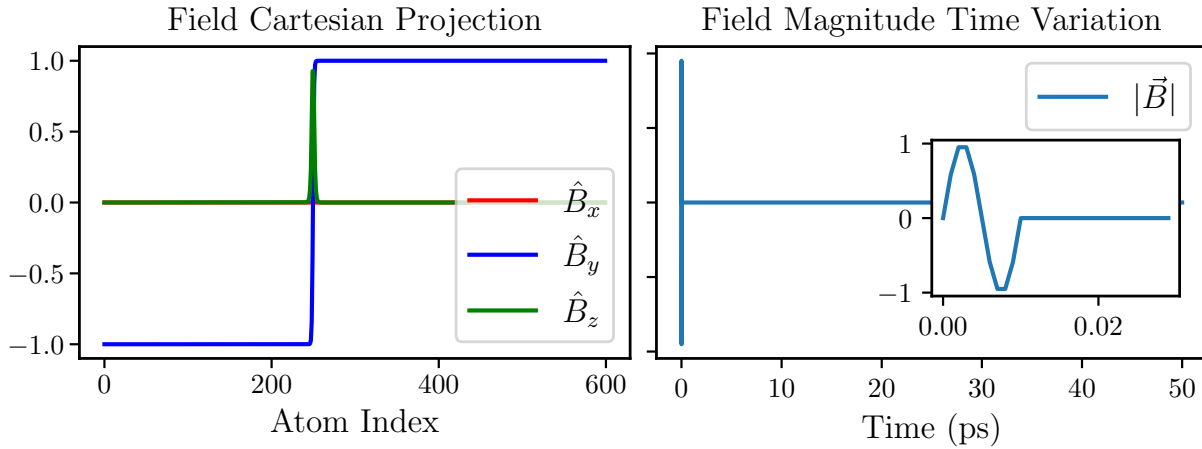
Figure 2.15: Orientation of the applied field at each atom as well as the time dependence of the field magnitude. The very sharp bipolar perturbation dumps a large amount of turbulent energy into the system which is then allowed to propagate, settling into the natural frequencies of the spin system which constitute the magnon spectrum. The high-frequency sinusoidal magnitude also promotes high-frequency oscillations.

For these investigations, a lattice 300 atoms long was used to allow the long wavelength magnons to propagate. Regarding the material parameters, for this magnon investigation, values closer to those observed in MRG [62, 63] were used to ensure the applicability of the results to this material:

$$J_{aa} = 1.2 \, \text{meV}, \quad J_{cc} = 0.3 \, \text{meV}, \quad J_{ac} = -3.4 \, \text{meV}, \quad K_{a,c} = 0.01 \, \text{meV}, \quad J_{DM} = 0.1 \, \text{meV}$$

The DMI was deliberately overestimated in this case, it was found that it does not contribute massively to the magnon spectrum where chirality is not relevant: the oscillations

are dominated by exchange. The significant difference between the intra-sublattice exchange values should create two separate branches in the magnon spectra. In addition, a realistic magnitude was used for the damping: $\alpha = 0.05$ was used. The spins were initially uniformly aligned along the y axis, with the applied field correspondingly bipolar along y with a sharp rotation through the yz plane. The magnitude of the applied field corresponds to one period of a 100 THz AC field.

The LLG equation was used to simulate the evolution of the spin system, typically a time step of 0.25 fs and around 10^5 steps for a total length of 25 ps was used, a smaller step is useful to accurately capture high-frequency dynamics, especially in the beginning of the simulation when the effective fields and torques are very large. Following the numerical integration, the 2D discrete Fourier transform is computed from the z (or x) projection of the spins and a subset of the time steps using, for example, the NumPy multi-dimensional fast Fourier transform (FFT) function (documentation here). This directly converts the space and time coordinates into frequency and momentum space, yielding the magnon spectrum.

2.2.4.2   Results

The evolution of the spins on one of the sublattices (c) are plotted in a colour-map format in Figure 2.16. The sharp perturbation at the center of the lattice is evident in the x and z projections. With the normalised colour scale, we can clearly see the large number of magnons that are created and propagate outwards from the center due to this perturbation. In this case, looped boundary conditions were used so the magnons loop around the chain back towards the centre, creating interesting interference patterns, clearly visible in Figure 2.16. Loose, fixed or damped boundary conditions are also implemented; for the damped boundary conditions, the Gilbert damping is exponentially increased over the last few atoms either end of the chain so that oscillations are damped before the magnon "hits" the end of the chain (recall that time and position are shown on the horizontal and vertical axes respectively).

The S_x (or equivalently S_z) data, which is centred around 0, was Fourier transformed and folded for both sublattices (only one sublattice is shown but the same data is recorded for both). The dispersions for the two sublattices are added together and normalised: the
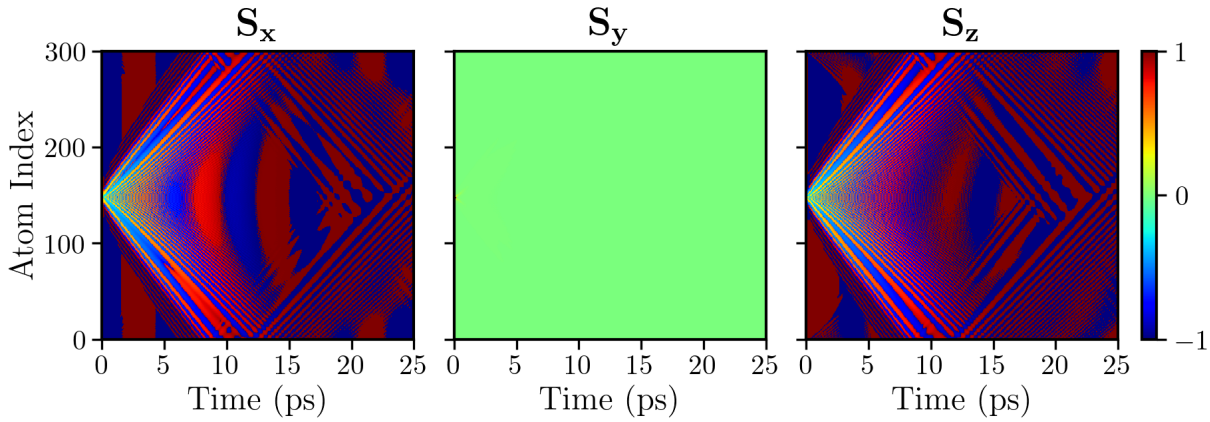
Figure 2.16: The magnitude of the x (left), y (middle) and z (right) projection of the c sublattice spins as a function of atom position and time. A normalised log scale is leveraged to make the small projections off the easy axis evident: the maximum value of S_x or S_z was ≈ 0.01 while the minimum value of S_y was ≈ 0.99995. The colour-bar therefore indicates the relative tilt away from the initial value which was uniform spin projection along y. N atoms $= 300$, pulse width $= 1$ atom, freq $= 100$ THz

normalisation is performed independently for each k-value to visualise the position of the bands, population information is lost in this particular case. The resulting magnon spectra, for two sets of material parameters, are shown in Figure 2.17. The effect of changing the material parameters is illustrated in the figure, indicating that our simple method is capable of accurately calculating all the features of a magnon spectrum. The maximum frequency of the magnon modes is proportional to the direct exchange interaction: the white lines in Figure 2.17(b) are free-electron-like dispersions fit to the magnon spectra at large k-values yielding effective masses of roughly 260 and 170 electron masses respectively, the ratio is approximately 1.5, equal to the intra-sublattice exchange ratio. Note the low-frequency gap due to the uniaxial anisotropy, which is made obvious in (b) with a large value for $K_{a,c}$[4]. The dashed black line in Figure 2.17 follows $1 - \cos(ka)$, the typical equation for a magnon dispersion [3, §5.4.1], with linear scaling and shifting applied.

Information about the population of the magnon branches can also be obtained if the spectra are not normalised. Thus the dependence of the population on the material parameters and the properties of the perturbation can be investigated quite efficiently. The first half of magnon spectra for various properties of the applied field perturbation are

---

[4]For comparison, the elemental material with the strongest magnetocrystalline anisotropy, Co (hcp), has a uniaxial anisotropy constant $K_{a,c} \approx 0.035\,\text{meV}$ [3, §5.5.2]
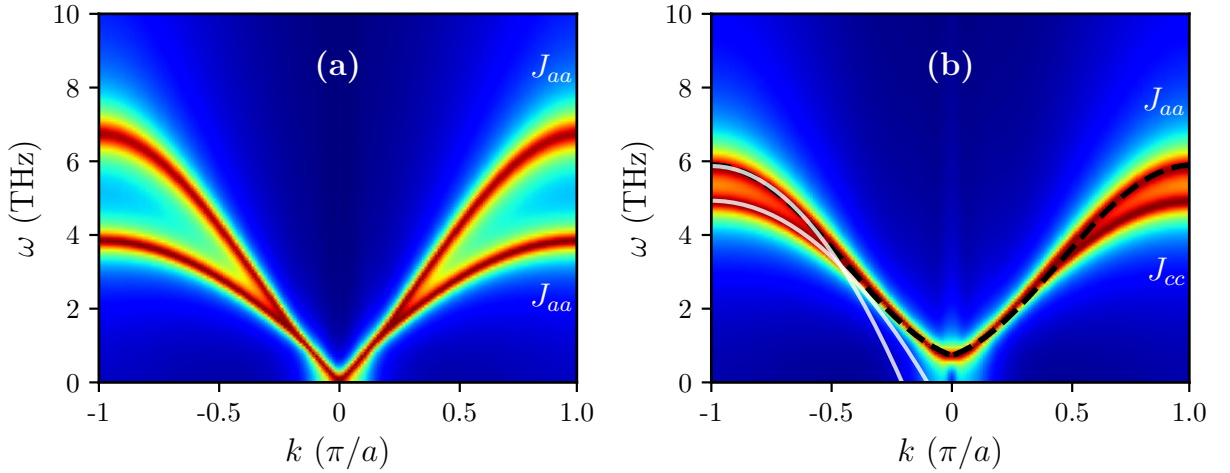
Figure 2.17: Two magnon spectra computed by taking the 2D discrete FFT of the z projection of the spins and the time on both sublattices separately, then adding the two and normalising the spectra for a consistent colour scale. In **(a)** the values used are $J_{aa} = 2$, $J_{cc} = 0.5$, $J_{ac} = -3.0$, $K_{a,c} = 0.01$ (all meV), in **(b)** $J_{aa} = 1.5$, $J_{cc} = 1.0$, $J_{ac} = -3.0$, $K_{a,c} = 0.1$ (all meV).

shown in Figure 2.18. There is a clear dependence of the population of the magnon branch on the perturbing field, higher frequency field pulse provides energy to populate higher frequency and wavevector magnon modes. What is interesting is that either increasing spatial or temporal frequency populates the higher energy magnons, increasing both is not necessary.

We have shown that our spin-propagation model based on the LLG equation can successfully capture the magnon dynamics of both branches in a two-sublattice system. The possibilities for future work are numerous, examples of potential developments of this model include:

- Extending the model to higher dimensions for more realistic exchange interactions and the implicit inclusion of crystal symmetries.

- Adding additional exchange parameters: 2nd and 3rd nearest neighbour interactions are especially important in multidimensional lattices.

- Using the model to confirm experimental results or the reverse, devising experiments to test the model, is an important step in development and testing.
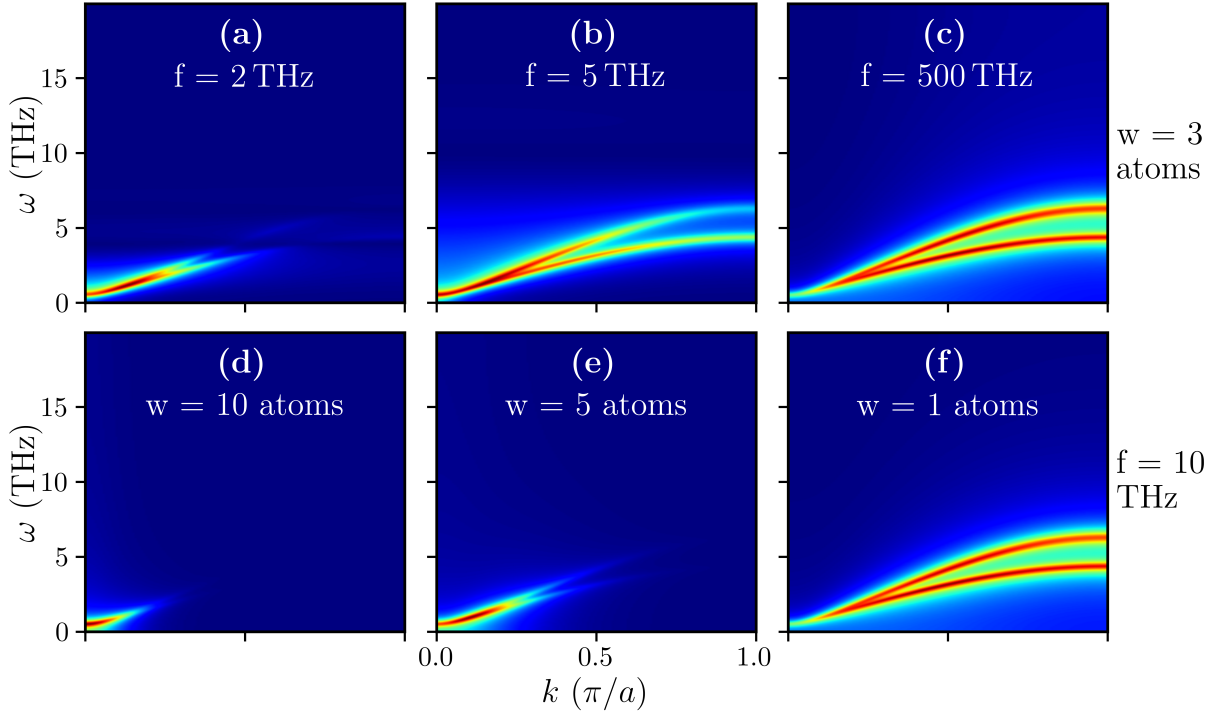
Figure 2.18: The non-normalised magnon spectra for different values of the spatial and temporal frequency of the perturbing field, corresponding to how sharp the rotation at the center of the field is, and the frequency of the sinusoid that determines the magnitude of the field with time, see Figure 2.15. Horizontal lines evident particularly in **(a)** are artefacts of the Fourier transform due to the finite size of the system.

2.2.4.3   Discussion, In An Experimental Context

The astute reader may have noticed that the AFM magnon modes that are particularly interesting for their potential high frequency were not observed. These modes (Figure 2.14) are difficult to excite in a classical spin model. Essentially, in order to excite the AFM modes, we need a perturbation which is staggered such that it is a different sign on each sublattice [64], an external applied field cannot achieve this. However, there is potential for current-induced SOT (subsubsection 2.2.1.3) to satisfy the requirement. As a relativistic correction, the spin-orbit effects are intrinsically proportional to the local magnetisation and in a crystal with broken inversion symmetry, a damping-like torque can be generated [31, §III.F]. Recall that a damping-like torque pushes the magnetisation towards or away from the effect field while the field-like torque causes precession about the external field, thus a field-like torque would cause the FM magnon modes while the damping-like torque could excite an AFM mode. The non-adiabatic spin-torque described in subsub-

section 2.2.1.3 due to Zhang and Li [36] could also excite AFM modes if the conduction electrons travelled from one sublattice to another, this will be discussed again later.

Bulk broken inversion symmetry is not necessary to excite SOT but to generate the sublattice staggered effective fields which could excite AFM magnons, it is required. MRG is a ferrimagnetic Heusler alloy with broken inversion symmetry and could be a good candidate for this. Despite its lack of any heavy elements with large spin-orbit coupling, MRG's conduction attributed to states originating from one Mn sublattice and is thus significantly spin-polarised with only DOS for one electron spin state present at the Fermi level [65, 66]. MRG has been shown to exhibit large damping-like SOT before [67] and is a good candidate material to investigate, although current-induced switching or AFM magnons have not been experimentally demonstrated yet.

2.2.5   "Frozen" Dynamics Simulations

Going from a 1D model to a $3d$ model almost automatically accomplishes the development points listed in the previous section. Considering the real position of the spins rather than just an index in an array allows for the material parameters to trivially be made functions of inter-atomic separation. The inclusion of an additional matrix to store the positions and the computation of pair-wise separations at each time step is a significant increase in computational complexity however. To circumvent this problem initially, we decided to use a "frozen dynamics" approach, where an assumed dynamic state is imposed on the system and the energy is calculated relative to the ground state, so no numerical integration is actually performed. Thus we have essentially swapped the benefits and disadvantages with the previous approach based on integration of the LLG equation in 1D.

2.2.5.1   Frozen Magnons

For the calculation of the frozen magnon dispersions, the same classical Heisenberg Hamiltonian for the spins was used, but rather than invoking the LLG equation and numerically integrating that differential equation to investigate the dynamics, we use the energy terms for the interatomic interactions to calculate the total energy penalty for a given magnon mode, in a $3d$ lattice of spins. Rather than manually setting the value of the exchange for two or three pair-wise interactions, a functional exchange which depends on distance

was implemented. The exchange followed an RKKY-like oscillatory trend as a function of inter-atomic distance, with the inter-sublattice exchange J_{ac} 90° out of phase relative to the inter-sublattice exchanges J_{aa}, J_{cc}, to ensure the signs are correct to yield antiferromagnetic and ferromagnetic couplings. The exchange for different atom pairs is plotted in Figure 2.19.
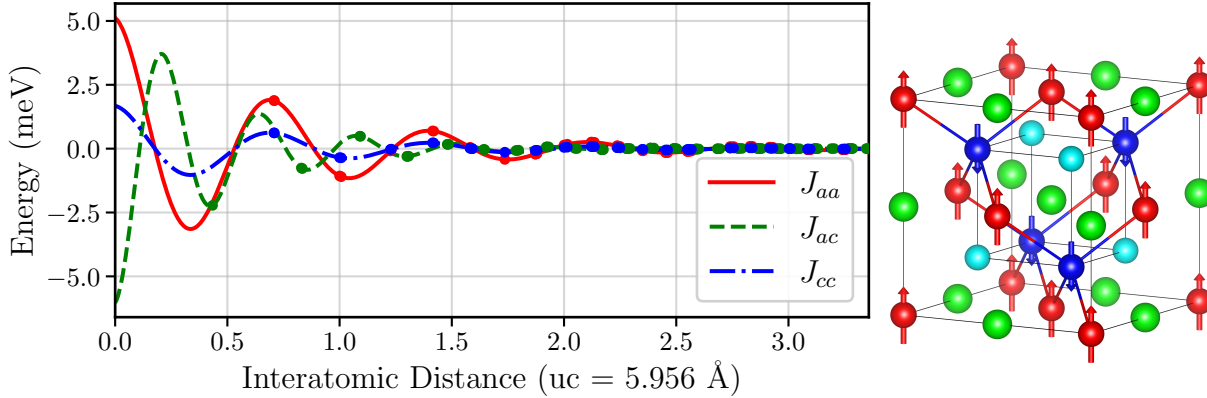
Figure 2.19: Exchange as a decaying oscillatory function of distance for the three possible pairs of atom types: J_{aa}, J_{cc} and J_{ac}. The inter-sublattice exchange J_{ac} is negative for first nearest neighbour and overall but not necessarily for all pairs of atoms, as in real materials such as MRG, evidenced by DFT calculations (performed by Zsolt Gercsi, unpublished). The discrete inter-atomic distances in MRG are shown as points. The MRG Heusler alloy unit cell is also shown, with Mn atoms in red (a) and blue (c), to illustrate the points plotted in the main figure.

To investigate magnon dispersions, a certain direction is chosen for the magnon propagation direction sense of rotation, generally we used a crystal lattice extended in the x direction with the phase increasing along this direction. For a range of wavenumbers between $k = 0$ and $k = 1$ in units relative to the unit cell size, we impose a magnon mode with said wavevector on the spin system and calculate the total energy of the system in this magnonic state. The energy of the system in the ground state (usually uniform spins) can then be subtracted yielding the energy of the magnon. Recall that smaller wavenumbers (longer wavelengths, more spread out magnons) implies a slower variation of the spins and smaller misalignment between adjacent spins, meaning a smaller energy penalty from the exchange interaction.

Calculating the energy once for a pre-defined magnon mode is of course a much faster calculation than any dynamic simulations. The caveat is that the magnon modes are strictly imposed in order to calculate their energy and they may not exactly correspond to

those which are true natural modes of the spin system, particularly for more complicated $3d$ systems with many different high-symmetry directions. To emulate magnon modes we rotate the spins by a small angle ($\approx 1°$) away from the easy axis, which we will assume is the z axis. They can then be rotated **around** the z axis such that their projection along x and y varies sinusoidally, with a period equal to the reciprocal of the wavevector, as illustrated in Figure 2.13. For the FM mode, the spins on the two sublattices precess in phase so they remain collinear at all times, while for the AFM mode, the spins precess out of phase. In this AFM mode, the strong inter-sublattice exchange comes into play and raises the energy of the magnon further. This procedure is illustrated in Figure 2.20.
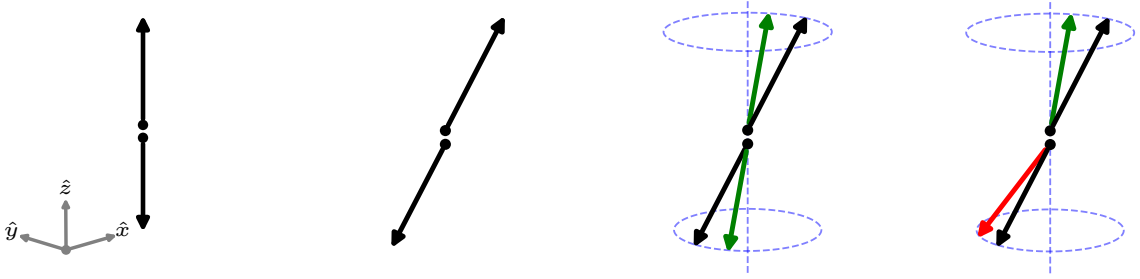
Figure 2.20: The procedure for generating the frozen magnon modes for z as the easy axis: rotation about y away from the easy axis, then in-phase or out-of-phase rotation **about** the easy axis proportional to the atom position and the magnon wavenumber. The out-of-phase rotation causes a finite tilt angle between the spins of the two sublattices, resulting in a higher energy magnon as the J_{ac} exchange begins to contribute. The magnitudes of the tilting is greatly exaggerated.

The results of some frozen magnon calculations for constant nearest-neighbour exchange and distance-dependent long-range exchange, for two sets of material parameters, are shown in Figure 2.21. The lattice used for the calculation was $3d$, consisting of $40 \times 2 \times 2$ unit cells of MRG, which is a cubic Heusler alloy of size $a = b = 5.956 \,\text{Å}, c = 6.0 \,\text{Å}$. The anisotropy easy-axis was chosen to be z while the in-plane projection of the spins varied the host sites x position, along the long axis of the crystal.

The shape of the magnon dispersion follows the canonical $1 - \cos(ka)$ trend when only nearest neighbour interactions are considered, as in Figure 2.21(a,c). With continuous distance-dependent exchange, some more interesting features are evident, particularly around the center point corresponding to a phase of 180°. The AFM magnon mode, wherein the spins on the opposing sublattices oscillate out of phase, has a higher energy ($E_{optical}$) than the FM mode ($E_{acoustic}$) as expected, with finite energy at $k = 0$, which in
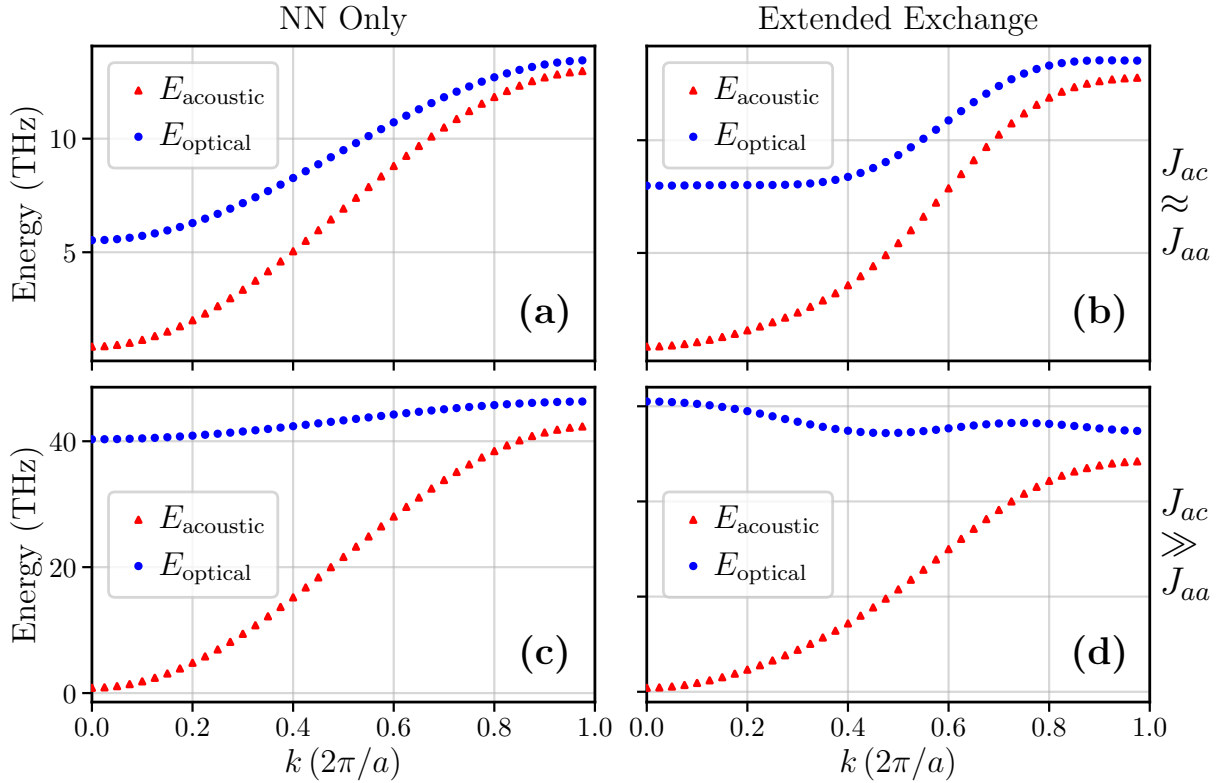
Figure 2.21: Frozen magnon spectra for four distinct cases: **(a)** Using MRG material parameters and nearest neighbour interactions, **(b)** Using MRG material parameters and extended distance-dependent interactions, **(c)** Using large inter-sublattice exchange and nearest neighbour interactions, **(d)** Using large inter-sublattice exchange and extended distance-dependent interactions.

this case corresponds to the spins within each sublattice remaining collinear throughout but the two sublattice average moments becoming non-collinear. If J_{ac} is larger than J_{aa} and J_{cc} by a sufficiently large amount, the dispersion of the AFM magnon can even exhibit a negative slope, becoming reminiscent of the acoustic-optical phonon dispersion for a diatomic chain [68, Figure 4.7]. Interplay between distinct magnon modes in a multi-sublattice material can result in interesting effects, for instance it has been hypothesised that angular momentum transfer between two magnon modes aides in the all-optical-switching process of some rare-Earth transition-metal alloys [1].

2.2.5.2 Combined Magnon-Phonon Modes

Combined magnon-phonon dispersions are rarely seen due to the difficulty of their realisation. They are very computationally expensive to simulate, effectively squaring the computation time needed, as the motion of the atoms (spins) and re-calculation of the ex-

change energies has to be performed for every time step before the effective field on each of the spins can be calculated. They are also quite difficult and expensive to measure experimentally, requiring advanced techniques in large facilities such as time-of-flight resolved inelastic neutron diffraction [69], BLS (Brillouin Light Scattering) [70] or RIXS (resonant Inelastic X-ray Scattering) [71]. Nonetheless, the interaction of these two quasi-particles is becoming an active sub-field of research in the greater spintronics community [72].
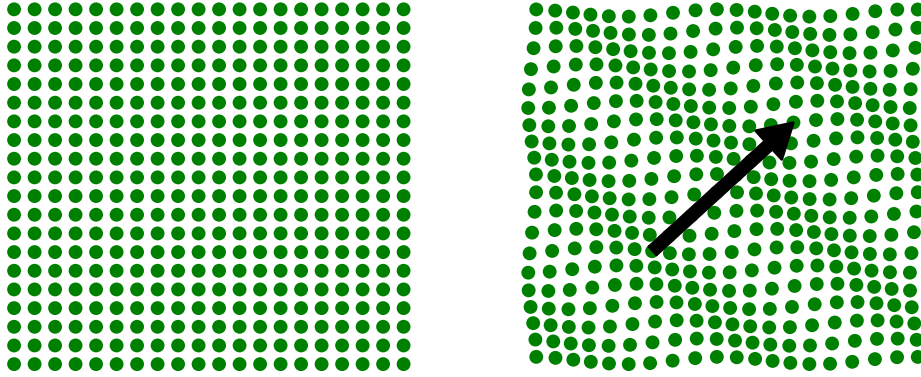
Figure 2.22: An (exaggerated, as usual) example of a phonon in a 2D square lattice, in the direction of the arrow shown. The equilibrium positions (left) and phonon mode (right) are shown. In order to investigate the coupling of magnons and phonons, the material parameters which control the magnons, namely exchange, must be made distance dependent so that the atomic movement due to the phonons changes the properties of the magnons.

Within this frozen framework, the addition of phonons to the model is very simple as we already have distance-dependent exchange. The only new addition required is some function to govern the energy penalty suffered by moving the atoms away from their equilibrium positions, i.e. a restoring potential. Directly measuring phonon stiffness or restoring potentials is not a trivial matter. inelastic neutron scattering is used to measure phonons but will not yield sufficient signal for thin films. Nano-indentation using an AFM-type setup is another method which can be used to measure stiffness but again, in thin films it is very difficult to separate the contributions from the substrate and capping layers etc. The physical properties of the metals which make up MRG are of course well-known and to get an estimate for the relative magnitudes of the restoring force, the stiffness of the bonds for the different sublattices is estimated from their relative atomic masses, mean

free paths and elemental Young's moduli via dimensional analysis:

$$E = \frac{Y}{m_{rel}} \left(\frac{L}{2} \right)^3$$

This estimate gives approximately correct relative phonon energies for the sublattices, for example Mn is considerably stiffer than Ga (due in part to its differing orbital structures and bonding) so phonons propagating in directions with more Mn will be higher in energy. The values are scaled to yield photons of similar energies to the magnons. With unit-less relative atomic mass used, the correct energy units are obtained, one issue with this estimate is that the stiffness is implicitly assumed to be isotropic within sublattices. Phonons are defined in the system by their propagation and phase direction, respectively the direction in which atoms are displaced and the direction in which the phase of the oscillation increases, or

$$d\vec{R} = A \cos\left(2\pi k \frac{R_x}{a} \right) \vec{d},$$

where A is an amplitude, $\vec{d}$ is the vector direction of displacement, k is the phonon wavevector, R_x is the atomic positions along the x-axis and a is the unit cell size along the x-axis, this is visualised in Figure 2.23. Thus k is specified in units of π/a and controls the wavevector on the unit-cell scale: when $k = 0$ all atoms shift the same amount in the same direction and there is no energy change; when $k = 1$, adjacent atoms (which are a minimum half unit-cell apart) are shifted in opposite directions. The change in interatomic spacing, i.e. the compression or expansion, is scaled by the stiffness energy and summed to yield the phonon energy:

$$E_{ph} = \sum_{j}^{n} \sum_{i}^{N-1} E_j \left| d\vec{R}_i - d\vec{R}_{i+1} \right|,$$

where j is over all n sublattices and i is over all but one atom within each sublattice (N atoms are joined by $N-1$ bonds in one direction). The atoms are displaced in one direction only so only that axis needs to be summed over to account for all changes in interatomic spacing.

The calculation procedure is identical to the frozen magnon case: magnon and phonon modes of given wavevectors are imposed on the system and the energy is calculated and
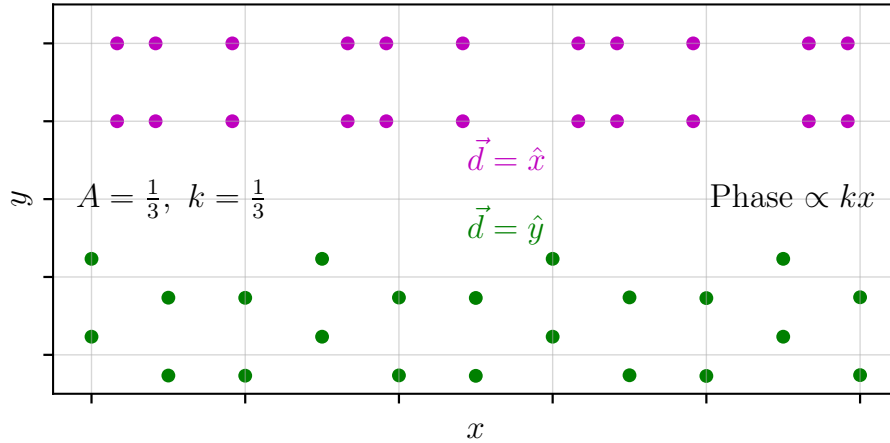
Figure 2.23: Two phonon modes with phase increasing along the x-axis. The displacement vector is directed along x and y in the top and bottom examples. The real simulation is three-dimensional and not a simple-cubic lattice but the principle is the same. The magnitude of the displacement is greatly exaggerated: $A = 0.005$ was used for the simulations below.

this is repeated for a 2D grid of values. The total system energy is a sum of the magnon and phonon energies and as the exchange is distance dependent, the phonon modes should alter the magnon energy. As the total energy is calculated for only a few hundred discrete states, the 2D dispersion surface only takes a few seconds to compute[5]. Some resulting magnon-phonon dispersion surfaces are shown in Figure 2.24. The spectra were computed using a $102 \times 2 \times 2$ unit cell lattice of MRG, with identical magnetic material parameters to previous sections. The phonon stiffness was estimated as described above. The non-magnetic atoms are, of course, included for the phonon simulations while they were ignored for magnon-only calculations. There is little observable difference between the frozen magnon modes with and without phonons being simultaneously imposed. The small displacement in the atomic positions does not change the pairwise exchange interaction strengths appreciably. The nature of these frozen calculations means that natural interference or coupling of the modes cannot occur, we would have to get lucky with our imposed modes, such is the limitation of a frozen model.

---

[5]With reasonably optimised code, or a few minutes to compute with code written in just a few minutes in a simple but slow language.
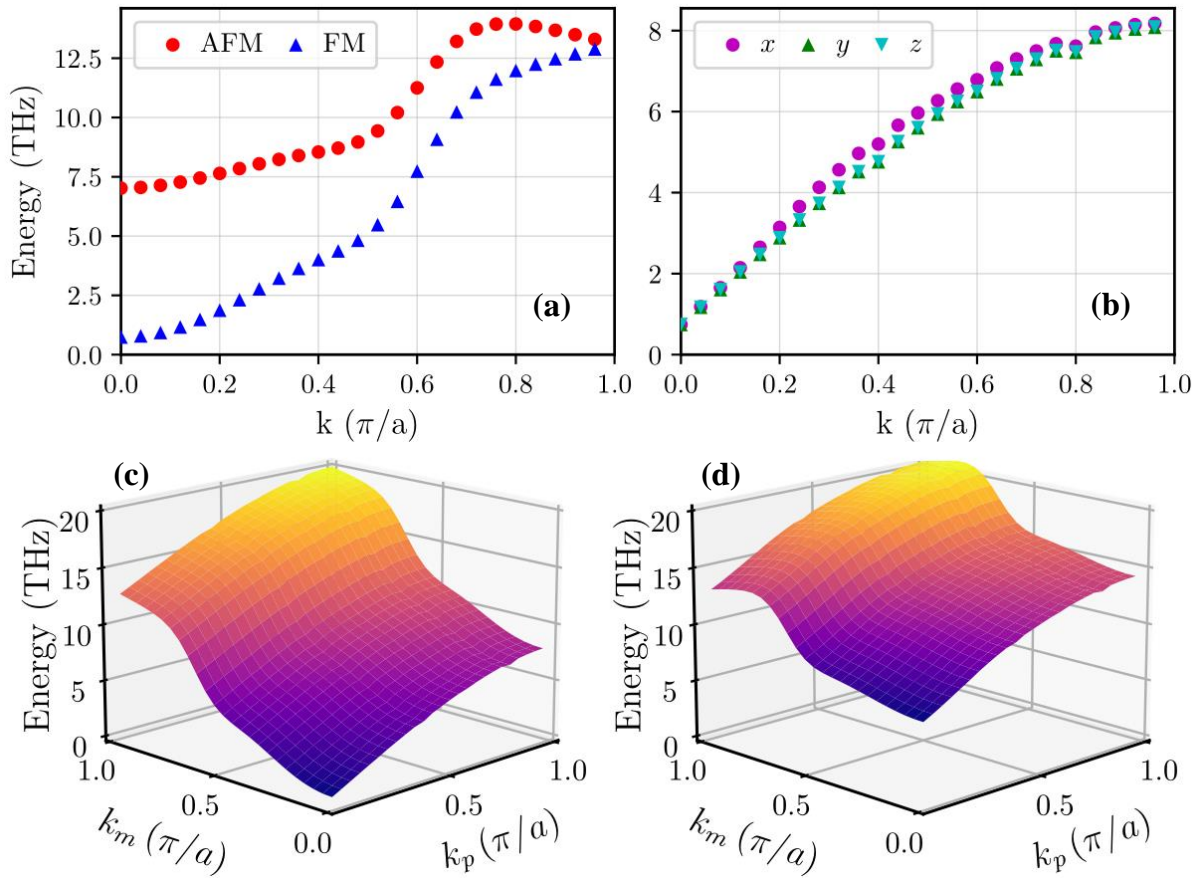
Figure 2.24: Combined magnon-phonon dispersions. Four dispersions were computed, three with acoustic magnons and phonons displaced along the three Cartesian axes and one with optical magnons and phonon displacement along the x axis. All had phonons travelling along the x axis. **(a)** The pure magnon modes for a $k = 0$ phonon along x **(b)** The phonon modes for a $k = 0$ acoustic magnon. Surface plots show the 2D magnon-phonon dispersions for **(c)** acoustic magnons and longitudinal phonons and **(d)** optical magnons and transverse phonons. The kinks of $E(k)$ for the calculated phonon dispersion are likely due to beating from the finite lattice size (150 unit cells in x direction).

2.3 Ehrenfest Dynamics Model

Combining the multi-dimensional lattice and distance-dependent interactions of the frozen model with the time-dependent numerical integration of the dynamics model was a natural next step along the model development path. As discussed at length in previous sections, this kind of model requires an updated implementation which makes use of compiled code[6]

---

[6]Compiled code is translated into the binary machine language which runs natively on computing devices, and is often optimised, before being run. This is in contrast to *interpreted* programming language where the interpreting engine runs and recognises human commands and can run they on the fly, this allows for easier writing and testing but slower less efficient code.

and parallel execution to be computable in a reasonably short time. Since the move to highly-optimised code is necessitated, it was decided that a true molecular dynamics (MD) model for nuclear motion and electronic density with the familiar spin-dynamics should be attempted.

The most general way to model MD is by attempting to solve the many-body Schrödinger equation for the electrons and nuclei but this is not feasible for more than a handful of particles. As a first step, the electron and nuclear sub-systems can be separated and then there are numerous ways to treat the problem of solving for the electronic density as a function of position in a crystal lattice, DFT being the first that comes to mind. Many MD models calculate the ground-state electronic wavefunction, often via DFT, and treat the nuclear motion as occurring in the potential landscape therein. This is known as the Born-Oppenheimer (BO) approximation and it a physically reasonable approximation to make: the excitation timescales for electrons and nuclei is vastly different due to their difference in mass (three orders of magnitude) so transient dynamics in the electronic system will propagate and decay before the nuclei have time to react, thus from the perspective of the nuclei, the electrons are indeed usually in, or very close to, their ground state. This is also known as the adiabatic approximation as the electrons do not change state, the density can only be continuously deformed [73].

There is a large amount of interest in "beyond-BO" formalisms in modern MD, in particular for researchers investigating the interaction of photons with molecules, chemical bonds, and chemical reaction rates [74, 75, 76]. In recent times, full-blown time-dependent DFT has used to calculate the electron DOS at each step [73], something which was not computationally feasible in the past: for example the first-principles calculation of time-dependent magnon spectra in the $3d$ ferromagnets [77]. There are other "in-between" methods which are easier to use.

A bridging method known as trajectory surface hopping (TSH) involves the initial calculation of a handful of potential electron wavefunctions and what amounts to a quantum mechanical interpolation between the states when modelling the dynamics, this is an effective approach, especially for small systems with only a few potential wavefunctions where the entire physics can then be captured.

Then comes the idea of Ehrenfest dynamics where the electronic states are treated as

a mix (superposition) of all possible states. In this formalism, the nuclei are treated classically as electric point charges and the electron density enters the propagation equations for the classical nuclei via the expectation value for the mixed quantum state. The nuclei in turn enter the Hamiltonian for the electrons parametrically via their position, which can be treated as a perturbation to the equilibrium periodic potential. This is the formalism we have chosen to implement: the simple connection between the quantum and classical systems, via the expectation value of the operators for the electrons, makes it easy to link to the classical spin dynamics model.

The MD accounts for the electron-electron, nuclei-nuclei and electron-nuclei interactions. The now familiar LLG-based classical magnetisation dynamics model handles the spin-spin interactions as before. The direct spin-nuclei interactions are very small and are neglected, however, the dependence of the pairwise exchange interactions on interatomic separation, as seen in the frozen magnon-phonon model, means that the nuclear motion does indirectly affect the spin system. Lastly, the spin-electron interactions are handled via conventional *sd* exchange coupling between the conduction and core electrons. The Ehrenfest dynamics model is thus two-thirds classical with expectation value of the appropriate operators of the quantum electronic system used in the equations for the classical systems. The interaction of the system with external perturbations such as photons can be simulated in an *ad hoc* fashion by adding an oscillating electromagnetic field to the potential terms for the systems, this is similar to how current-driven spin-torque terms are conventionally added to the LLG model, but with the quantum electron system in this model, the spin-torque terms are modelled with a real physical basis. Some of the various quasi-particles arising from the interactions of electrons with the crystal lattice are discussed by Patterson and Bailey [78, Table 4.1], including plasmons (electron-electron), polarons (electron-phonon), polaritons (photon-magnon/plasmon) and more. We are particularly interested in electron/plasmon-magnon scattering.

2.3.1 Parallelisation for Combined Dynamics

Dynamic simulations of systems governed by partial differential equations require time steps an order of magnitude (or two) shorter than the time in which the dynamics of interest occur, for example, in order to accurately simulate magnon dynamics up to $f =$

$100\,\text{THz}$ $(10^{14}\,\text{s}^{-1})$ a time-step δt on the order of fs or smaller is required. The electron system reacts faster than the spin system. The plasma frequency which is characteristic of the electron system is typically on the order of $f = 10^{15}\,\text{Hz}$ (coupling to ultraviolet radiation of wavelength $\lambda \approx 300\,\text{nm}$), thus requiring time steps significantly smaller than $\delta t = 1\,\text{fs}$. To simulate both magnon and plasmon excitations, the time step must be $\delta t < 0.01\,\text{fs}$ but the total time must be $t > 1\,\text{ps}$: long enough for the magnon to be visible ("visible" as in its frequency contribution is resolvable in a Fourier transform). This all means that at least 10^5 time steps will generally be necessary. If calculating the energy or effective field for a single step takes around one second then the total simulation will take over 24 hours, just for a few hundred atoms. Clearly a new, more efficient, method of implementation must be chosen.

Up to now, all calculation were effectively done serially, whether through MathCad or Python. To increase performance, a parallel paradigm was needed and to provide the widest adaptability and performance, we chose to use the OpenCL framework [44]. OpenCL is a *framework* for writing programs that execute across *heterogeneous* platforms. What this essentially means is that it acts as a middle-man language for writing programs that will then execute in parallel on a variety of different hardware architectures, such as standard CPUs, discrete gaming GPUs or dedicated vector processors, without any change to the OpenCL code. This is achieved by having the processor manufacturers program their device drivers to execute OpenCL functions. Most modern processors and graphics cards are OpenCL compliant, thus enabling the coder to write programs that will take advantage of parallel hardware on (almost) any device. CPUs typically have $4 - 12$ computing cores while basic GPUs have 24+ and modern gaming GPUs can have 1000s. In the ideal case, a speed-up of computation proportional to the number of computing cores could be expected. Of course the reality is more nuanced, in particular, the bottleneck in high-performance computing is often memory transfer speed as opposed to computing speed. More information on parallel computing with a focus on OpenCL can be found at the Khronos Group web page `https://www.khronos.org/opencl/`.

In practice, the most time consuming parts of the computation, the various matrix operations which loop over the position index performing the same simple calculations for every spin/atom, can be written as OpenCL compute kernels which are in turn called

from another code written in C which handles all the memory allocation and copying. This computation pipeline is then compiled into libraries which are callable from other programs. With a few extra steps in the compilation to ensure the data interfaces correctly, the libraries can be made callable in MathCad or Python, allowing the same efficient and familiar work-flow to be used as before but with the platform-independent parallelisation provided by the OpenCL functionality.

2.3.2 The Model

2.3.2.1 Conduction Electron System

It is necessary to treat the conduction electrons quantum mechanically and refer to their continuous probability density ρ. A tight-binding Hamiltonian which facilitates hopping between adjacent atomic sites is used; while a single tight-binding Hamiltonian is not appropriate for a true metallic system (with more electrons than, say, Na), it is nonetheless useful for modelling many-body systems, especially those that are less conductive or low-dimensional. It is possible to use a few tight-binding models together for distinct electron bands in a metallic system, provided electron-electron interactions are not too strong and the band structure is not too complicated. See any condensed matter theory text book for details on this type of Hamiltonian [78, §3.2.3] [79, §2.2].

The tight-binding Hamiltonian for N discrete sites can be written in a linear equation format as

$$\mathcal{H}_{i,j} = \delta_{i=j} \left(\varepsilon_0 - U_i^E(t) + J_{sd} \left(\vec{s}_{i,j} \cdot \vec{S}_i \right) \right) + \delta_{i=j\pm1} \left(t_{hop} \right) + \delta_{i=0,j=N-1} \left(\lambda_0 \right) + \delta_{i=N-1,j=0} \left(\lambda_N \right),$$

or in matrix format as:

$$\mathcal{H} = \begin{bmatrix} \varepsilon_i & t_{hop} & \ldots & 0 & \lambda_0 \\ t_{hop} & \varepsilon_i & t_{hop} & 0 & 0 \\ \vdots & t_{hop} & \ddots & t_{hop} & \vdots \\ 0 & 0 & t_{hop} & \varepsilon_i & t_{hop} \\ \lambda_N & 0 & \ldots & t_{hop} & \varepsilon_i \end{bmatrix} \qquad \varepsilon_i = \varepsilon_0 - U_i^E(t) + J_{sd} \left(\vec{s}_{i,j} \cdot \vec{S}_i \right) \qquad (2.12)$$

The on-site energy at site i, ε_i, is the sum of the ground energy due to the periodic

potential ε, an external electric bias potential U_i^E, and the last term is energy due to the sd exchange coupling to the core electrons of the atom at site i. The conduction electron polarisation vector $\vec{s}_{i,j}$ is the product of the electron density matrix $\rho_{i,j}$ with the Pauli vector $\vec{\sigma} = \sigma_{\mathbf{x}}\hat{x} + \sigma_{\mathbf{y}}\hat{y} + \sigma_{\mathbf{z}}\hat{z}$. The hopping parameter for nearest neighbours t_{hop} indicates the likely of hopping, or the conductance in a sense, while λ_0, λ_N control the boundary conditions. In the current iteration of the model, the electron-nuclei interaction is neglected so that ε_0 is constant. In principle, it can become a function of the nuclear positions r_i.

The density matrix is equal to:

$$\rho = \sum_i \mathrm{DOS}(E_i)\varphi_i\varphi_i^*$$

where E_i and φ_i are the eigenvalues and eigenvectors of the Hamiltonian $\mathcal{H}_i$, respectively, and the density of states is smeared using a finite-temperature Fermi-Dirac distribution where the effective electron temperature is generally chosen as $k_B T = 0.025\,\mathrm{eV}$ ($T \approx 290\,\mathrm{K}$, room temperature).

The electron density is propagated through time using the quantum Liouville equation (a.k.a. von Neumann equation) which describes the time evolution of a density operator [80, §3.4].

$$\frac{\partial \rho}{\partial t} = \frac{1}{i\hbar}\left[\mathcal{H}, \rho\right] \quad \rightarrow \quad \rho(t + \delta t) = \rho(t) + \frac{1}{i\hbar}\left[\mathcal{H}, \rho\right]\delta t, \tag{2.13}$$

where the square brackets denote the commutator of the operators. The same procedure for numerical integration is used for this combined model as for the classical spins model propagated via the LLG equation, the only different is the equation used to calculate the integration step, in this case it is the quantum Liouville equation.

2.3.2.2 Nuclear System

We use the famous Lennard-Jones (LJ) potential to model the pairwise interaction between two nuclei, the total potential on a nucleus i is the sum of the pairwise potentials from

the other nuclei:

$$U_i^N = \sum_{j \neq i}^{N} \varepsilon_4 \left[\left(\frac{c}{|\vec{R}_{i,j}|} \right)^{12} - \left(\frac{c}{|\vec{R}_{i,j}|} \right)^{6} \right], \qquad \vec{R}_{i,j} = \vec{r}_i - \vec{r}_j, \qquad (2.14)$$

so that the directional force on the nucleus is:

$$\vec{F}_i^N = \frac{\vec{R}_{i,j}}{\left| \vec{R}_{i,j} \right|} \frac{\mathrm{d}}{\mathrm{d}\tilde{R}_i} U_i^N = \sum_{j \neq i}^{N} 6\varepsilon_4 \left(c^6 \frac{\vec{R}_{i,j}}{|\vec{R}_{i,j}|^8} - 2c^{12} \frac{\vec{R}_{i,j}}{|\vec{R}_{i,j}|^{14}} \right), \qquad (2.15)$$

where ε_4 is the overall LJ factor (four times the depth of the potential well) and c is the core LJ factor (distance at which the potential is zero).

Given the force on the nuclei, their motion is governed via Newton's classical equations of motion with an additional phenomenological velocity-dependent damping (viscosity) term:

$$\vec{r}_i(t + \delta t) = \vec{r}_i(t) + \vec{v}_i(t)\delta t + \frac{1}{2}\vec{a}_i(t)\delta t^2,$$

$$\vec{v}_i(t + \delta t) = \vec{v}_i(t) + \vec{a}_i(t)\delta t, \qquad (2.16)$$

$$\vec{a}_i(t + \delta t) = \frac{\vec{F}_i(t + \delta t)}{m_N} - \eta \vec{v}_i(t),$$

where m_N is the effective nuclear mass, η is the aforementioned damping parameter and δt is the integration time step, the other terms are self-explanatory. The effect of the conduction electrons on the nuclei, when implemented, will be incorporated as an additional term in $\vec{F}_i^N$ which depends on $\rho_{i,j}$ or more formally $\rho_{i,j}\rho_{i,j}^*$ since only the expectation values can enter the classical dynamics. See future work subsection 2.3.5.

2.3.2.3 Localised Spin System

The localised atomic spin system is treated identically to the original LLG model subsection 2.2.1. The additional contribution from the sd exchange with the conduction electrons enters as an effective field in to the LLG equation:

$$H_i = H_{Heisen} + J_{sd}\,\vec{s}_i, \qquad (2.17)$$

where $\vec{S}$ is the classical atomic Heisenberg spin as usual and $\vec{s}$ is the conduction electron polarisation calculated from the density and Pauli matrices and H_{Heisen} is the effective

field due to the classical Heisenberg Hamiltonian, see subsection 2.2.1.

2.3.3 Procedure

The initialisation of the three subsystems in the model is performed separately before propagation commences. The ground state for the electron density is computed from eigenvalues and eigenvectors of the Hamiltonian with the Fermi-Dirac distribution. The bias potential is a function of both position (site) and time, with a negative bias being applied to the first 3 sites and positive to the last 3 sites. This stimulates current flow through the system. The spin system is initialised to a DW configuration and the nuclear positions are chosen to be at the potential minima of the pairwise LJ potential, which will be close to the equilibrium position but not exactly there due to the long range interactions and the asymmetry at the ends of the atom chain. The initial state of the three subsystems is visualised in Figure 2.25.

After initialisation, the system is propagated by numerical integration as before, with the step for the electrons, spins and nuclei computed via the quantum Liouville equation Equation 2.13, LLG equation Equation 2.1, and Newton's equations of motion Equation 2.16, respectively.

2.3.4 Results

Some preliminary results from the Ehrenfest dynamics model are described here. No substantial phase investigation has been attempted yet, so these results essentially constitute the basic propagation of the individual subsystems. The system initialised as shown Figure 2.25 is shown again after propagation in Figure 2.26. The propagation was for $n = 40000$ steps of length $\delta t = 0.002\,\text{fs}$ for a total time of $t = 80\,\text{fs}$.

2.3.4.1 Domain-Wall Precession

The action of an electric current in the presence of sd exchange coupling to to exert a non-adiabatic spin-torque on the magnetic moments due to the angular momentum being transferred from localised spin to localised spin through the atom chain, via the conduction electrons. This process was illustrated in Figure 2.4 and is referred to as Zhang-Li or non-adiabatic spin-torque [36]. However, while this term is introduced phenomenologically in
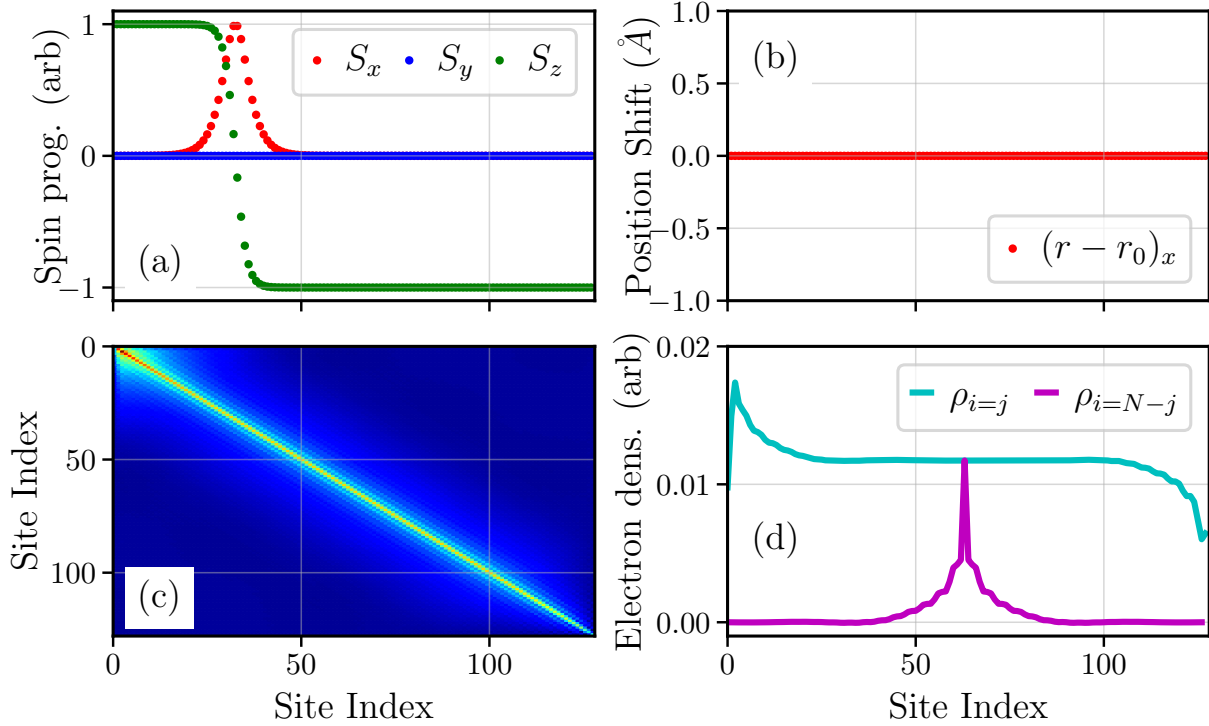
Figure 2.25: The initialised states of the model showing: **(a)** The classical Heisenberg spin components for each atom with a DW configuration, **(b)** The shift in nuclear positions, zero at $t = 0$, for the x-axis (in principle this is a 3D model but a 1D atom chain along $\hat{x}$ is specified) and **(c)** The density matrix (which is fully real at $t = 0$) showing near-constant magnitude in the middle of the chain with significant difference at the ends due to the applied bias potential. **(d)** Shows the diagonal ($(i = j)$ terms) and the anti-diagonal ($i = N - j$ terms where N is the size of the square matrix) of the density matrix for clarity.

the conventional magnetisation dynamics via a general equation like Equation 2.9, this Ehrenfest dynamics model introduces the effect in a rigorous physical way.

The reproduction of the current-induced spin-torque, shown in Figure 2.26, from what is essentially a first-principles model is a great success and shows the worth of the Ehrenfest model in an era where current-excited spin-torques are the hottest topic in the field of spintronics.

2.3.4.2 Atom Chain Relaxation

The simple but telling result from the nuclear subsystem is the relaxation of the atom chain with inter-atomic spacing increasing at the ends of the chain. This is due to the asymmetry at the ends: the end atoms have only one other atom **strongly** pulling them in towards the center of the chain and no additional atoms on the outside pushing them
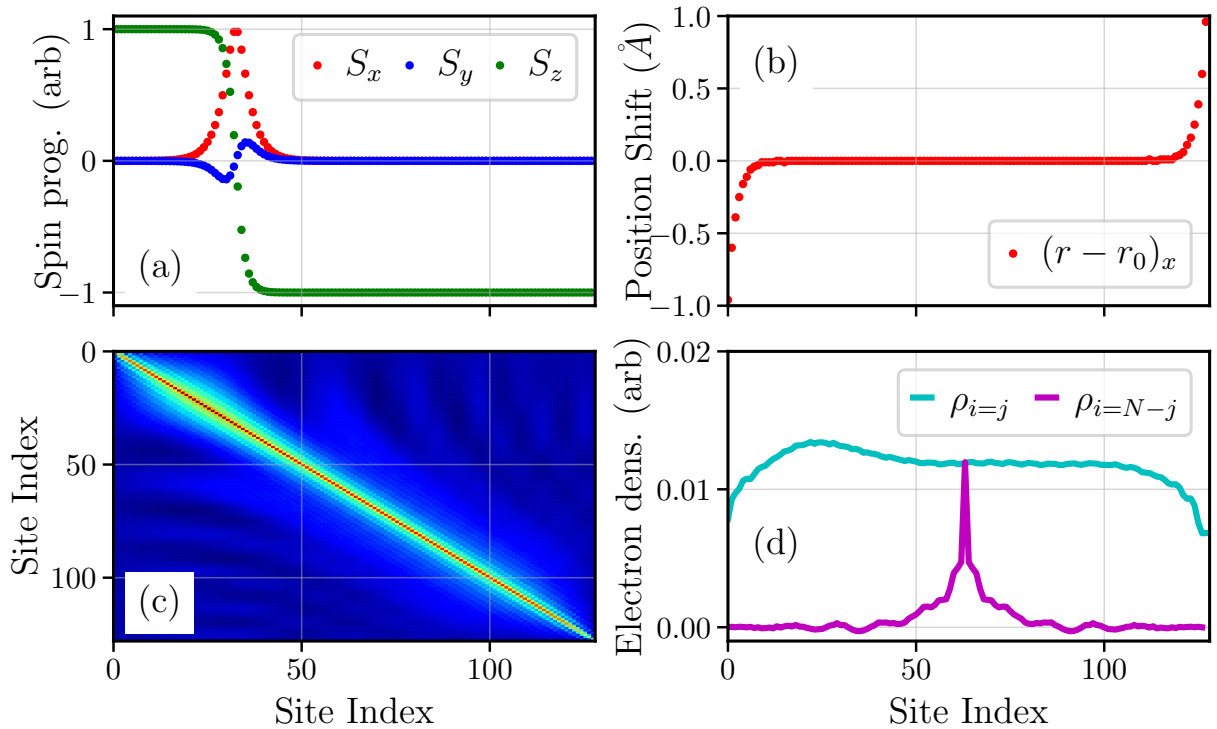
Figure 2.26: The $t = 80\,\text{fs}$ states of the model showing: **(a)** The beginning of DW precession (magnetisation dynamics are closer to ps in timescale than fs), **(b)** Nuclear chain expansion along the x-axis, **(c)** The relaxation of the density matrix after the bias potential is turned off, density is no longer bunched at one end due to the bias and spreads out in the center of the chain and **(d)** The diagonal and anti-diagonal of the density matrix again.

inwards. This indicates the fundamental LJ potential and nuclear motion is correctly implemented, see Figure 2.26.

2.3.4.3 Electron Density Relaxation

When the steady state bias which defined the initial state in Figure 2.25 is turned off, the electron density immediately begins to relax and homogenise, spreading out across the atom chain, which is equivalent to a conventional electric current travelling from right to left. The aforementioned interaction of the electron density with the DW through the sd exchange is the most interesting phenomena here. Also of note however, is the increase of the off-diagonal terms in the electron density (which are no longer fully real, resulting in the negative values in Figure 2.26), this is due to scattering as the hoping electrons move through the various potential barriers defined by the TB model.

2.3.4.4 Plasmon Dispersion Spectrum

Plasmons are the electronic density analogues of phonons and magnons, being quantised oscillations in the density of electrons as a function of space. Their dispersion is distinct to that of magnons and phonons. Analogously to how the magnon dispersion was calculated for the spin system in Figure 2.17, the FFT of the time evolution of the real part of the density matrix was performed to obtain the **plasmon** spectrum, some results are shown in Figure 2.27 and Figure 2.28. The plasmon spectrum is very rich, due to the sharp
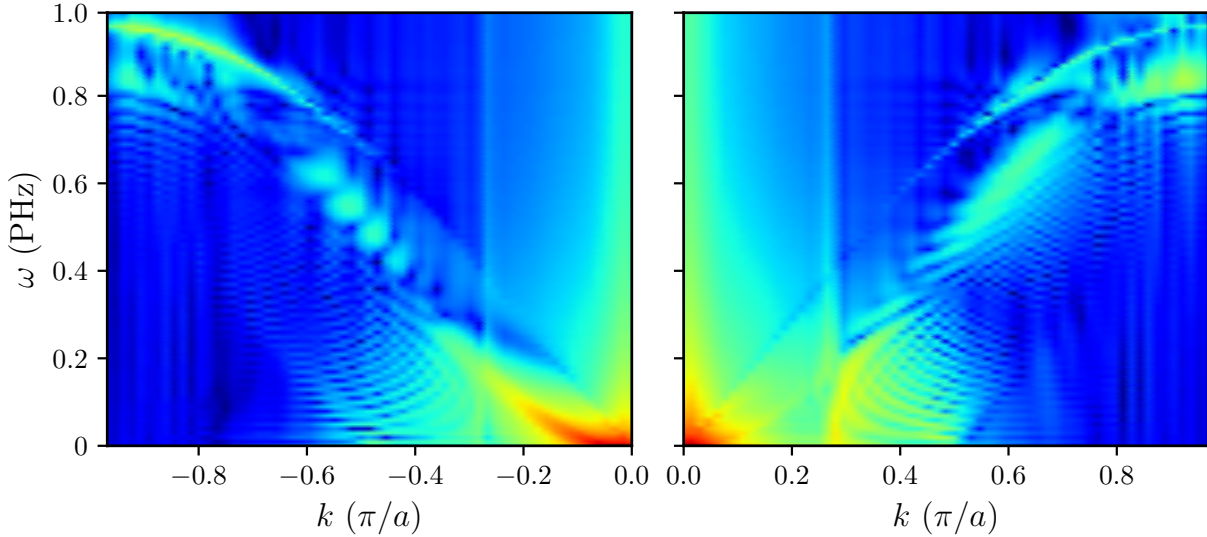
Figure 2.27: The forward and backward travelling plasmon spectra for our model system, calculated by taking the Fourier transform of the time evolution of the real part of the electron density matrix. A time step of $\delta t = 0.002$ fs per step was used for $n = 50001$ steps, meaning the total simulated time was $t = 100$ fs. This spectrum was calculated with the system starting with an applied bias on the chain ends which was then switched off.

shock the system experienced. Two distinct modes appear to be visible, one linear and one sinusoidal at low k, with both becoming sinusoidal near the edge of the Brillouin zone. Most of the intensity is built up at low k (long wavelength, low energy). This spectrum exhibits similarity to the continuum of excitations for interacting Fermions on a lattice, illustrated diagrammatically by Pereira [81, Fig. 17]. The upper boundary in particular is well-reproduced. The diagram in the aforementioned citation was computed for spinless Fermions: the inclusion of spin in our model adds more structure to the spectrum. The discretisation in Figure 2.27 (and Figure 2.28) is due to the finite size and boundary conditions of the atom chain that was used when computing the spectrum.

There is a slight difference between the forward and backward propagating plasmons due to the interaction with the bound magnetic electrons - the spin subsystem. The DW acts as a moving potential via the *sd* exchange and exerts a force on the conduction electrons which is different depending on their direction (and speed) of propagation due to the Doppler effect. To illustrate another parallel between subsystem interactions, the same phenomena can in principle be observed in phonon spectra due to magnetostrictive effects: DW motion causes localised lattice strain due to the exchange striction which naturally propagates outwards as phonons, the dispersions of which will be anisotropic due to the motion of the DW and resulting Doppler effect.
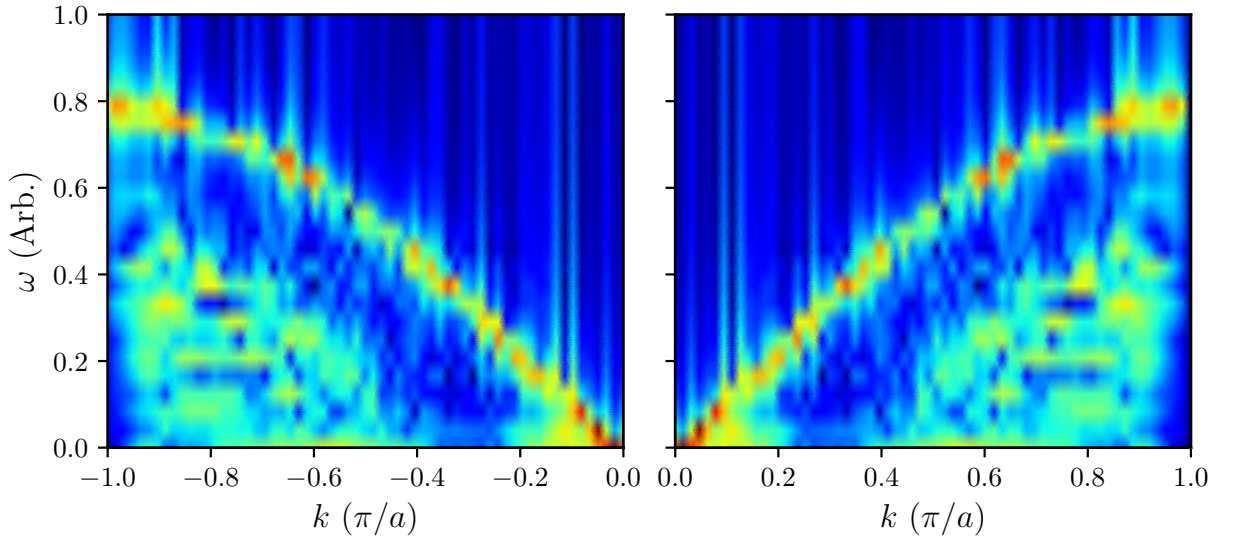
Figure 2.28: These spectra were obtained by performing the same FFT after propagation with a time step of $\delta t = 0.002$ fs for $n = 20001$ steps, meaning the total simulated time was $t = 40$ fs. In this case, propagation started after the system had been relaxed for an additional 80 fs with no bias applied. The significance of this is explained in the text.

The short applied bias pulse was identical for both situations shown here. However, for the first spectra (Figure 2.27) the ground state is calculated from the Hamiltonian with the bias applied so we can actually consider the "pulse" as having been applied for infinite time and the system is effectively in equilibrium with the bias applied, thus when the bias is sharply turned off, the shock is propagated for all the remaining steps. This is contrast to the second case (Figure 2.28), where the system starts in a relaxed state with no bias and when the bias is briefly turned on, there are a limited number of time steps for the bias to impact the electron density through the Liouville equation, the eigenstates of the bias-

on Hamiltonian are only slightly mixed into the relaxed electron density, resulting in much less turbulence being introduced and a more clearly defined plasmon spectrum (the lower number of steps and shorter time simulated contributes to the lower resolution). Only the upper boundary plasmon branch which is linear at small k, reminiscent of acoustic phonons, is evident in this case. Additionally there is no observable difference in the forward and backward travelling spectra, since the electron density is never as asymmetric as shown in Figure 2.25(c) due to this simulation being pre-relaxed for 80 fs before the data input to the FFT was recorded.

2.3.5 Future Work

2.3.5.1 Electron - Nuclei Interaction

The most notable omission from the current version of the model is the conduction electron - nuclei coupling which would enable plasmon-phonon scattering.

The force on the nuclei due to the electronic density in a current-carrying steady state can be written, after Todorov, as [82, §3.1]:

$$\vec{F}_i^N = \cdots - 4 \sum_{j \neq i}^{N} \mathrm{Re}[\rho_{i,j}] \frac{\mathrm{d}}{\mathrm{d}\tilde{\mathrm{R}}_i} \mathcal{H}_i,$$

where $\mathcal{H}_i$ is the electron Hamiltonian. Only off-diagonal elements contribute so $\mathcal{H}_i$ is equal to the hopping integral in the tight-binding model, which in principle can be a power-function of inter-atomic separation [82], but in our present case is a constant value for nearest-neighbours only. This is a simple approximation where summation over multiple potential states for each site is assumed. The choice of form for the tight-binding integral (specifically the dependence on $\vec{R}$) is very important. This follows from the Hellman-Feynmann theorem which states that once the distribution of electrons in space is known (the density matrix) then all the forces in the system can be treated classically [83, 84], which also is essentially the basis of Ehrenfest dynamics in general.

Though a possible equation to satisfy the electron-nuclei coupling is known, integrating this into the existing parallel computer code in an optimised way is not trivial and will take some time to implement, hence the existence of this section under "future work".

2.3.5.2   All-Optical-Switching

The ultimate goal of this model would to fully explain, for each stage of the process, the AOS switching of a material like Mn_2Ru_xGa, where the energy from the incident photon beam transfers primarily to the electrons, then through the spin system and eventually to the lattice (nuclei). We hypothesise that the transfer of energy proceeds from photons to hot electrons, the electrons then thermalise and the energy is transferred to the high-energy optical (AFM) magnonic branches. The magnons scatter and thermalise by shifting their population, along the branch, to the position of maximum group velocity (largest slope of $E(k)$), there they can transfer energy and momentum to their acoustic magnon counterparts. The acoustic magnon population travels down its branch and can transfer energy, resonantly or non-resonantly, to the multitude of phonons in the lattice (in film itself and ultimately the substrate on which it sits). Thus the photon energy is eventually dissipated. Modelling the plethora of quasi-particle interactions throughout this process is a daunting task but the essence of the behaviour should nevertheless be captured by a 1D two-sublattice model of the dynamics of the type described here.

2.3.5.3   Different Hamiltonian

There are a number of "elaborations" or reversal of approximations that can be done on the current version of the model as described above. One particular alteration of interest is replacing the constant nearest-neighbour hopping parameter t with a functional t which depends on the inter-atomic separation between sites [82]. This inclusion of longer range terms can more closely model a real conductor which is not strictly 1D and, as we observed in in the frozen magnon simulations when switching from nearest-neighbour to long-range exchange interactions, this change can qualitatively alter the relevant quasi-particle dispersion, plasmons in this case and magnons for the exchange interaction.

2.3.5.4   Systematic Phase-Space Investigation

Akin to the anisotropy and DMI phase space exploration to determine skyrmion stability, changing the various input parameters; hopping strength, bias potential, etc., and observing the change on the overall system behaviour is of great interest.

2.3.5.5 Polish and Publish

A potential but as yet distant end goal would be the polishing and publishing of the simulation code, in a callable command-line format as well as a more-universally accessible GUI (graphical user interface) format. Aspirations such as multi-dimensional phase space exploration and even incremental additions/improvements to the model go much more rapidly with more "cooks".

References

[1] J. Barker, U. Atxitia, T. Ostler, O. Hovorka, O. Chubykalo-Fesenko, and R. Chantrell, "Two–magnon bound state causes ultrafast thermally induced magnetisation switching," *Scientific reports*, vol. 3, no. 1, pp. 1–6, 2013. [Cited on pages 32 and 72]

[2] J. Barker and U. Atxitia, "A review of modelling in ferrimagnetic spintronics," *Journal of the Physical Society of Japan*, vol. 90, no. 8, p. 081001, 2021. [Cited on pages 32 and 33]

[3] J. M. D. Coey, *Magnetism and magnetic materials*. Cambridge university press, 2010. [Cited on pages x, xii, 7, 9, 10, 12, 15, 32, 38, 40, 41, 42, 49, 56, 66, and 212]

[4] R. F. Evans, "Atomistic spin dynamics," *Handbook of Materials Modeling: applications: Current and Emerging Materials*, pp. 427–448, 2018. [Cited on pages 33, 39, 43, and 55]

[5] K. Kormann, S. Holmgren, and H. O. Karlsson, "Accurate time propagation for the Schrödinger equation with an explicitly time–dependent Hamiltonian," *The Journal of chemical physics*, vol. 128, no. 18, p. 184101, 2008. [Cited on page 33]

[6] M. J. Donahue and D. G. Porter, "OOMMF user's guide, version 1.0," 1999. [Cited on page 34]

[7] B. Sjodin, "What's the difference between FEM, FDM, and FVM," *Machine Design*, vol. 414, 2016. [Cited on page 34]

[8] M. Beg, R. A. Pepper, and H. Fangohr, "User interfaces for computational science: A domain specific language for OOMMF embedded in Python," *AIP Advances*, vol. 7, no. 5, p. 056025, 2017. [Cited on page 34]

[9] J. Sanders and E. Kandrot, *CUDA by example: an introduction to general–purpose GPU programming*. Addison–Wesley Professional, 2010. [Cited on page 34]

[10] R. F. Evans, W. J. Fan, P. Chureemart, T. A. Ostler, M. O. Ellis, and R. W. Chantrell, "Atomistic spin model simulations of magnetic nanomaterials," *Journal of Physics: Condensed Matter*, vol. 26, no. 10, p. 103202, 2014. [Cited on pages 35, 41, 48, and 53]

[11] N. T. Binh, S. Ruta, O. Hovorka, R. F. Evans, and R. W. Chantrell, "Influence of finite–size effects on the Curie temperature of $L1_0$–FePt," *Physical Review B*, vol. 106, no. 5, p. 054421, 2022. [Cited on page 35]

[12] A. Ceballos, A. Pattabi, A. El-Ghazaly, S. Ruta, C. P. Simon, R. F. Evans, T. Ostler, R. W. Chantrell, E. Kennedy, M. Scott, *et al.*, "Role of element–specific damping in ultrafast, helicity–independent, all–optical switching dynamics in amorphous (Gd, Tb) Co thin films," *Physical Review B*, vol. 103, no. 2, p. 024438, 2021. [Cited on page 35]

[13] A. Vansteenkiste, J. Leliaert, M. Dvornik, M. Helsen, F. Garcia-Sanchez, and B. Van Waeyenberge, "The design and verification of MuMax3," *AIP advances*, vol. 4, no. 10, p. 107133, 2014. [Cited on page 35]

[14] U. Atxitia, D. Hinzke, and U. Nowak, "Fundamentals and applications of the Landau–Lifshitz–Bloch equation," *Journal of Physics D: Applied Physics*, vol. 50, no. 3, p. 033003, 2016. [Cited on page 36]

[15] A. Jha, *Electronic transport studies of highly–polarized compensated ferrimagnetic thin films: Mn_2Ru_xGa*. PhD thesis, Trinity College Dublin, School of Physics, Magnetism and Spin Electronics Group, 2022. [Cited on page 36]

[16] C. Fowley, K. Rode, Y.-C. Lau, N. Thiyagarajah, D. Betto, K. Borisov, G. Atcheson, E. Kampert, Z. Wang, Y. Yuan, *et al.*, "Magnetocrystalline anisotropy and exchange probed by high–field anomalous Hall effect in fully compensated half–metallic Mn_2Ru_xGa thin films," *Physical Review B*, vol. 98, no. 22, p. 220406, 2018. [Cited on pages 36 and 55]

[17] M. Stamenova, P. Stamenov, F. Mahfouzi, Q. Sun, N. Kioussis, and S. Sanvito, "Spin transfer torque in Mn_3Ga–based ferrimagnetic tunnel junctions from first principles," *Physical Review B*, vol. 103, no. 9, p. 094403, 2021. [Cited on page 36]

[18] R. W. Larsen, *Introduction to Mathcad 15*. Prentice Hall Press, 2010. [Cited on pages 37 and 50]

[19] G. Joyce, "Classical Heisenberg model," *Physical Review*, vol. 155, no. 2, p. 478, 1967. [Cited on page 38]

[20] W. Töws and G. Pastor, "Many–body theory of ultrafast demagnetization and angular momentum transfer in ferromagnetic transition metals," *Physical review letters*, vol. 115, no. 21, p. 217204, 2015. [Cited on page 38]

[21] A. Hirohata, K. Yamada, Y. Nakatani, I.-L. Prejbeanu, B. Diény, P. Pirro, and B. Hillebrands, "Review on spintronics: principles and device applications," *Journal of Magnetism and Magnetic Materials*, vol. 509, p. 166711, 2020. [Cited on pages 3, 39, 45, and 46]

[22] L. D. Landau, J. S. Bell, M. Kearsley, L. Pitaevskii, E. Lifshitz, and J. Sykes, *Electrodynamics of continuous media*, vol. 8. elsevier, 2013. [Cited on page 39]

[23] T. L. Gilbert, "A phenomenological theory of damping in ferromagnetic materials," *IEEE transactions on magnetics*, vol. 40, no. 6, pp. 3443–3449, 2004. [Cited on page 39]

[24] M. O. Ellis, R. F. Evans, T. A. Ostler, J. Barker, U. Atxitia, O. Chubykalo-Fesenko, and R. W. Chantrell, "The Landau–Lifshitz equation in atomistic models," *Low Temperature Physics*, vol. 41, no. 9, pp. 705–712, 2015. [Cited on page 39]

[25] E. R. Callen, "Temperature dependence of ferromagnetic uniaxial anisotropy coefficients," *Journal of Applied Physics*, vol. 33, no. 3, pp. 832–835, 1962. [Cited on page 41]

[26] I. Dzyaloshinsky, "A thermodynamic theory of 'weak' ferromagnetism of antiferromagnetics," *Journal of physics and chemistry of solids*, vol. 4, no. 4, pp. 241–255, 1958. [Cited on page 42]

[27] P. W. Anderson, "New approach to the theory of superexchange interactions," *Physical Review*, vol. 115, no. 1, p. 2, 1959. [Cited on page 42]

[28] T. Moriya, "Anisotropic superexchange interaction and weak ferromagnetism," *Physical review*, vol. 120, no. 1, p. 91, 1960. [Cited on page 42]

[29] A. Fert, V. Cros, and J. Sampaio, "Skyrmions on the track," *Nature nanotechnology*, vol. 8, no. 3, pp. 152–156, 2013. [Cited on page 42]

[30] A. Fert, N. Reyren, and V. Cros, "Magnetic skyrmions: advances in physics and potential applications," *Nature Reviews Materials*, vol. 2, no. 7, pp. 1–15, 2017. [Cited on page 42]

[31] A. Manchon, J. Železný, I. M. Miron, T. Jungwirth, J. Sinova, A. Thiaville, K. Garello, and P. Gambardella, "Current–induced spin–orbit torques in ferromagnetic and antiferromagnetic systems," *Reviews of Modern Physics*, vol. 91, no. 3, p. 035004, 2019. [Cited on pages 43 and 68]

[32] J. C. Slonczewski, "Current–driven excitation of magnetic multilayers," *Journal of Magnetism and Magnetic Materials*, vol. 159, no. 1–2, pp. L1–L7, 1996. [Cited on page 44]

[33] A. Manchon and S. Zhang, "Theory of spin torque due to spin–orbit coupling," *Physical Review B*, vol. 79, no. 9, p. 094422, 2009. [Cited on pages 45 and 46]

[34] J. Železný, H. Gao, A. Manchon, F. Freimuth, Y. Mokrousov, J. Zemen, J. Mašek, J. Sinova, and T. Jungwirth, "Spin–orbit torques in locally and globally noncentrosymmetric crystals: antiferromagnets and ferromagnets," *Physical Review B*, vol. 95, no. 1, p. 014403, 2017. [Cited on page 46]

[35] T. Jungwirth, X. Marti, P. Wadley, and J. Wunderlich, "Antiferromagnetic spintronics," *Nature nanotechnology*, vol. 11, no. 3, pp. 231–241, 2016. [Cited on page 46]

[36] S. Zhang and Z. Li, "Roles of nonequilibrium conduction electrons on the magnetization dynamics of ferromagnets," *Physical review letters*, vol. 93, no. 12, p. 127204, 2004. [Cited on pages 47, 69, and 83]

[37] U. Atxitia, O. Chubykalo-Fesenko, R. W. Chantrell, U. Nowak, and A. Rebei, "Ultrafast spin dynamics: the effect of colored noise," *Physical Review Letters*, vol. 102, no. 5, p. 057203, 2009. [Cited on page 48]

[38] K. Siewierska, G. Atcheson, A. Jha, K. Esien, R. Smith, S. Lenne, N. Teichert, J. O'Brien, J. M. D. Coey, P. Stamenov, *et al.*, "Magnetic order and magnetotransport in half–metallic ferrimagnetic Mn_yRu_xGa thin films," *Physical Review B*, vol. 104, no. 6, p. 064414, 2021. [Cited on pages 49, 55, 165, 169, and 181]

[39] J. C. Slater, "Atomic shielding constants," *Physical Review*, vol. 36, no. 1, p. 57, 1930. [Cited on page 49]

[40] J. E. Lennard-Jones, "Cohesion," *Proceedings of the Physical Society*, vol. 43, no. 5, p. 461, 1931. [Cited on page 49]

[41] G. Van Rossum, F. L. Drake, *et al.*, *Python reference manual.* Centrum voor Wiskunde en Informatica Amsterdam, 1995. [Cited on page 50]

[42] C. R. Harris, K. J. Millman, S. J. Van Der Walt, R. Gommers, P. Virtanen, D. Cournapeau, E. Wieser, J. Taylor, S. Berg, N. J. Smith, *et al.*, "Array programming with NumPy," *Nature*, vol. 585, no. 7825, pp. 357–362, 2020. [Cited on page 50]

[43] J. D. Hunter, "Matplotlib: A 2D graphics environment," *Computing in Science & Engineering*, vol. 9, no. 3, pp. 90–95, 2007. [Cited on page 50]

[44] A. Munshi, "The OpenCL specification," in *2009 IEEE Hot Chips 21 Symposium (HCS)*, pp. 1–314, IEEE, 2009. [Cited on pages 50 and 79]

[45] W. contributors, "Runge–Kutta methods," 2023. `https://en.wikipedia.org/w/index.php?title=Runge-Kutta_methods&oldid=1151548276`, Accessed: 2023–04–25. [Cited on page 52]

[46] W. contributors, "Linear multistep method," 2023. `https://en.wikipedia.org/w/index.php?title=Linear_multistep_method&oldid=1136115186`, Accessed: 2023–01–29. [Cited on page 52]

[47] W. H. Press, S. A. Teukolsky, W. T. Vetterling, and B. P. Flannery, *Numerical recipes in C*. Cambridge university press, 1992. [Cited on pages 52 and 53]

[48] J. O'Brien, "Numerical–integration," 2023. `https://github.com/eljackobrien/Numerical-Integration/tree/7ab608b7796ec40164c4d04692e8c05cd78ed8f3`, Permanent URL: 2024–02–09. [Cited on page 53]

[49] M. F. Fathoni and A. I. Wuryandari, "Comparison between Euler, Heun, Runge–Kutta and Adams–Bashforth–Moulton integration methods in the particle dynamic simulation," in *2015 4th International Conference on Interactive Digital Media (ICIDM)*, pp. 1–7, IEEE, 2015. [Cited on page 53]

[50] R. Mannella, "Integration of stochastic differential equations on a computer," *International Journal of Modern Physics C*, vol. 13, no. 09, pp. 1177–1194, 2002. [Cited on page 54]

[51] C. W. Gardiner *et al.*, *Handbook of stochastic methods*, vol. 3. springer Berlin, 1985. [Cited on page 54]

[52] M. Strungaru, S. Ruta, R. F. Evans, and R. W. Chantrell, "Model of magnetic damping and anisotropy at elevated temperatures: application to granular FePt films," *Physical Review Applied*, vol. 14, no. 1, p. 014077, 2020. [Cited on page 55]

[53] O. N. Mryasov, U. Nowak, K. Y. Guslienko, and R. W. Chantrell, "Temperature–dependent magnetic properties of FePt: effective spin Hamiltonian model," *Europhysics Letters*, vol. 69, no. 5, p. 805, 2005. [Cited on page 55]

[54] T. A. Ostler, R. F. Evans, R. W. Chantrell, U. Atxitia, O. Chubykalo-Fesenko, I. Radu, R. Abrudan, F. Radu, A. Tsukamoto, A. Itoh, *et al.*, "Crystallographically amorphous ferrimagnetic alloys: comparing a localized atomistic spin model with experiments," *Physical Review B*, vol. 84, no. 2, p. 024407, 2011. [Cited on page 55]

[55] S.-H. Yang, R. Naaman, Y. Paltiel, and S. S. Parkin, "Chiral spintronics," *Nature Reviews Physics*, vol. 3, no. 5, pp. 328–343, 2021. [Cited on page 56]

[56] C. Back, V. Cros, H. Ebert, K. Everschor-Sitte, A. Fert, M. Garst, T. Ma, S. Mankovsky, T. Monchesky, M. Mostovoy, *et al.*, "The 2020 skyrmionics roadmap," *Journal of Physics D: Applied Physics*, vol. 53, no. 36, p. 363001, 2020. [Cited on page 56]

[57] T. H. R. Skyrme, "A unified field theory of mesons and baryons," *Nuclear Physics*, vol. 31, pp. 556–569, 1962. [Cited on page 56]

[58] G. Chen, A. T. N'Diaye, S. P. Kang, H. Y. Kwon, C. Won, Y. Wu, Z. Qiu, and A. K. Schmid, "Unlocking Bloch–type chirality in ultrathin magnets through uniaxial strain," *Nature communications*, vol. 6, no. 1, p. 6598, 2015. [Cited on page 57]

[59] S. Rohart and A. Thiaville, "Skyrmion confinement in ultrathin film nanostructures in the presence of Dzyaloshinskii–Moriya interaction," *Physical Review B*, vol. 88, no. 18, p. 184422, 2013. [Cited on page 61]

[60] X. Wang, H. Yuan, and X. Wang, "A theory on skyrmion size," *Communications Physics*, vol. 1, no. 1, p. 31, 2018. [Cited on page 61]

[61] J.-V. Kim, F. Garcia-Sanchez, J. Sampaio, C. Moreau-Luchaire, V. Cros, and A. Fert, "Breathing modes of confined skyrmions in ultrathin magnetic dots," *Physical Review B*, vol. 90, no. 6, p. 064410, 2014. [Cited on page 61]

[62] C. Fowley, K. Rode, Y.-C. Lau, N. Thiyagarajah, D. Betto, K. Borisov, G. Atcheson, E. Kampert, Z. Wang, Y. Yuan, *et al.*, "Magnetocrystalline anisotropy and exchange probed by high–field anomalous Hall effect in fully compensated half–metallic Mn_2Ru_xGa thin films," *Physical Review B*, vol. 98, no. 22, p. 220406, 2018. [Cited on pages 20 and 64]

[63] F. Jakobs and U. Atxitia, "Atomistic spin model of single pulse toggle switching in Mn$_2$Ru$_x$Ga heusler alloys," *Applied Physics Letters*, vol. 120, no. 17, p. 172401, 2022. [Cited on page 64]

[64] J. Železný, H. Gao, K. Výborný, J. Zemen, J. Mašek, A. Manchon, J. Wunderlich, J. Sinova, and T. Jungwirth, "Relativistic Néel–order fields induced by electrical current in antiferromagnets," *Physical review letters*, vol. 113, no. 15, p. 157201, 2014. [Cited on page 68]

[65] D. Betto, K. Rode, N. Thiyagarajah, Y.-C. Lau, K. Borisov, G. Atcheson, M. Žic, T. Archer, P. Stamenov, and J. M. D. Coey, "The zero–moment half metal: How could it change spin electronics?," *AIP Advances*, vol. 6, no. 5, 2016. [Cited on pages 20 and 69]

[66] M. Žic, K. Rode, N. Thiyagarajah, Y.-C. Lau, D. Betto, J. M. D. Coey, S. Sanvito, K. J. O'Shea, C. A. Ferguson, D. A. MacLaren, *et al.*, "Designing a fully compensated half–metallic ferrimagnet," *Physical Review B*, vol. 93, no. 14, p. 140202, 2016. [Cited on pages 69 and 161]

[67] S. Lenne, Y.-C. Lau, A. Jha, G. Y. Atcheson, R. E. Troncoso, A. Brataas, J. M. D. Coey, P. Stamenov, and K. Rode, "Giant spin–orbit torque in a single ferrimagnetic metal layer," *arXiv preprint arXiv:1903.04432*, 2019. [Cited on pages 21 and 69]

[68] C. Kittel, *Introduction to solid state physics*. John Wiley & sons, inc, 2005. [Cited on page 72]

[69] A. J. Princep, R. A. Ewings, S. Ward, S. Tóth, C. Dubs, D. Prabhakaran, and A. T. Boothroyd, "The full magnon spectrum of yttrium iron garnet," *npj Quantum Materials*, vol. 2, no. 1, p. 63, 2017. [Cited on page 73]

[70] T. Sebastian, K. Schultheiss, B. Obry, B. Hillebrands, and H. Schultheiss, "Micro–focused Brillouin light scattering: imaging spin waves at the nanoscale," *Frontiers in Physics*, vol. 3, p. 35, 2015. [Cited on page 73]

[71] Z. Xiong, T. Datta, K. Stiwinter, and D.-X. Yao, "Magnon–phonon coupling effects on the indirect K–edge resonant inelastic X–ray scattering spectrum of a two–dimensional Heisenberg antiferromagnet," *Physical Review B*, vol. 96, no. 14, p. 144436, 2017. [Cited on page 73]

[72] D. Bozhko, V. Vasyuchka, A. Chumak, and A. Serga, "Magnon–phonon interactions in magnon spintronics," *Low Temperature Physics*, vol. 46, no. 4, pp. 383–399, 2020. [Cited on page 73]

[73] A. Ojanperä, V. Havu, L. Lehtovaara, and M. Puska, "Nonadiabatic Ehrenfest molecular dynamics within the projector augmented–wave method," *The Journal of chemical physics*, vol. 136, no. 14, 2012. [Cited on page 77]

[74] X. Li, J. C. Tully, H. B. Schlegel, and M. J. Frisch, "Ab–initio Ehrenfest dynamics," *The Journal of chemical physics*, vol. 123, no. 8, 2005. [Cited on page 77]

[75] A. Scherrer, F. Agostini, D. Sebastiani, E. Gross, and R. Vuilleumier, "On the mass of atoms in molecules: beyond the Born–Oppenheimer approximation," *Physical Review X*, vol. 7, no. 3, p. 031035, 2017. [Cited on page 77]

[76] F. P. Bonafé, B. Aradi, B. Hourahine, C. R. Medrano, F. J. Hernández, T. Frauenheim, and C. G. Sánchez, "A real–time time–dependent density functional tight–binding implementation for semiclassical excited state electron–nuclear dynamics and pump–probe spectroscopy simulations," *Journal of Chemical Theory and Computation*, vol. 16, no. 7, pp. 4454–4469, 2020. [Cited on page 77]

[77] N. Tancogne-Dejean, F. Eich, and A. Rubio, "Time–dependent magnons from first principles," *Journal of Chemical Theory and Computation*, vol. 16, no. 2, pp. 1007–1017, 2020. [Cited on page 77]

[78] J. D. Patterson and B. C. Bailey, *Solid–state physics: introduction to the theory.* Springer Science & Business Media, 2007. [Cited on pages 78 and 80]

[79] A. Altland and B. D. Simons, *Condensed matter field theory.* Cambridge university press, 2010. [Cited on page 80]

[80] J. J. Sakurai and J. Napolitano, *Modern quantum mechanics, second edition.* Addison–Wesley, 2010. [Cited on page 81]

[81] R. G. Pereira, S. R. White, and I. Affleck, "Spectral function of spinless fermions on a one–dimensional lattice," *Physical Review B*, vol. 79, no. 16, p. 165113, 2009. [Cited on page 86]

[82] T. Todorov, J. Hoekstra, and A. Sutton, "Current–induced forces in atomic–scale conductors," *Philosophical Magazine B*, vol. 80, no. 3, pp. 421–455, 2000. [Cited on pages 88 and 89]

[83] R. P. Feynman, "Forces in molecules," *Physical review*, vol. 56, no. 4, p. 340, 1939. [Cited on page 88]

[84] M. Di Ventra and S. T. Pantelides, "Hellmann–Feynman theorem and the definition of forces in quantum time–dependent and transport problems," *Physical Review B*, vol. 61, no. 23, p. 16207, 2000. [Cited on page 88]

Chapter 3

Structural Investigation by X-ray and neutron Diffraction

The atomic scale structure of materials defines that materials' macroscopic properties. In the development of new materials, characterisation of the structural properties is an imperative task in the optimisation process, this is especially true for thin films, whose vertical extent is microscopic itself. X-rays with wavelengths of a similar order to the interatomic spacings in crystals provide a powerful method to probe the structural properties via diffraction. The interatomic spacing in crystals is typically of the order $1 - 10\,\text{Å}$, which roughly translates to photons with energies in the range $10 - 1\,\text{keV}$.

For over a century now, X-rays have been most commonly generated using X-ray tubes, where electrons are emitted by a hot cathode wire and accelerated towards a metal anode material using a high voltage, generally $> 20\,\text{keV}$. These electrons hit the metal and are inelastically scattered and slowed, emitting "bremsstrahlung" radiation in the process. More importantly, the electrons can strike atoms and cause inner K-shell electrons in the atom to be ejected, provided the impinging electrons have more kinetic energy than the binding energy. When this occurs, the hole in the atomic energy level of the atom in the metal will typically be filled by an electron from the next shell up, and to conserve energy, this electron must emit a photon with energy equal to the difference in energy between the atomic levels $E_\gamma = E_b(n=1) - E_b(n=2)$. Due to this dependence on the exact energy of the atomic levels, these photons are characteristic of each element, and a photon emitted concurrent to the energy level transition from the second to first level $(2p_{3/2} \rightarrow 1s)$ is known as a K_{α_1} photon. The most common anode material for X-ray tubes is Cu, with

$E_\gamma = 8.05\,\mathrm{keV}$ and $\lambda_\gamma = 1.54\,\mathrm{\mathring{A}}$ for the K_{α_1} radiation (these values are perfect for X-ray diffraction). In addition, Cu is easily cooled and potentiated due to its large thermal and electrical conductivity. Mo is another common material with $E_\gamma = 17.5\,\mathrm{keV}$: shorter wavelengths grants accessibility to smaller values of interatomic spacing, as will become clear below when Bragg's diffraction equation is introduced.

Much more advanced sources of X-rays come in the form of synchrotrons and free-electron lasers. These large-scale facilities have far higher spectral power, providing far more photons per unit time, allowing for much faster acquisitions and larger signal-to-noise ratios, especially for thin films with smaller numbers of atoms. However, they are in very high demand and it is difficult to justify their use and gain access (and none exist in Ireland of course) and I have not made use of them during my work, so I will not go into any further detail.

3.1 Theory

3.1.1 Photon Scattering

3.1.1.1 Scattering from an Electron

Given their electromagnetic nature, photons will interact with and be scattered by the electromagnetic potential of charged particles. The low-energy, elastic phenomenon of Thompson scattering describes the coherent scattering of electromagnetic radiation by a charged particle such as an electron. This elastic limit is always valid for the photon energies we are interested in (when the wavelength is a similar size to the crystalline interatomic distances) around $1\,\mathrm{keV} - 10\,\mathrm{keV}$.

In this classical theory, the total scattering cross section for an electromagnetic plane wave incident on a charged particle is obtained by equating the oscillation of the charged particle to that of the electric component of the electromagnetic field, treating the particle as a dipole antenna and integrating the radiated power of the antenna over a solid angle [1]:

$$\sigma = \frac{8\pi}{3}\left(\frac{q^2}{4\pi\varepsilon_0 mc^2}\right)$$

In materials science, the charged particles we are interested in are electrons and protons.

Given the charge and mass of these particles $|q| = 1.602 \times 10^{-19}\,\mathrm{C}$, $m_e = 9.109 \times 10^{-31}\,\mathrm{kg}$ and $m_p = 1.673 \times 10^{-27}\,\mathrm{kg}$, their scattering cross sections are $\sigma_e = 6.652 \times 10^{-29}\,\mathrm{m^2}$ and $\sigma_p = 1.973 \times 10^{-35}\,\mathrm{m^2}$, thus we can assume the photons are only scattered by electrons in a crystal lattice. The polarisation of the electric field is considered later in subsubsection 3.1.2.1.

3.1.1.2 Scattering from a Periodic Potential

For a detailed derivation of the diffracted intensity from a crystal, see for example [2, §1.3]. Central to theory of diffraction is the concept of constructive interference of waves. A coherent incident monochromatic plane wave will scatter elastically from two scattering centres, and the resulting waves interfere constructively, if the difference in path length is equal to some integer multiple of the wavelength. W. L. Bragg's initial theory considered the plane wave being partially specularly reflected by a series of mirror planes in a crystal [3]. This yielded the very familiar equation for Bragg diffraction
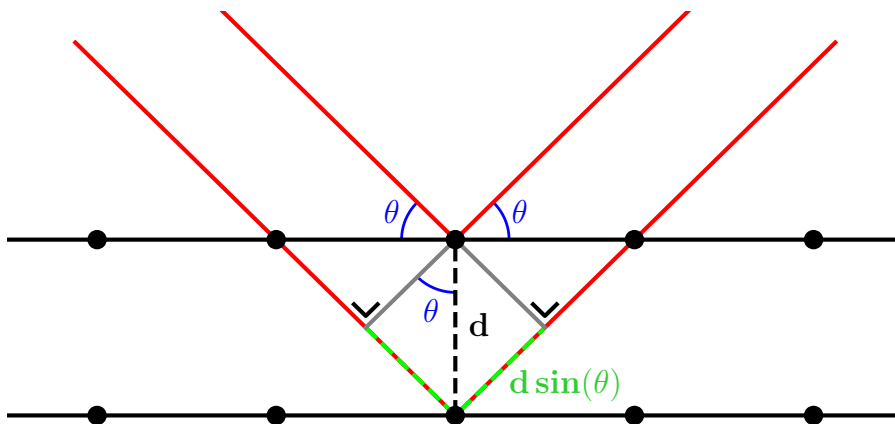
Figure 3.1: Diffraction from a crystal according to Bragg.

$$n\lambda = 2d\sin(\theta_B), \tag{3.1}$$

where λ, d and θ are the wavelength, inter-plane spacing and angle of incidence respectively. Despite its simplicity, this is a remarkably useful result that is still used in everyday crystallography. However, to capture the full essence of diffraction from a crystal we must consider the Thomson scattering of photons from the individual electrons: we should use

a vector approach and integrate over the electron density. From Figure 3.2, the total scattered field is proportional to the integral of the waves which are Bragg scattered by each infinitesimal point in the electromagnetic potential:
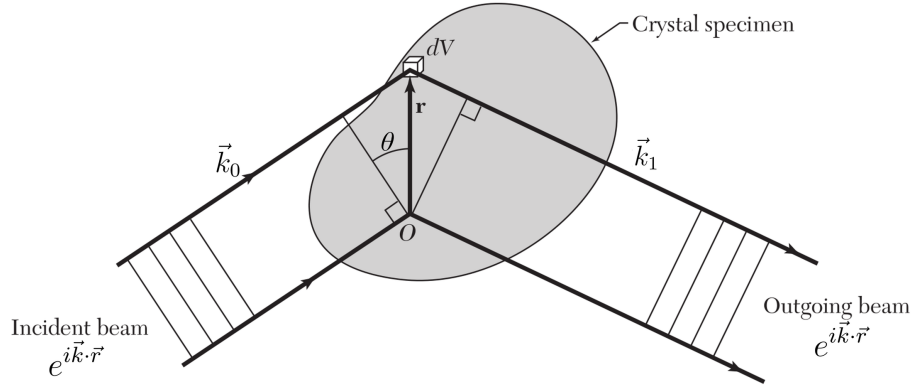
Figure 3.2: The geometrical construction is similar to the Bragg case. The path difference is the sum of the projections of $\vec{r}$ onto the incoming and outgoing photon wavevectors, equal to $(-\vec{k}_0 \cdot \vec{r}) + (\vec{k}_1 \cdot \vec{r}) = \vec{Q} \cdot \vec{r}$. Picture reproduced from Kittel [4].

$$\int \rho_e(\vec{r}) \exp\left(-i\vec{Q} \cdot \vec{r}\right) \mathrm{dr} \tag{3.2}$$

Where $\vec{Q}$ is the scattering (or momentum transfer) vector:

$$\vec{Q} = 2\pi\vec{q} = \vec{k}_1 - \vec{k}_0, \qquad |\vec{k}| = \frac{2\pi}{\lambda}, \qquad |\vec{Q}| = 2\pi|\vec{q}| = \frac{4\pi \sin(\theta)}{\lambda} \tag{3.3}$$

These relations for the scattering vector $\vec{Q}$ and reduced scattering vector $\vec{q}$ will become useful later on.

Now, any periodic function, or a function defined in a finite volume, such as that describing the atomic sites in a crystal lattice, can be expanded in a Fourier series of sines and cosines. The electronic density in a crystal can be written

$$\rho_e(\vec{r}) = \sum_{\vec{G}} n_{\vec{G}} \exp\left(i\vec{G} \cdot \vec{r}\right) \tag{3.4}$$

where $\rho_e(\vec{r})$ is the electronic density at a point $\vec{r}$ from the origin, $\vec{G}$ is a set of vectors in the Fourier space that leaves $\rho_e(\vec{r})$ unaltered and $n_{\vec{G}}$ are the Fourier coefficients. In fact, the vectors which describe the translational symmetry of a crystal are sums of integer multiples of the **reciprocal lattice vectors**: $\vec{G} = h\hat{x}^* + k\hat{y}^* + l\hat{z}^*$. On substituting Equa-

tion 3.4 into Equation 3.2, the phase factor becomes $\exp\left(-i(\vec{G} - \vec{Q}) \cdot \vec{r}\right)$. The intensity is proportional to the absolute square of the total field and in fact vanishes, except when the scattering vector differs appreciably from a reciprocal lattice vector sum. Therefore our new scattering condition can be stated as $\vec{G} = \vec{Q}$ for constructive interference: we will have diffracted intensity when the scattering vector is equal to a linear combination of reciprocal lattice vector.

3.1.1.3 Scattering from an Atom (Form Factors)

If we now consider the scattering of photons from a single atom, the scattered field will be proportional to the integral over the electronic density around the atom. The **atomic form factor** is defined:

$$f = \int_{at} \rho_e(\vec{r}) \exp\left(-i\vec{Q} \cdot \vec{r}\right) dr \tag{3.5}$$

The electronic density will increase for larger atoms with more electrons, while coherent photons scattering from different points of the atomic charge density will slightly lose coherency. Accurate values for each atom (and oxidation state) have been calculated using various quantum mechanical methods and tabulated in tables such as [5].

3.1.1.4 Scattering from a Lattice (Structure Factors)

The atomic form factors and the scattering condition $\vec{G} = \vec{Q}$ are in fact all that is necessary to determine the intensity of each reflection for simple cubic structures where all atoms are identical, however, for more general structures, we must integrate over the unit cell, which is equivalent to summing the integral contribution from each of the N atoms in the unit cell:

$$F = \int_{uc} \rho_e(\vec{r}) \exp\left(-i\vec{Q} \cdot \vec{r}\right) = \sum_{n=1}^{N} \int_{at} \rho_e(\vec{r}) \exp\left(-i\vec{Q} \cdot (\vec{r} - \vec{r}_n)\right) dr$$

where the atomic form factors Equation 3.5 can be factored out to yield the **Structure factors** for a given crystal:

$$F = \sum_{n=1}^{N} f_n \exp\left(-i\vec{Q} \cdot \vec{r}_n\right)$$

The structure factors give the intensity of coherent scattering from the atoms in a unit cell for a given scattering vector. The additional condition for constructive interference from the crystal is $\vec{G} = \vec{Q}$. Writing the position vector for an atom (in a cubic unit cell) as $\vec{r} = x_n\hat{x} + y_n\hat{y} + z_n\hat{z}$ where i_n are the fractional coordinates and $\hat{i}$ the lattice primitive unit vectors, the dot product in the phase factor is equal to $\vec{G} \cdot \vec{r} = (h\hat{x}^* + k\hat{y}^* + l\hat{z}^*) \cdot (x_n\hat{x} + y_n\hat{y} + z_n\hat{z}) = 2\pi(hx_n + ky_n + lz_n)$ where i_n^* are the reciprocal lattice vectors, so finally:

$$F(hkl) = \sum_{n=1}^{N} f_n \exp(-i2\pi\,(hx_n + ky_n + lz_n))$$

To see the effect of the structure factors, it is instructive to now take the example of body-centred and face-centred cubic lattices made up of identical atoms: For the body-
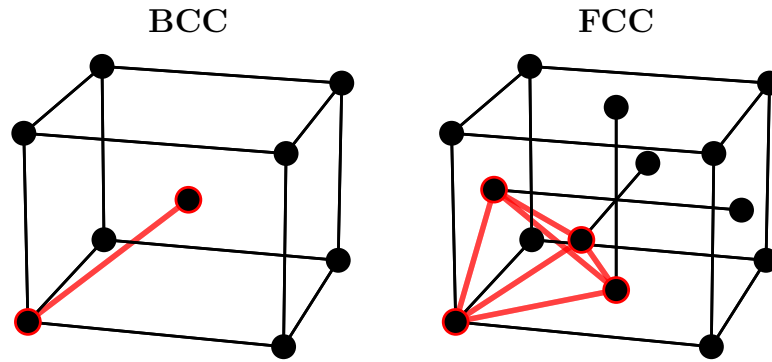
Figure 3.3: bcc and fcc lattices with the primitive atoms needed to periodically replicate the unit cell indicated.

centred-cubic (bcc) lattice, there are two atoms in the primitive unit cell, situated at $(0,0,0)$ and $\left(\frac{1}{2}, \frac{1}{2}, \frac{1}{2}\right)$. For the face-centred-cubic (fcc) lattice, there are four atoms in the primitive cell, situated at $(0,0,0)$, $\left(\frac{1}{2}, \frac{1}{2}, 0\right)$, $\left(\frac{1}{2}, 0, \frac{1}{2}\right)$ and $\left(0, \frac{1}{2}, \frac{1}{2}\right)$. The respective structure factors for the two types of lattice can then be written:

$$F_{bcc}(hkl) = f_0 \left(1 + \exp(-i\pi\,(h + k + l))\right)$$

$$F_{fcc}(hkl) = f_0 \left(1 + \exp(-i\pi\,(h + k)) + \exp(-i\pi\,(h + l)) + \exp(-i\pi\,(k + l))\right)$$

Per the definition of $\vec{G}$, (hkl) are the integer multiples of the reciprocal lattice vectors, or in other words the miller indices of the lattice. This result tells us that in addition to

satisfying the diffraction condition $\vec{G} = \vec{Q}$, there are reflections which are forbidden based on the symmetry of the primitive lattice. For example, for the fcc lattice, if we consider the (111) and (103) reflections and recall the Euler formula $\exp(ix) = \cos(x) + i\sin(x)$:

$$F_{fcc}(111) = f_0 \left(1 + 3\exp(-i2\pi)\right) = 4f_0$$

$$F_{fcc}(103) = f_0 \left(1 + \exp(-i\pi) + \exp(-i4\pi) + \exp(-i3\pi)\right) = f_0 \left(1 - 1 + 1 - 1\right) = 0$$

See, for example, Kittel [4, §2], for more details. So we see how the reciprocal lattice notation has allowed us to construct a rather elegant method of determining the intensity diffracted from families of lattice planes. For more complicated structures with multiple types of atoms, the exponents are scaled by their atomic form factors f_n and we generally get partial constructive or destructive interference and significantly more non-negligible reflections. Calculation of full diffraction patterns is always done on computers in modern times and offers a method to fingerprint crystal structures. Common tools for calculating structure factors include FullProf [6] and VESTA [7].

3.1.1.5 The Laue Interference Function

Another important concept in diffraction is the interference function, which will become especially useful later when considering the shapes and widths of diffracted peaks. We have seen that the total diffracted field amplitude, due to constructive interference, is proportional to a sum over all N diffracting centres:

$$F \propto \sum_{n=1}^{N} \exp\left(-i\vec{Q} \cdot \vec{r}_n\right)$$

The position vector can be split into its three Cartesian components, as was done for the structure factors but not just over the unit cell in this case $\vec{r}_n = n_1 a\hat{x} + n_2 b\hat{y} + n_3 c\hat{z}$, where a, b, c are the primitive lattice lengths. This leads to a triple sum over all the atoms in the three orthogonal directions:

$$F \propto \sum_{n_x=0}^{N_x-1} \sum_{n_y=0}^{N_y-1} \sum_{n_z=0}^{N_z-1} \exp(-iQ_x n_x a) \exp(-iQ_y n_y b) \exp(-iQ_z n_z c) \qquad (3.6)$$

We can utilise the fact that these sums are equivalent to a geometric series:

$$\sum_{n=0}^{N-1} r^n = \frac{1 - r^N}{1 - r}$$

Let $k = Qa\hat{x}^*$ for each sum:

$$\sum_{n_x=0}^{N_x-1} \exp(-ikn_x) = \sum_{n_x=0}^{N_x-1} (\exp(-ik))^{n_x} = \frac{1 - (\exp(-ik))^{N_x}}{1 - \exp(-ik)}$$

and then multiplying with the complex conjugate:

$$\frac{1 - \exp(-ikN_x)}{1 - \exp(-ik)} \cdot \frac{1 - \exp(ikN_x)}{1 - \exp(ik)} = \frac{1 - (\exp(-ikN_x) + \exp(ikN_x))}{1 - (\exp(-ik) + \exp(ik))}$$

$$= \frac{1 - 2\cos(kN_x)}{1 - 2\cos(k)} = \frac{\sin^2\left(N_x\frac{k}{2}\right)}{\sin^2\left(\frac{k}{2}\right)}$$

Taking this knowledge back to Equation 3.6, we finally obtain:

$$I \propto |F|^2 \propto \frac{\sin^2\left(Q_x a\frac{N_x}{2}\right)}{\sin^2\left(Q_x a\frac{1}{2}\right)} \cdot \frac{\sin^2\left(Q_y b\frac{N_y}{2}\right)}{\sin^2\left(Q_y b\frac{1}{2}\right)} \cdot \frac{\sin^2\left(Q_z c\frac{N_z}{2}\right)}{\sin^2\left(Q_z c\frac{1}{2}\right)} \tag{3.7}$$

There are no cross terms while taking the complex conjugate due to the mutual orthogonality of the Cartesian vector basis. This formulation makes the diffraction condition more obvious, e.g. for maximum intensity $Q_z c = 2\pi L$ along the $\hat{z}$ direction. And is useful when discussing the origins of peak broadening in later sections.

3.1.2 Instrumental Corrections

3.1.2.1 Polarisation Correction

The scattering of a photon from an electron was introduced in the beginning of this section. What was not considered is the electric field and its polarisation. It is convenient to separate the polarisation into components in and normal to the scattering plane, denoted E_π and E_σ. Consider the acceleration of an electron by the electric field of an incident photon and the resulting field produced by the radiating dipole at a point R in Figure 3.4 below:
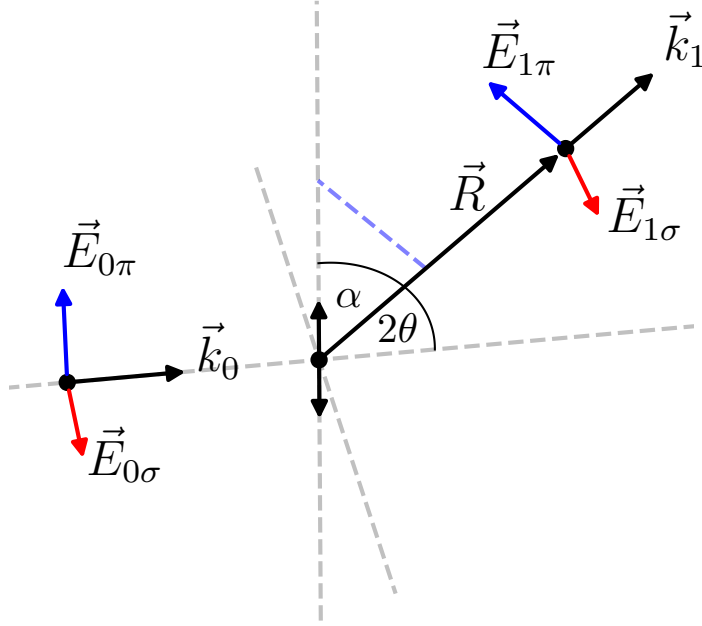
Figure 3.4: Electric field components for a photon elastically scattered by an electron.

Only looking at the angular dependencies, the perpendicular component is unaltered: $E_{1\sigma} = E_{0\sigma}$. For the component in the scattering plane, an observer at R will see the projection of the radiating dipole perpendicular to the vector $\vec{R}$, so $E_{1\pi} = E_{0\pi} \sin(\alpha) = E_{0\pi} \cos(2\theta)$, as $\alpha = 90° - 2\theta$. If we consider the common case of an unpolarised X-ray beam diffracted first by a monochromating crystal and then by our sample with the scattering vectors all coplanar, the resulting electric field polarised in the plane at R is then $E_\pi = E_{0\pi} \cos(2\theta_M) \cos(2\theta)$ where θ_M is the Bragg scattering angle of the monochromating crystal. The perpendicular component is still unaltered. The intensity of the radiation is proportional to the absolute square of the electric field $I \propto \langle E^2 \rangle = \langle E_\pi^2 \rangle + \langle E_\sigma^2 \rangle$. We have worked out that $E_\pi = E_{0\pi} \cos(2\theta_M) \cos(2\theta)$ and $E_\sigma = E_{0\sigma}$, and for an unpolarised initial X-ray beam we know that $\langle E_{0\sigma}^2 \rangle = \langle E_{0\pi}^2 \rangle = \frac{1}{2} \langle E_0^2 \rangle$, leading to the final expression for the polarisation correction for the intensity:

$$I \propto \frac{1}{2} \left[1 + \cos^2(2\theta_M) \cos^2(2\theta) \right]$$

3.1.2.2 Lorentz Correction

The exact meaning of the Lorentz factor can cause confusion at first as it has a different useful form depending on whether one is investigating polycrystalline or single crystal thin film and bulk samples [8, §6.2.4]. When considering single-crystal diffraction, the Lorentz factor is most often discussed in terms of the angular velocity of the scan along the given axis of rotation, however, most scans in modern diffractometers rotate a given angular step and record intensity with the entirety of the system stationary for a set integration time. It is more aptly referred to as a geometrical factor in this case.

The correction arises from the fact that a scan linear in a real-space angle is not linear in reciprocal space units. The correct form is given in the international tables [8, §6.2.4] or for example by Smilgies [9] and a more general solution for arbitrary scan types was given by McIntyre and Stansfield [10]. The correction in our case is usually of the form $L_{corr} \propto 1/\sin(2\theta)$. Alternate forms are described when necessary in the following sections.

3.1.2.3 Illuminated Volume Correction

The most common geometry used in XRD is the parafocusing Bragg-Brentano geometry used for powder diffraction. The source, sample and detector lie on the focusing circle with the entire sample illuminated. This geometry has the benefit of a very high intensity but due to the focusing constraints can only be used to measure reflection with scattering vectors normal to the surface of the sample.

In my work, I am interested in a wide range of reflections with a variety of orientation angles. We instead use the much more versatile collimated-beam geometry. This geometry is more suited to thin film investigation and is comparatively simple to visualise. One additional correction that is introduced is the illuminated volume correction. For a beam with a constant cross-sectional area and a sample of finite size, the volume of material illuminated, and therefore the number of atoms which contribute to the diffracted intensity, depends on the angle of incidence of the incoming X-ray beam. A simple geometric construction, as in Figure 3.5, helps to visualise the situation and we can infer that the volume correction is equal to $V_{corr} = b \cdot t/\sin(\omega)$. We are generally only interested in the relative intensities of reflections from a given sample so we simply say $V_{corr} \propto 1/\sin(\omega)$.

One thing to note is that the simple correction as we have introduced it above assumes
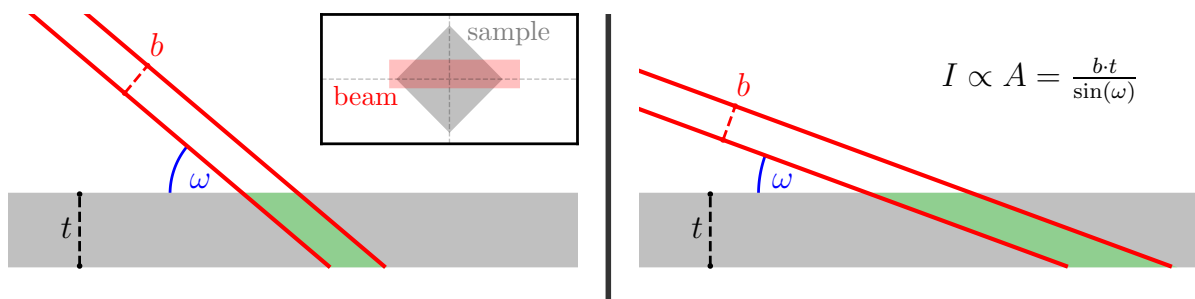
Figure 3.5: 2D projection of the illuminated volume in a collimated beam XRD scan for incident angles $\omega = 40°$ and $\omega = 20°$, with film thickness greatly exaggerated for clarity. The inset shows how the X-ray beam may overflow the sample and be imperfectly centred.

that the entire X-ray beam is incident on the sample and that there are no elemental inhomogeneities etc. If part of the X-ray beam should fall outside the sample surface, especially if the sample is oriented diagonally, the volume correction will need to be altered slightly, as illustrated in the inset of Figure 3.5.

3.1.2.4   Monochromation and Collimation Correction

Radiation produced by any kind of source is rarely perfectly monochromatic. As was discussed at the beginning of this section, most laboratory systems typically produce radiation by bombarding an anode metal with high-energy electrons, resulting in continuous "bremsstrahlung" radiation as well as sharp peaks in intensity at energies characteristic to the anode material. A spectrum that might be observed from a copper target is shown in Figure 3.6. The largest number of photons are produced from the $n = 2$ to $n = 1$ atomic transition K_α in the Cu with energy $E = 8.05 \, \text{keV}$, but there is a significant background from the bremsstrahlung and the characteristic peak is quite broad due to the high temperature etc. To be more useful, the radiation must be monochromated. The most basic way to do this is to simply use a filter (or filters) with an absorption edge just above (and below) the desired characteristic energy, such as a Ni foil. However, the K_α line is actually a doublet since the $2p$ energy levels are split by their total quantum number, consisting of K_{α_1} and K_{α_2}, with the latter having a slightly lower energy of $E = 8.03 \, \text{keV}$ with around half the intensity. If using the filter-monochromating method, one therefore must account for this doublet when analysing data, while peaks in the emission spectrum further from this energy (such as K_β lines) can safely be ignored. A more effective way is
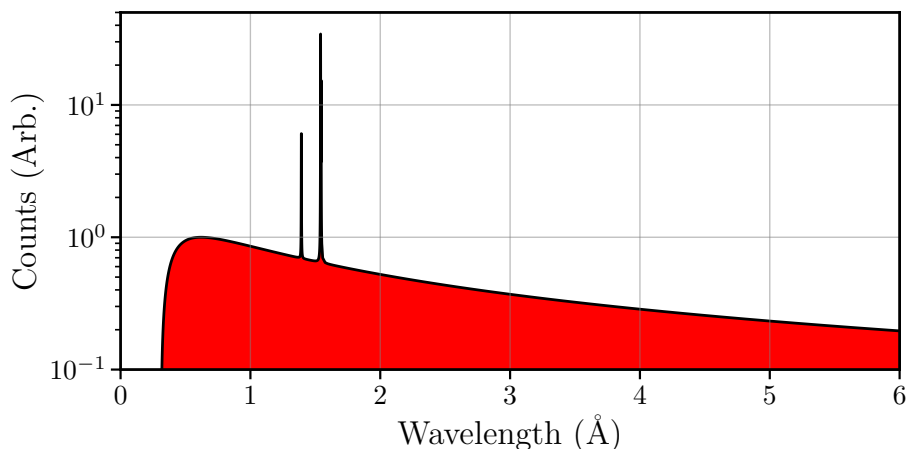
Figure 3.6: A calculated X-ray emission spectrum for an X-ray tube with a Cu anode operated at $40\,\text{kV}$. The bremsstrahlung is calculated using Kramer's law [11] and the values for the characteristic X-ray peaks are from Hölzer et al. [12].

to use diffraction to monochromate (in order to perform more diffraction), for which very high-quality crystals are needed because a resolution of $0.25\,\%$ is required to separate the K_α sub-peaks. Luckily, the unhalting progress of the semiconductor industry has provided us with macroscopic atomically perfect crystals of semiconductors such as Si and Ge. An example of a modern monochromator used in a laboratory system for Cu K_{α_1} radiation is the Ge (220) double-bounce monochromator; given the photon energy $E = 8.0478\,\text{keV}$ ($\lambda = 1.5406\,\text{Å}$) and Ge cubic lattice size $a = 5.658\,\text{Å}$, we can rearrange Equation 3.1 to obtain $\theta_M = 45.296°$. Doing the Bragg diffraction twice gives a very good monochromation which suppresses the K_{α_2} to an intensity typically less than $1\,\%$ the magnitude of K_{α_1}, enough that it can be ignored during data analysis, greatly simplifying that part of the experimental procedure. The benefits of various crystal monochromator configurations are analysed by Konya [13].

Collimation for parallel-beam experiments is generally performed in tandem with the monochromation. The simplest collimation method is the use of shadowing slits, thus extracting a roughly collimated beam by geometry alone. Collimation slits work in tandem with wavelength dispersive diffracting crystals enhancing monochromation. In addition to diffraction from perfect semiconductor crystals, a *graded curved multilayer*, known as a Göbel mirror, can be used for combined monochromation and collimation [14]. These parabolically curved mirrors consist of alternating layers (often W/Si or Ni/C), deposited on a curved substrate such that the layer thickness increases as the parabolic curve radius

decreases, with the source positioned at the focal point, the divergent photons emitted will be collimated and monochromated by Bragg diffraction from different points on the mirror. Göbel mirrors offer similar collimation to shadowing slits with a factor 10 increased intensity [15, §1.2] Excellent collimation and monochromation can be achieved by coupling the output of the Göbel mirror into a Ge (220) double-bounce channel-cut crystal monochromator, allowing through the Cu K_{α_1} photons with wavelength of $\lambda_\gamma = 1.5406\,\text{Å}$ but as little as possible of the K_{α_2} with $\lambda_\gamma = 1.5444\,\text{Å}$ [16]. Absorbing slits are often additionally used to control the size and divergence of the beam. For the highest possible resolution, additional monochromating crystals are sometimes used on the detector side of the setup as well, known as "analyser crystals" instead of monochromators in this case. The downside is that the overall intensity is of course significantly reduced, meaning that the various monochromation and collimation methods all have their preferred applications depending on the system being investigated: there is a trade-off between resolution and intensity. Monochromation by crystal diffraction in particular alters the polarisation of the X-ray beam which impinges on the sample, as was discussed in the polarisation correction section.

3.1.2.5 Absorption Correction

Photons travelling through a material can be absorbed via the photoelectric effect as well as inelastically Compton-scattered. The well-known mass absorption cross-sections describe how likely photons are to interact in a material at a given energy. NIST maintains a database of these coefficients at `https://dx.doi.org/10.18434/T48G6X`. For example, from the NIST calculator, the inelastic mass absorption coefficient at $E = 8.0478\,\text{keV}$ for a material that I have worked with, $\text{Mn}_2\text{Ru}_x\text{Ga}$, is $\sigma = 182\,\text{cm}^2\,\text{g}^{-1}$. This material has a density of roughly $\rho = 8\,\text{g}\,\text{cm}^{-3}$, resulting in a linear attenuation coefficient $\mu = \rho\sigma = 1456\,\text{cm}^{-1}$. The reciprocal of this characterises the average penetration depth $z_{av} = 6.87\,\mu\text{m}$. I have dealt exclusively with diffraction on thin films with $t < 100\,\text{nm}$, far smaller than this penetration depth, showing that the effects of absorption can be safely ignored.

3.1.3 Material-Dependent Corrections

3.1.3.1 Thermal Vibrations

This is the appropriate place to introduce the effect of thermal vibrations. These vibrations of the atoms cause a larger effective spread of the electronic density and a resulting reduction of the diffracted intensity. We can obtain an expression for the effect of these vibrations by including a shift of position into the atomic form factors Equation 3.5:

$$f_T = \int_{at} \rho_e(\vec{r}) \exp\left(-i\vec{Q} \cdot \left(\vec{r} + \vec{\delta r}\right)\right) dr$$

Splitting the exponential term

$$f_T = \int_{at} \rho_e(\vec{r}) \exp\left(-i\vec{Q} \cdot \vec{r}\right) \exp\left(-i\vec{Q} \cdot \vec{\delta r}\right) dr$$

The experimentally relevant quantity here is the time average, we perform this average for the vibrational term. In addition, since the displacements of the atoms from their equilibrium positions is small, we can approximate the exponential by its Taylor series:

$$f_T = f\langle\exp\left(-i\vec{Q} \cdot \vec{\delta r}\right)\rangle = f\left(1 - i\vec{Q} \cdot \langle\vec{\delta r}\rangle - \vec{Q}^2 \cdot \langle\vec{\delta r}^2\rangle + i\vec{Q}^3 \cdot \langle\vec{\delta r}^3\rangle + O(4)\right)$$

If the displacements $\vec{\delta r}$ are isotropic around 0, then the odd powers will average to 0. We can convert back to a single exponential using the same small displacement assumption after dropping these terms:

$$f_T = f\left(1 - \vec{Q}^2 \cdot \langle\vec{\delta r}^2\rangle\right) = f\exp\left(-\frac{1}{2}\vec{Q}^2 \cdot \langle\vec{\delta r}^2\rangle\right)$$

The squared magnitude of the scattering vector is $|\vec{Q}|^2 = 16\pi^2 \sin^2(\theta)/\lambda^2$ and we can replace the average of the displacement vector with the mean displacement along the scattering vector direction for a given atom to yield:

$$f_T = f\exp\left(-\frac{8\pi^2}{\lambda^2}\sin^2(\theta)\bar{u^2}\right) = f\exp\left(-B(T)\frac{\sin^2(\theta)}{\lambda^2}\right)$$

Where $B = 8\pi^2 \bar{u^2}$ is usually called the Debye temperature factor. Finally the new structure factors, corrected for thermal vibrations of the atoms, are:

$$F_T = \sum_{n=1}^{N} f_n \exp\left(-B(T)\frac{\sin^2(\theta)}{\lambda^2}\right) \exp\left(-i\vec{Q}\cdot\vec{r}_n\right)$$

We see that thermal vibrations cause a reduction in intensity that increases for larger temperatures and angles. The Debye factor is usually absorbed into the atomic form factor.

3.1.3.2 Finite Size Broadening

Simple diffraction formulae such as Bragg's law implicitly assume infinite diffracting crystals. If we are to derive an expression for the effect of a finite-sized diffracting crystallite on the shape of a real-life detected peak, we can follow the method of Birkholz [17] and refer back to the interference function Equation 3.7. For simplicity, we will assume that the scattering vector is vertically oriented such that $Q_x = Q_y = 0$. We then have:

$$I \propto \frac{\sin^2\left(Qc\frac{N_z}{2}\right)}{\sin^2\left(Qc\frac{1}{2}\right)}$$

We can convert to the dimensionless scattering coordinate $\xi = Qc$, where the main peak in the spectrum then extends from $-\pi$ to $+\pi$, as shown in Figure 3.7. The integrated
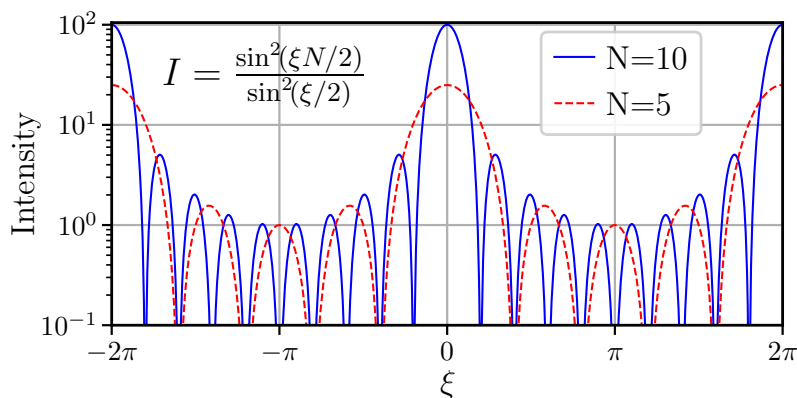
Figure 3.7: The interference function as a function of the scattering coordinate for two values of N, the numbers of atoms along the diffraction vector direction.

intensity of the peak is then simply calculated:

$$I_{int} = \int_{-\pi}^{\pi} \frac{\sin^2(\xi N_z/2)}{\sin^2(\xi/2)} d\xi = 2\pi N_z$$

while the amplitude of the peak is simply $I_0 = N_z^2$. This means the **integral breadth** of the peak is $\beta_\xi = I_{int}/I_0 = 2\pi/N_z$. Converting back to Q by multiplying by $dQ/d\xi = 1/c$ and noting that the crystallite size along the scattering vector direction is $D_z = cN_z$, we finally obtain:

$$D_z = \frac{2\pi}{\beta_Q}$$

This result was first derived, in terms of 2θ, by Scherrer [18] and is typically referred to as the Scherrer equation. Note that the subscript z is used because we assumed the scattering vector was directed OOP, in general, the crystallite size along the direction of the scattering vector is what is measured. This remarkably simple result relates the observed broadening of a diffracted peak to the size of the crystallites in the diffracting medium. It generalises trivially to scattering vectors which are not coincident with a particular crystal axis, as in this case, with a few caveats. For non-cubic crystallites, the apparent crystallite size will be different depending on exactly what part of the crystallite that the photon impinges on. To properly account for the shape anisotropy of the crystallite, dividing the crystallite into columns of unit cells of different heights is a useful method, more details can be found in, for example, [17, §3.4.2]. For spherical crystallites, a more realistic assumption, the secondary peaks will be smoothed out since the sum over the intensity from different columns will have different values of N and therefore different oscillation frequencies. The integral breadth can be shown to be $D_{sph} = (6/\pi)^{\frac{1}{3}} D_{cube} = 1.241 D_{cube}$. The correction factors for various crystal shapes were calculated by Langford et al. [19]. The second important factor to consider is that the crystallite size value obtained is a **volume average** and so is heavily weighted towards larger crystallites in the sample. The distribution of crystallite sizes is often close to log-normal in shape, as per Hinds [20]. These facts must be considered when attempting to quantitatively interpret the crystallite size estimated using this method. Lastly, due to how small the breadths become when the crystallite size grows and N becomes very large, the Scherrer equation is only truly accurate for $D \leq 100\,\text{nm}$ [18]. Beyond that, the finite-size broadening becomes a

tiny fraction of the total observed peak width and cannot be accurately determined. In summary, smaller coherently diffracting crystallites result in broader reflections due to the nature of constructive interference (less atoms means a smaller number of sinusoids to sum and a less sharp peak) and non-cubic crystallites result in a smoothing out of the peak due to the summing of sinusoids with different frequency.

3.1.3.3 Microstrain Broadening

Microstrain in the context of XRD refers to local distortions in the interatomic or interplanar distance d within individual coherently diffracting crystallites. These distortions generally are caused by defects in the crystal lattice which form as a result of strain. Epitaxial thin films typically grow with a large amount of compressive or tensile strain in the plane due to mismatch between the substrate and sample equilibrium lattice parameters. In most cases, the relaxation of the atomic bond lengths as sample atoms become further away from the substrate is accompanied by lattice defects, although for extremely thin films it can be the case that not enough strain has built up. One of the more common types of lattice defect in epitaxial thin films is known as a dislocation. In addition to their prevalence, they cause a distortion in interatomic distances that scales as r^{-1} while some other defects such as lattice faults decay as r^{-2} [17, §3.5], so it is somewhat justified to only consider microstrain due to dislocations when interpreting the breadth of diffracted peaks from epitaxial thin films.

For an isotropic Gaussian (normal) distribution of strain ε, as would be caused by random dislocations, the apparent strain η is given, after Stokes and Wilson [21], by the equation:

$$\eta = \frac{\beta_{2\theta}}{\tan(\theta)} = 2\sqrt{2\pi\bar{\varepsilon}^2}$$

Converting from units of 2θ to Q by means of Equation 3.3 and its derivative:

$$\frac{\beta_{2\theta}}{\tan(\theta)} = \frac{\beta_Q}{\tan(\theta)}\frac{\lambda}{2\pi\cos(\theta)} = \frac{\beta_Q\lambda}{2\pi\sin(\theta)} = \frac{2\beta_Q}{Q_0} = 2\sqrt{2\pi}\varepsilon_{rms}$$

Alternatively, the weighted average strain, again assuming a Gaussian distribution, is given by:

$$\tilde{\varepsilon} = \frac{1}{2}\sqrt{2\pi}\varepsilon_{rms} = \frac{\beta_Q}{2Q_0}$$

3.1.4 Neutron Diffraction

Neutron diffraction is a very useful technique which has proved invaluable in condensed matter research over the previous decades, however the technique is not as ubiquitous as X-ray diffraction because of the necessity for a nuclear reactor or a particle accelerator facility complete with moderators and special optics, a summary of facility types and a short list of locations are given by Baruchel et al. [22, §V.1.2]. Neutron diffractometer facilities have many of the advantages that large-scale X-ray facilities achieve, such as tunable wavelength (De Broglie wavelength is simply proportional to the velocity for non-relativistic massive particles). Neutron diffraction has two distinct advantages over X-ray diffraction: elements with similar atomic numbers and even isotopes can easily be distinguished due to the erratic variation of the neutron scattering length with the number of protons and neutrons in a nucleus, and neutrons scatter magnetically due to their magnetic moment which facilitates an atomic scale probe of the magnetic moment density of a sample.

The coherence conditions for constructive interference and thus strong diffraction are identical in the X-ray and neutron cases as wave mechanics are still wave mechanics, but the underlying scattering mechanisms are very different, albeit quite complementary. Photons, being the force carriers of the electromagnetic field, scatter strongly off the electronic density around atoms, while neutrons are neutral and do not. However, neutrons are composite fermions which interact via the strong (and the weak) force and also weakly interact electromagnetically via their magnetic moment. This leads to two separate terms in the neutron structure factors, a nuclear and a magnetic term, as shown in subsection 3.1.4. The reader should refer to Chatterji [23, §1.6] for more details.

$$|F_N|^2 = \left| \sum_{n=1}^{N} b_n \exp\left(-i\vec{Q} \cdot \vec{r}_n\right) \right|^2 + \left| \sum_{n=1}^{N} p_n \vec{\mu}_n \exp\left(-i\vec{Q} \cdot \vec{r}_n\right) \right|^2$$

where b and p are the nuclear and magnetic scattering lengths for the particular isotope/atom, and $\vec{m}u$ is the magnetic interaction vector equal to the difference between the magnetic moment of the scattering electron and its projection onto the scattering vector $\vec{\mu} = \hat{m} - \vec{Q}(\vec{Q} \cdot \hat{m})/|\vec{Q}|^2 = \hat{m} - \hat{Q}\cos(\theta)$. This interesting result means that the magnetic structure factor is 0 when the scattering vector is collinear with the magnetic moments
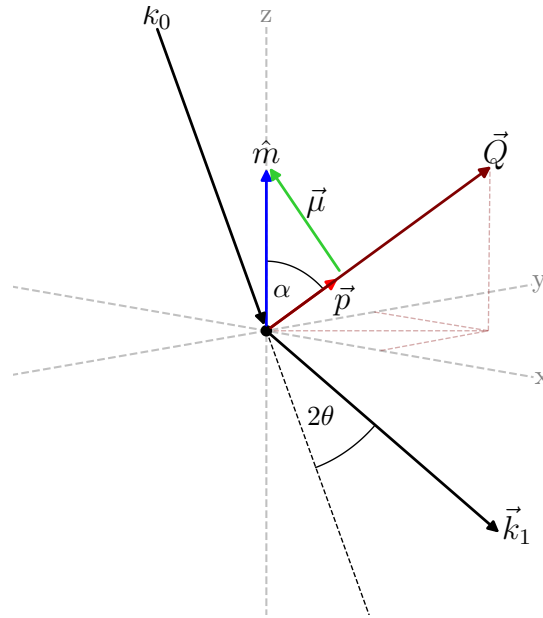
Figure 3.8: The magnetic interaction vector $\vec{\mu}$, illustrated for scattering vector $\vec{Q} =$ [111] and magnetic moment $\vec{m} = $ [001]. $\vec{p}$ is the projection of $\hat{m}$ onto $\hat{Q}, = \vec{Q}(\vec{Q} \cdot \hat{m})/|\vec{Q}|^2 = \hat{Q}\cos(\alpha)$ in the figure. $2\theta \approx 31°$, corresponding to a cubic lattice with $a \approx 5$ Å. The vector lengths may appear slightly inconsistent due to the 3D projection.

in the sample, and maximum for 90° orientation, allowing the local magnetic orientation to be probed. This sensitivity to local atomic magnetism makes neutron diffraction one of the most powerful methods for investigating the magnetisation of antiferromagnets or compensated materials, as most magnetometry techniques probe the macroscopic average. Some conceptual details about the two terms are discussed below.

The nuclear strong force is very strong but also very short range, extending roughly the size of a nucleus ($\approx 10^{-15}$ m). Neutrons used for diffraction naturally have wavelengths on the order of inter-atomic distances ($\approx 10^{-10}$ m), much larger than the range of the strong force and so the potential can be treated as a delta-function. To first order, this means that the scattering amplitude, and therefore the scattering length, of a given nucleus is equal to a constant b [24, 25], i.e. it does not change with the length of the scattering vector. This scattering length is generally a complex number where the imaginary part accounts for absorption. There is no theory for the strong force near as developed as electromagnetism which allows accurate calculations from first principles, but the nuclear scattering lengths have been determined experimentally and tabulated in literature [8, §4.4.4]. The scattering lengths depend on the internal structure of the nucleus and exhibit

large variations between similar sized atoms and also between isotopes of the same element. For so-called "thermal neutrons" used for diffraction (with $\lambda \approx 2\,\text{Å}$), the scattering lengths are constant as a function of energy (or wavelength/wavenumber/frequency/velocity...) except for some heavy isotopes, for which resonant interactions occur.

The other important contribution is the magnetic scattering of neutrons. While still electromagnetic in origin, it differs from the photon case in that the scattering field comes from the unpaired electrons in the outer shells of atoms. The magnetic interaction is relatively long range but is also relativistic in origin and much weaker than the strong force, so perturbation theory is still valid and analytical models can be derived. Detailed derivations can be found in the crystallography tables [8], by Chatterji [23] or Zaliznyak [25], for example. The scattering potential which defines the magnetic form factor is proportional to the magnetic density of the atom, which is proportional to an integral over the radial parts of the relevant wavefunctions of the atoms. As in the photonic case, the scattering length p as a function of scattering vector length $|\vec{Q}|$ is solved for numerically using a Hartree-Fock or similar solution to the wave equations. The solved points can then be interpolated via least-squares regression by a series of sums of Gaussian profiles, the coefficients for the approximations are again given in [8, §4.4.4.5].

The magnetic scattering lengths p_n in subsection 3.1.4 are of the order 5 fm, very similar to the nuclear scattering lengths. The nuclear and magnetic structure both contribute equally to diffraction and both can be resolved simultaneously, in addition, heating a material above its Curie temperature for example will remove the magnetic periodicity and only the nuclear structure will contribute to diffraction.

3.2   Techniques - Experimental Concerns

3.2.1   Reciprocal Space

We saw earlier that diffraction occurs when the photon scattering vector is equal to a reciprocal lattice vector of the crystal being irradiated. To investigate reciprocal space, we need to be able to change the length and orientation of the photon scattering vector. This is done by rotating the source and detector around the sample as shown in Figure 3.9.

Properly understanding the layout of the reciprocal space for a crystal and the traversal
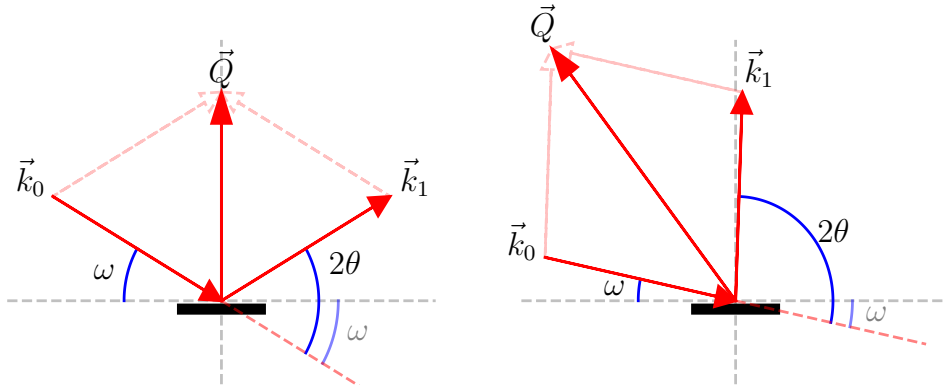
Figure 3.9: An example of how the length and orientation of the scattering vector is controlled via the angle of inclination of the source and detector, for a symmetric or asymmetric scan.

of the scattering vector through this space is imperative to measuring and interpreting diffraction data. The inclination of diffraction planes, and their corresponding reciprocal lattice vectors τ, is a simple matter of the geometry of the unit cell and choice of reflection, the length of the vectors is inversely proportional to the interplanar spacing, for a square-angled lattice:

$$\tau = \arctan\left(\frac{c}{l}\sqrt{\frac{h^2}{a^2} + \frac{k^2}{b^2}}\right), \qquad d = \left(\frac{h^2}{a^2} + \frac{k^2}{b^2} + \frac{l^2}{c^2}\right)^{-\frac{1}{2}} \tag{3.8}$$

and d can be inserted into Equation 3.1 to calculate 2θ for a given reflection. The diffractometer angles for a reflection are then $\omega = \theta - \tau$ and detector $= \theta + \tau = 2\theta - \omega$. Working in the reduced scattering units of Equation 3.3 is convenient for some types of scans. The components of this vector are easily worked out from Figure 3.9:

$$q_x = \frac{1}{\lambda}\left[\cos(2\theta - \omega) - \cos(\omega)\right] \qquad q_z = \frac{1}{\lambda}\left[\sin(2\theta - \omega) + \sin(\omega)\right] \tag{3.9}$$

A figure showing the 3D reciprocal space for a cubic elemental fcc lattice, with the scattering vector, is shown below. For this type of lattice, as shown in subsubsection 3.1.1.3, only reflections with the Miller indices h, k, l all even or all odd are non-zero. The scattering vector is coincident with the (204) plane normal in the figure, thus the Bragg condition for diffraction is satisfied and intensity would be observed.
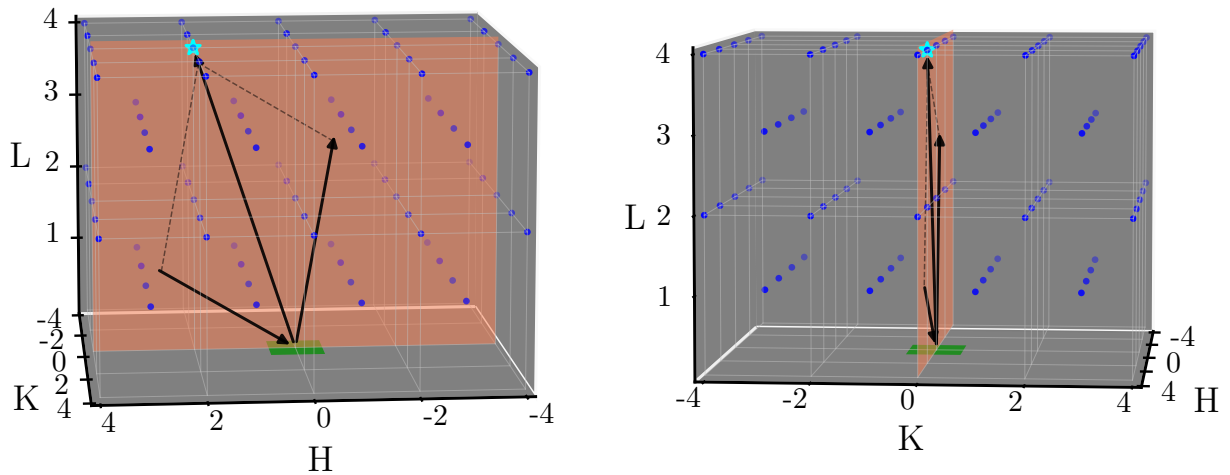
Figure 3.10: Geometry for diffraction from the (204) plane of an elemental fcc lattice, with a wavelength equal to $\frac{a}{3}$ where a is the unit cell lattice parameter: $\omega = 21.6°$ and $2\theta = 96.4°$.

Clearly, if the crystal structure of the film being investigated is known, the layout of the reciprocal space is as well, and we can measure the intensity of reflection from any peak that is accessible in the geometry. The reverse problem is usually more pertinent however, we want to determine the exact crystal structure by scanning the expected positions in reciprocal space. In the next section, some common types of XRD scans are described and the particular diffractometer(s) that I have had access to are detailed.

3.2.2 Diffractometer

Some common scans (in the scattering plane) which are typically available in the software of high-resolution diffractometers are shown in Figure 3.11. The area which is accessible depends on the geometry, in the reflection geometry, only the space above the sample can be probed. An animation showing how the accessible area is traced out as a function of the source and detector positions can be found on my GitHub [26].

Not shown in Figure 3.11 are pole figures where the sample is rotated around the z axis (φ scan) to move different members of the same family of reflections into the scattering plane (e.g. (204) and (024) reflections). These scans are more pertinent for texture and grain orientation analysis of polycrystalline samples.

The apparatus I have primarily used is a Bruker D8 Discover diffractometer. The source is a sealed-tube Cu anode, operated at 40 kV and water-cooled, which provides intense
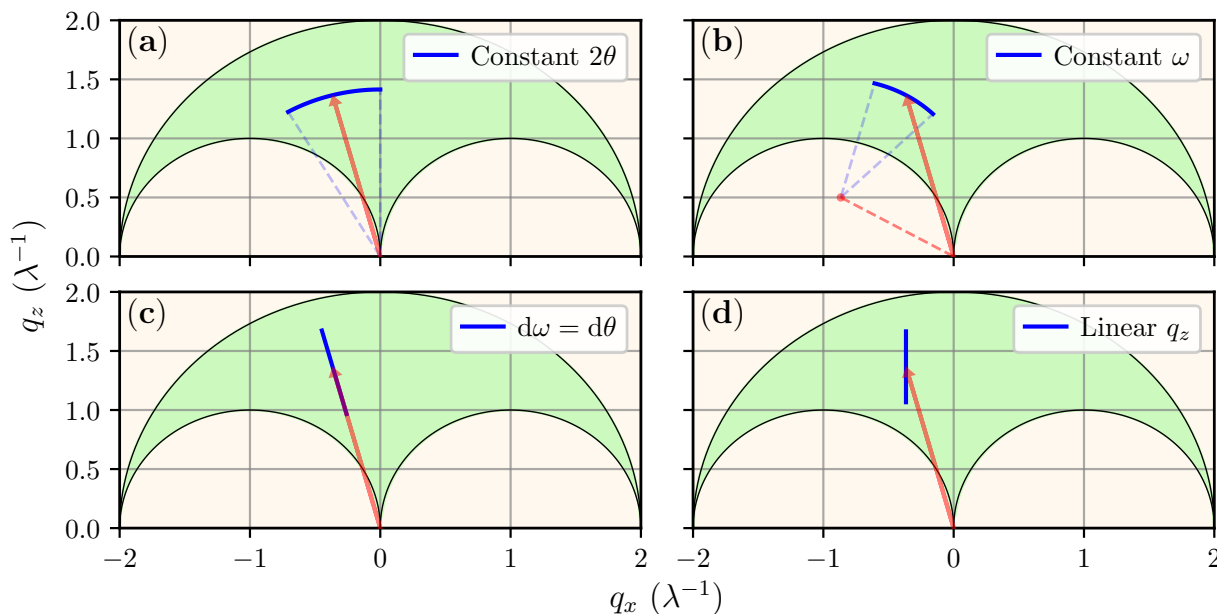
Figure 3.11: Conventional scans in reciprocal space including: **(a)** "constant 2θ" or "rocking curve" scan, **(b)** "constant ω" or "detector" scan, **(c)** "$d\omega = d\theta$" or "$\omega/2\theta$" or "unlocked coupled" scan and **(d)** "linear q_z" or "l" (Miller index) scan. The green region is accessible in the reflection geometry for a standard two-circle diffractometer; the large and small circles have radii $2/\lambda$ and $1/\lambda$ respectively, see Figure 3.9.

K_α radiation with energy $E_\gamma = 8.048\,\text{keV}$ equivalent to a wavelength of $\lambda_\gamma = 1.5406\,\text{Å}$. A Göbel parabolic mirror subsubsection 3.1.2.4 is used to collimate and provide initial monochromation on the divergent beam from the source, with a Ge (220) double-bounce channel-cut crystal used to attenuate as much as possible the K_{α_2} with $\lambda_\gamma = 1.5444\,\text{Å}$. We often use 5 mm and 0.2 mm absorbing slits in the y-axis and 2θ-axis direction to yield a relatively large rectangular parallel beam (similar to Figure 3.5), more aggressive collimation is used if better resolution is required.

The sample stage is capable of motion in the x, y and z Cartesian directions in order to facilitate centring of the sample in the beam. Additionally, φ and X rotations of the stage (rotations not in the diffracting plane) are possible to adjust the sample such that the diffracted beam is centred on the detector. The inclination of the source and detector can be changed independently (rotations in the diffracting plane) to move the scattering vector and probe a large swath of reciprocal space. A diagram of a typical two-circle diffractometer, accurate for the Bruker D8 that has been available to me, is shown in Figure 3.12.
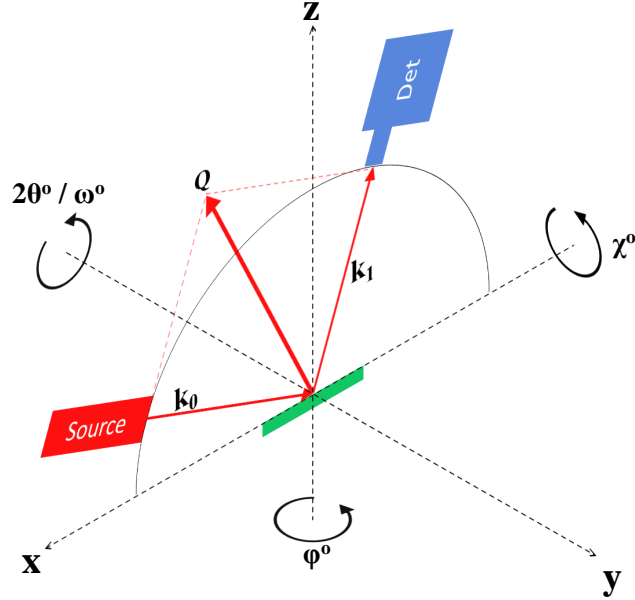
Figure 3.12: A diagram of a typical two-circle diffractometer. The xz-plane is the scattering plane and φ or X rotations are used to move the desired reciprocal lattice vectors into the plane. ω and 2θ angles then move the scattering vector in the plane to be coincident with the reciprocal lattice vector ($\vec{Q} = \vec{G}$).

Before detection, a Soller slit [27] is used to remove divergent reflected photons from the sample, this is a simple sets of thin absorbing planes where photons that are not at the precisely correct angle will impinge on the planes and be absorbed. The detector is a LYNXEYE-XE 1D line detector. The active area is 14.4 mm long, consisting of 192 separate silicon strip detectors of 75 μm each, and covers an angular range of $\Delta 2\theta = 2.6°$ with the geometry we use. The detector can be used in 0D mode with a subset of the individual strips active (or rotated for large azimuthal acceptance) for conventional XRD scans. Alternatively, in the 1D mode, a 2.6° wide range of 2θ values are scanned simultaneously by treating each strip as an independent detector. This greatly speeds up the acquisition time for 2D scans known as Reciprocal Space Maps (RSMs) as essentially only $\sqrt{n}$ as much time is needed compared to a 0D detector (provided we only need a $\Delta 2\theta = 2.6°$ range in one dimension).

Despite all the conditioning, the X-ray beam from the source will never be perfectly monochromatic or collimated. As a result, even for infinite perfect materials, the detected intensity around each reflection will be somewhat spread in a peak with finite angular

width. This is the instrumental profile and is generally accounted for empirically by measuring some "Standard Reference Material". The standard reference material for characterising instrument response of the type we are interested in (high-resolution single-crystal diffraction) is a sintered alumina (Al_2O_3) plate containing many large (quasi-infinite) crystallites with a huge amount of reflections accessible. Fitting of all of these peaks allows us to empirically verify the instrumental corrections (subsection 3.1.2) and obtain values for the instrumental broadening.

I have also used another diffractometer, the Panalytical X'Pert Pro, which is a Bragg-Brentano geometry, partially monochromated (by means of a Ni filter for the Cu K_β radiation) machine intended primarily for investigating powder samples. However, it is still useful for symmetric XRD scans on thin films where the Bragg-Brentano (parafocusing) geometry offers significantly higher intensity for the price of reduced resolution compared to a collimated beam. The detector for this diffractometer has an automatic attenuator to prevent excess photon flux from burning the active part, which can cause some artefacts in the recorded spectrum, as will be seen in the examples section later.

3.2.3 XRD - 1D $\theta/2\theta$ Measurements

The most common type of XRD scan in structural analysis is a "symmetric $\theta/2\theta$" scan. This is equivalent to the bottom left panel of Figure 3.11 with $q_x = 0$ such that the scattering vector is normal to the sample plane, the length of the scattering vector changes during the scan but not the orientation as the source and detector are moved symmetrically. Families of crystal planes which are perpendicular to the scattering vector are probed. As can be seen from the figure, having $q_x = 0$ also allows the largest range of 2θ values, and therefore scattering vector lengths, to be scanned in the accessible region. This type of scan is particularly useful for random powder samples where grains are oriented in random directions so that all reflections have reciprocal vectors pointing vertically upwards. This allows all reflections to be probed with a single scan and the use of the Bragg-Brentano parafocusing geometry's higher intensity.. For the single-crystal epitaxial thin films that I am more interested in, the c-axis (001) or another high-symmetry direction (often (110) or (111)) of the substrate is oriented OOP (out-of-plane) and the deposited film will generally be seeded by this and similarly grow with some high-symmetry direction oriented OOP.

Epitaxy implies that the IP (in-plane) lattice parameters of the deposited film are equal (or some multiple such as $\sqrt{2}a$ or $2a$) to those of the substrate and the positions of the reflections in the $\theta/2\theta$ scan allow us to infer the OOP lattice parameters. This is generally the first port of call in the structural characterisation of single-crystalline or polycrystalline thin films and can be performed in under an hour (longer may be necessary if the film is exceptionally thin).

3.2.3.1   Procedure

The first step in any XRD measurement is centring the sample on the stage to ensure the rotation axes coincide with the sample axes and provide maximum irradiation and intensity. For epitaxial single-crystal films, we additionally want to align to a substrate peak to ensure the surface normal is coincident with the instrument z-axis, since the deposited films generally have their IP lattice axes coincident with the substrate (or rotated $45°$ if the difference in lattice parameter size between the substrate and sample is large). For inclined reflections, we also want to rotate the desired reciprocal lattice point into the scattering plane via a φ rotation. Once aligned, the source and detector are stepped at the same speed from an inclination to the horizontal plane of roughly $5°$ up to $60°$ (for the symmetric, vertical scan), so $10° < 2\theta < 120°$.

3.2.3.2   Analysing a Single Peak

Most of the steps to analyse diffraction data have been independently discussed in the preceding section. The last piece of the puzzle is what mathematical model to use to describe the intensity as a function of angle or reciprocal space unit, in particular what peak shape to use for reflections. The various sources of broadening intrinsic to the sample, and due to the instrumental profile, yield both Lorentzian (Cauchy) and Gaussian type broadening, the former due to the finite lifetime effects of the electronic transitions which produce characteristic X-rays in the source and the latter due to the fact that crystal defects and errors in general typically result in a normal distribution of strain. To account for this, a Voigt profile, the convolution of a Lorentzian and a Gaussian profile, is typically used to fit the peaks. Other profiles such as the pseudo-Voigt have historically been popular but this was mainly due to the relatively arduous computation of the convolution for a

true Voigt profile, which is not a concern with modern computing power. The relevant formulae are as follows: The Voigt profile is defined as:

Table 3.1: Formulae for Gaussian and Lorentzian profiles

	Gaussian (G)	Lorentzian (L)
Intensity	$G = y_0 \exp\left(-\frac{(x-x_0)^2}{2\sigma^2}\right)$	$L = \frac{y_0\gamma^2}{(x-x_0)^2+\gamma^2}$
Height (I_0)	y_0	y_0
FWHM	$2\sigma\sqrt{2\ln(2)}$	2γ
Area (I_{int})	$y_0\sigma\sqrt{2\pi}$	$y_0\gamma\pi$
Breadth ($\beta = \frac{I_{int}}{I_0}$)	$\sigma\sqrt{2\pi}$	$\gamma\pi$

$$V(x,\sigma,\gamma) = G(x,\sigma) \circledast L(x,\gamma) = \int_{-\infty}^{\infty} G(x',\sigma)L(x-x',\gamma)\mathrm{d}x'$$

In practice a numerical convolution on a computer is performed where the amplitude of the profile is normalised to y_0 and in order to make sure the profile centroid is at the desired x_0, the Lorentzian profile is centred at x_0 while the Gaussian profile is centred **in the middle of the x interval** so the convolution does not shift the peak. For example, in Python [28] using the NumPy [29] package where x is an array, the following function returns a Voigt profile specifying the height for each value in x:

```python
def  Voigt(x, x0, sig, gam, y_0)
    G = numpy.exp(-(x - x.mean())**2 / (2*sig**2))    # Gaussian
    L = gam**2 / ( (x - x0)**2 + gam**2 )             # Lorentzian
    V = numpy.convolve( G, L, mode="same" )           # numpy convolve
    return (V / V.max()) * y_0                          # normalise to y_0
```

There are no analytical expressions for the properties of the Voigt profile as there are for the Gaussian and Lorentzian profiles, but there are many approximations with varying degrees of complexity and accuracy, the ones I have used are:

$$\text{FWHM} = a\gamma\sqrt{b\gamma^2 + c\sigma^2}; \qquad a = 1.0692, \ b = 0.86639, \ c = 5.54518$$

$$\beta = 2w\frac{1 + Ck + Dk^2}{E(1 + Ak + Bk^2)}; \qquad k = \frac{\gamma}{\sigma\sqrt{\pi}}, \quad \begin{matrix} A = 0.903965 & B = 0.769955 & C = 1.364216 \\ D = 1.136195 & E = 0.939437 \end{matrix}$$

$$I_{int} = \beta y_0$$

where the expressions for the FWHM and Breadth were given by Olivero [30] and Ahtee [31] respectively.

It can be shown [17, §3.3] that for a convolution of two Lorentzian profiles, the integral breadth of the convolution is simply equal to the sum of the integral breadths of the two constituents. For Gaussian profiles on the other hand, the breadth is equal to the square root of the sum of the squared original breadths:

$$\beta_L^{I\circledast S} = \beta_L^I + \beta_L^S \qquad \beta_G^{I\circledast S} = \sqrt{\left(\beta_G^I\right)^2 + \left(\beta_G^S\right)^2} \qquad (3.10)$$

This holds for Voigt profiles so that the Gaussian component of the breadth for a convolution of two Voigt profiles is equal to the root sum of squares of the Gaussian component of the breadths of the two constituent Voigts, and similarly for the Lorentzian components. The measured diffraction pattern is the convolution of the instrumental profile and sample profile, therefore, if we obtain the instrumental profile by measuring a perfect crystal standard, we can obtain the integral breadths due to sample broadening alone via Equation 3.10. It is always preferable to measure multiple different reflections since the two types of sample-based broadening discussed have different θ (or Q) dependence, but this single-line technique is invaluable nonetheless. It has been shown that the Gaussian
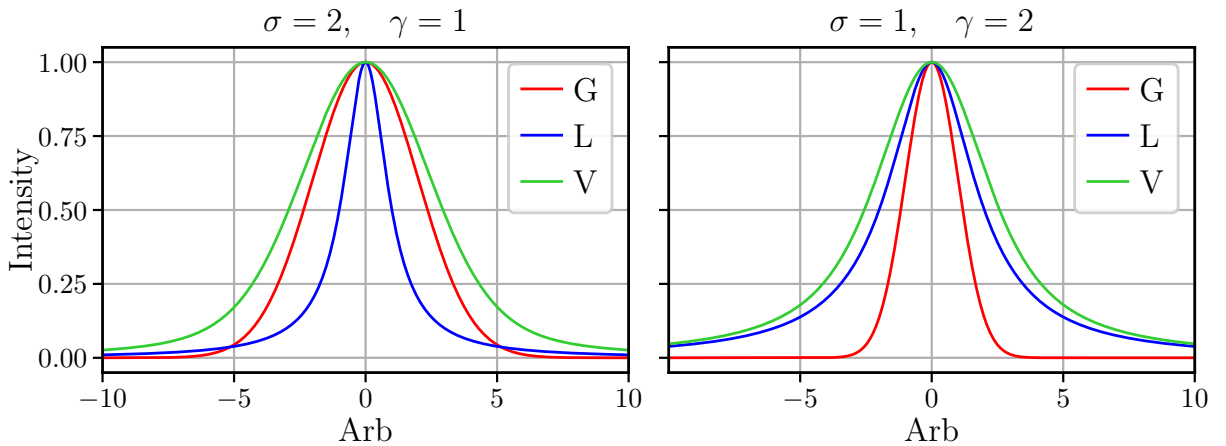
Figure 3.13: Gaussian and Lorentzian profiles and their convoluted Voigtian profile for different values of the Gaussian and Lorentzian broadening parameters σ and γ. In general, the larger the Lorentzian contribution, the larger the "tails" of the peak.

and Lorentzian breadths obtained separately from σ and γ and can be related to the

micro-strain and finite-size broadening of the sample, respectively. This fact has both some experimental and theoretical justification, see [32] and references therein. This is another reason to use a Voigt profile for fitting the diffracted peaks since the Lorentzian and Gaussian breadths are obtained separately and can easily be corrected for broadening due to the instrument. This provides a method to estimate the crystallite size and degree of micro-strain in a material from just one XRD scan of a single reflection:

$$D = \frac{2\pi}{\beta_L^S} \qquad \tilde{\varepsilon} = \frac{\beta_G^S}{2Q_0} \qquad\qquad (3.11)$$

Where the integral breadth is in reciprocal space units Q and Q_0 is the peak centre. The assumptions (such as isotropic strain) implicit in the derivation of these relations were discussed earlier and must be considered when reporting results. Some examples of the use of the formulae detailed in the section will be given later in the material case studies section.

3.2.3.3 Strain Profile Analysis

The previously discussed broadening due to microstrain in subsection 3.1.3 is applicable especially to polycrystalline or powder thin films. If the sample being investigated is very thin (10s of nanometres), epitaxial, and almost single crystalline with little-to-no dislocations, then the relaxation of the sample lattice parameters can occur smoothly over the thickness. We previously obtained an expression for the weighted average strain derived from assuming an isotropic and random strain distribution, by contrast, in this case, the displacement field as a function of depth into the sample ($u(z)$) will be highly asymmetric. Rather than causing a general broadening, this form of strain can cause asymmetry in the diffracted peaks. Additionally, with highly perfect and smooth (low interface roughness) thin films, the number of atoms in the z direction will be near-constant across large swaths in the planar directions (by the definition of smoothness), meaning the oscillations from the interference function of photons incident on different areas of the sample are not completely washed out by the summation of sinusoidal functions with different periods, as is usually the case.

Finding an expression for the diffracted intensity resolves to integrating over the range of different interplanar spacings which contribute to the diffraction, described by the strain

$$\varepsilon_{zz} = 0 \qquad\qquad \varepsilon_{zz} = f(z)$$
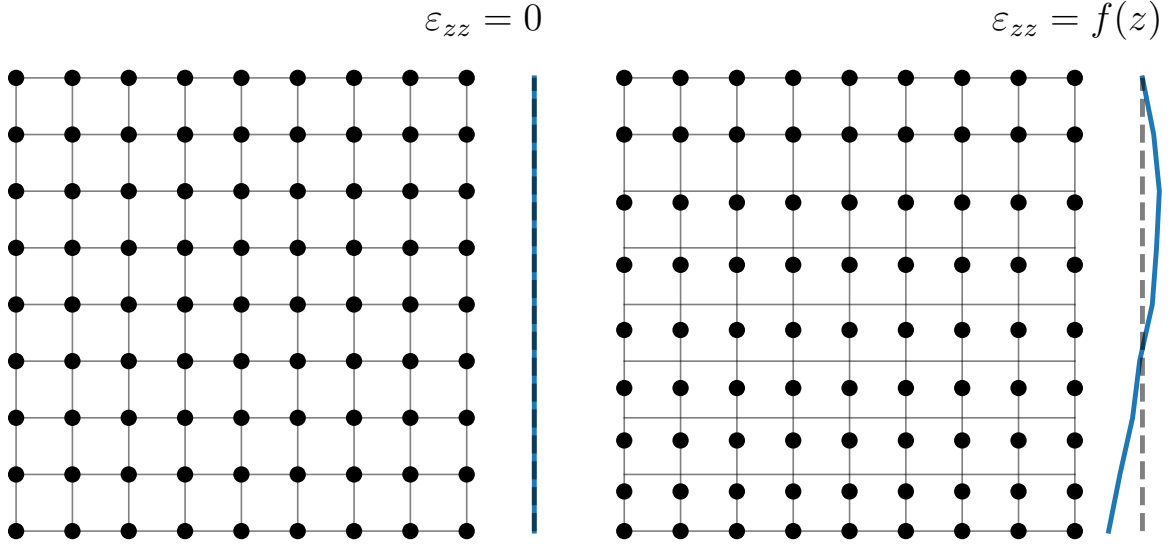
Figure 3.14: An illustration of how a vertical strain profile might form as a result of tensile IP strain due to epitaxial growth in a single-crystalline ultra-thin film, with displacements exaggerated by a factor of ten. In this diagram, the substrate interface clamping the sample atoms would be at the bottom.

field. The problem of obtaining the strain field from a measured intensity profile was discussed by Boulle et al. [33]. The method consists of finding a model for the strain field to insert into the expression for the intensity and then adjusting the input parameters of the model to match data via non-linear least-squares regression. The model they settled on for the strain field was a cubic-beta spline [34, 35]. This type of function is very useful thanks to a number of properties. An important feature is that the function has minimum curvature over the interpolated range, meaning it is very appropriate for modelling physical features where the wild oscillations of higher-order polynomials can give unphysical results. These splines can be defined as the weighted sum of an arbitrary number of basis functions where the bases are piece-wise-defined cubic polynomials. This means we have local control over the shape/curvature and with enough bases we can model almost any smoothly varying curve.

For modelling strain profiles of very thin films, it is sufficient to use circa 13 bases[1]. Practically, this adds 13 parameters to the non-linear regression, which does significantly slow down convergence. However, the parameters are not very strongly correlated and have physical meaning, i.e. they relate to the local strain in the corresponding section

---

[1]13 was the number of bases chosen by Boulle et al. which gave them adequate flexibility to fit realistic strain profiles while not being so large as to overly slow down computation time.

of the film. The details of the implementations of the functions are given in the original publication [33]:

$$I(q_z, t) = \left| F \int_0^\infty \Omega(z, t) \exp\left[-i\vec{G} \sum_{i=1}^N w_i B_{i,3}(z)\right] \exp(-ih_z z) \mathrm{d}z \right|^2 \qquad (3.12)$$

$$B_{0,3}(z) = \frac{1}{6} \begin{cases} z^3 & 0 < z \le 1 \\ -3z^3 + 12z^2 - 12z + 4 & 1 < z \le 2 \\ 3z^3 - 24z^2 + 60z - 44 & 2 < z \le 3 \, , \\ (4-z)^3 & 3 < z \le 4 \\ 0 & \text{otherwise} \end{cases} \qquad B_{i,3}(z) = B_{0,3}(z - i) \qquad (3.13)$$

where Ω is a shape factor between 0 and 1 characterising the roughness of the film at the interfaces, z is the distance from the substrate into the sample, w_i are the weighting factors for each basis, h_z is the z component of the reduced scattering vector $\vec{h} = \vec{Q} - \vec{G}$ (so maximum diffracted intensity occurs at $\vec{h} = 0$) and other symbols retain their usual meaning. The term in brackets in Equation 3.12 is the strain profile and would be replaced by a standard isotropic Debye-Waller factor for samples with small random thickness fluctuations. The weighting factors for the spline bases completely determine the shape of the curves, while the films thickness and roughness determine the frequency and damping of the oscillations of the interference function, respectively. Some example displacement profiles with underlying spline bases, and resulting strain profiles inset, are illustrated in Figure 3.15.

The diffracted intensity profile obtained by integrating Equation 3.12 for the displacement profiles in Figure 3.15, are shown in Figure 3.16.

The use of this method will be referred to as "strain fitting" in the examples section to distinguish from fitting simple peak profiles to data where intensity oscillations are not evident.
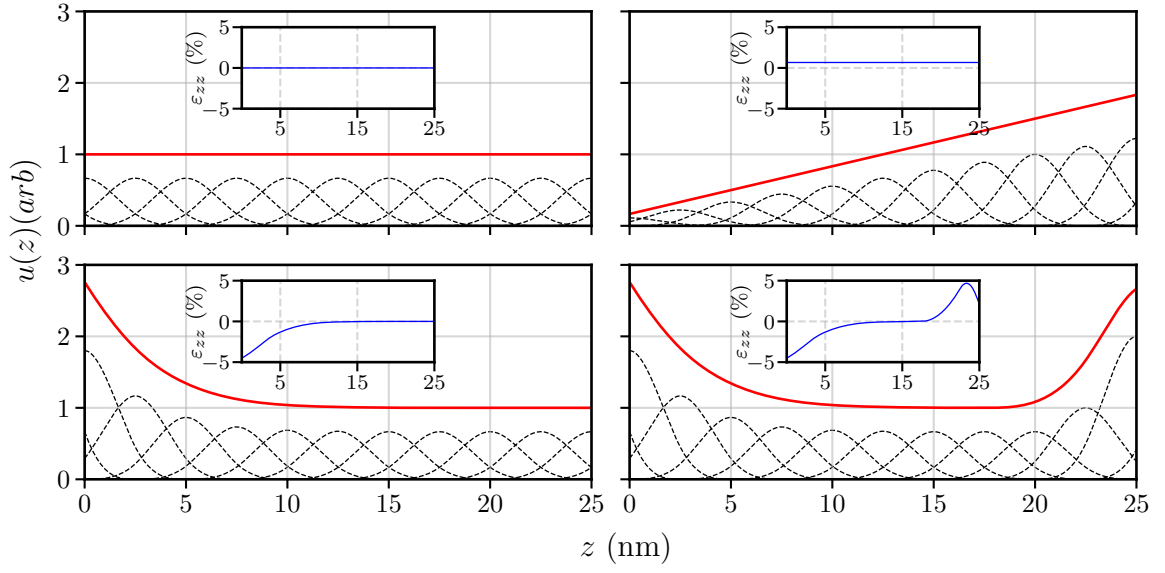
Figure 3.15: Four possible displacement profiles and the corresponding strain profile inset, modelled with 13 cubic beta spline bases.
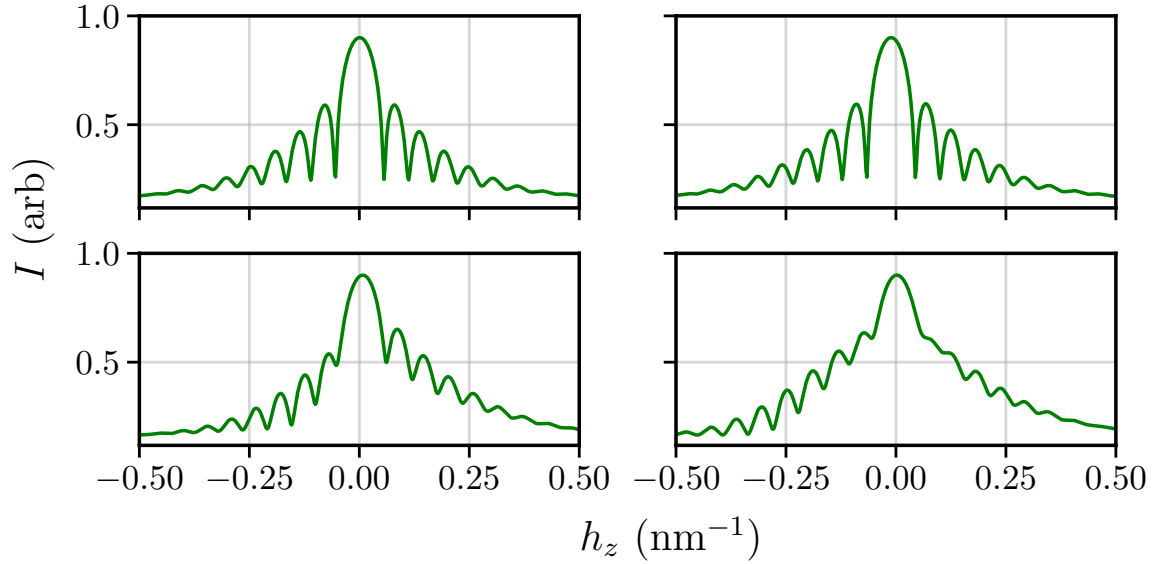
Figure 3.16: The results of integrating Equation 3.12 using the displacement profiles shown in Figure 3.15. Constant displacement is zero strain and an unchanged peak. Linear displacement is constant strain and a linearly shifted peak. Non-linear strain near the interfaces, as might realistically be expected in ultra-thin epitaxial films, results in asymmetric peaks. The data shown was calculated assuming a (004) reflection from an 18 nm film with lattice parameter $c = 5$ nm, $\sigma = 0.5$ nm interface roughness and $\sigma_{sub} = 0.2$ nm substrate roughness.

3.2.4   RSM - Adventures in Reciprocal Space

3.2.4.1   Geometry

Reciprocal Space Maps (RSM) are a natural extension of the one-dimensional XRD scans mentioned thus far. Simply put, rather than tracing out a line in reciprocal space, we measure a 2D area of reciprocal space. Ideally this type of measurement would be performed using a large, purpose-made, 2D detector, such as the modern EIGER2 detector offered by Bruker which has 5×10^5 pixels and thus simultaneously covers a large area of reciprocal space with good resolution. However, these new types of apparatus are prohibitively expensive and older technology is just as capable, albeit often with much slower measurement speed. It is important to note that a detector which is two-dimensional in real space does not measure a 2D section of the crystal reciprocal space since the source (and therefore ω is still constant). What it does incorporate is a wide range of ϕ and χ angles (see Figure 3.12), offering both a significantly higher counting rate (shorter acquisition time), and a plethora of additional information about the orientation of crystallites in the sample, for the same experimental geometry. As previously mentioned in subsection 3.2.2, our system is equipped with a LYNXEYE 1D position-sensitive detector (PSD) which spans a 2.6° range of 2θ values simultaneously, which corresponds to a parallel constant-ω scan in Figure 3.11, this will be referred to as a PSD scan henceforth. In practice, RSMs are constructed by coupling the PSD scan to a linear q_z scan (or $d\omega = d\theta$ scan) with our system: successive PSD scan arcs vertically shifted in reciprocal space covers a hatched area. The PSD scan consists of 177 points corresponding to the individual pixels, while 100 to approximately 250 shifted detector scans are performed. A discussion of the use of 1D PSDs for measuring RSMs has been published by Masson et al. [36], where the authors used a custom-built curved PSD covering a huge 2θ angle of 120° simultaneously. The particular limitations of pixel-type PSDs are discussed therein. If only one sharp diffraction peak is expected to lie within the measured range, a smaller number of points can be used for faster measurement time. As will be explained later, it is desirable to have a substrate peak in the same scan as the sample peak to allow for normalisation, if possible, and thus scans can be expanded to include both peaks. Finally, we primarily work with thin films with thicknesses of order 10 nm, in this case, fewer detector scans
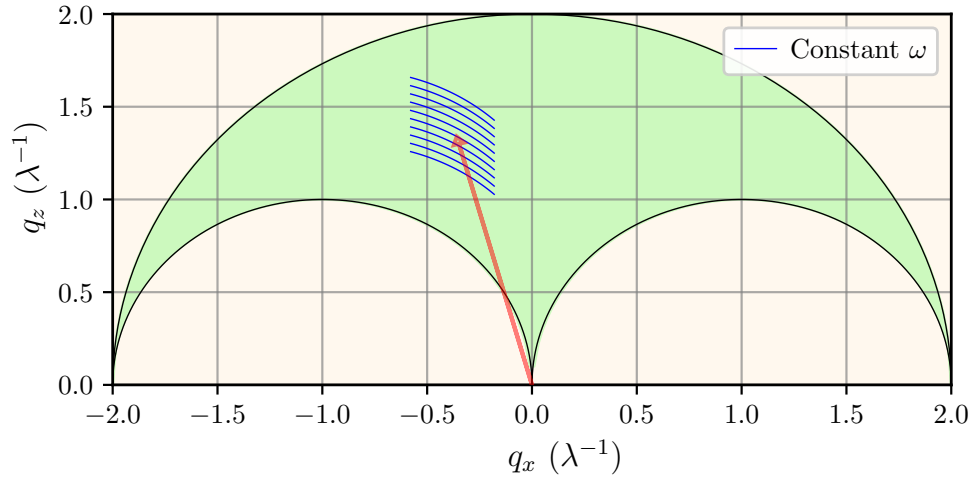
Figure 3.17: An example of an RSM scan covering a 2θ range of $10°$ and a q_z range of $0.4\,\lambda^{-1}$, with 10 constant-ω scans. In practice, a smaller range corresponding to $\Delta q_x \approx 0.05\,\lambda^{-1}$ and $\Delta q_z \approx 0.15\,\lambda^{-1}$ is used with the LYNXEYE PSD.

are desired (a sparser grid of points is measured) in order to maximise counting time for the performed scans and acquire an appreciable intensity from the minuscule diffracting volume.

Once an RSM has been measured, there are a number ways and degrees of complexity with which to analyse the data. First of all, the position of the peak in reciprocal space units directly translates to the a and c lattice parameters of the crystal being measured (with some caveats, discussed in the following sections). Vertical (constant q_x) and horizontal (constant q_z) slices can be taken through the peak centre and analysed in the same way as a traditional 1D XRD spectrum, offering structural information for the OOP and IP directions. If desired, one can perform a 2D non-linear regression to fit the entire peak, this is something I have explored to more accurately determine the position of the peak centre for noisy or unusual peak shapes, but does not offer much more information than the 1D slice method for much greater computational complexity and as such is not something I took further. A systematic determination and simulation of the 2D instrumental profile and analysis of measured data via deconvolution techniques is a pre-eminent method performed by some experts in the field, e.g. Boulle et al. [37], but is outside the scope of my work.

3.2.4.2 Procedure

The first step in the measurement of a reciprocal space map from an epitaxial thin film is to familiarise oneself with the location and intensity of the diffracted reflections in reciprocal space, for the sample and the substrate. All the relevant theory has been introduced already. I have written a program to show the position and intensity of reflections in the diffraction plane for a given azimuthal orientation of the substrate and sample, which greatly aides in the selection of regions to scan, it is available on my GitHub [26]. Ideally,
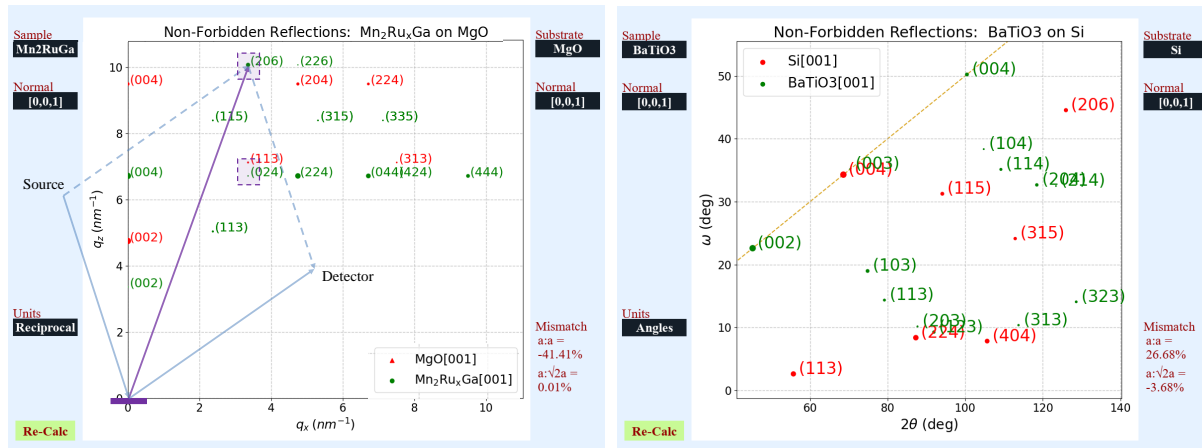
Figure 3.18: Screenshots from the program for visualising reciprocal space, for the case of Mn_2Ru_xGa grown on MgO and a BTO layer grown on a Si substrate. Different materials, surface orientations and plotting units can be chosen from a drop-down list and the lattice mismatch for two common types of epitaxy are shown in the corner. The source of detector of a typical diffractometer are overlaid on the left picture to show how the scattering vector relates to this picture.

it is best to perform a scan which encompasses both a substrate and sample peak so that the former can be used as a reference to correct for misalignments or any drift. Failing that, performing separate scans one after another without changing the initial alignment is recommended. The visualisation program is very useful for determining which peaks to scan to satisfy these conditions.

In order to calculate the peak positions, we must know the structure (space group) and size of the unit cells of a material. The space group is a useful concept which characterises the symmetry of a crystal lattice and thus, in the context of diffraction, makes it clear what reflections are allowed. In general, we always have an idea of the structure and size of the unit cells of the materials we are working with. The online database Materials Project is a useful source to obtain *.cif* files for various materials, both simulated and

experimentally verified, and the lattice parameters or compositions can be adjusted as needed thereafter. Generally, the first crystal structure characterisation step is a symmetric scan (subsection 3.2.3). This can be completed in an hour and gives the OOP lattice size, usually the c-axis (unless the sample grows with (111) oriented OOP for example). Substrates are always assumed to be perfect single crystal with known lattice parameters (although this is not always the case, unfortunately) and for thin films, we assume epitaxy such that our samples IP lattice is determined by the substrate: depending on the relative sizes of the relaxed lattices, the sample will grow "cube-on-cube" or rotated by 45°. Other orientations are possible but these are the most common. So to summarise, the IP and
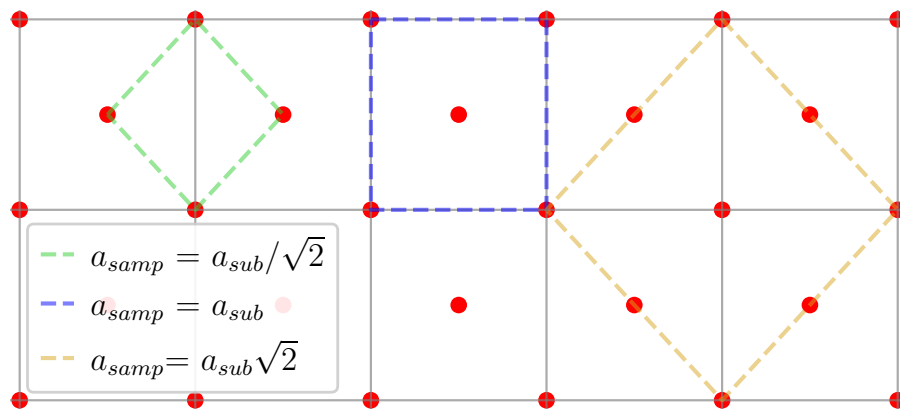
Figure 3.19: Possible orientations for a square sample to grow on a square fcc-lattice substrate, depending on whether the relaxed sample IP lattice parameter is closer to $a_{sub}/\sqrt{2}$, a_{sub} or $a_{sub}\sqrt{2}$.

OOP lattice parameters are obtained from assuming epitaxy and measuring a symmetric 1D XRD scan.

When we know what we want to scan and where to find it in reciprocal space, we start by aligning the sample position in the diffractometer as in the general XRD case. Next we must align to the substrate peak which we want, the diffractometer software should help with this, but even without any help, we have calculated where the peak should lie ourselves already. Aligning to the substrate peak ensures that the diffraction plane intersects all the peaks that we want as well as possible, especially important for very thin films or low-intensity reflections.

The Bruker "XRDWizard" software provides a means to perform RSMs where the desired scan coordinates are input relative to the current position of the source and detector, which should at this stage be aligned to the substrate peak. There is a graphical interface

very similar to Figure 3.17 where we can make sure the scan covers the desired range. Generally, a counting time of 30 s - 500 s is used for each constant-ω slice (depending on film thickness and expected diffracted intensity), with roughly 100 - 250 slices in the scan. Measurements can take anywhere from say 3 hours for thick high crystalline quality samples to an entire weekend for light 5 nm films. These values are sample and diffractometer specific but are a good ballpark for nanometric films and typical laboratory equipment.

3.2.4.3   Data Analysis

RSM data files generated by the diffractometer typically have 3 columns containing ω, 2θ and intensity with $> 10^4$ rows, with the exact number a multiple of 177, the default number of points in a constant-ω scan). Generally, we convert to reciprocal space units of Equation 3.9, where analysis is more simple. Fitting a full 2D surface to the entire data set is possible, or vertical (q_z) and horizontal (q_x) slices can be taken through the peak maximum and fit as 1D XRD spectra as described in the preceding sections. Using the 1D slices is much faster and mathematically easier with very little information sacrificed. Often, a basic 2D fit is used to accurately determine the center of the peak and the 1D slices are properly fit and their shape used to infer details about the crystal structure in the IP and OOP directions. A note here is that the hardware acceleration enabled by OpenCL code, discussed in detail in the simulations chapter, is also well suited to applications such as this: the computation of a numerical convolution in two dimensions. This can reduce the extra computation time of performing the more complicated fit to negligible values.

3.2.5 Rietveld Analysis of Single-Crystal Thin-Films

3.2.5.1 Geometry

The technique of "Rietveld refinement" simply refers to the least-squares refinement of a full calculated diffraction pattern parametrised by an assumed underlying structure. In the refinement, the only parameters changed are that of the crystal structure of the diffracting material until the calculated and measured patterns match as well as possible [38]. The reason the method is known thusly is because Rietveld was the first to use the method when it became feasible on computers at the dawn of the digital age [39, 40]. This method is essentially one step upwards from the single-peak fitting described in the previous section, the sum of all available peaks in the scan are refined simultaneously to give a good idea of the structure. The method was first described for neutron diffraction on powder samples and remains mainly applicable to powder samples because far more peaks are available in a single scan: for single-crystals or even highly textured films, only a few families of peaks will be correctly aligned. There are a number of Rietveld refinement computer programs available which will calculate a list of integrated intensities or an entire diffraction pattern, the most notable of which is probably FullProf (FP) [6], but this program is still somewhat outdated (latest manual version is 2001), possibly because with modern computers the data reduction which was the reason for the inception of the method is not necessary and anyone relatively computer savvy can write their own least-squares fitting program. As I deal with primarily single-crystal samples, I use an average method where I separately measure as many peak families as possible, obtain their corrected structure factors or integrated intensities and then perform a kind of reduced Rietveld refinement, using FP. This is a simple modification conceptually, but in practice the experiment is quite difficult to perform efficiently due to the strict alignment requirements and low diffracted intensity of epitaxial thin films. As mentioned, only one or two peaks can typically be measured in a single scan with our setup and sample morphology so a large number of scans are needed. To justify the comparison of integrated intensities from different peaks, the alignment must be equally good for all peaks. Re-aligning the sample for every measurement is not really an option as this would take an exorbitant amount of human-time between scans (spending 15 minutes every few hours as opposed to letting the scans run overnight or

over the weekend). To this end I wrote a computer code with Dr. Karsten Rode, to calculate the so-called "UB-matrix" of Busing and Levy [41] for a given sample from three or four alignment scans of the substrate peaks and subsequently generate *.job* files for the diffractometer with the alignment angles calculated for 20+ scans of sample reflections. Thus maybe 30 minutes of alignment to substrate peaks is all that is necessary and the multitude of sample scans can be performed sequentially over the weekend. This method does assume perfect epitaxy of the sample growth on the film and neglects possible drift or interruptions that could occur over 48 hours of scanning but is still a very useful technique to thin-film structure analysis. The UB matrix is the product of the crystal matrix which relates the [*hkl*] Miller-index vectors to reciprocal lattice vectors **B**, and the orientation matrix **U** which relates the reciprocal lattice vectors to the Cartesian vectors in the diffractometer frame of reference. More details will be given in the procedure section.

3.2.5.2   Procedure

It is useful to define a number of coordinate systems related by transformation matrices to mathematically simplify the problem of calculating the angular position of sample reflections. Firstly there is the reciprocal lattice defined by the Miller indices $\vec{\nu}_h$. We define a crystal Cartesian system anchored to the reciprocal lattice defined by $\vec{\nu}_c = \mathbf{B}\vec{\nu}_h$ where **B** is a 3×3 matrix that depends on the lattice parameters and angles. Finally we define what I will refer to as a diffractometer Cartesian system anchored to the ϕ axis of the diffractometer $(\vec{\nu}_\phi)$ and a diffractometer angular system defined by the angles input into the diffractometer software, $\vec{\nu}_\theta$. The laboratory Cartesian system is related to the angular one by the three rotation matrices around the diffractometer axes: $\mathbf{\Phi}$, $\mathbf{X}$ and $\mathbf{\Omega}$ corresponding to the typical ϕ, χ and ω axes of the diffractometer, see Figure 3.12, $\vec{\nu}_\theta = \mathbf{\Phi X \Omega}\vec{\nu}_\phi$. The crystal-Cartesian $\vec{\nu}_c$ and Diffractometer-Cartesian $\vec{\nu}_\phi$ systems can be superimposed on one another (and this is in fact the diffraction condition in this formalism) and the transformation for this is given by the orientation matrix $\vec{\nu}_\phi = \mathbf{U}\vec{\nu}_c$. To summarise, we have:

$$\vec{\nu}_\theta = \mathbf{\Phi X \Omega U B}\vec{\nu}_h \tag{3.14}$$

where $\mathbf{\Phi}$, $\mathbf{X}$ and $\mathbf{\Omega}$ are the rotation matrices defined by the angular settings of the diffractometer, **B** is the crystal matrix determined by the crystal structure and **U** is the orien-

tation matrix defined by the orientation of the crystal in the diffractometer. The sample is assumed to be perfectly epitaxial with the substrate so that they have the same **U** so determining the substrate orientation is sufficient.

Actually determining **U** for the substrate is done by least squares regression after measuring at least three substrate reflections which are not close to coincident and have components along each Cartesian axis, these might be the (204), (024) and (004) reflections for example. At least two are required to form an orthonormal basis and measuring more allows for determining the matrix via regression. The diffractometer angles are obtained in the usual manner for alignment to find the position of maximum intensity and the large, crystallographically perfect substrate yields huge diffracted intensity so that this can be performed quickly. It is important to note that 2θ (i.e. the length of the scattering vector) is never refined here, which is equivalent to not varying the lattice parameters of the crystal. For a full description of each matrix and a method generalised to more advanced diffractometers such as the 4-axis ones found at synchrotrons, refer to the original publication [41]. Once the orientation matrix is determined, Equation 3.14 yields the "aligned" diffractometer settings for arbitrary sample reflection. It is then trivial to program whatever diffractometer software is used to perform rocking curves (constant-2θ scans) around chosen reflections.

3.2.5.3 Data Analysis

The procedure described above allows for the efficient measurement of tens of reflections from an epitaxial thin film sample while only having to align a single time. Once all the data has been measured, the reflections are each fit with Voigt profiles and the integrated intensity, or peak area, is noted. It is very important to then consider all the instrumental and sample corrections that need to be performed. In particular, the irradiated volume, Lorentz and polarisation corrections discussed in subsection 3.1.2 can have a very large effect, particularly for reflections that are far from the film normal with a small ω angle. The corrected intensity should be equal to the square of the structure factors and thus directly related to crystal structure. These measured structure factors are to be compared to those calculated by FullProf or similar. As explained in subsubsection 3.1.1.3, the symmetry of the lattice mainly dictates what reflections are allowed, the size of the lattice

dictates the positions, and the details of the relative peak intensities depends on the atomic form factors. In general, larger atoms with higher electron density have a larger interaction cross section. So when refining the structure to match experimentally observed structure factors, we can theoretically obtain the symmetry, size and site-specific atomic composition of a lattice if the data is numerous and precise enough. For powder samples this is often possible, but for our epitaxial thin films, we can fix the structure and lattice size (determined by other methods already mentioned) and use this Rietveld-style analysis to try and resolve information about the atomic composition.

3.3 Case Studies Mn$_2$Ru$_x$Ga

3.3.1 Motivation

Mn$_2$Ru$_x$Ga is a member of the versatile Heusler alloy class of materials. Heusler alloys have the chemical formula X_2YZ where X and Y are transition metal elements and Z is a p-block element. The four constituents sit on four inter-penetrating fcc sublattices. The potential inclusion of magnetic, metallic or semiconducting elements often results in unique and interesting magnetic and electronic properties. Ferrimagnetism is one such property wherein two or more magnetic sublattices with different magnetic moments are antiferromagnetically coupled such that the net moment per formula unit is far less than the constituent atomic moments. Macroscopically, these materials are immune to external field perturbations and can be miniaturised to a greater degree than materials which create large external fields. The distinct sublattices in ferrimagnetic materials often exhibit different temperature dependence of their atomic magnetic moments, meaning that it is sometimes possible to find a temperature or composition which has zero net moment (compensation point) despite large atomic moments and lower symmetry than antiferromagnets. As well as the insensitivity to external field and demagnetising effects, low-moment materials should have low damping and high magnetic resonance frequencies, since these are related to the anisotropy, which is proportional to the reciprocal of magnetisation and thus diverging. Another feature exhibited by some specific materials, many of which are Heusler alloys, is half-metallicity. This hard-to-predict phenomena occurs when there is a gap in the electronic band structure for just one spin band at the Fermi level, meaning that the low-bias conductance is intrinsically full spin-polarised. Half-metals have a plethora of potential applications in next-generation devices [42]. A hybrid material which is both ferrimagnetic and half-metallic could represent a great step forward in spin electronics as the atomic magnetic moments could be controlled/influenced directly by applying a normal voltage. These so-called zero-moment half-metals (ZMHM) could combine the benefits of compensated ferrimagnets and half-metals.

Since half-metallicity results from a gap in the electronic density of states (DOS) for one spin-band, it is very hard to accurately predict. The only way to even have a

chance is through advanced density functional theory (DFT) simulations which calculate the spin-resolved band structure. DFT is quite involved, especially with complicated multi-elemental materials like Heusler alloys. It is also nigh impossible to take account of things like strain and epitaxy in the small representative unit cells that are used to make calculations feasible, the result is that DFT often fails to predict experimental reality in the form of false-positives. Either the predicted half-metals will not have truly zero DOS for the minority spin band or the gap does exist but not at the Fermi level. The current best approach involves a lot of expensive and time-consuming trial and error, informed by DFT calculations.

Kurt et al. [43] experimentally demonstrated the first ZMHM in Mn_2Ru_xGa (MRG). MRG is an **inverse** full-Heusler (*XA* structure) where the Mn atoms sit on two chemically inequivalent sublattices, with the space group $F\bar{4}3m$ (#216) as opposed to $Fm\bar{3}m$ (#225) thanks to the inequivalent Mn sites. Mn sits just before the ferromagnetic 3d elements in the periodic table with the electron configuration $[Ar]3d^54s^2$ and has an exchange integral which is very sensitive to the interatomic distances. Pure Mn metal has a net negative exchange energy as per the Bethe-Slater curve [44] but is paramagnetic at room temperature. In MRG, the Mn atoms sit on two crystallographically inequivalent sites, $4a$ and $4c$, with the Ga and Ru on the $4b$ and $4d$ sites respectively. The nearest-neighbour distance between Mn atoms on the same sites (red-red or blue-blue in Figure 3.20) is 4.211 Å while the inter-sublattice distance between Mn atoms on different sites (red-blue in Figure 3.20) is 2.591 Å. This results in ferromagnetic exchange within each sublattice but antiferromagnetic exchange between the two different sublattices. In addition, the $4a$ Mn atoms are tetrahedrally coordinated by Ru and octahedrally coordinated by Ga, while the opposite is true for the $4c$ Mn atoms, this difference in chemical environments results in different net magnetic moment for the two types of Mn atoms. MRG was found to have a gap in the minority spin DOS and the Fermi level could be shifted into this gap by varying the Ru content of the alloy. Adding Ru to MRG adds electrons and electronic states, shifting the Fermi level, as well as increasing the lattice size due to the chemical pressure from the larger element, thereby changing the shape of the DOS. Of course, changing the composition and strain also affects compensation and other properties, as does disorder [45], and optimising the material for a certain application is a fine balancing

act of the deposition conditions and post-deposition treatments.

In the context of the above paragraphs, the ideal outcome in terms of experimental deposition is MRG films with consistent controllable properties, in particular large-magnitude easy-axis anisotropy, low damping and high-domain wall mobility with large domain size. Much of these secondary properties can be controlled via the crystal structure: anisotropy will correlate to tetragonal strain, domain size to crystallite size and defect density etc. Thus a desirable outcome of the MRG deposition experiments in the context of the overall research motivation is good control over the crystal structure.

MRG has a lattice parameter $a \approx 6.0\,\text{Å}$ which makes it suitable for deposition on MgO. MgO is one of our preferred substrates which is available in single-crystalline form with (001) oriented OOP. It has a cubic structure with lattice parameter $a = 4.2112\,\text{Å}$. Rotating $45°$ gives $\sqrt{2}a_{MgO} = 5.9555\,\text{Å}$, which is very close to MRG ($< 1\,\%$ strain) and thus facilitates good-quality epitaxial growth. The slight compressive strain induced by the substrate results in a larger OOP lattice parameter for MRG (volume-conserving strain) and therefore a tetragonal strain which breaks the cubic symmetry and allows access to lower-symmetry phenomena. This effect naturally varies with film thickness and crystalline quality.
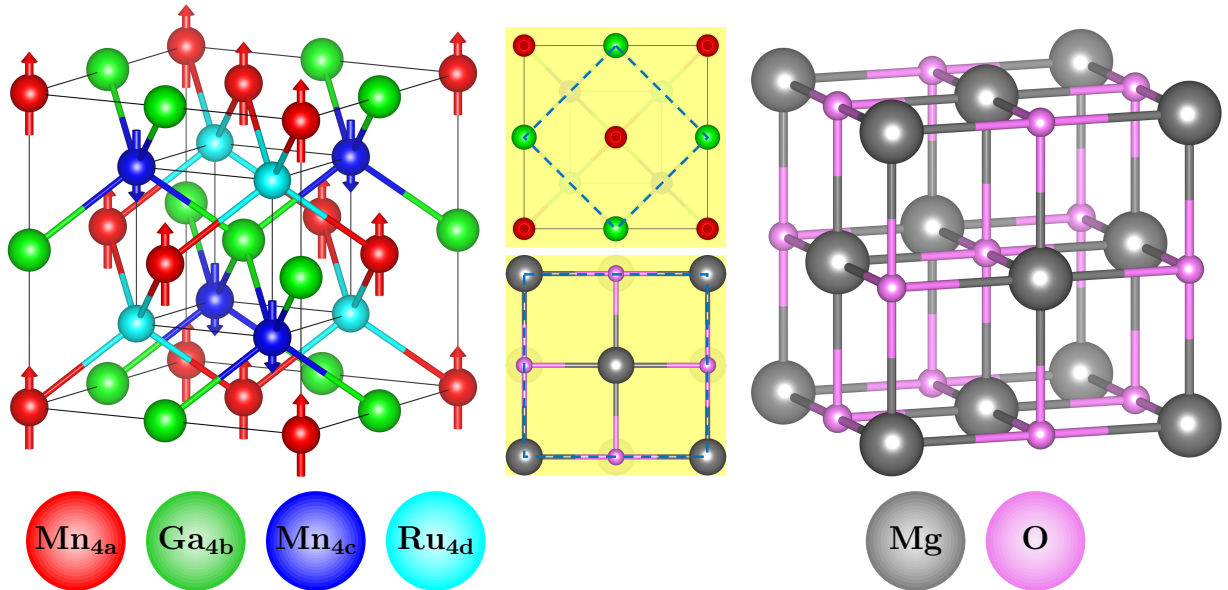
Figure 3.20: Isometric and top-down views of the MRG and MgO unit cells, showing epitaxial relation.

A huge amount of research has been performed into the effect of the deposition con-

ditions on the qualities and exhibited phenomena of MRG. In particular, varying the Ru and Mn content, magnetic annealing and changing the thickness. A thorough overview can be found in the dissertation of Dr. Siewierska [46]. In this work, the temperature of the MgO substrate was varied during deposition while keeping other variables constant: a Ru content of $x = 0.9$ was chosen and films of thickness $t = 20 - 25\,\text{nm}$ were deposited via magnetron sputtering and capped with an insulating oxide layer. It was previously observed that the structural and magnetic properties were different for sample deposited at lower and higher temperatures and so a systematic investigation was warranted: ten MRG samples of similar thickness were grown with substrate temperatures ranging from $T_{dep} = 200\,^{\circ}\text{C}$ to $T_{dep} = 425\,^{\circ}\text{C}$ in $25\,^{\circ}\text{C}$ intervals. This temperature was maintained throughout deposition before being allowed passively cool once the desired thickness was reached and deposition stopped. Detailed sample deposition conditions are shown in Table 3.2, for completeness and to enable reproduction of results, assuming the reader is in possession of a similar sputtering system. It should be noted that the MRG films were co-sputtered from a stoichiometric Mn_2Ga target and a Ru target, so only the relative Ru concentration could be varied. The thicknesses listed in the table are determined from XRR measurements. The $2\,\text{nm}$ Al metal capping layer oxidises in atmosphere to form the a robust AlO_x capping layer. No post-deposition treatments were performed to any of the films.

In addition, many of the useful phenomena MRG is predicted or observed to exhibit are second order effects (which involved spin-orbit coupling etc.) and therefore rely on the broken inversion symmetry of the space group (a fancy way of saying the Mn sublattices must be inequivalent or some effects will cancel), for example we cannot have (collinear) ferrimagnetism with identical Mn sites. It is therefore important to somehow characterise the chemical ordering of the MRG system to ensure the three elements mainly occupy the sites they are supposed to. Heusler alloys often crystallise in the non-inverse, $L2_1$ structure with the space group $Fm\bar{3}m$ (#225), obtained by swapping the Mn_{4a} and Ru_{4d} sites in MRG in Figure 3.20. All Mn sites are equivalent in this structure.

Table 3.2: Detailed deposition conditions for the 10 MRG films discussed in this chapter. Thickness listed is derived from fitted XRR data.

Sample id	T_{dep} (°C)	thickness (nm)	Ar Flow (sccm)	Op. Pressure (mTorr)	Deposition Time (s)	Capping (nm)
GA200714A	200	25.95	30	4	178.7	Al(2)
GA200527D	225	20.97	30	4	145	Al(2)
GA200527B	250	20.96	30	4	145	Al(2)
GA200521C	275	20.99	30	4	145	Al(2)
GA200521A	300	21.35	30	4	145	Al(2)
GA200515E	325	20.97	30	4	145	Al(2)
GA200518A	350	20.93	30	4	145	Al(2)
GA200518B	375	21.07	30	4	145	Al(2)
GA200518D	400	21.12	30	4	145	Al(2)
GA200521E	425	21.17	30	4	145	Al(2)

3.3.2 XRD

Each of the ten MRG samples was first[2] investigated via a symmetric $\theta/2\theta$ scan with the scattering vector perpendicular to the sample surface using the **non-monochromated**, Bragg-Brentano, Panalytical diffractometer, the results are shown in Figure 3.21.

There is a clear trend in the position of the MRG reflections as a function of temperature. The MRG (004) peaks have large intensity and fitting Voigt profiles to them to accurately determine the peak centre allows accurate determination of the MRG OOP lattice parameter (parallel to the (004) axis). The fitting procedure shown in Figure 3.22 above is a way to accurately obtain the peak positions and therefore the MRG lattice parameter c. There is also a clear trend in the peak width and disappearance of the intensity oscillations for $T_{dep} = 350$ °C and a less obvious but still evident increase in the (002) peak intensity with temperature. These can also be obtained from the Voigt fit, but the intensity oscillations cannot be properly accounted for so a more thorough analysis of all the additional parameters will be relegated to the strain fitting section, subsection 3.3.4. It should be reiterated that the simple Voigt model will still very accurately determine

---

[2]Samples are often investigated *in situ* using reflection high-energy electron diffraction (RHEED) to probe surface smoothness during growth, not shown in this work.
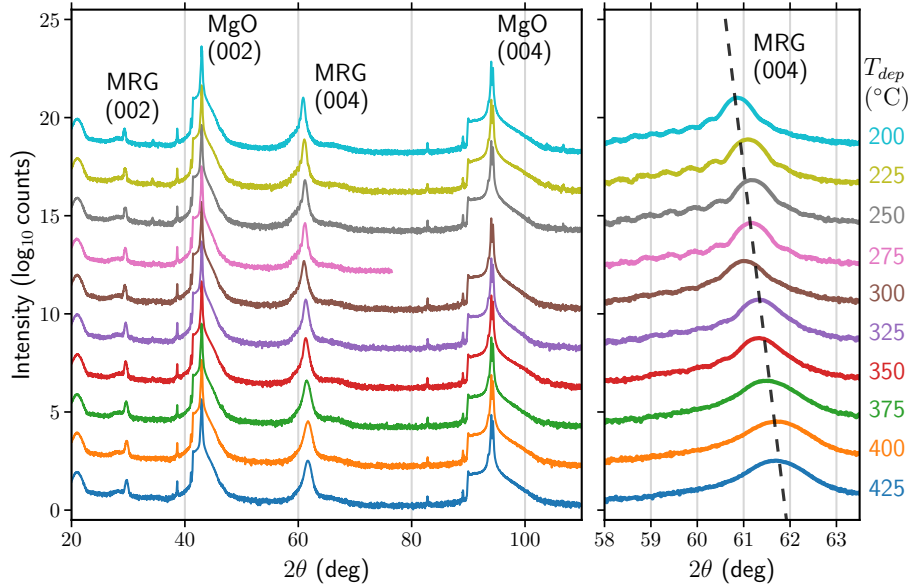
Figure 3.21: XRD spectra measured on MRG samples with $x = 0.9$ and deposited on MgO with varying substrate temperatures. The intensity is normalised to the noise level around $2\theta \approx 75°$ and the angles are normalised to the position of the substrate reflections. The MRG reflections shift to higher 2θ and have greater broadening as the substrate temperature increases, implying a decreasing OOP lattice parameter and more disorder. The dashed line in the second panel is a guide for the eye. The strange plateaus left of the substrate peaks are due to the automatic attenuator activating and all unlabelled peaks are artefacts due to the sample stage and/or X-ray optics.
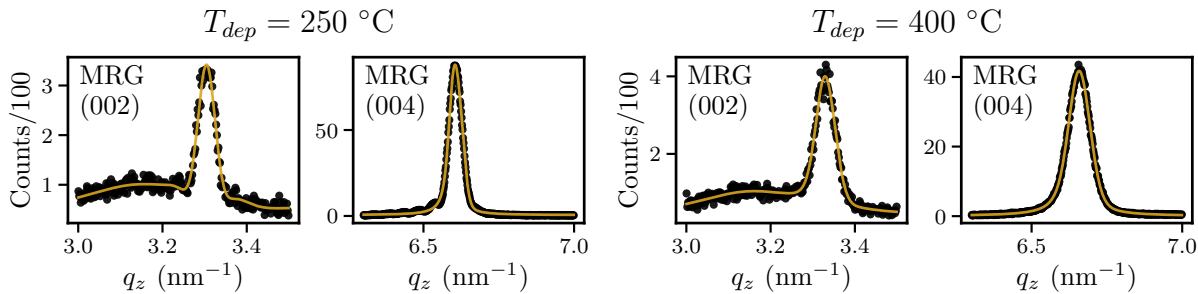
Figure 3.22: Example of fitting Voigt profiles to the MRG (002) and (004) reflections. Two peaks are used to account for the Cu K_{α_1} and K_{α_2} radiation with intensity ratio 2 : 1 for this diffractometer. Additional broad Gaussians are used to fit the background under the (002) reflection. These peaks are all present in the envelope evident in the figures.

the peak center and thus the lattice parameter, and for less well-ordered samples without fringing, the breadths are accurately determined as well.

The ratio of the corrected integrated intensities of the (002) and (004) peaks of MRG is equal to the ratio of the squared structure factors and therefore depends on the positions

and form factors of the atoms in the unit cell. We denote this ratio $S_{002/004}$. The ideal structure factors can be calculated using a program such as *VESTA* or manually via subsubsection 3.1.1.4. The reduced MRG unit cells for the *XA* and $L2_1$ MRG lattices are shown below in Figure 3.23, with the (002) and (004) diffraction planes marked, to visualise why the structure factor ratios differ.

MRG XA (004)   MRG XA (002)   MRG $L2_1$ (004)   MRG $L2_1$ (002)

Mn_{4a} Ga_{4b} Mn_{4c} Ru_{4d}
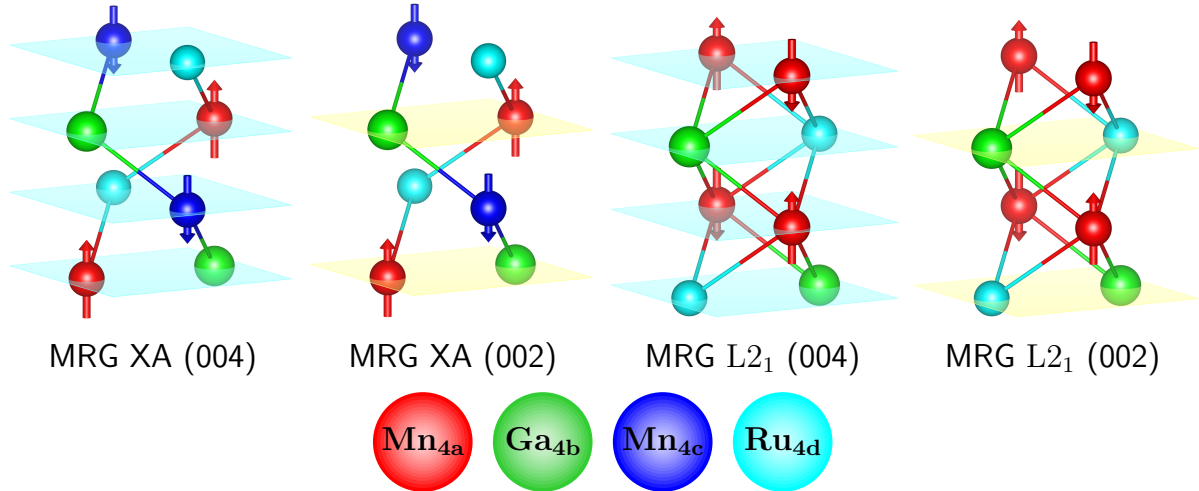
Figure 3.23: MRG reduced unit cells for *XA* and $L2_1$ structures, showing the (002) and (004) diffraction planes. Note that the (004) planes contain the same atoms for both structures, whereas the (002) planes contain Ru for the $L2_1$ structure but not for *XA*.

We see that the (004) planes contain the same atoms for both structures, whereas the (002) planes contain Ru only for the $L2_1$ structure. This already suggests that $S_{002/004}$ will be larger for the $L2_1$ structure as Ru is the largest atom with the highest electron density. To properly calculate the structure factors, the atomic form factors are first required. The atomic form factors depend on the length of the scattering vector $|Q|$ and the most accurate evaluation is done by solving the relativistic Hartree-Fock wavefunctions for every $|Q|$. Various calculated values for the atomic form factors can be found in the International Tables of Crystallography, Volume C [8, §6.1.1.3]. A commonly used approximation is a sum of four or five Gaussian profiles plus a constant, which is fit to the calculated values, this can also be found in the reference. A Python script which uses this approximation for the atomic form factors and then subsubsection 3.1.1.4 to calculate the structure factors for any given lattice and reflection can be downloaded from my GitHub [26] if the reader wants to see how the formulae are implemented in code, otherwise it

is suggested to use a developed program such as VESTA. From these values, we can see

Table 3.3: Structure factors for ideal XA and $L2_1$ MRG lattices, as well as a "disordered" lattice between the two where half the Mn_{4a} and Ru_{4d} have been swapped, calculated using VESTA.

	$F\bar{4}3m$ - XA	$Fm\bar{3}m$ - $L2_1$	Mn_{4a}-Ru_{4d} disorder
F_{002}	21.8	45.7	12.0
F_{004}	157.4	157.4	157.4
$S_{\frac{002}{004}}$	0.019	0.084	0.006

that the "order parameter" $S_{002/004}$ can give us an idea of what structure the MRG lattice has crystallised in and to what degree the atoms are chemically disordered (atoms having swapped positions without any structural changes). Structural disorder, among other phenomena, can have correlated effects on the structure factors, so drawing quantitative conclusions from this parameter along is discouraged. This parameter is plotted as a function of substrate deposition temperature at the end of the case study.
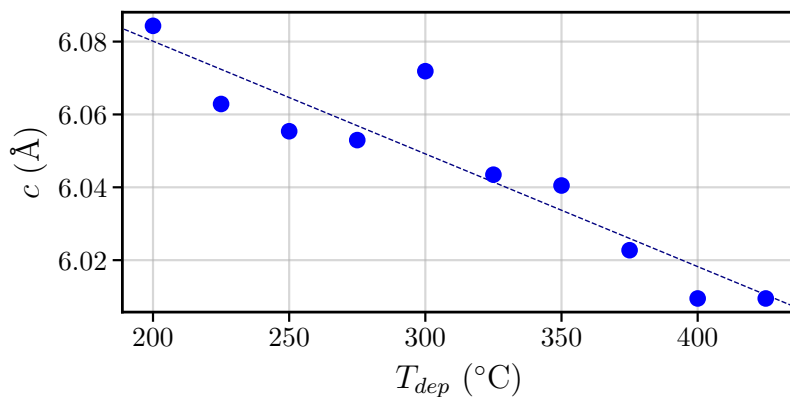
Figure 3.24: The trend of the OOP lattice parameter c with deposition temperature for MgO/MRG films, obtained from the position of the peak centres of the (004) reflections.

There is a clear linear decrease in the OOP lattice parameters in Figure 3.24. This is common in films which experience **volume-conserving substrate-induced compressive strain**. The epitaxial relation with the substrate squeezes the IP lattice parameters, causing the lattice to expand in the OOP direction. Higher temperatures allow for the formation of more dislocations and a "faster" relaxation of the tetragonal distortion. This linear trend in practice means that we can control the OOP lattice parameter and therefore

the degree of tetragonal distortion in MRG films simply by changing the substrate temperature at deposition. Annealing, heating the substrate and sample up post-deposition, has a similar but less pronounced effect in allowing the crystal structure to relax. For the same temperatures, the sample is slightly more relaxed when deposited at that temperature compared to one deposited at low temperature and then annealed. This variation with temperature should allow some control over the magnetocrystalline anisotropy as more tetragonal distortion will increase the "easiness" of the OOP magnetic easy axis. In addition, all the previously mentioned second-order effects which are forbidden by cubic symmetry can be destroyed or made possible at will.

The outlying peak at $T_{dep} = 300\,°C$ in Figure 3.24 cannot be explained simply by a difference in deposition conditions. We can see from Figure 3.21 that this peak is more asymmetric than most, so the simple symmetric peak profile used here may not have been ideal. Additionally, due to the sensitivity of these materials to their deposition conditions, any small changes in the atmosphere of the UHV chamber can have a relatively large effect: it is possible there was excess oxygen in the chamber following the deposition of an unrelated material by other researchers, for example.

3.3.3 RSM

We have seen that symmetric XRD scans yield a plethora of information about the lattice parameter, crystalline quality and even chemical ordering, but only projected on the (001) axis (in the OOP direction). We can infer information about epitaxy from the crystalline quality but no direct information is obtained when the scattering vector is perpendicular to the plane. When stated this way, the obvious solution is to measure with the scattering vector **not** perpendicular to the sample plane, as in Figure 3.11 panel (c). This scan will have an IP and an OOP component but they are not separable. To independently get IP and OOP information, we should perform a 2D scan and an RSM, as shown in Figure 3.17 and described in subsubsection 3.2.4.2. When we have 2D information in reciprocal space, we can take horizontal and vertical slices to separately investigate the IP and OOP lattice conditions.

To gain IP information, a reflection with finite IP projection must be chosen. The accessible reflections of Mn_2Ru_xGa and MgO, calculated using the Python script described

in subsubsection 3.2.4.2, are shown below in Figure 3.25. Given the expected values for the MRG IP lattice parameters, this material should grow rotated 45° with respect to the MgO, MRG[100] ∥ MgO[110]. The closest pair of substrate/sample peaks that satisfy this are MRG(204) and MgO(113), which should be close enough in reciprocal space to both be scanned in one measurement. MRG(206), with potential re-alignment to MgO(224), is a higher-intensity reflection that could be scanned.
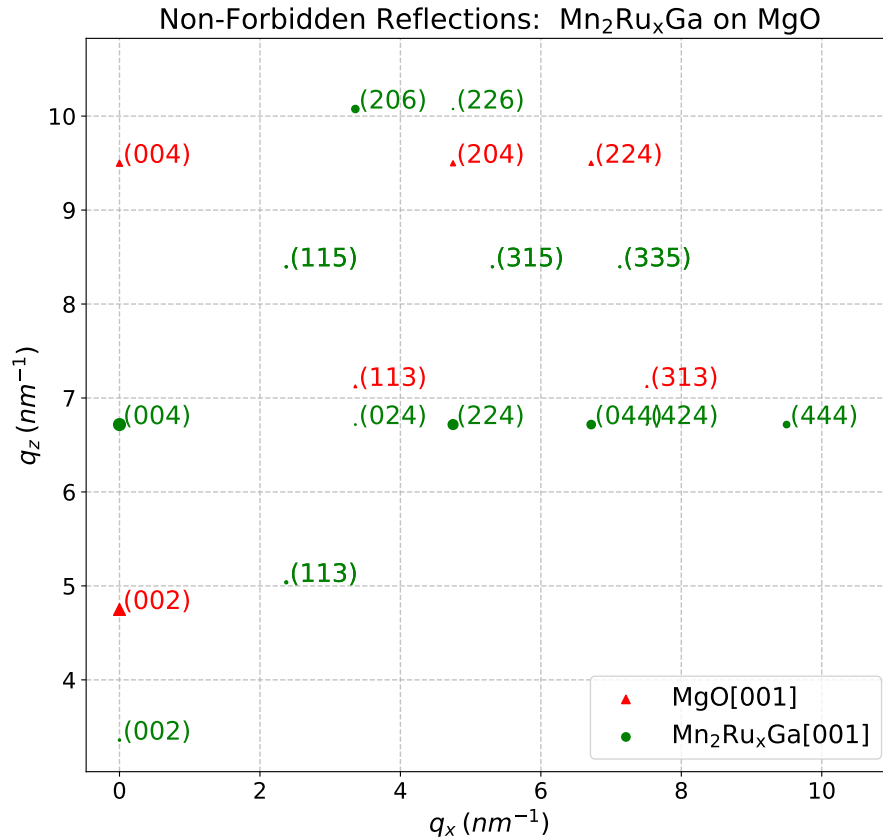
Figure 3.25: Accessible, non-forbidden reflections in reciprocal space, rotated into the scattering plane, for Mn_2Ru_xGa on MgO. As MRG is tetragonal, H and K are used interchangeably: $(024) = (204)$. The size of the plotted points is proportional to expected intensity. Geometrically inaccessible regions of reciprocal space are not shown (towards the bottom and top right corner).

Two RSM measurements were performed on a number of the MRG samples, one encompassing the MgO(113) and MRG(204) reflections and another of the MRG(206) reflection. The substrate is assumed to be a perfect crystal and the position of the MgO reflection is used to normalise the axes. Despite the much lower intensity, the MRG lattice parameters measured from the (204) peak position are more credible due to the proximity to the normalising MgO peak. For shape analysis however, the more intense (206) peak can

provide better statistics. Example of data from three MRG samples with distinct T_{dep} are shown in Figure 3.26 below:
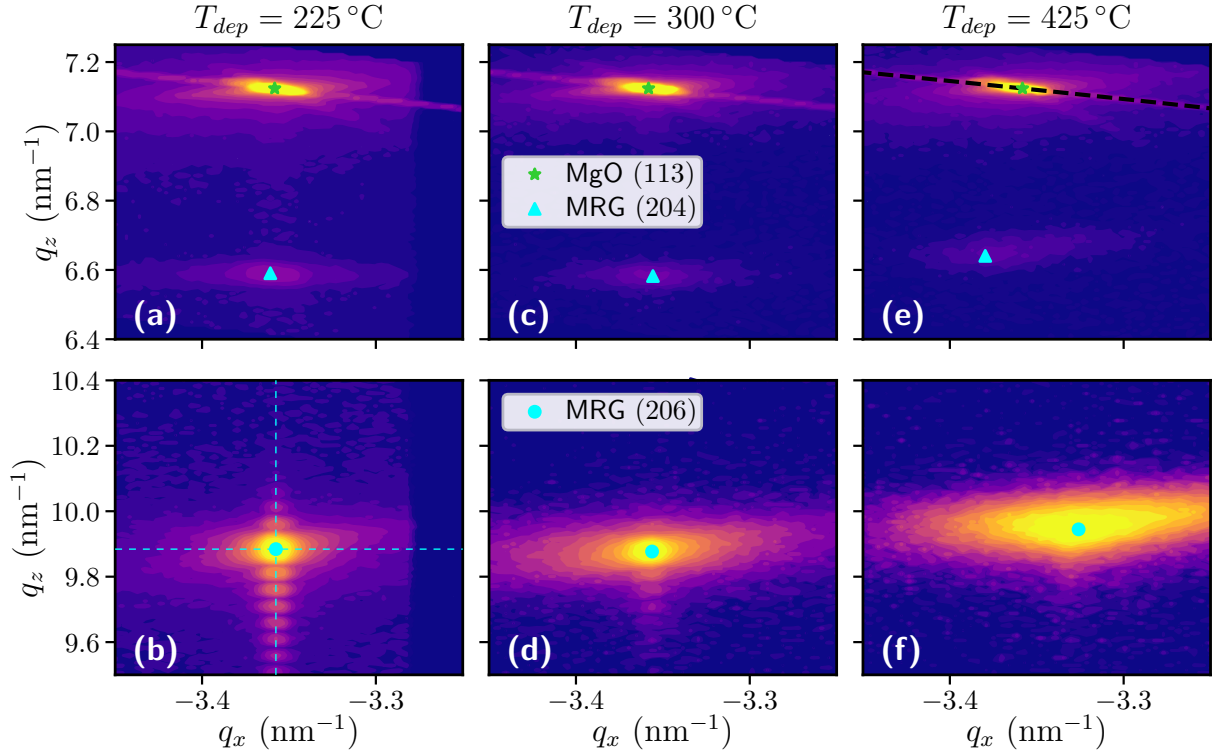
Figure 3.26: RSM scans on the (204) and (206) reflections of three exemplary MRG samples deposited at different temperatures. Alignment was to the MgO (113) reflection in all cases. Note the excellent epitaxy, especially in samples with lower T_{dep}, and the variable MRG peak shape (width and interference fringing). The dashed lines in panel (b) correspond to the slices taken for further analysis. The dashed line in panel (e) highlights the detector streak and is along the 2θ (constant-ω) axis. It is due to bleed-over from the pixels in the 1D detector at high intensity.

A 3D projection of the (206) reflection from the sample deposited at low temperature (Figure 3.26 panel (b)) is shown below in Figure 3.27. The vertical and horizontal slices are extracted and fit with Voigt profiles to obtain values for the lattice parameter, coherence length (finite size of coherently diffracting domains which result in broadening) and random strain in both the IP and OOP directions. This is the typical method for analysis of diffraction data from thin films, but from the figure, we can see that this is not adequate for the highly-crystalline and smooth epitaxial thin films, due to the thickness fringes which appear in the OOP direction.
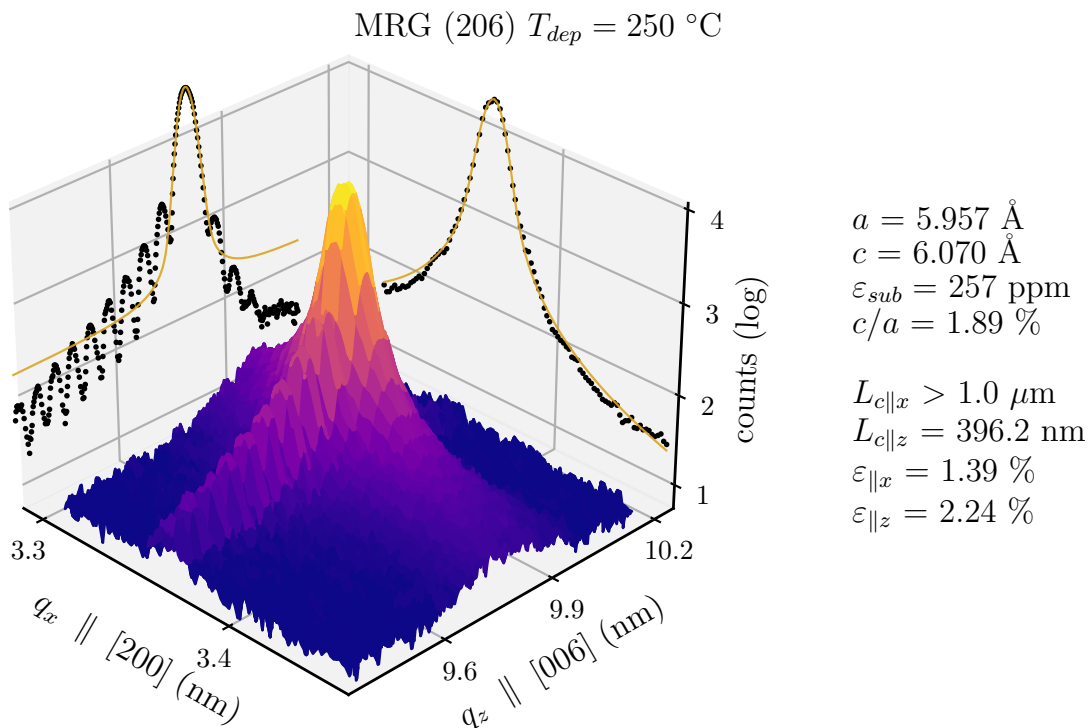
Figure 3.27: An example of fitting the IP and OOP slices of an RSM scan on the MRG (206) peak. The data is the same as in Figure 3.26 panel (b). The slices are fit with simple Voigt profiles and the coherence length and strain are calculated using Equation 3.11. This is one of the highest-quality MRG thin film grown, with coherent domains far larger than can be accurately determined by the Sherrer method and large thickness fringes which are not at all well fit. The asymmetry also points to some non-uniform strain, meaning both paths of Equation 3.11 are technically invalid: the strain-fitting method must be used for these low T_{dep} samples.

3.3.4   Strain Profile Analysis

In order to fit the asymmetric interference fringes observed in high-quality MRG films, we use the strain-fitting technique described in subsubsection 3.2.3.3. This involves manually integrating (or summing) the interference function Equation 3.7 with variable lattice parameters described by the strain field and a smoothness function which effectively characterises the number of atoms in the OOP direction which coherently diffract as a function of position. Recall that a rough film implies that our interference function is the sum of many sinusoids witih differing frequencies and so the oscillations are washed out, and that non-uniform smooth strain results in asymmetric peaks as opposed to the Gaussian broadening of uniform random strain.

The strain fitting method, Figure 3.28, offers a much closer match to the observed data
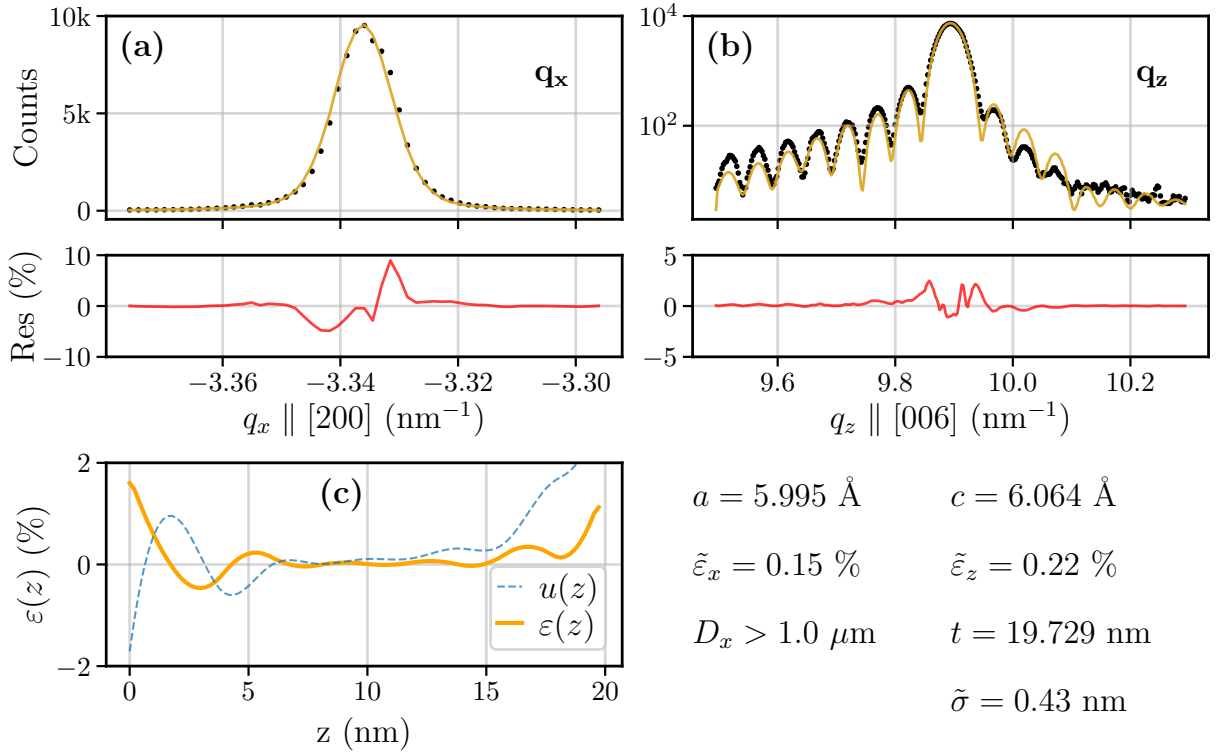
Figure 3.28: Vertical and horizontal slices through the (206) reflection of $T_{dep} = 225\,°C$ MRG, as in Figure 3.26(b) and Figure 3.27. **(a)** Voigt profile fit to the q_x slice, yielding IP lattice parameter a, and the volume-average average strain and coherence length $\tilde{\varepsilon}_x$ and $\varepsilon(z)$ from the Gaussian and Lorentzian Breadths respectively. **(b)** Strain-fitting function of A. Boulle (subsubsection 3.2.3.3) applied to the q_z slice, yielding the OOP lattice parameter c from the peak centre, the average strain $\varepsilon(z)$ from the average of the strain field, the film thickness t from the period of the fringes, and the average roughness $\tilde{\sigma}$ from the damping of the fringes. The roughness is somewhat analogous to the coherence length when considering the OOP direction as the film is fully coherent across the 10s of nanometres. **(c)** shows the displacement field (in arbitrary units) which yielded the fringes in panel (b) and its derivative, the strain field.

than the "standard" Voigt profile fit, Figure 3.27, for near-perfect epitaxial thin films in the OOP direction. This is because the samples are coherently diffracting across their entire thickness and have smooth interfaces, resulting the thickness fringes. Comparing the IP and OOP information obtained from the Voigt profile and strain fitting, different but analogous information is obtained in each case. The Voigt profile, always used for IP projections or imperfect films, yields the lattice parameter with volume averaged strain and crystallite size. Strain fitting yields the lattice parameter, the entire strain profile (which can then be averaged) and the thickness and roughness which are analogous to crystallite size projected onto the scattering vector. It should be pointed out that random strain due

to dislocations can also be included if the strain-fitting peak is too narrow, by virtue of additional Gaussian convolution, which mathematically can conveniently be included by adding to the Gaussian breadth of the instrumental profile, as per Equation 3.10, removing the need for another computationally expensive convolution.

Of course, RSMs are not required to perform strain fitting, a simple 1D symmetric XRD scan will do. The MRG (004) peaks of highly-crystalline samples often exhibit fringing, as seen in Figure 3.22 and these peaks can be fit using the strain method, as seen in Figure 3.29. There are no inherent downsides to using the 1D scan except for the obvious lack of IP information compared to RSMs and RSMs are significantly more time consuming, taking ($O(N^2)$ vs $O(N)$) time. However, one must be aware of the properties of the diffractometer they use. 1D symmetric XRD scans are typically performed using the non-monochromated, Bragg-Brentano geometry, Panalytical diffractometer. Compared to the collimated and monochromated Bruker, this results in lower resolution, meaning the fringes are not as discernible, and the additional K_{α_2} can complicate the fitting procedure. Some diffractometers are also capable of measuring a linear q scan, as in Figure 3.11 panel (d). By default, intensity is measured as a linear function of 2θ and the x axis is therefore not linear when converted to q. A diffractometer capable of measuring as a linear function of q removes this potential problem. One cannot take advantage of 1D detectors in this case, as they necessarily measure a range of 2θ values.

The strain profiles shown here, for high-quality MRG films deposited at low temperature, all have similar features. There is significant strain at the interface, a relaxed region in the middle of the film and often additional strain at the capping layer, sometimes even greater than at the substrate interface. To further elucidate the structure of these MRG films, we sent some to have scanning transmission electron microscopy (STEM) measurements performed. This atomic-resolution spectroscopy technique allows for extreme resolution mapping of the atomic order of materials as a function of thickness. Two complimentary techniques that are very important and useful for our purposes are high-angle annular dark field (HAADF) imaging and energy-dispersive X-ray (EDX) spectroscopy. The results are shown in Figure 3.30. In HAADF, the **incoherent** scattering of the electrons from the nuclei in the sample generate a "dark field" image, the scattering length is very sensitive to atomic number and so therefore so is the brightness
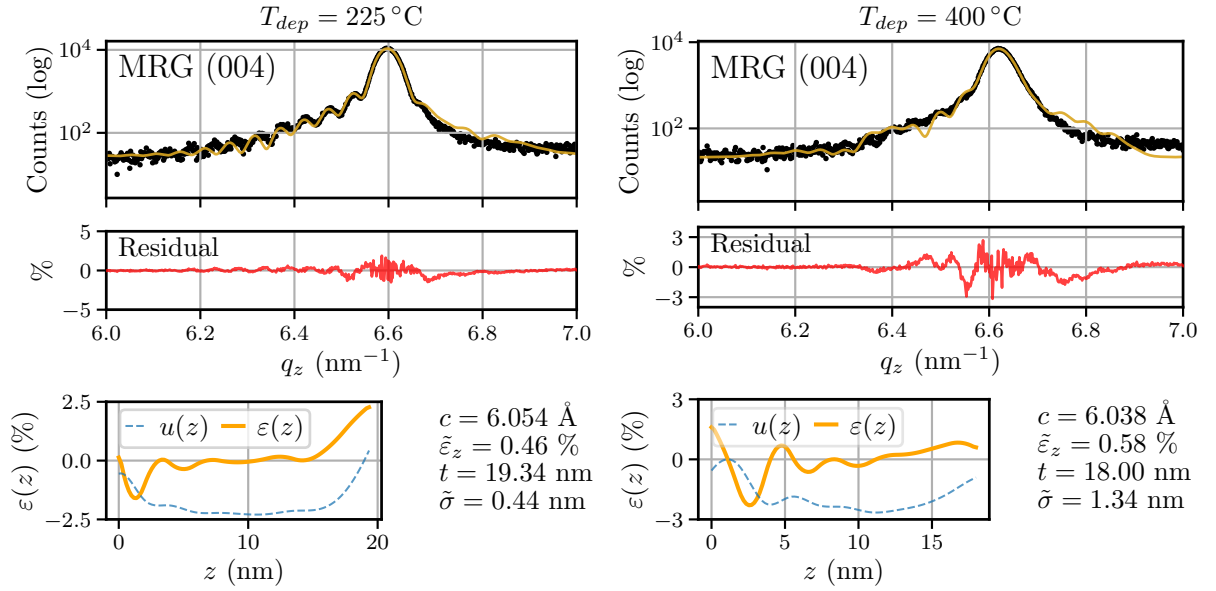
Figure 3.29: Fit of MgO and MRG (002) and (004) peaks from XRD spectra (Figure 3.21), using the strain fitting technique and accounting for the Cu K_{α_2} radiation as these were measured using a non-monochromated diffractometer. The MRG samples were deposited at $T_{dep} = 250\,°C$ and $T_{dep} = 400\,°C$ respectively. Both peaks are well fit with small residuals, but the lack of fringe contrast in the $T_{dep} = 400\,°C$ case means that the fit parameters are ill-determined: a simple Voigt fit would be more efficient in this case.

of the image, resulting in a grey-scale atom-level mapping of the structure of the material with elemental resolution (provided they are not too similar in atomic number). EDX has poorer spatial resolution than HAADF but stronger elemental resolution since it utilises the characteristic X-rays of the atoms with energy-dispersive detection. This allows a map of the composition of the material as a function of depth to be generated. For most of these TEM-style measurements, much of the effort goes into cutting and milling the sample to gain access to different slices throughout the depth. More information on all these techniques can be found in Pennycook and Nellist [47, §1.5, §7] The measurements were performed by Dr. Andrew Naden of the University of St. Andrews, Scotland.

There are a number of interesting features in the EDX data in Figure 3.30: there is significant Mn diffusion into the Al_2O_3 capping layer with little counter-diffusion and some diffusion into the substrate. In addition, there are very clear peaks in relative Ru concentration near both the substrate and capping layer interfaces. These facts together help to explain the strain profiles of this MRG film, which shows much larger values at the interfaces. The Ru-rich regions are also evident in the HAADF images. The lattice
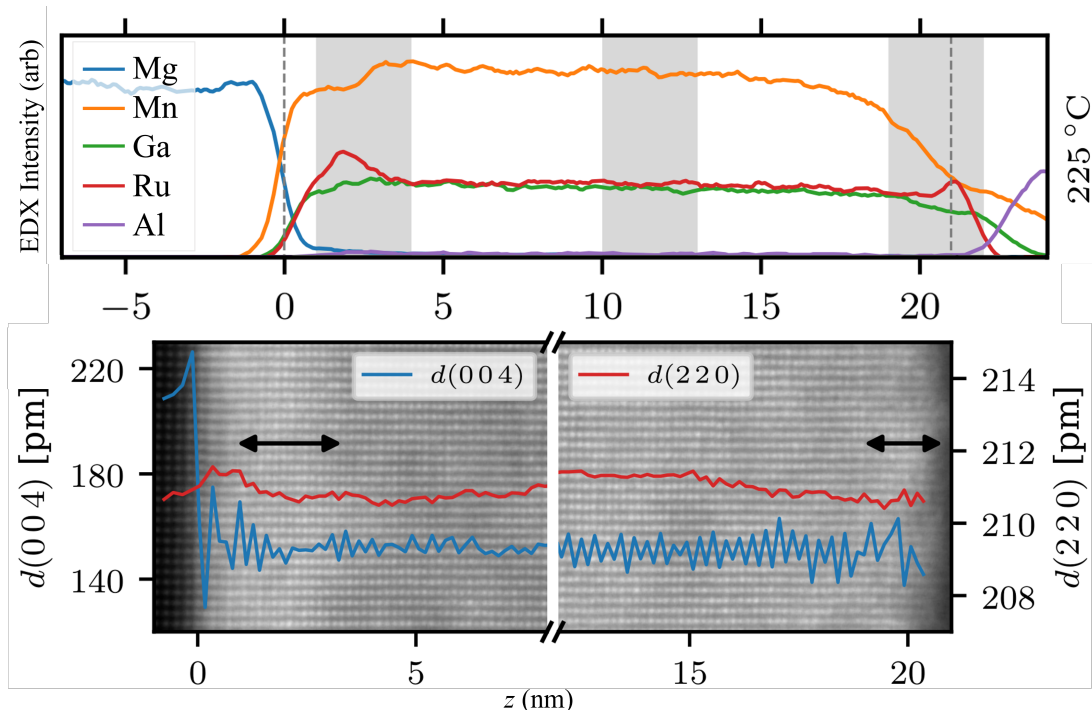
Figure 3.30: EDX (top) and HAADF (bottom) spectra obtained on a $T_{dep} = 225\,°C$ sample of Mn_2Ru_xGa.   A value of $z = 0$ corresponds to the substrate interface while $z \approx 22$ corresponds to the capping layer. distinct regions are shaded in the EDX spectrum, while the arrows in the HAADF indicate regions of high relative Ru concentration, resulting in brighter contrast due to Ru's high atomic number.

parameter mapping in the HAADF, OOP along (004) and IP along (220), does not show any very striking trends as it is difficult to directly fit atom positions from these types of images.

3.3.5   Summary of MRG parameters from X-ray diffraction

In practice, when investigating materials using diffraction, the exact data analysis method used is decided on a sample-by-sample basis. Using strain-fitting when appropriate and Voigt profile fitting where possible, we modelled the data from the XRD scans (and RSM slices) of each of the ten MRG samples in the series. The results are summarised in Figure 3.31.

   The OOP lattice parameters (c) are calculated from the 1D XRD spectra which are generally higher resolution than the RSM scans while the IP lattice parameters (a) are necessarily calculated from the RSM scans. The (204) peak is preferred for this as the substrate peak is contained within the same scan (Figure 3.26) and can be used for more
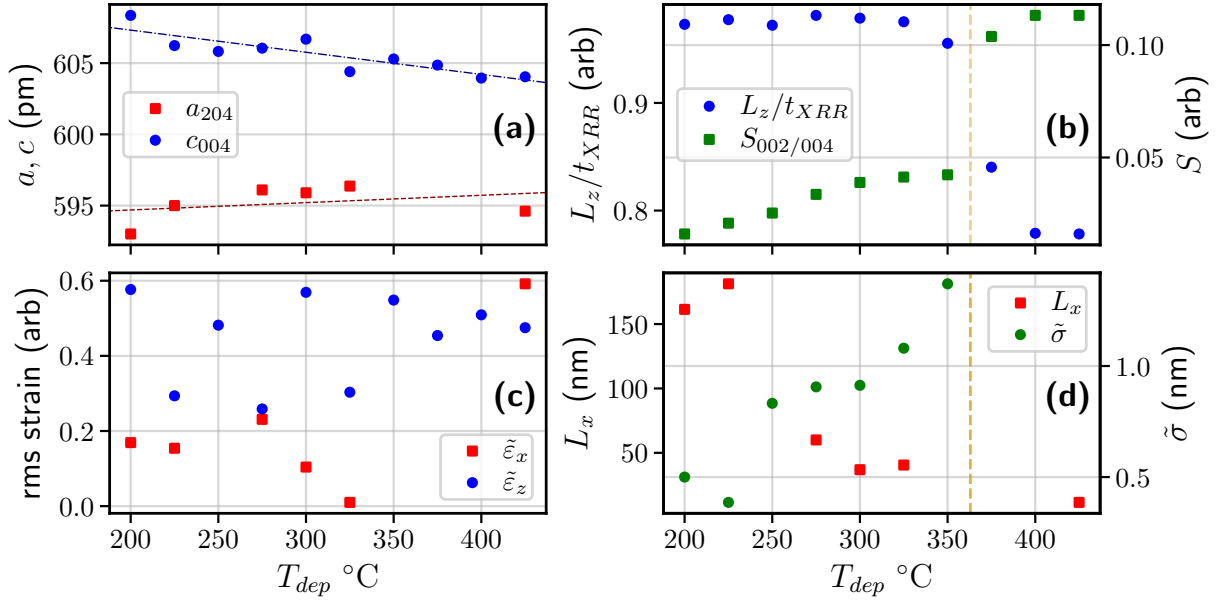
Figure 3.31: Summary of variation of MRG crystal parameters with deposition temperature. **(a)** IP and OOP lattice parameters. **(b)** OOP coherence length L_z and order parameter $S_{002/004}$. **(c)** The rms strain in IP and OOP directions. **(d)** IP coherence length L_x the interface roughness $\tilde{\sigma}$. Note the linear trends of many parameters with T_{dep} and the discontinuity around $T_{dep} = 375\,°C$, where the films are no longer continuous in the z direction. The results are explained in detail in the text.

accurate calibration.

The IP and OOP crystal coherence lengths L_x and L_z, and the average strains $\tilde{\varepsilon}_x$ and $\tilde{\varepsilon}_z$, are obtained via Equation 3.11 from either the Voigt profiles or, in the case of L_z for the high-quality films, from the Lorentzian breadth converged to by the strain-fitting algorithm. Due to the low film thickness, the OOP coherence length is shown normalised by thickness obtained from XRR measurements, t_{XRR} (data not shown here). A value of unity indicates the film is fully coherent in the OOP direction, which is the case up until a clear threshold in deposition temperature. It is important to note that due to the inverse relationship between measured peak breadth and crystallite size or coherence length, large coherence lengths over a few hundred nanometres cannot be accurately resolved as they contribute negligible broadening to the measured peak.

The surface roughness $\tilde{\sigma}$ is obtained from the strain fitting and is therefore only available when the films are high enough quality to exhibit the thickness fringes.

The clear threshold drawn in the right-hand panels of Figure 3.31 corresponds to the point at which the films are no longer fully-coherent in the OOP direction such that L_Z

begins to drop and $\tilde{\sigma}$ is no longer available. L_x continues to drop and $\tilde{\varepsilon}_x$ continues to rise through this temperature threshold. More interestingly, the order parameter $S_{002/004}$ jumps to a larger value at this threshold. While initially at a small value as one would expect from a high-quality XA MRG lattice (Table 3.3), the jump indicates chemical and/or crystal disorder above this deposition temperature, which is the likely cause of the changes in the other effective parameters.

3.3.6 Rietveld Analysis on Single-Crystal Thin-Films

A more thorough way to investigate structural and chemical disorder is to perform Rietveld analysis, which is essentially comparing the structure factors for multiple reflections. This is a much more justifiable way to estimate the crystalline quality than the $S_{002/004}$ value, but of course takes much longer than a single symmetric XRD scan. The technique was described in subsection 3.2.5 and its application to MRG thin films is described here. Suitable reflections to investigate have already been visualised, in Figure 3.25, while measuring reciprocal space maps. There are five reflections with sizeable intensity and three peaks from the each of these families are measured for statistical purposes in case minor misalignment would cause one orientation to have higher observed intensity than the other, except for the $(00L)$ peaks which have lower multiplicity. In addition, four low intensity peak families are measured with one reflection and one very high multiplicity family $(H \neq K \neq L)$ was measured via four separate reflections. The plot of $F^2(2\theta)$ and the chosen reflections are shown below.
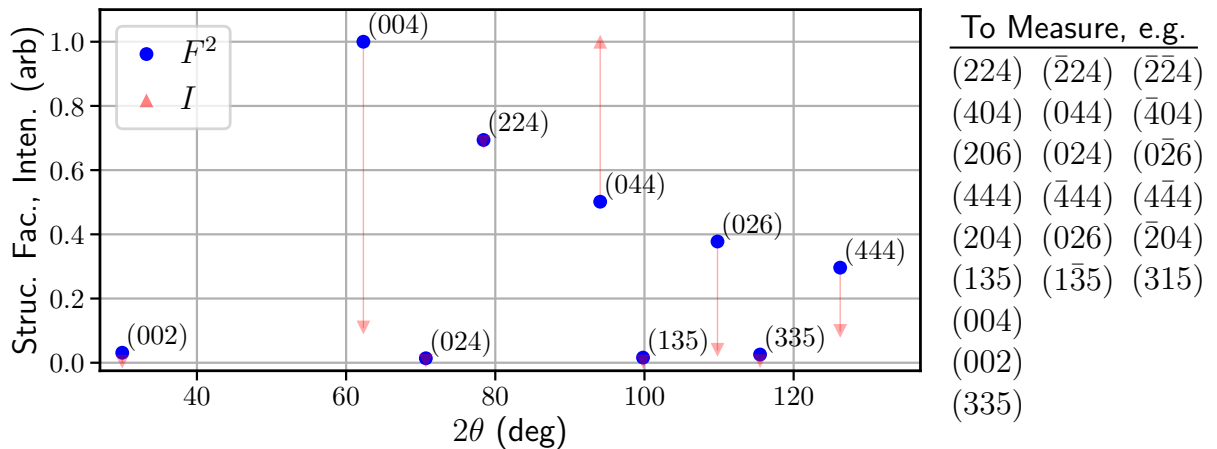
Figure 3.32: Calculated (with VESTA) squared structure factors and corrected intensity for and Mn_2Ru_xGa with $x = 0.9$ and lattice parameters $a, b = 5.955\,\text{Å}$ and $c = 6.04\,\text{Å}$. The lattice parameters are important because the irradiated volume correction depends on the X-ray incident angle, which in turn depends on the aspect ratio of the unit cell. The table shows a list of scans that might be performed: as many ϕ angles (rotation around the vertical axis) are probed as possible to mitigate possible misalignment effects.

3.3.6.1 High-Temperature MRG

As a proof of concept, a thick ($t = 100\,\mathrm{nm}$, to provide high diffracted intensity) and relatively relaxed MRG sample deposited at $T_{dep} = 425\,^{\circ}\mathrm{C}$ was investigated using this new method, as described in subsection 3.2.5. A number of non-coplanar substrate peaks were measured to determine the sample orientation in the diffractometer reference frame. The lattice parameters were already known from XRD/RSM measurements identical to those previously desribed in this material case study. A Python script I wrote determines the position of all sample reflections in the diffractometer reference frame and selects a large suitable subset to measure, based on the available time on the diffractometer tool, printing out the positions and counting time for each. These can then be agglomerated into a *.job* file readable by the diffractometer (via another script) and loaded up to perform all the chosen measurements. The resulting data and its analysis is shown below. When extracting values for the squared structure factors from the observed diffracted intensity, the order of operations is important. For this type of refinement on data from separate scans of multiple peaks (as opposed to the original whole-pattern fitting of powder diffraction data), the general procedure is as follows:

- Account for different counting times for different reflections.

- Perform a fit of a suitable function to the background away from the main peaks and subtract.

- Only after removing the background can the irradiated volume correction be applied via multiplying by the sin of the incidence angle: $\sin(\omega)$. The background does not originate primarily from the sample so should be removed prior to correcting for the irradiated volume of the very thin sample.

- Now fit a Voigt profile to the peaks. The other instrumental corrections depend on 2θ rather than ω so can be applied to the integrated intensities.

- Apply the Lorentz/polarisation/monochromation corrections to the integrated intensities to obtain the structure factors.

Similar work from which this procedure took inspiration was performed by Wadley et al. [48] and interested readers are encouraged to read their excellent manuscripts. Our
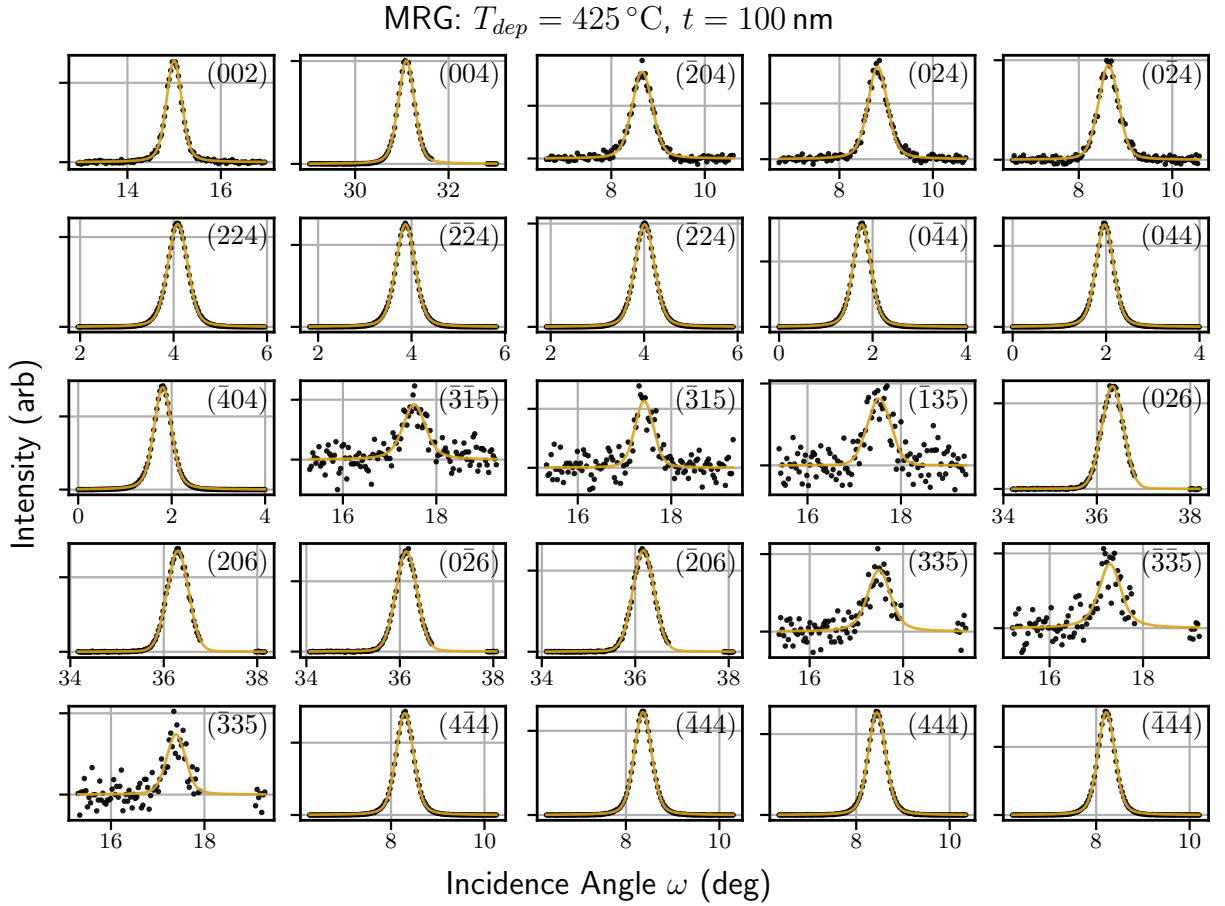
Figure 3.33: Rocking curves measured around a large number of reflections from an MRG film deposited at $T_{dep} = 425\,°C$, with Voigt profile fit. Alignment was performed via measurement of four substrate reflections as described in subsection 3.2.5 and all scans were performed over $\approx 60\,$hrs in one weekend.

technique and ones like it exist in a no-man's-land between powder and single-crystal diffraction. As mentioned, in powder scans, all the possible reflections can generally be recorded in a single 1D measurement and the pattern fitted with software such as FullProf [6] which utilise Rietveld refinement [38]. Proper single crystal diffraction (not on thin films) is generally recorded with a large 2D detector with the many resulting dots forming a matrix characteristic of the atomic structure of the diffracting material. A commercial software that could be used for analysing single-crystal diffraction data is SingleCrystal 4 by CrystalMaker [49]. Other software have been compiled by the International Union of Crystallography online [50], and they also maintain a software "museum" going back half a century here [51].

The averaged integrated intensities for the reflection families, corresponding to the raw

data shown in Figure 3.33, are shown in Figure 3.35. The importance of the correction factors, particularly the irradiated volume correction for a collimated beam and thin film sample, are evident. The reciprocal of the peak breadth is plotted as a function of the ratio of the sine of the incident and exit angles in Figure 3.34. The data is unremarkable in this particular case but for the thin MRG film (discussed in the next section), the trend is distinct so it is important to show the equivalent data for this sample.
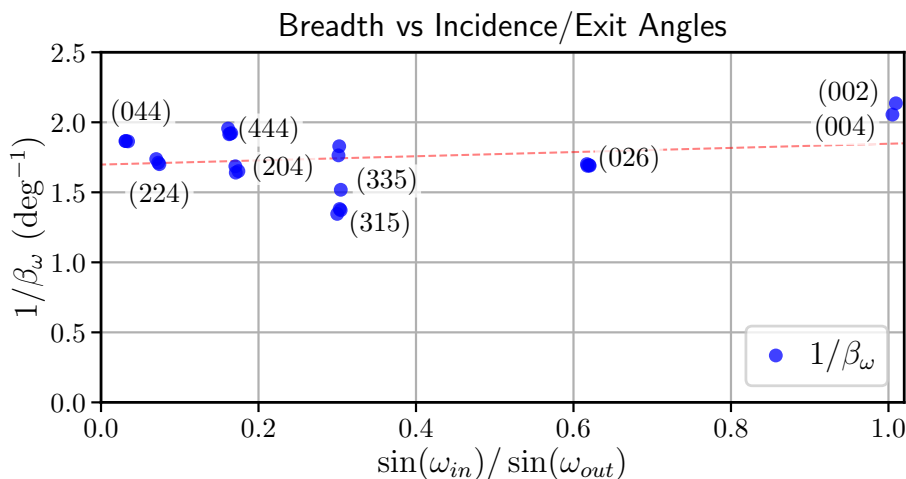
Figure 3.34: Peak breadth (of the fit Voigt profile) as a function of the photon incidence angle for MRG with $t = 100\,\mathrm{nm}$ and $T_{dep} = 425\,°\mathrm{C}$. The breadth is roughly constant across the range of incidence and exit angles, indicating that the breadth primarily originates from the sample itself, through finite-size or strain broadening.
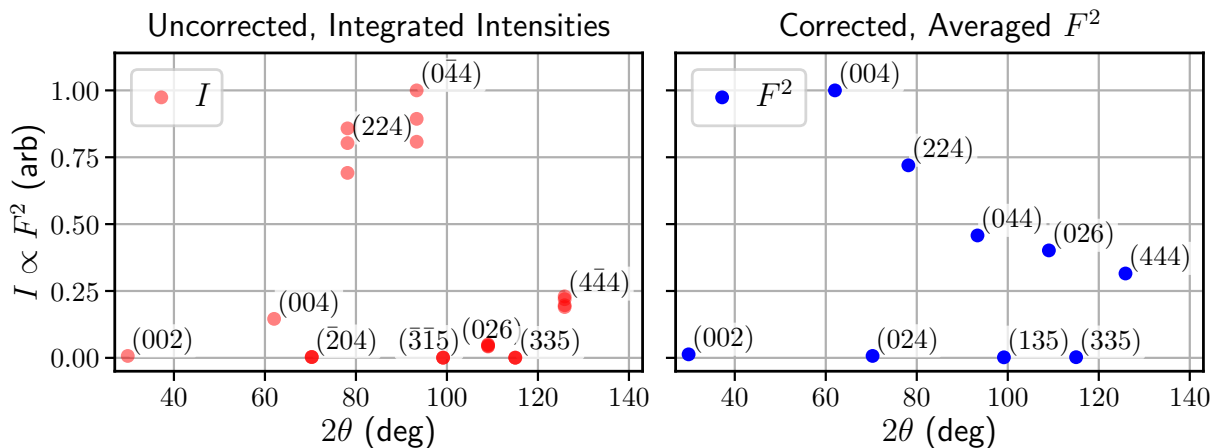
Figure 3.35: Intensities of the Voigt profiles fit to the raw, uncorrected data in Figure 3.33. On the right are the averaged integrated intensities for each peak family after applying all corrections in subsection 3.1.2, which should be equal to the squared structure factors. The similarities of both to the calculated values in Figure 3.32 are evident.
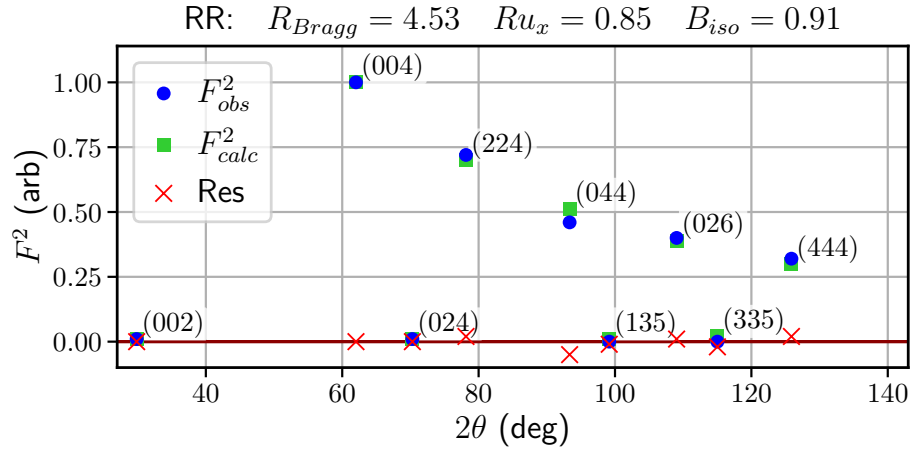
Figure 3.36: Results of performing Rietveld Refinement on the measured structure factors using the FullProf program. Since the lattice parameters and crystalline structure were already known, only the scale, Ru content and the Debye temperature factor B_{iso} were varied in the fit. The discrepancy for the (404) peak is likely due to problems with the fitting caused by the low incidence angle and resulting, large, highly non-linear irradiated volume correction.

The result of Rietveld refinement using FullProf is shown in Figure 3.36. The goodness of fit parameter R_{Bragg} is simply the residuals as a percentage of the observed intensity and anything less than 5% is considered a good fit. The refinement yielded a stoichiometric Ru concentration of $Ru_x = 0.85$, in agreement with the nominal composition and density calculations. Formally, B_{iso} is related to reduced intensity due to the thermal vibration of atoms causing de-coherence of the diffracted photons, however it is strongly correlated with other random isotropic disorders and is often treated as a general disorder parameter for this reason. A B_{iso} value around unity is unremarkable and suggests that the crystal is ordered as expected (i.e. as defined in the FullProf input file).

So called site-swapping defects had been proposed as a mechanism to explain some of the unusual and inconsistent observed magnetic phenomena in MRG films [52]. I attempted to refine the degree of different types of disorder between the different MRG sites, but due to the small number of reflections and unfortunate relative interaction cross sections of the atoms[3], even qualitative conclusions proved difficult to make and the data is not shown here.

---

[3]Mn, Ga and Ru are all metals with relatively similar

3.3.6.2 Low-Temperature MRG

Another MRG sample that was investigated was an exceptionally thin ($t = 10\,\mathrm{nm}$) sample, deposited at $T_{dep} = 225\,°\mathrm{C}$. The technique was the same as before but less peaks were measured and for longer counting times since there was so little diffracting volume. The results are shown in Figure 3.37.
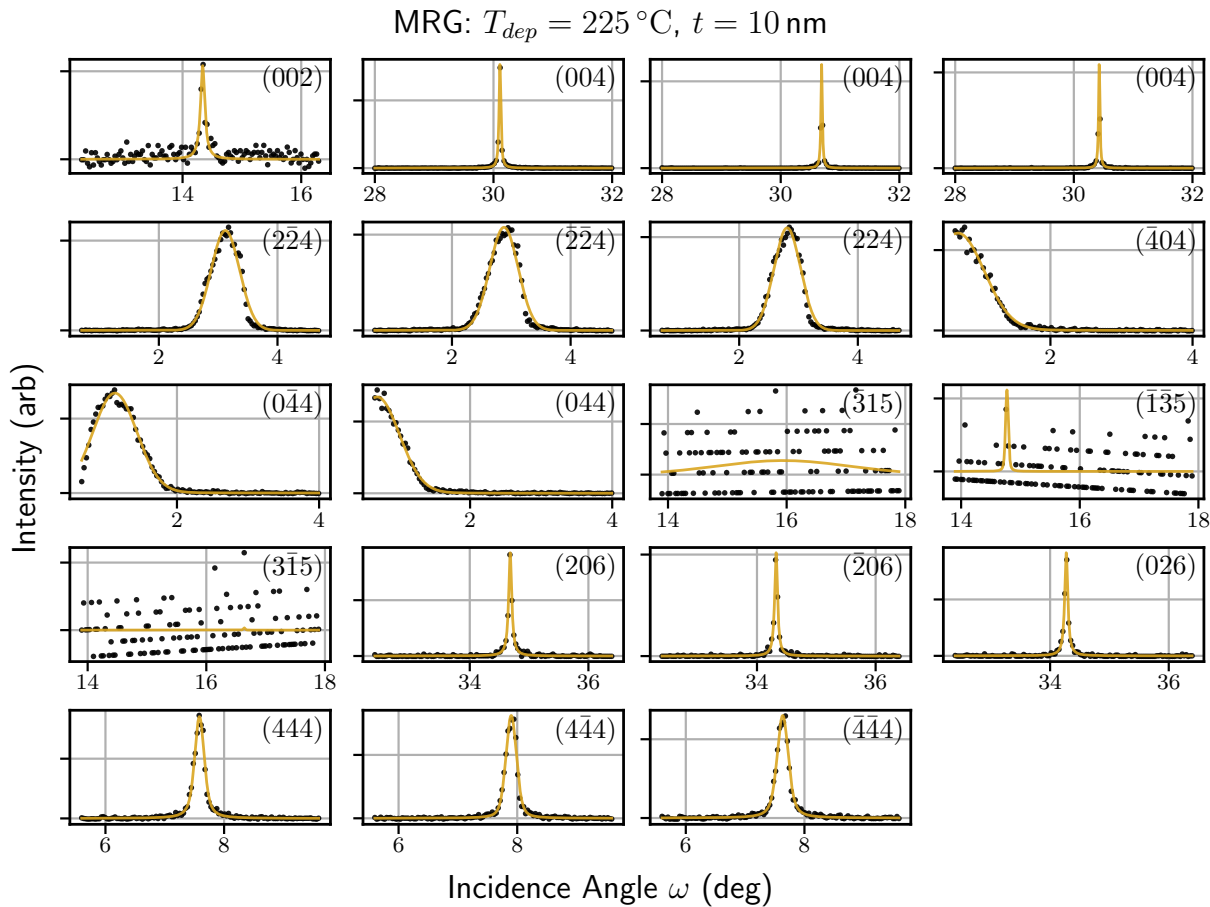
Figure 3.37: Rocking curves measured around a large number of reflections from an MRG film deposited at $T_{dep} = 225\,°\mathrm{C}$, with Voigt profile fit. The fits here are not quite perfect as some of the peaks do exhibit thickness fringing, but not a huge amount and the asymmetry is a larger obstacle to a perfect fit. The much larger aspect ratio of this thin, low-T_{dep} MRG film when compared to the previous example results in the peaks shifting to lower 2θ and ω values. Some of the peaks are cut off by the sample/stage due to the low incidence angle and two families, (404) and (224), are very strongly affected by the irradiated volume correction. There is also a clear decreasing trend in peak width as ω increases.

There are two primary differences in between the high and low temperature deposited samples. The low temperature one has a larger OOP axis as usual, and less relaxation occurs due its thinness. This results in the reflections with an IP component shifting to

lower incidence angles because the diffracting planes are more inclined to the horizontal (001) plane. This has an adverse effect on the (404) peaks in particular which are almost made inaccessible in the reflection geometry. The other interesting feature is the trend of decreasing peak breadth with increasing ω angle, as illustrated in Figure 3.38, compared to a more or less constant breadth for the thick, high temperature film. By plotting the inverse of the breadth as a function of the ratio of the sin of the incidence and exit angles, we obtain a straight line, indicating that this trend is caused by beam expansion: for collimated beams in particular, when the incidence angle is much lower than the exit angle in asymmetric scans, the apparent beam width is increased due to the geometry. This is evident in this sample because of its extremely high-quality crystallinity from being deposited at low temperature, while the previous sample has significant material-dependent broadening which drowns out this effect.
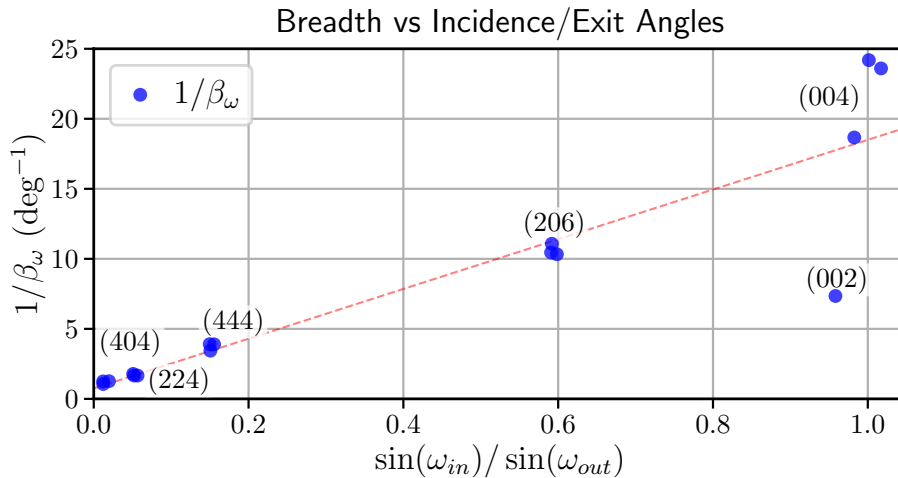
Figure 3.38: Peak breadth (of the fit Voigt profile) as a function of the photon incidence angle for MRG with $t = 10\,\mathrm{nm}$ and $T_{dep} = 225\,°\mathrm{C}$. The linear trend is clear, indicating that the broadening is primarily due to collimated beam expansion. The (002) peak has low SNR (Figure 3.37), resulting in its breadth being poorly defined.

The goodness of fit R_{Bragg} is very low and the Ru content is as expected again. The Debye temperature factor in this case is quite large as a result of peaks at higher 2θ values having lower intensity. A quantitative explanation for this has not been found, but the thickness fringing of intense peaks results in a sub-optimal fit with the Voigt profile and the anisotropic strain profile exhibited by thin low temperature MRG could also result in a $|q|$-dependent de-coherence and reduction in intensity. Here, we have successfully performed
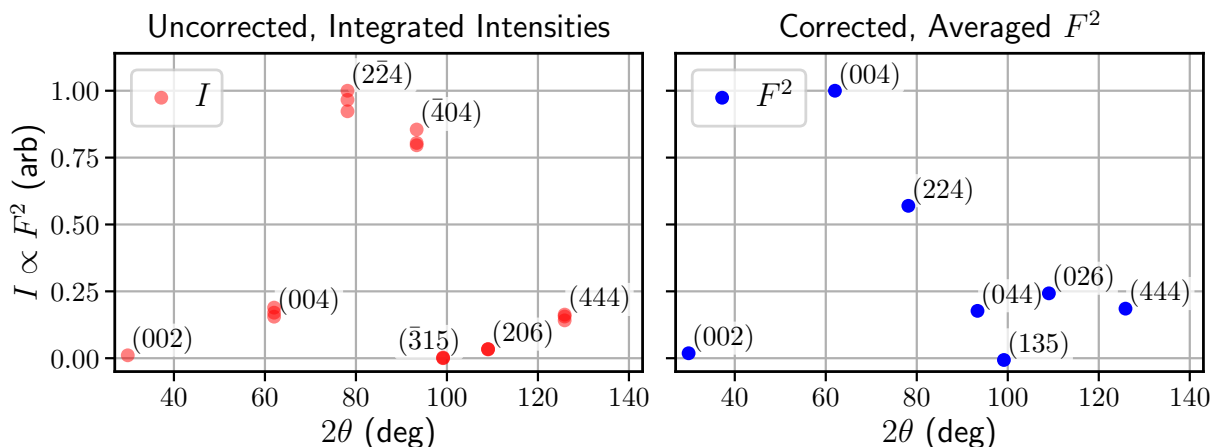
Figure 3.39: Intensities of the Voigt profiles fit to the raw, uncorrected data in Figure 3.37. On the right are the averaged integrated intensities for each peak family after applying all corrections in subsection 3.1.2, which should be equal to the squared structure factors. The similarities of both to the calculated values in Figure 3.32 are evident.
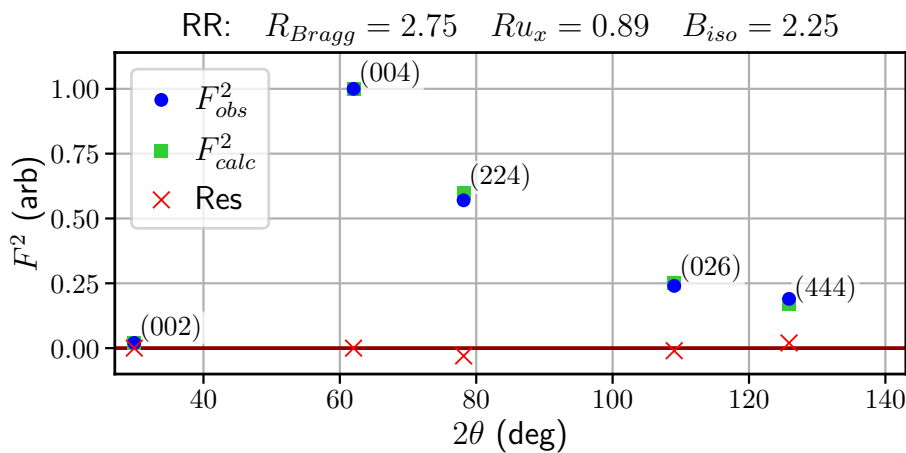
Figure 3.40: Results of performing Rietveld Refinement on the measured structure factors using the FullProf program. Since the lattice parameters and crystalline structure were already known, only the scale, Ru content and the Debye temperature factor B_{iso} were varied in the fit. The (404) reflection is excluded in this case, from Figure 3.37, we can see that the peak is measured with the X-ray beam almost parallel to the sample surface and the peak is partially cut off with the remaining portion extremely distorted thanks to the diverging volume correction. This unfortunately reduces the available non-zero intensity peak families to just five.

Rietveld refinement on a $t = 10$ nm single-crystalline thin film, with a remarkably good fit to the structure factor data, and obtained the Ru content and Debye temperature factor of the material, showing that with the right techniques, laboratory diffractometers can continue to push boundaries in metrology.

3.3.7 Neutron Diffraction

3.3.7.1 Motivation

While MRG is a ferrimagnetic material, is has been observed that films of different crystalline quality or stoichiometry (higher/lower Ru content) can exhibit qualitatively different responses of their magnetisation to external fields and currents. In particular, SQUID (superconducting quantum interference device) and AHE (anomalous Hall effect) measurements, which are sensitive to the external magnetic field produced by a material and to the magnetism of the materials electrons at the Fermi level respectively, both exhibit unusual pinched hysteresis curves for certain MRG samples [53, 54]. SQUID and AHE measurements for MRG samples deposited at low, medium and high temperatures are shown in Figure 3.41. All measurements were performed at 150 K. The SNR in the
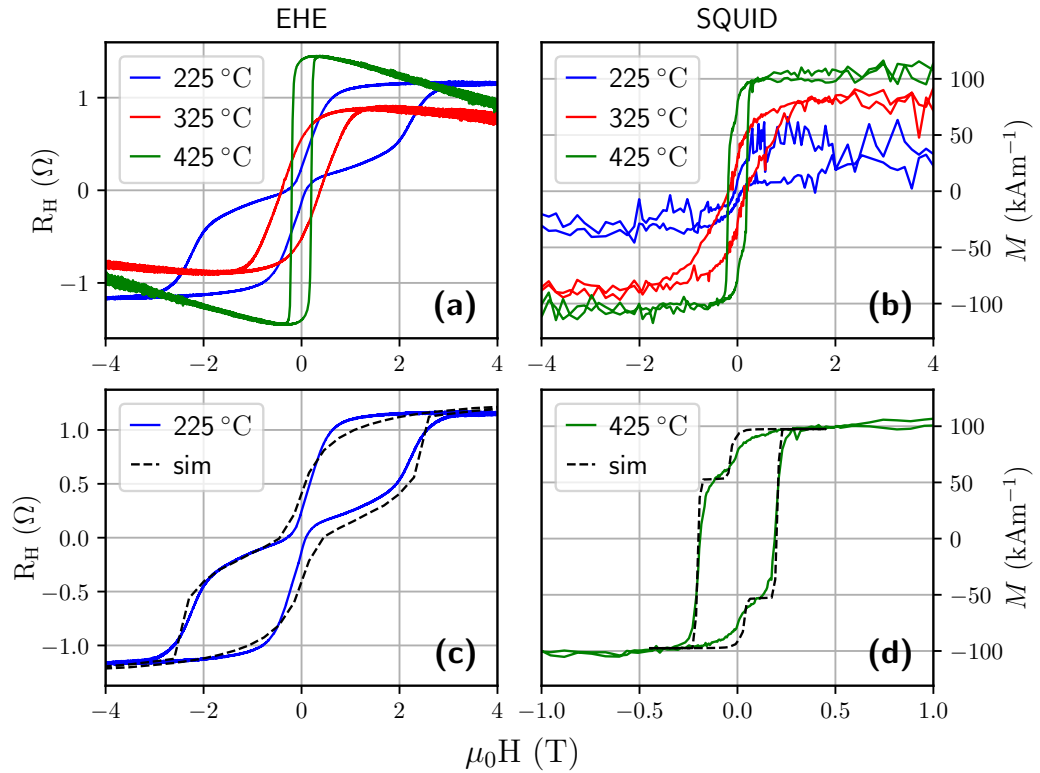
Figure 3.41: **(a)** AHE hysteresis loops for three different MRG samples, note the very pinched loop for the lower temperature sample. **(b)** SQUID measurements for the MRG samples, note the small kink in the high-temperature sample. **(c)** The pinched hysteresis loop and a simulated loop utilising Monte-Carlo methods and assuming a simple spin Hamiltonian with uniaxial anisotropy. **(d)** Similar fitting for the SQUID loop.

SQUID measurements in Figure 3.41 is intrinsically low due to the ferrimagnetic nature and resulting low net moment of the MRG films. The Hall effect measurements are electrical and so depend on the polarisation of the electrons at the Fermi level, thus giving a clearer picture. The Monte-Carlo simulations were performed by Professor Stamenov to show that the unusual loops can indeed be fit with a simple uniaxial anisotropy model, though not necessarily with realistic parameters.

3.3.7.2 Theory

In order to properly elucidate the magnetic structure of the films, it was decided to perform neutron diffraction on the lowest-temperature, highest crystalline quality MRG which exhibited the most pronounced pinch in the hysteresis. We applied for neutron diffraction beam-time at the D10 instrument at the Institut Laue-Langevin (ILL) in Grenoble, one of Europe's premier condensed matter research facilities. A sample of thickness 25 nm, deposited at $T_{dep} = 225\,°C$, and confirmed by various X-ray methods to have high crystalline quality, was selected to be investigated. This was a highly ambitious project as 25 nm provides very little diffracting volume for the relatively weakly interacting neutrons, but it was thought that by focusing on particular peaks, worthwhile information could still be obtained. The original plan of measuring three samples proved infeasible for the same reason. In addition to the magnetic information, the different elemental contrast in neutron diffraction should give more information on the crystal structure as well. The neutron data is available, after an embargo period, from the ILL data repository [55].

The selected (monochromated) neutron wavelength at the D10 beam-line was $2.36\,\text{Å}$, access to higher-order peaks via shorter wavelengths is not critical since neutrons are penetrating and remove the restriction of the reflection geometry that exists for the laboratory X-ray measurements. The nuclear scattering lengths of Mn, Ru and Ga are -3.75, 7.03 and 7.29 respectively [8, Tab. 4.4.4.1]. Mn having a negative value approximately half the magnitude of the positive values for Ru and Ga results in some interesting structure factors for various peaks. The neutron diffraction structure factors for a few peaks for XA and $L2_1$ MRG are shown in Table 3.4, as in the X-ray diffraction case:

From the table, it is clear that neutron diffraction allows us to very easily tell the different space groups of MRG apart in addition to the sensitivity to local magnetism.

Table 3.4: Nuclear neutron structure factors for *XA* and $L2_1$ MRG lattices, calculated using VESTA. Many of the peaks have identical structure factors (before instrumental correction) because the neutron form factors are independent of $|Q|$, unlike in the X-ray case.

	$F\bar{4}3m$ - *XA*	$Fm\bar{3}m$ - $L2_1$
F_{002}	0.516	43.64
F_{111}	30.86	0.516
F_{311}	30.86	0.516

Numerous peaks can have the same structure factors if the defining planes contain the same atoms, the (111) and (113) planes of the cubic MRG unit cell contain alternating Ru and Ga in the *XA* case but just Mn in the $L2_1$ case while the opposite is true for the (002) peaks. Neutron atomic form factors are independent of scattering vector length (as a good approximation) leading to numeric match-up which cannot occur in the X-ray case since the form factors are $|\vec{Q}|$ dependent then. Regarding the magnetic structure factors, only the Mn atoms have a magnetic moment with the atoms on the $4a$ sites and $4c$ sites antiferromagnetically coupled, as in Figure 3.20. This leads to strong constructive interference from the (002) planes in particular but weak magnetic diffraction from the (004) planes as the moments are out of phase. The predicted total neutron structure factors for MRG, calculated using FullProf, are shown below in Figure 3.42 for rotating magnetic field to show the change in diffracted intensity as a function of the angle between the scattering vector and the magnetic moments.

3.3.7.3   Results

Shown below is an excerpt from the neutron diffraction data recorded from the MRG film. A subset of peaks and a list of all scans is included. The data is quite noisy but that is to be expected for such a small diffracting volume. From the Gaussian profile fits to the data, the peak areas are obtained and can be converted to structure factors via the appropriate corrections. There is no irradiated volume correction of course so it is just the Lorentz and polarisation corrections. The appropriate form for neutron diffraction is given in the FullProf manual [6, eq. (3.26)] but is very similar to the forms I derived for monochromated, collimated X-ray diffraction in subsection 3.1.2.
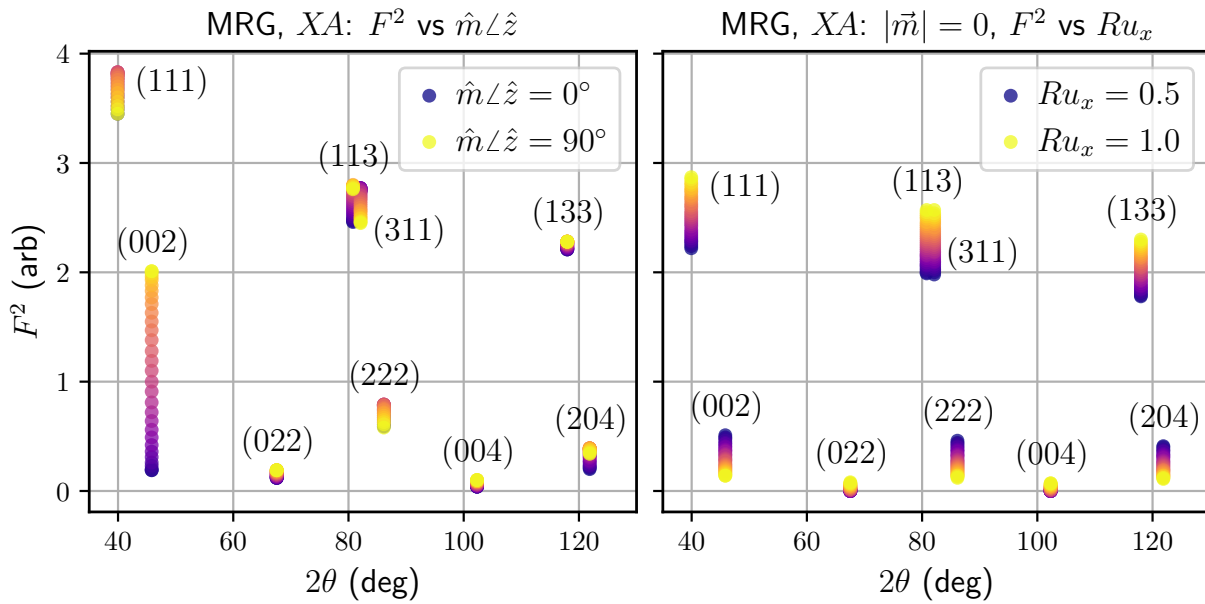
Figure 3.42: Neutron structure factors for *XA* structure MRG. Left panel shows them as a function of the magnetic moment orientation, rotating from $\hat{z}$ to $\hat{x}$ about $\hat{y}$. Right panel shows the nuclear (non-magnetic) F^2 as a function of Ru content, assuming vacancies in the lattice for reduced content.
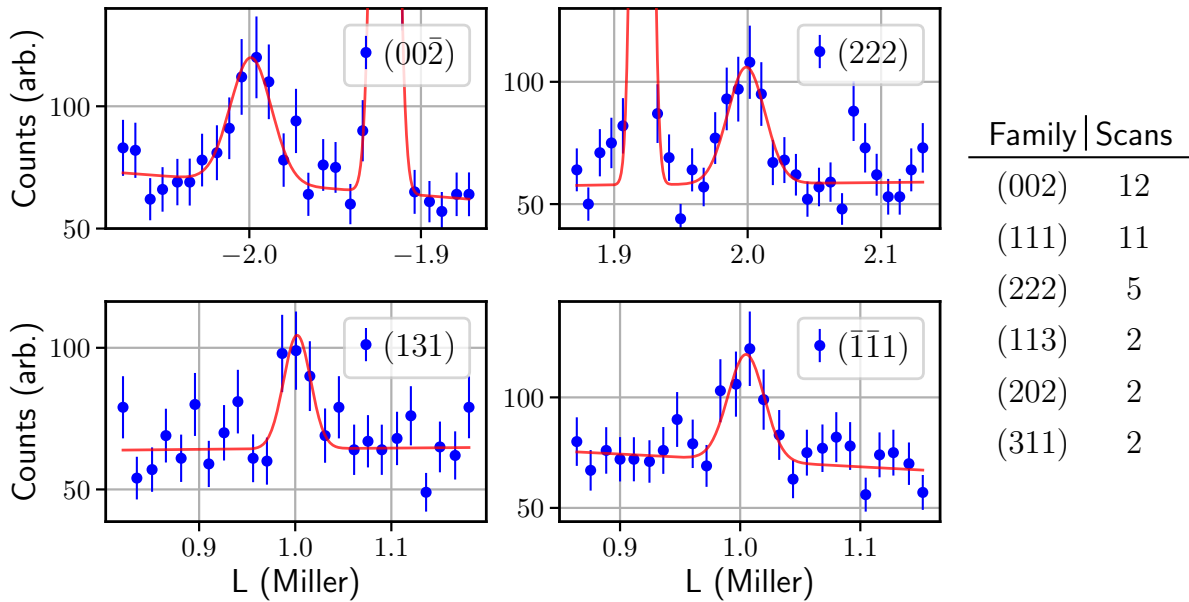
Figure 3.43: Some examples of the raw neutron data for different reflections, fit with Gaussian profiles. The large peaks near $L = 1.9$ in the upper panels is due to the substrate. The peaks are quite noisy but the SNR ratio is quite good considering the 25 nm thickness of the film. On the right is a list of all the peaks that were scanned (excluding substrate alignment).

One of the advantages of the D10 beam-line at the ILL is its cryogenic capabilities and neutron diffraction data was measured at a number of temperatures. Unfortunately, this

MRG sample has a Curie temperature far above room temperature so it was not possible to measure just the nuclear structure factors. Shown below is a subset of data measured at the two extreme temperatures.
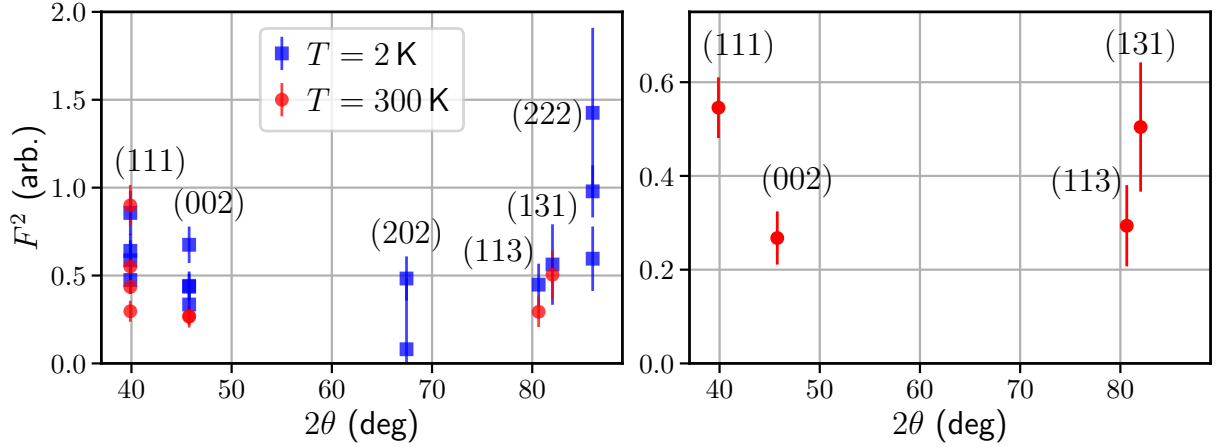
Figure 3.44: The squared structure factors (Lorentz and polarisation corrected integrated intensities) for peaks measured at $T = 2\,\mathrm{K}$ and $T = 300\,\mathrm{K}$. On the right are the averaged values for the room-temperature scans. These peaks are the most suitable for combined refinement with the X-ray data in the previous section.

We see in Figure 3.44 that there is a larger diffracted intensity at lower temperatures. This is expected due to both the de-coherence caused by thermal vibrations of the atoms and lowering of the total magnetic moment by thermal fluctuations for those magnetic peaks. From the neutron diffraction data, there are a number of conclusions we can draw. The large values for the (111) and (311) structure factors imply that the MRG is crystallised in the XA structure as expected, see Table 3.4. The large value for the (002) structure factor cannot be due to nuclear scattering in this case and therefore implies that the magnetic moment for the sample is primarily IP $((HK0)$: perpendicular to (002)) across all the temperatures measured, this IP magnetisation is an important result. MRG films exhibit perpendicular magnetic anisotropy when measured by applying an external magnetic field [53, 54] but this neutron diffraction data shows the magnetic moments lie IP at zero field. In fact, this could explain some of the unusual kinks seen in the hysteresis loops: if the magnetisation is initially IP at zero external perturbing field but is quickly rotated OOP before slowly saturating, for example. At this end of this section, the possible spin structure of the Mn atoms will be discussed in the context of magnetisation data. The room-temperature neutron diffraction data, right panel of Figure 3.44, was also

simultaneously Rietveld refined with X-ray data also recorded at room temperature, result shown in Figure 3.45.
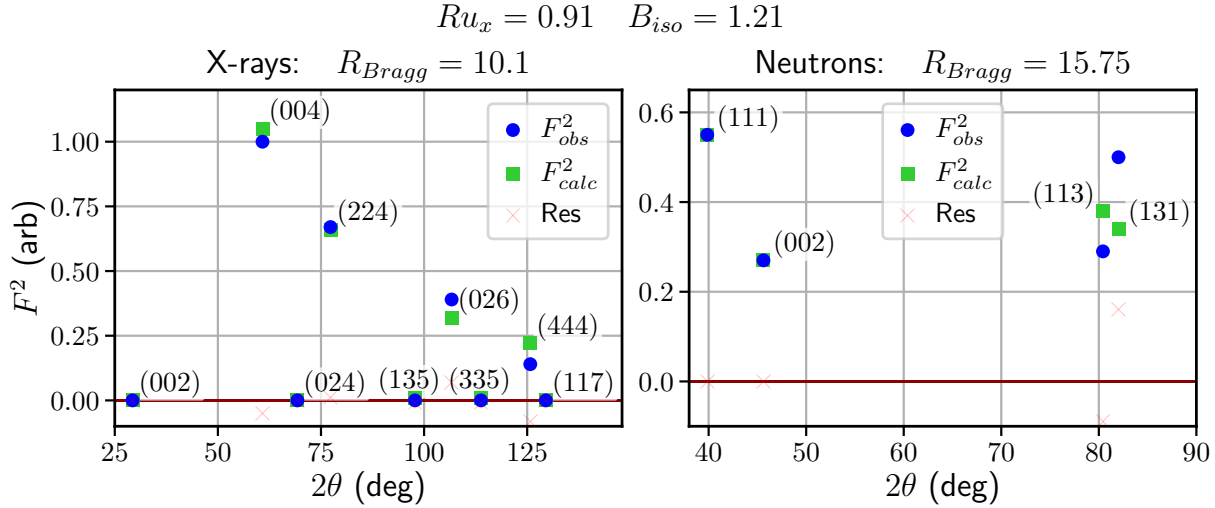
Figure 3.45: Result of simultaneous Rietveld refinement on neutron and X-ray diffraction data from the MRG sample ($t = 25\,\text{nm}$, $T_{dep} = 225\,°\text{C}$). The goodness of fit is not as impressive as for other samples demonstrated, but the refinement was still a success. The (404) reflection in the X-ray case is again left out due to being at too low of an incidence angle to be accurately measured.

Some important parameters for the Rietveld refinement from the 25 nm MRG thin film are tabulated in Table 3.5. The values for the combined refinement are in the rightmost column. The values in the leftmost column were obtained after fitting the X-ray data with Voigt profiles and applying the relevant corrections. For the values in the central column, the raw data for all measured X-ray peaks was simultaneously fit with Voigt profiles of the same width: despite visibly worse fits to the data, the quality of the Rietveld refinement is very similar.

The beauty of the combined refinement is that the X-ray diffraction data effectively fixes the structure, Ru content, Debye-Waller factors and more, allowing the neutron diffraction refinement to really focus on the magnetic contribution. We see sensible values for the Ru content and Debye-Waller factor. The latter is much smaller than for the $t = 10\,\text{nm}$ sample shown earlier and slightly larger than for the $t = 100\,\text{nm}$ sample, which makes sense if we assume the inflation is due to anisotropic strain for thin samples. In the end, the magnetic moments of the Mn atoms on the $4a$ and $4c$ sites were found to be $2.55\,\mu_{\text{B}}$ and $-2.77\,\mu_{\text{B}}$ respectively, both along $\hat{x}$. The magnetism was confined to be along $\hat{x}$ following the simulations shown in Figure 3.42. When refinement was attempted varying

Table 3.5: Parameters from Rietveld refinement of X-ray data (col A, B) and of combined X-ray and neutron data (col C) from the same 25 nm MRG film. The input data for col A and B was obtained from uncoupled and coupled Voigt fits to the measured X-ray peaks respectively, see text for details.

	Voigts	Coupled Voigts	Combined Fits
Ru Occupancy	0.7838	0.5896	0.91
B_{iso}	1.0981	1.6835	1.21
Scale	1.02×10^{-6}	1.34×10^{-6}	7.77×10^{-4}
$m_{x_{4a}}$	NA	NA	2.55
$m_{x_{4a}}$	NA	NA	-2.77
$m_{z_{4a}}$	NA	NA	NA
$m_{z_{4a}}$	NA	NA	NA
R_{Bragg}	10.2	9.57	neutron: 15.75 X-ray: 10.09

the $\hat{x}$ and $\hat{z}$ components of either sublattices' moments, the procedure quickly diverged and returned nonsensical values for the parameters. The values obtained strictly from Rietveld refinement come with the caveat that, as can be seen in Table 3.5, a similar goodness of fit can be obtained with parameter converged to significantly different values. In essence, this is due to the fact that Rietveld refinement is originally meant to be performed on large-volume polycrystalline or powder samples rather than single-crystalline thin films. Due to the limitations, I would not recommend emulating this method for similar thin films.

3.3.7.4 Conclusions

For the final refinement shown in Figure 3.45, I experimented thoroughly with rotating magnetisation OOP and changing the magnitude, as well as introducing excess Mn atoms to the $4d$ sites, while changing the Debye-Waller factor and Ru content as usual. No improvements to the fit were observed. It should be noted that changing Ru_x and B_{iso} have a similar effect and can improve the fit for some peaks while worsening others, therefore having little effect on the overall R_{Bragg} values, in other words, the parameters are strongly correlated which adds some uncertainty to the conclusions. However, I believe it is safe to say this sample is magnetised IP at zero field, which is the key takeaway.

Additional SQUID [56] data measured on another $T_{dep} = 225\,°C$ MRG sample can add some support to these assertions, see Figure 3.46. SQUID measurements are a macroscopic probe that obtains essentially the volume average of the magnetisation, in contrast to the atom-resolved signal from the neutron diffraction. The remanence (zero-field) moment of
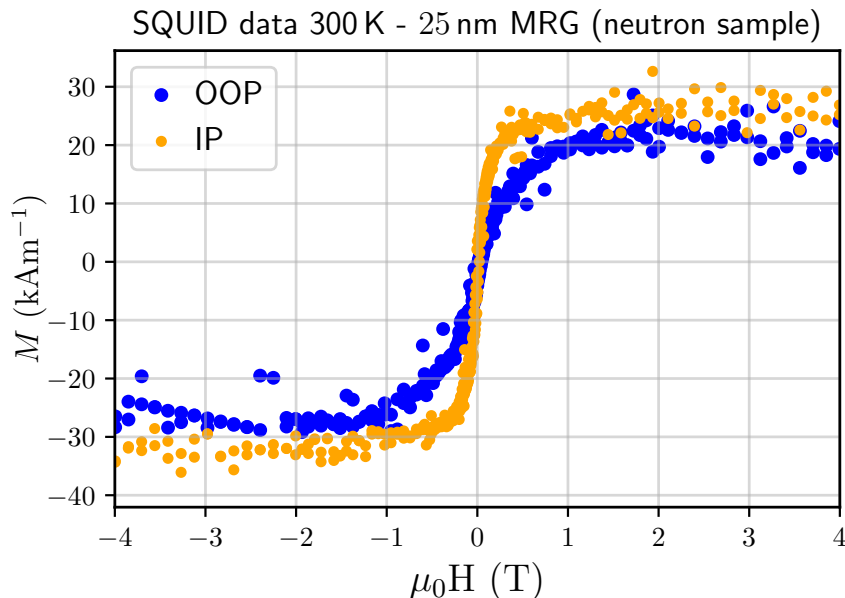
Figure 3.46: SQUID magnetisation data measured at room temperature on the same $T_{dep} = 225\,°C$ MRG sample that neutron diffraction was performed on. The moment is very small and almost perfectly compensated at remanence with no hysteresis loop evident.

the neutron sample does appear to be near zero, moreover, the saturation (maximum at high-field) moment is very small, less than $m_z = 0.2 \cdot 10^{-7}\,\mathrm{A\,m^2}$. This is also true for the different $T_{dep} = 225\,°C$ MRG sample SQUID data shown in Figure 3.41(b), although that sample does possibly show some hysteresis (it is hard to definitely say for such low net moments). This macroscopic unit can be converted to one which is more comparable to the neutron results. The approximate number of Mn atoms in the sample is simply the sample volume divided by the unit cell volume multiplied by the number of Mn atoms in the unit cell. From there it is trivial to convert the magnetic moment to $m_z \approx 0.1\,\mu_\mathrm{B}\,\mathrm{Mn^{-1}}$. This is indeed in line with the net moment in the neutron results. The neutron (large IP moments) and SQUID (very small net moment) results can together be explained by a small canting angle between the sublattices with the resulting net moment oriented roughly perpendicular to the two sublattice moments. An external magnetic field, as used SQUID or magnetotransport measurements, acts on this net moment (rather ineffectively

due to the size), while radiation or particle based probes like neutron diffraction resolve the comparatively large individual moments. Additional neutron diffraction results with

$$|\vec{m}_{net}| \approx 0.2\,\mu_B$$

$$|\vec{m}_{4a}| \approx 2.55\,\mu_B \qquad |\vec{m}_{4c}| \approx 2.77\,\mu_B$$
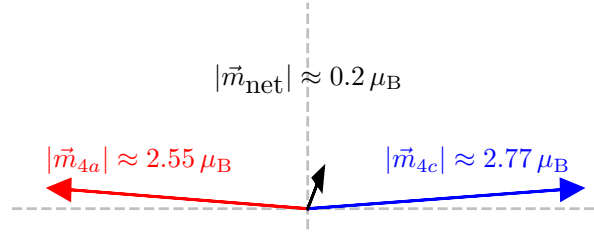
Figure 3.47: Possible spin configuration for the two MRG sublattices. A very small canting angle results in a **net** moment which is roughly perpendicular to the individual atomic moments.

finite applied fields, on high-temperature and medium-temperature MRG would be useful in confirming and reinforcing results, however the measurements were already difficult with the small sample volume available and gaining more neutron beam time would be difficult.

3.3.8 Other Heuslers: Co-Ti-Si

3.3.8.1 Motivation

Co_2TiSi is one of many Heusler alloys predicted to be half-metallic at the Fermi level [57]. Heusler alloys are versatile materials with the chemical formula X_2YZ where X and Y are transition metal elements and Z is a p-block element. The four constituents sit on four fcc sublattices. The inclusion of often magnetic d-block elements in combination with the others often results in many unique and interesting magnetic and electronic properties. A half-metal is a material with density of states (DOS) from only one spin at the Fermi level [58], such that the low-bias conductance is completely spin-polarised. Half-metals have a plethora of potential applications in next-generation devices [42]. Co_2TiSi has been grown in bulk previously [59] but rarely in thin film form.

3.3.8.2 XRD

Co-Ti-Si was deposited in the appropriate ratio on an MgO substrate by sputtering. MgO, a common substrate for Heusler alloy materials, has a lattice parameter of $a_{MgO} = 4.211\,\text{Å}$. If the corner-to-corner distance is considered, which is the distance likely to match up

with the side of the Heusler alloy unit cell, we have $a_{MgO} = 5.956\,\text{Å}$. Co$_2$TiSi has a lattice parameter of $a_{Co2TiSi} = 5.72\,\text{Å}$, resulting in a mismatch of $4\,\%$. This is a substantial number but not so large as to preclude epitaxial growth of thin films, in fact non-negligible strain is often desired to induce tetragonality in the sample structure, allowing access to effects otherwise suppressed by the cubic symmetry. The Co$_2$TiSi unit cell and the relation to the substrate is shown in Figure 3.48.
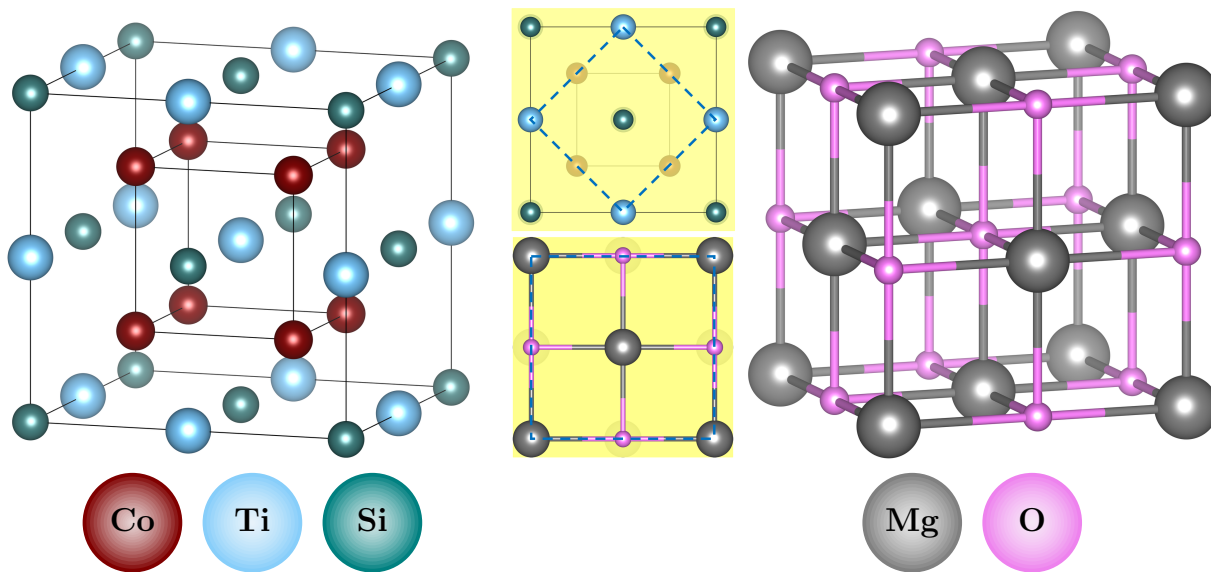
Figure 3.48: Isometric and top-down views of the Co$_2$TiSi and MgO unit cells, showing epitaxial relation.

The expected XRD spectrum for a vertical $\theta/2\theta$ scan, for substrate and sample oriented with their c-axes OOP, would be as in Figure 3.49, using the Bragg law to get the positions from the lattice parameter and assuming arbitrary broadening. The relative intensities for each material is calculated using VESTA and the relative intensities between the two materials is estimated based on their thickness and crystalline quality.

When the XRD spectrum was measured however, there were far more reflections than expected present in the scan. The measured data is shown in Figure 3.50:

If we assume the peaks are $(00L)$ reflections with L even, we can calculate the OOP lattice parameter as $c = 11.23\,\text{Å}$, approximately double what was expected. Looking at the literature, the stable compound Co$_{16}$Ti$_6$Si$_7$ matches the observed lattice parameter and has been observed by authors trying to obtain Co$_2$TiSi [60]. The structure and epitaxial relation for Co$_{16}$Ti$_6$Si$_7$ on MgO is shown in Figure 3.51:
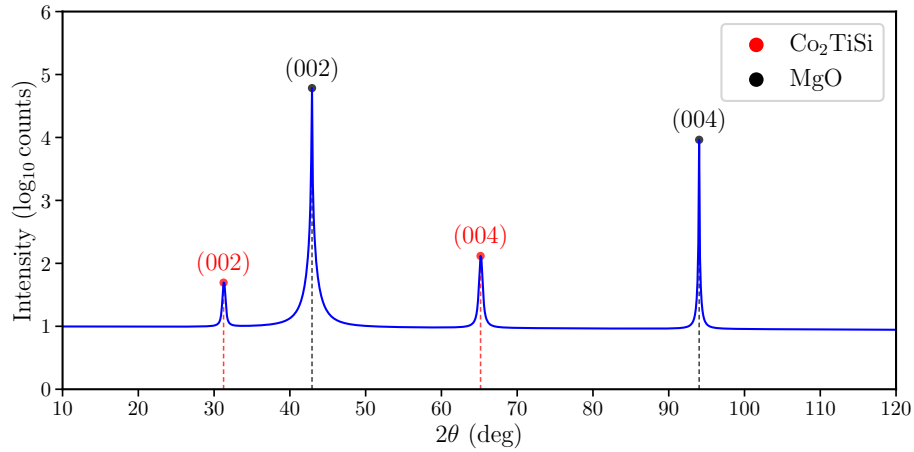
Figure 3.49: Predicted $\theta/2\theta$ scan for single-crystalline, (001) oriented Co_2TiSi/MgO.
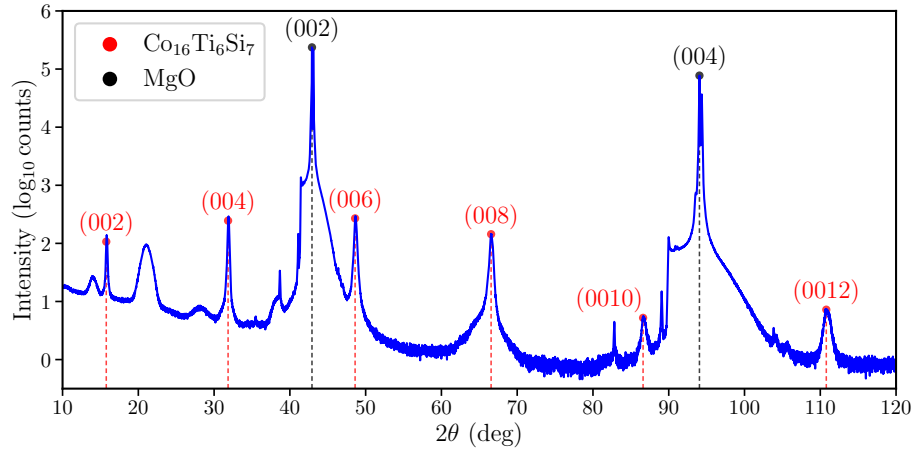
Figure 3.50: An XRD scan of a Co-Ti-Si thin film epitaxially grown on an MgO substrate. The large number of peaks within the 2θ range implies a large unit cell. The peaks shown in red are were calculated from Equation 3.1 using $d = 11.23/L$. This spectrum was recorded on a different diffractometer than the aforementioned Bruker, in the Bragg-Brentano geometry, resulting in higher SNR, but poorer resolution and more instrumental artefacts: the "cliff edges" to the left of the substrate peaks in the spectrum are due to the adaptive filter of the detector, above a certain intensity threshold, the detector switches to a strong filter to protect itself.

The excellent agreement between the measured and predicted peak positions confirm that it is $Co_{16}Ti_6Si_7$ which was grown. Assuming the epitaxial relation shown in Figure 3.51 is the correct one, the lattice mismatch is 5.7%, which is again quite large. It is more likely in this case that there are some dislocations present to facilitate high-quality epitaxial growth. Unfortunately, $Co_{16}Ti_6Si_7$ does not have any of the interesting electrical or magnetic properties that Co_2TiSi is predicted to exhibit and this material, though it yields an interesting XRD pattern, was not characterised further. Why was the
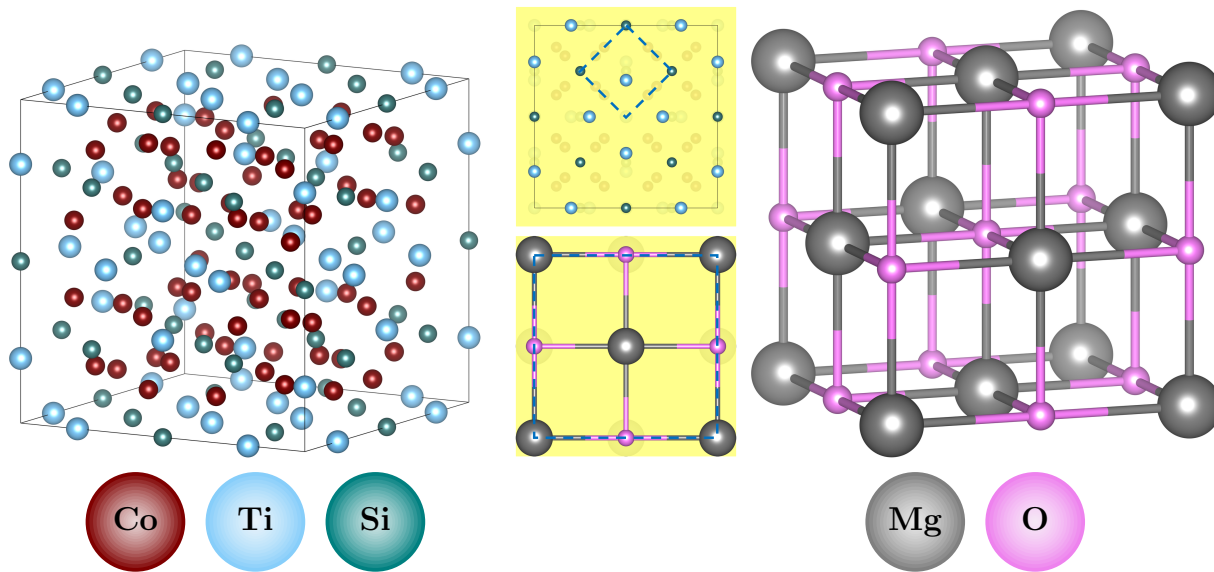
Figure 3.51: Isometric and top-down views of the $Co_{16}Ti_6Si_7$ and MgO unit cells, showing assumed epitaxial relation.

wrong material obtained in this case? Well $Co_{16}Ti_6Si_7$ corresponds to an atomic ratio of $Co_2Ti_{0.75}Si_{0.875}$ as opposed to Co_2TiSi, so there is an excess of Co present. Growing with a lower flux of Co atoms, if possible, could help, in addition to growing more slowly.

This is a prime example of the usefulness of a simple $\theta/2\theta$ scan in material identification and measurement of the OOP lattice parameter.

3.4 Case Studies: MgO/Mn$_4$N

3.4.1 Motivation

Generally when magnetic order is discussed, we think of the atomic spins as collinear i.e. parallel or anti-parallel for ferro or antiferro/ferrimagnetism, such as in the Ising model. However, **frustrated** magnetism arises when the atomic layout is such that the energy minimum no longer has adjacent spins exactly collinear. This is often a result of the different strengths and signs of exchange interactions between identical elements at different distances, in particular elements like Mn whose exchange interaction is especially sensitive to distance. In a unit cell with numerous crystal sites of different symmetries, having more than one of these sites occupied by Mn atoms will result in some magnetic frustration due to the different pairwise separations of the atoms, non-collinear magnetic orientation with, for example, triangular symmetry of the spins and unusual anomalous effects in electronic transport properties due to the Hall (deflection of electric current due to the materials magnetism, both intrinsically through the band structure and via magnetic scattering) and/or Nernst (Similar to Hall but the origin of the electric current is thermal gradients) effects [61]. One material that exhibits frustrated triangular ferrimagnetism in the bulk form is Mn$_4$N[62]. The material was grown in thin film form by our group, and the magnetic effects observed did not match up with the bulk magnetic structure as observed, as discussed by Coey et al. [63]: e.g. the magnetic moment was significantly smaller in the films compared to the bulk. So began an extensive characterisation process to elucidate the source of the discrepancy, as detailed by Yangkun He et al. [61]. My role in the project was primarily to perform X-ray diffraction, specifically RSMs, to determine the lattice parameters and epitaxial relationship of the grown films with their substrates. The investigation of this material was part of the over-arching goal of developing high-frequency magnetisation dynamics devices. The complex non-collinear spin structure expected could be one more possible route towards that goal.

3.4.2 RSM

Bulk Mn_4N has a cubic lattice with a N atom at the centre of an fcc lattice populated by Mn, the space group is $Pm\bar{3}m$ (#221). The lattice parameter from literature is $3.86\,\text{Å}$ [63]. The substrate used was MgO and XRR/XRD measurements indicated good quality crystalline growth of the Mn_4N layer, with the diffraction peaks exhibiting Laue oscillations. This was somewhat unexpected due to the large mismatch in lattice parameters (the lowest mismatch was for cube-on-cube growth: $8.3\,\%$). RSMs were very much desired to explain the observed result. The accessible reflections of Mn_4N and MgO, calculated using the Python script described in Figure 3.18, are shown below in Figure 3.52: We can
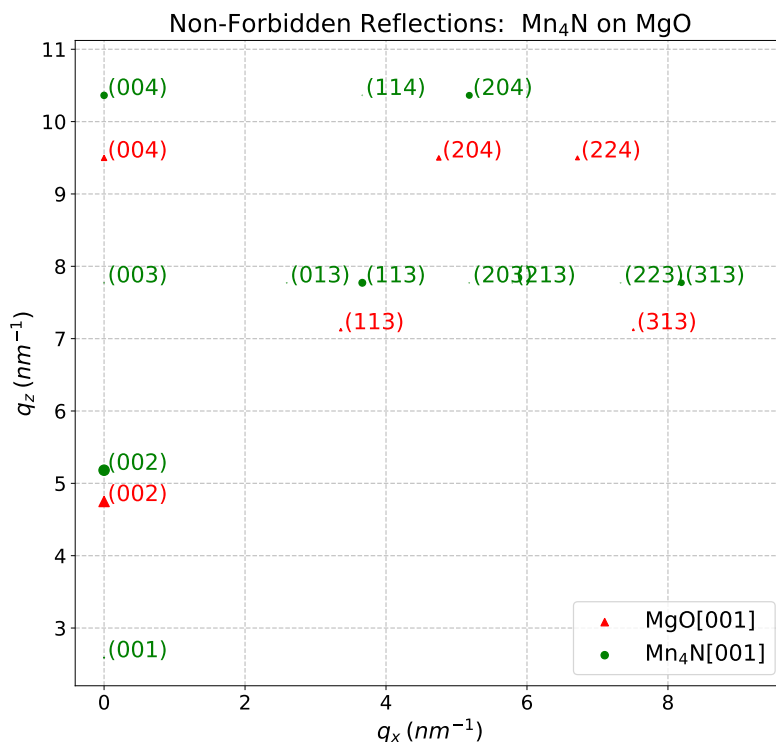
Figure 3.52: Accessible, non-forbidden reflections in reciprocal space, rotated into the scattering plane, for Mn_4N on MgO.

see that the (113) and (204) reflections have the highest intensity for Mn_4N, as is often the case for fcc-type lattices. If the growth was cube-on-cube such that the azimuth of the film and substrate were coincident, the (113) reflection of the substrate is quite close to that of the sample and could be used for alignment (possibly both could be encompassed in one scan). If the epitaxial relation was $45°$ rotated, then the Mn_4N (204) peak with alignment to the MgO (224) would be feasible. I first aligned to the MgO (113) reflection and

performed a 2θ vs q_z RSM scan with a range containing both substrate and sample reflections. This (educated) guess was correct with both sample and substrate peaks appearing in the scan, shown in Figure 3.54, confirming that the growth was cube-on-cube (Mn$_4$N (113) ∥ MgO (113)), as indicated in Figure 3.53. The IP lattice parameter $a = 3.874\,\text{Å}$,
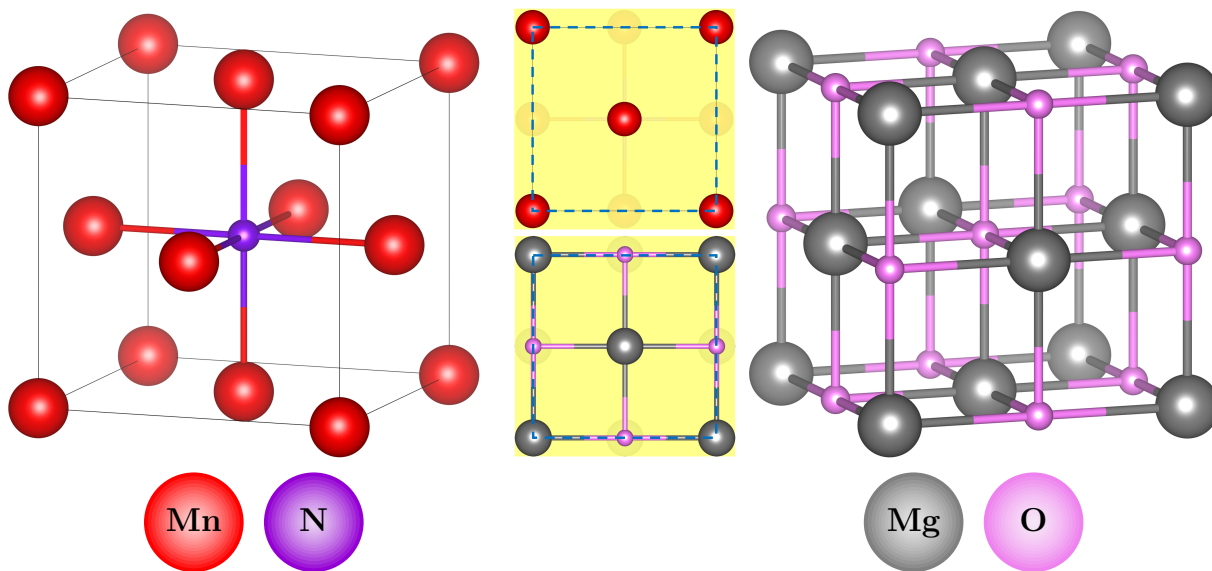
Figure 3.53: Isometric and top-down views of the Mn$_4$N and MgO unit cells, showing epitaxial relation.

close to the bulk value, means there is a mismatch of $8.0\,\%$ with the substrate. This is far larger than would typically be possible with elastic strain, but the small width of the reflection implies a relatively small amount of dislocations and a similarly small spread in lattice parameters. XRR measurements suggested that there might be an interfacial MnO layer between the MgO and Mn$_4$N that might explain the epitaxy. MnO has a cubic structure identical to MgO with a lattice parameter $a = 4.263\,\text{Å}$ [64]. This is an even larger mismatch, but the ratio of $a_{MnO}/a_{Mn_4N} = 1.1$ might indicate one dislocation per 11 atoms. Alternatively, all the strain could be localised in the MnO layer in some fashion and therefore not be evident in the Mn$_4$N diffraction pattern. To nail down the epitaxial relationship, TEM or a similar atomic-scale spatial measurement would ideally be performed.

The thin film form exhibited $-0.9\,\%$ tetragonal strain resulting from the tensile IP strain exerted by the substrate. This breaks the cubic symmetry and leaves us with the space group $P4/mmm$ (#123). In the cubic structure, the spins of the Mn sublattice on
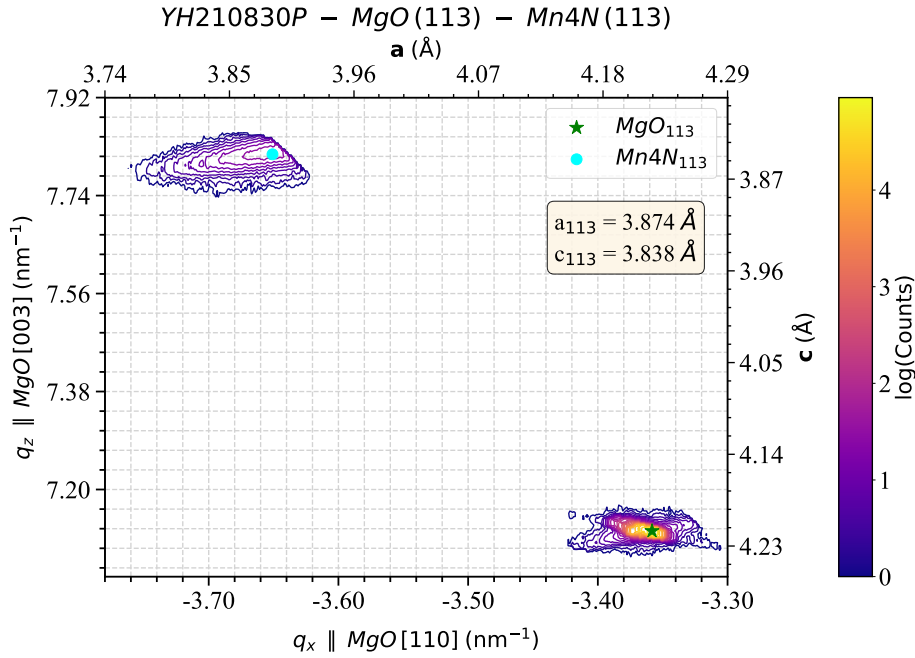
Figure 3.54: Reciprocal space map of Mn_4N/MgO, aligned to the MgO (113) peak. The Mn_4N (113) peak was centred at $\vec{q} = (3.651, 7.817)\,\text{nm}^{-1}$, yielding lattice parameters $a = 3.874\,\text{Å}$ and $c = 3.838\,\text{Å}$, with a ratio $c/a = 0.99$. The negative numbers on the x-axis are simply due to the preference for measuring in grazing incidence and the definitions of the Cartesian axes, as in Figure 3.17.

the corners of the unit cell (Wyckoff $1a$ site) point along the (111) direction while the Mn spins on the faces of the unit cell (Wyckoff $3c$ site) point towards the corners (so the sublattice average moment is also along (111)) in an example of triangular frustration due to distance-dependent exchange [62, 65]. In thin film form on an MgO (001) substrate, the tetragonal distortion is credited with changing the overall magnetic easy axis from the (111) direction to (001). An additional magnetic sublattice is needed as the Mn on the top faces no longer cooperate with the Mn on the side faces of the unit cell while those on the corners swivel to point OOP [61, Figure 2]. The exact magnetic structure has not been rigorously experimentally verified, but examination of the distance-dependence of Mn exchange interactions from DFT [61] and comparison with bulk, doped Mn_4N spin configurations [66] suggests that this is the case. The degree of tetragonal distortion is likely to correlate to the strength of the easy-axis anisotropy and the resulting magnetic properties, making RSM a very powerful tool to help with investigations.

3.5 Summary

In this chapter on diffraction, or perhaps more aptly "crystal structure investigation", I first introduced the basic theory of scattering for photons and neutrons. This involves the diffraction and coherence conditions fundamental to the wave mechanics, and the underlying mechanism of the scattering from electromagnetic or strong force interactions. I discussed some of the important experimental considerations, namely the everyday instrumental corrections that must be taken into account for two common types of diffractometer, in order to relate the observed diffraction data to the underlying crystal structure.

I discussed in detail many of the techniques I used for crystal structure investigation over the past few years. The list is of course not exhaustive but contains many of the most useful and commonly performed measurements, from simple one-dimensional scans to more custom procedures which combine various techniques in the literature and apply them in new ways. In many cases, the thin single-crystal films which I have worked on are not the original intended subject of investigation for techniques in literature and represent a new demonstration of the wide applicability. In particular, the semi-automated procedure for performing measurements to enable Rietveld refinement on single-crystal films as thin as $t = 10\,\text{nm}$ is quite remarkable given the usual large-volume powder samples that are used. Of some note are the various Python "helper" functions which I wrote and have published for use on my GitHub [26]. One of my goals in doing this was to help researchers new to the field to understand reciprocal space better rather than simply going through the motions of a strict operating procedure without properly understanding the techniques. While this can still yield results, it stifles discovery and technological advancement as young researchers can have incorrect assumptions about how or why some techniques work.

Demonstrations of the techniques in action and data acquired are given in the form of case studies, with most amount of work done, and the largest set of data, for Mn_2Ru_xGa thin films. This material has been a focus of the Magnetism and Spin-Electronics Group here in Trinity for a number of years, with many publications and a thesis already in the literature [45, 53, 43, 46]. With the construction of the **Trifolium Dubium** deposition and characterisation national access facility in 2019, funded by the €3.2 M SFI grant 15/RI/3218, new capabilities were unlocked for thin film deposition, in particular lower-

pressure vacuum and high sample throughput allowed for higher quality crystal structures than ever before. The timing was not ideal with the COVID pandemic beginning shortly afterwards... but the system was operational for the majority of 2020 and 2021, and much of my characterisation work was on samples deposited during this period. I focused here on the effect of substrate temperature on the quality of highly-epitaxial thin films of MRG, a publication is currently in preparation regarding this work [54]. A brief mention of $Co_{16}Ti_6Si_7$ was given as X-ray characterisation proved very useful in determining the structure and the data was very stark, therefore constituting a good example. The reciprocal space mapping of Mn_4N was discussed in some detail because the data proved invaluable in determining the epitaxial relationship of the sample with the substrate. The growth was highly epitaxial despite the large mismatch, possibly indicative of a seed layer forming at the interface, which is not implausible considering the affinity of Mn for O in O-containing substrates. This data was also included in a publication [61].

References

[1] A. André, *Dynamical Theory of X–ray Diffraction.* Oxford University Press, 2001. [Cited on page 99]

[2] M. Birkholz, *Thin film analysis by X–ray scattering.* John Wiley & Sons, 2006. [Cited on page 100]

[3] W. L. Bragg, "The structure of some crystals as indicated by their diffraction of X–rays," *Proceedings of the Royal Society of London. Series A, Containing papers of a mathematical and physical character*, vol. 89, no. 610, pp. 248–277, 1913. [Cited on page 100]

[4] C. Kittel and P. McEuen, *Introduction to solid state physics.* John Wiley & Sons, 2018. [Cited on pages xvii, 101, and 104]

[5] E. N. Maslen, A. G. Fox, and M. A. O'Keefe, "X–ray scattering," in *International Tables for Crystallogrphy* (E. Prince, ed.), vol. C, p. 555, Springer Science & Business Media, 2004. [Cited on page 102]

[6] J. Rodríguez-Carvajal, "FullProf," *CEA/Saclay, France*, vol. 1045, pp. 132–146, 2001. [Cited on pages 104, 135, 159, and 167]

[7] K. Momma and F. Izumi, "VESTA 3 for three–dimensional visualization of crystal, volumetric and morphology data," *Journal of applied crystallography*, vol. 44, no. 6, pp. 1272–1276, 2011. [Cited on page 104]

[8] E. Prince, *International Tables for Crystallography, Volume C: mathematical, physical and chemical tables.* Springer Science & Business Media, 2004. [Cited on pages 107, 116, 117, 145, and 166]

[9] D.-M. Smilgies, "Geometry–independent intensity correction factors for grazing–incidence diffraction," *Review of scientific instruments*, vol. 73, no. 4, pp. 1706–1710, 2002. [Cited on page 107]

[10] G. McIntyre and R. Stansfield, "A general lorentz correction for single–crystal diffractometers," *Acta Crystallographica Section A: Foundations of Crystallography*, vol. 44, no. 3, pp. 257–262, 1988. [Cited on page 107]

[11] H. A. Kramers, "XCIII. on the theory of X–ray absorption and of the continuous X–ray spectrum," *The London, Edinburgh, and Dublin Philosophical Magazine and Journal of Science*, vol. 46, no. 275, pp. 836–871, 1923. [Cited on pages xvii and 109]

[12] G. Hölzer, M. Fritsch, M. Deutsch, J. Härtwig, and E. Förster, "$K_{\alpha_{1,2}}$ and $K_{\beta_{1,3}}$ X–ray emission lines of the 3d transition metals," *Physical Review A*, vol. 56, no. 6, p. 4554, 1997. [Cited on pages xvii and 109]

[13] T. Konya *et al.*, "X–ray thin–film measurement techniques," *The Rigaku Journal*, vol. 25, no. 2, pp. 1–8, 2009. [Cited on page 109]

[14] M. Schuster and H. Gobel, "Parallel–beam coupling into channel–cut monochromators using curved graded multilayers," *Journal of Physics D: Applied Physics*, vol. 28, no. 4A, p. A270, 1995. [Cited on page 109]

[15] U. Pietsch, V. Holy, and T. Baumbach, *High–resolution X–ray scattering: from thin films to lateral nanostructures.* Springer Science & Business Media, 2004. [Cited on page 110]

[16] C. Michaelsen, P. Ricardo, D. Anders, M. Schuster, J. Schilling, and H. Göbel, "Improved graded multilayer mirrors for XRD applications," *Adv. X–ray Anal*, vol. 42, pp. 308–320, 2000. [Cited on page 110]

[17] M. Birkholz, *Thin film analysis by X–ray scattering.* John Wiley & Sons, 2006. [Cited on pages 112, 113, 114, and 125]

[18] F. T. L. Muniz, M. R. Miranda, C. Morilla dos Santos, and J. M. Sasaki, "The Scherrer equation and the dynamical theory of X–ray diffraction," *Acta Crystallographica Section A: Foundations and Advances*, vol. 72, no. 3, pp. 385–390, 2016. [Cited on page 113]

[19] J. I. Langford and A. Wilson, "Scherrer after sixty years: a survey and some new results in the determination of crystallite size," *Journal of applied crystallography*, vol. 11, no. 2, pp. 102–113, 1978. [Cited on page 113]

[20] W. C. Hinds and Y. Zhu, *Aerosol technology: properties, behavior, and measurement of airborne particles.* John Wiley & Sons, 2022. [Cited on page 113]

[21] A. Stokes and A. Wilson, "The diffraction of X–rays by distorted crystal aggregates–I," *Proceedings of the physical society*, vol. 56, no. 3, p. 174, 1944. [Cited on page 114]

[22] J. Baruchel, J. Hodeau, M. Lehmann, J. Regnard, and C. Schlenker, eds., *Neutron and Synchrotron Radiation for Condensed Matter Studies*. Springer–Verlag, 1993. [Cited on page 115]

[23] T. Chatterji, *Neutron scattering from magnetic materials*. Elsevier, 2005. [Cited on pages 115 and 117]

[24] J. Dawidowski, J. R. Granada, J. R. Santisteban, F. Cantargi, and L. A. R. Palomino, "Neutron scattering lengths and cross sections," in *Experimental Methods in the Physical Sciences*, vol. 44, pp. 471–528, Elsevier, 2013. [Cited on page 116]

[25] I. A. Zaliznyak and S.-H. Lee, "Magnetic neutron scattering," in *Spin*, vol. 5, 2005. [Cited on pages 116 and 117]

[26] J. O'Brien, "Diffraction repository," 2023. `https://github.com/eljackobrien/Diffraction/tree/ac229afd8886e33a7c6c7fae8cd78ac03329e667`, Permanent URL: 2023–06–08. [Cited on pages 119, 132, 145, and 181]

[27] W. Soller, "A new precision X–ray spectrometer," *Physical Review*, vol. 24, no. 2, p. 158, 1924. [Cited on page 121]

[28] P. S. Foundation, "Python language reference." [Cited on page 124]

[29] C. R. Harris, K. J. Millman, S. J. Van Der Walt, R. Gommers, P. Virtanen, D. Cournapeau, E. Wieser, J. Taylor, S. Berg, N. J. Smith, *et al.*, "Array programming with NumPy," *Nature*, vol. 585, no. 7825, pp. 357–362, 2020. [Cited on page 124]

[30] J. J. Olivero and R. Longbothum, "Empirical fits to the Voigt line width: a brief review," *Journal of Quantitative Spectroscopy and Radiative Transfer*, vol. 17, no. 2, pp. 233–236, 1977. [Cited on page 125]

[31] M. Ahtee, L. Unonius, M. Nurmela, and P. Suortti, "A Voigtian as profile shape function in Rietveld refinement," *Journal of applied crystallography*, vol. 17, no. 5, pp. 352–357, 1984. [Cited on page 125]

[32] T. H. De Keijser, J. Langford, E. J. Mittemeijer, and A. Vogels, "Use of the Voigt function in a single–line method for the analysis of X–ray diffraction line broadening," *Journal of Applied Crystallography*, vol. 15, no. 3, pp. 308–314, 1982. [Cited on page 126]

[33] A. Boulle, O. Masson, R. Guinebretière, and A. Dauger, "A new method for the determination of strain profiles in epitaxic thin films using X–ray diffraction," *Journal of applied crystallography*, vol. 36, no. 6, pp. 1424–1431, 2003. [Cited on pages 127 and 128]

[34] I. Schoenberg, "Cardinal interpolation and spline functions," *Journal of Approximation theory*, vol. 2, no. 2, pp. 167–206, 1969. [Cited on page 127]

[35] M. Unser, A. Aldroubi, and M. Eden, "B–spline signal processing. I. theory," *IEEE transactions on signal processing*, vol. 41, no. 2, pp. 821–833, 1993. [Cited on page 127]

[36] O. Masson, A. Boulle, R. Guinebretière, A. Lecomte, and A. Dauger, "On the use of one–dimensional position sensitive detector for X–ray diffraction reciprocal space mapping: data quality and limitations," *Review of scientific instruments*, vol. 76, no. 6, p. 063912, 2005. [Cited on page 130]

[37] A. Boulle, O. Masson, R. Guinebretière, A. Lecomte, and A. Dauger, "A high–resolution X–ray diffractometer for the study of imperfect materials," *Journal of applied crystallography*, vol. 35, no. 5, pp. 606–614, 2002. [Cited on page 131]

[38] H. M. Rietveld, "The Rietveld method: a retrospection," 2010. [Cited on pages 135 and 159]

[39] H. Rietveld, "Line profiles of neutron powder–diffraction peaks for structure refinement," *Acta Crystallographica*, vol. 22, no. 1, pp. 151–152, 1967. [Cited on page 135]

[40] H. M. Rietveld, "A profile refinement method for nuclear and magnetic structures," *Journal of applied Crystallography*, vol. 2, no. 2, pp. 65–71, 1969. [Cited on page 135]

[41] W. R. Busing and H. A. Levy, "Angle calculations for 3–and 4–circle X–ray and neutron diffractometers," *Acta Crystallographica*, vol. 22, no. 4, pp. 457–464, 1967. [Cited on pages 136 and 137]

[42] W. E. Pickett and J. S. Moodera, "Half metallic magnets," *Physics Today*, vol. 54, no. 5, pp. 39–45, 2001. [Cited on pages 139 and 173]

[43] H. Kurt, K. Rode, P. Stamenov, M. Venkatesan, Y.-C. Lau, E. Fonda, and J. M. D. Coey, "Cubic Mn_2Ga thin films: crossing the spin gap with ruthenium," *Physical review letters*, vol. 112, no. 2, p. 027201, 2014. [Cited on pages 20, 140, and 181]

[44] R. Cardias, A. Szilva, A. Bergman, I. D. Marco, M. Katsnelson, A. Lichtenstein, L. Nordström, A. Klautau, O. Eriksson, and Y. O. Kvashnin, "The Bethe–Slater curve revisited;

new insights from electronic structure theory," *Scientific reports*, vol. 7, no. 1, p. 4058, 2017. [Cited on page 140]

[45] K. Siewierska, G. Atcheson, A. Jha, R. Smith, G. Dennehy, S. Lenne, P. Stamenov, J. M. D. Coey, and K. Rode, "Fermi level engineering of Mn_2Ru_xGa thin films," in *2018 IEEE 18th International Conference on Nanotechnology (IEEE–NANO)*, pp. 1–2, IEEE, 2018. [Cited on pages 140 and 181]

[46] K. E. Siewierska, *Development and Characterisation of a Zero–Moment Half–Metal.* PhD thesis, Trinity College Dublin, School of Physics, Magnetism and Spin Electronics Group, 2021. [Cited on pages 142 and 181]

[47] S. J. Pennycook and P. D. Nellist, *Scanning transmission electron microscopy: imaging and analysis.* Springer Science & Business Media, 2011. [Cited on page 153]

[48] P. Wadley, A. Crespi, J. Gazquez, M. Roldan, P. Garcia, V. Novak, R. Campion, T. Jungwirth, C. Rinaldi, X. Marti, *et al.*, "Solving and refining novel thin film phases using Cu X–ray radiation: the epitaxy–induced CuMnAs tetragonal phase," *arXiv preprint arXiv:1301.5227*, 2013. [Cited on page 158]

[49] D. C. Palmer, "Visualization and analysis of crystal structures using CrystalMaker software," *Zeitschrift für Kristallographie–Crystalline Materials*, vol. 230, no. 9–10, pp. 559–572, 2015. [Cited on page 159]

[50] Commission on Crystallographic Computing, "Software," 2021. `https://www.iucr.org/resources/commissions/computing/software`, Accessed: 2024–02–09. [Cited on page 159]

[51] Commission on Crystallographic Computing, "Software museum," 2021. `https://www.iucr.org/resources/commissions/computing/software-museum`, Accessed: 2024–02–09. [Cited on page 159]

[52] M. Žic, K. Rode, N. Thiyagarajah, Y.-C. Lau, D. Betto, J. M. D. Coey, S. Sanvito, K. J. O'Shea, C. A. Ferguson, D. A. MacLaren, *et al.*, "Designing a fully compensated half–metallic ferrimagnet," *Physical Review B*, vol. 93, no. 14, p. 140202, 2016. [Cited on pages 69 and 161]

[53] K. Siewierska, G. Atcheson, A. Jha, K. Esien, R. Smith, S. Lenne, N. Teichert, J. O'Brien, J. M. D. Coey, P. Stamenov, *et al.*, "Magnetic order and magnetotransport in half–metallic

ferrimagnetic Mn_yRu_xGa thin films," *Physical Review B*, vol. 104, no. 6, p. 064414, 2021. [Cited on pages 49, 55, 165, 169, and 181]

[54] J. O'Brien, A. Naden, K. Siewierska, B. Ouladdiaf, J. M. D. Coey, K. Rode, P. Stamenov, and G. Atcheson, "Exchange–driven anomalous magnetism in epitaxial Mn_2Ru_xGa.". [Cited on pages 165, 169, and 182]

[55] K. E. Siewierska, K. Beauvois, S. Felton, S. Kovalev, and B. Ouladdiaf, "Crystal and magnetic structure of compensated half metallic ferrimagnetic thin films," 2021. doi:10.5291/ILL-DATA.5-54-328. [Cited on page 166]

[56] R. Fagaly, "Superconducting quantum interference device instruments and applications," *Review of scientific instruments*, vol. 77, no. 10, 2006. [Cited on page 172]

[57] H. C. Kandpal, G. H. Fecher, and C. Felser, "Calculated electronic and magnetic properties of the half–metallic, transition metal based Heusler compounds," *Journal of Physics D: Applied Physics*, vol. 40, no. 6, p. 1507, 2007. [Cited on page 173]

[58] R. De Groot, F. Mueller, P. v. van Engen, and K. Buschow, "New class of materials: half–metallic ferromagnets," *Physical review letters*, vol. 50, no. 25, p. 2024, 1983. [Cited on page 173]

[59] J. Barth, G. H. Fecher, B. Balke, T. Graf, A. Shkabko, A. Weidenkaff, P. Klaer, M. Kallmayer, H.-J. Elmers, H. Yoshikawa, *et al.*, "Anomalous transport properties of the half–metallic ferromagnets Co_2TiSi, Co_2TiGe and Co_2TiSn," *Philosophical Transactions of the Royal Society A: Mathematical, Physical and Engineering Sciences*, vol. 369, no. 1951, pp. 3588–3601, 2011. [Cited on page 173]

[60] P. Liu, B. Li, Z. Zhou, C. Lin, and S. Zou, "Growth of epitaxial $CoSi_2$ film on Si (100) substrate induced by an interfacial Ti layer," *Materials Letters*, vol. 17, no. 6, pp. 383–387, 1993. [Cited on page 174]

[61] Y. He, S. Lenne, Z. Gercsi, G. Atcheson, J. O'Brien, D. Fruchart, K. Rode, and J. M. D. Coey, "Noncollinear ferrimagnetism and anomalous Hall effects in Mn_4N thin films," *Physical Review B*, vol. 106, no. 6, p. L060409, 2022. [Cited on pages 177, 180, and 182]

[62] D. Fruchart, D. Givord, P. Convert, P. l'Heritier, and J. Senateur, "The non–collinear component in the magnetic structure of Mn_4N," *Journal of Physics F: Metal Physics*, vol. 9, no. 12, p. 2431, 1979. [Cited on pages 177 and 180]

[63] J. M. D. Coey, D. Givord, and D. Fruchart, "Metallic nitride and carbide perovskites: history and prospects," *ECS Journal of Solid State Science and Technology*, vol. 11, no. 5, p. 055002, 2022. [Cited on pages 177 and 178]

[64] S. Sasaki, K. Fujino, and Y. Takéuchi, "X–ray determination of electron–density distributions in oxides, MgO, MnO, CoO, and NiO, and atomic scattering factors of their constituent atoms," *Proceedings of the Japan Academy, Series B*, vol. 55, no. 2, pp. 43–48, 1979. [Cited on page 179]

[65] M. Uhl, S. F. Matar, and P. Mohn, "Ab–initio analysis of magnetic properties in non-collinearly ordered Mn_4N," *Physical Review B*, vol. 55, no. 5, p. 2995, 1997. [Cited on page 180]

[66] R. Zhang, Y. He, D. Fruchart, J. M. D. Coey, and Z. Gercsi, "Rare–earth–free noncollinear metallic ferrimagnets $Mn_{4-x}Z_xN$ with compensation at room temperature," *Acta Materialia*, vol. 234, p. 118021, 2022. [Cited on page 180]

Chapter 4

Backscatter Mössbauer Spectroscopy

4.1 Introduction

The performance of magnetic materials depends on their intrinsic properties, including anisotropy, coercivity and the magnitude of their magnetic moment. These properties depend in turn on the interatomic interactions within the material and thus the atomic composition and crystal structure. Mössbauer spectroscopy (MöS) is a potent tool to probe these relevant properties, especially of Fe-containing samples [1]. This technique utilises the resonant absorption of γ-ray photons, emitted by a source[1] following a radioactive decay, to probe the energy levels of ^{57}Fe nuclei with a startling relative sensitivity approaching 10^{12}. We have developed a custom, highly-effective setup for this technique [3]: The simultaneous detection of the characteristic X-rays, γ-rays and non-resonant photons, with a single broadband detector, allows for optimal post-acquisition discrimination discrimination and background correction. In this chapter the apparatus and the steps in the data analysis will be described in detail, after some background theory is introduced. Four distinct examples of the technique in action are described to show its effectiveness and wide applicability, offering far more accessibility to this type of material probe than previously available.

---

[1]A bandwidth approaching that of the nuclear emission has been achieved at a synchrotron facility, by monochromating the very bright but broadband photon beam using pure-nuclear Bragg diffraction from an enriched ^{57}FeBO$_3$ crystal heated to its Néel temperature T_N [2].

4.2 Theory

Rudolph Mössbauer discovered in 1958 [4] that excited nuclei in crystals can emit a γ-ray with a finite probability of exciting no phonons. In this case, the recoil momentum is imparted to the whole lattice, resulting in a negligible recoil energy due to the enormous mass of the lattice relative to a single atom. To illustrate the importance of this phenomena to the measurement technique, consider the first transition of ^{57}Fe. For a free 57 a.u. ^{57}Fe atom emitting a 14.4 keV photon, the atom must recoil to conserve momentum with energy $E_R = \frac{p^2}{2m} = \frac{E_\gamma^2}{2mc^2} = 2\,\mathrm{meV}$. If say, a $100\,\mathrm{nm}^3$ grain of Fe, containing roughly $8.5 \cdot 10^7$ atoms, were to do the same and recoil as one body, the energy would be divided by the number of atoms, so $E_R = 0.02\,\mathrm{neV}$. Considering linewidths of nuclear photons are typically of the order 1 neV, it is clear that the transitions need have some phonon-free fraction in order to be useful.

4.2.1 ^{57}Fe Nuclear Details

A number of isotopes have suitable nuclear energy level transitions which exhibit the Mössbauer effect [1], but only a few are practically useful; these include ^{119}Sn and ^{197}Au but most notably ^{57}Fe. The details of the energy levels of ^{57}Fe can be obtained from the nuclear data sheets via the online database of the International Atomic Energy Agency [5]. The table of γ-ray emissions is reproduced in Table 4.1. The first nuclear transition of ^{57}Fe is a $E_\gamma = 14.4\,\mathrm{keV}$, $I = \frac{3}{2} \to \frac{1}{2}$ decay (Figure 4.1), that has a significant phonon-free fraction thanks to its low energy. The 98.2 ns lifetime gives a natural linewidth of $\Gamma \approx 6.7\,\mathrm{neV}$ from Heisenberg uncertainty, so the theoretical relative sensitivity is of order $E_\gamma/\Gamma \approx 10^{12}$.

Table 4.1: The relevant γ-ray emissions for ^{57}Fe

Δn	ΔJ^π	$\tau_{1/2}$	E (keV)	I_{rel}	Mult	δ	α_{T}
$1 \to 0$	$\frac{3}{2}- \to \frac{1}{2}-$	98.3 ns	14.41	100	M1 + E2	0.0022	8.56
$2 \to 1$	$\frac{5}{2}- \to \frac{3}{2}-$	8.7 ns	122.1	89.3	M1 + E2	0.120	0.024
$2 \to 0$	$\frac{5}{2}- \to \frac{1}{2}-$	8.7 ns	136.3	10.7	E2		0.137

The vector sum of the spins for the transition and thus the multi-polarity, $\mathbf{J} = |\mathbf{I_1} \pm \mathbf{I_2}|$,
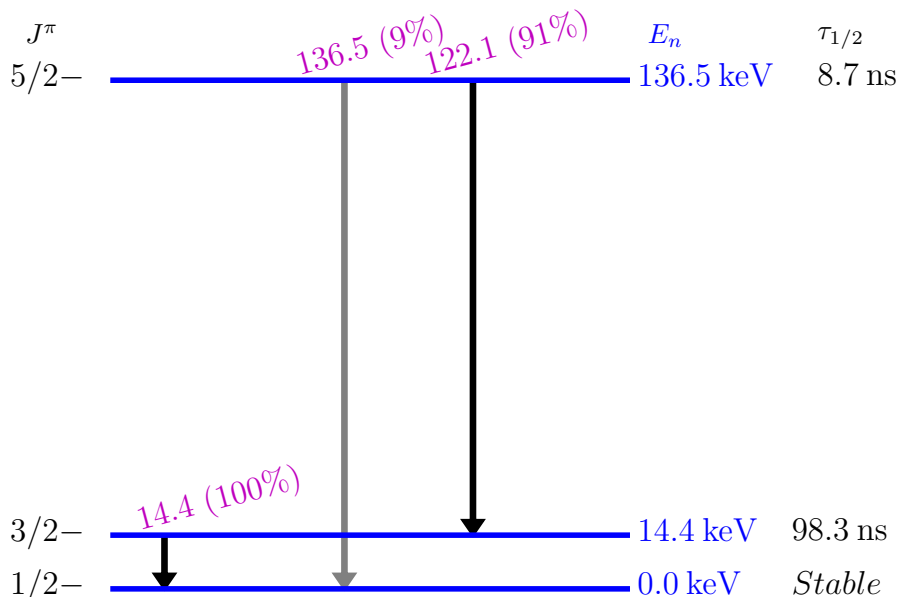
Figure 4.1: The first three energy levels of ^{57}Fe, with transitions [5]. Not to scale.

can be 1 or 2. This means the transition can be magnetic dipole (M1) or electric quadrupole (E2). The γ-ray mixing ratio, $\delta = 0.0022$, characterises the probability for each of these transitions as $\frac{1}{1+\delta^2}$ and $\frac{2\delta^2}{1+\delta^2}$ respectively, meaning the transition is essentially purely M1, which simplifies analysis, giving the quantum number selection rule $\Delta m = 0, \pm 1$.

The Total Electron Conversion Coefficient $\alpha_T = 8.56$ gives the ratio of probability for electronic versus photonic decay of an excited ^{57}Fe nucleus. The excess nuclear energy can be imparted to s-electrons which have finite density inside the nucleus, these $1s$ electrons have binding energy $E_b = 7.1$ keV and are therefore ejected with kinetic energy $E_k = 7.3$ keV. $2p$ electrons ($E_b = 0.7$ keV) then fall to fill the $1s$ holes, resulting in the characteristic X-rays with energy 6.4 keV. This preference for electronic decay is why the characteristic 6.4 keV X-rays are so much more intense than the 14.4 keV γ-rays in backscatter MöS, and why the closely related technique of CEMS (conversion electron MöS) is often used to study purely surface ^{57}Fe states (the electrons themselves can only escape from a depths ranging from 10s to 100s of nm).

4.2.2 Spectroscopy

The Mössbauer effect allows for the resonant emission and absorption of the 14.4 keV γ-ray between identical nuclei by ensuring that the effective recoil energy is smaller than the

energy linewidth. However, should the ^{57}Fe nuclei in an absorber experience a different electromagnetic potential to those in the source, the nuclear energy levels of the absorber nuclei will be shifted by an energy greater than the linewidth and resonance cannot occur. To re-establish resonance, the energy of the emitted γ-rays must be scanned over an appropriate energy range of order $\pm 0.5\,\mu\text{eV}$, slightly larger than the Zeeman splitting of ^{57}Fe in α-Fe. This can conveniently be satisfied via the relativistic Doppler effect, invoked by oscillating the source with velocity up to $v \approx 10\,\text{mm s}^{-1}$. The natural linewidth in these units is $\Gamma_0 \approx 0.14\,\text{mm s}^{-1}$, while typical spectral features are generally of order $1.0\,\text{mm s}^{-1}$.

4.2.3 Spectral Features

In ^{57}Fe MöS there are three main features which are typically observed in measured spectra[1]; these illustrated in Figure 4.2 and discussed below:
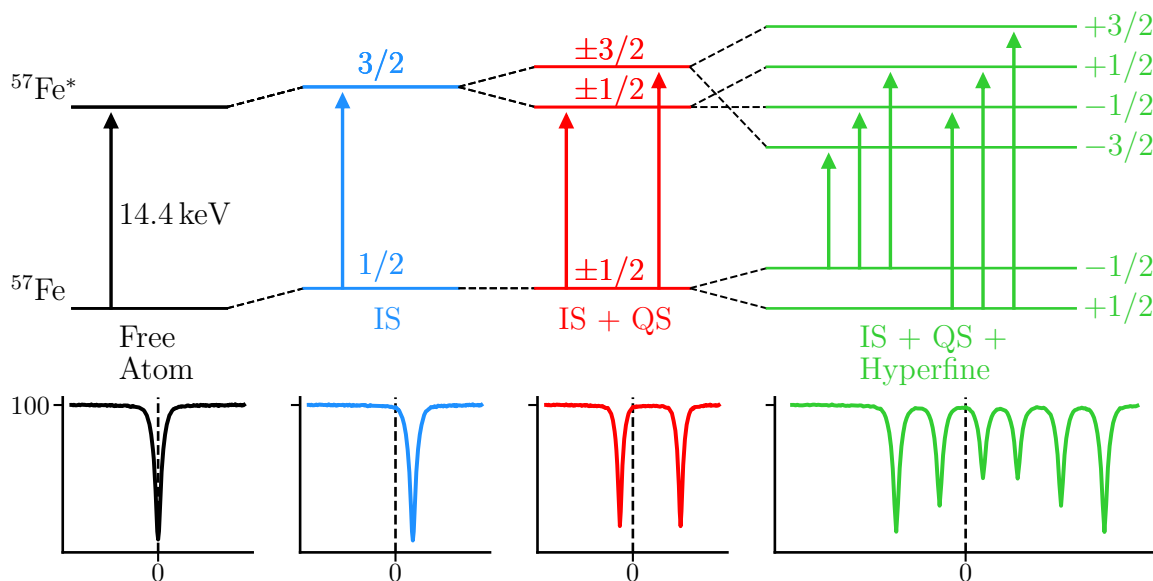
Figure 4.2: Typical patterns observed in ^{57}Fe MöS, with splitting greatly exaggerated, adapted from [6]. IS and QS stand for isomer shift and quadrupole splitting respectively.

- **Chemical Isomer Shift** (IS) refers to a constant shift in the energy levels of the source nucleus relative to those of the absorber. Electrons residing in the s orbitals of atoms have a finite probability density $|\psi_s(0)|^2$ within the nuclear volume and excited nuclei generally have a different radius R compared to their ground state counterparts, and these facts affect the nuclear energy levels of the nucleus and thus

the energy of the photon related to the transition between the levels. For distinct source S and absorber A nuclei, there is a shift of the *transition* energy proportional to $(|\psi_s(0)_S|^2 - |\psi_s(0)_A|^2)\,\delta R$: Chemical bonding affects the screening of s electrons, changing their probability density within the nucleus and causing the "isomer shift" to be non-zero. This is equivalent to the electric monopole, or Coulomb, contribution.

- **Quadrupole Splitting** breaks the degeneracy of nuclear energy levels with spin $J > \frac{1}{2}$. Nuclei satisfying this condition have a non-spherical charge distribution, which means that an electric field gradient, which is not spherically symmetric, will split the energy levels of the nucleus into those with different quantum numbers $|J_z|$. The magnitude of this splitting is proportional to the product of the nuclear quadrupole moment and the electric field gradient maximum at the nucleus, the latter of which again depends on the specifics of the chemical environment and local crystal field.

- **Hyperfine Splitting** results from the Zeeman effect of an external or contact magnetic field at the nucleus. Zeeman splitting separates the nuclear energy levels by their magnetic quantum number, resulting in $2J + 1$ sub-levels, which means four sub-levels for the 1st excited state of ^{57}Fe and two sub-levels for the ground state. This results in eight possible transitions between sub-levels of the two nuclear states that must be considered. The magnetic dipole nature of the transition limits the change in magnetic quantum number to $\delta m = 0, \pm 1$, reducing the number of possible transitions to six, for all but extremely distorted local environments and high hyperfine fields. This yields the familiar sextet that is often observed in MöS.

In any particular absorbing sample, each distinct crystallographic site that is populated by an ^{57}Fe atom will independently contribute to the Mössbauer signal, with the positions of the peaks in the spectra determined by the three effects mentioned above. Even in disordered or amorphous systems, the atomic distribution within highly local environments can be investigated.

4.2.4 Model

To model the data, we adapt the *ab initio* method of [7], where the intensity of each line in the spectrum is represented as the normalised power absorbed by each nuclear sub-level transition, which is equal to the square modulus of the multipole field of the photons incident at the absorbing nucleus. The photons' multipole field is modelled in terms of vector spherical harmonics [8]. The eigenvectors of the Hamiltonians of the nuclear excited and ground states, as well as the Clebsch-Gordan coefficients, enter as the coefficients multiplying the spherical harmonics after [9]. The general Hamiltonians for the two nuclear states are written in matrix form after [10]. Piecing together all this information gives us a complete model for the position and intensity of each line in each spectrum (generally a sextet but in principle the approach can handle octets as well). The peak positions and heights are then convoluted with pseudo-Voigt profiles, the broadening of which depends primarily on the crystal structure; alternatively they may be convoluted with time-differential or dynamic lineshapes. A full derivation of the model is given in the appendix section 4.A. In the usual case of a homogeneously magnetised absorber, the formula used to represent the observed intensity I as a function of source velocity v is denoted by the function:

$$I = C_1 \cdot SC(v, \Gamma, \sigma, \mu, \delta, Q, B_{\text{hf}}, \Theta) + C_2 \tag{4.1}$$

In Equation 4.1, Γ, σ and μ are the Lorentzian width, Gaussian width and mixing ratio of the pseudo-Voigt profiles, respectively; δ, Q and B_{hf} are the isomer shift, effective quadrupole moment and magnetic hyperfine field at the nucleus, respectively and Θ is the polar angle describing the direction of the source γ-ray incident on the absorber with respect to the direction magnetic hyperfine field of the absorber ^{57}Fe nuclei. C_1 and C_2 are scaling constants. The function is labelled SC in this case as it corresponds to the single crystal case. Averaged polycrystalline versions can also be used.

The parameter Θ is key to investigating the magnetic orientation within a sample. In an ^{57}Fe MöS sextet, the relative areas of peaks 2 and 5 within the sextet vary with Θ as $x = 4\sin^2(\Theta)/(1 + \cos^2(\Theta))$, where the peak area ratios are 3:x:1:1:x:3 (see section 4.A). For magnetically isotropic absorbers, the model is integrated with respect to Θ, yielding

195
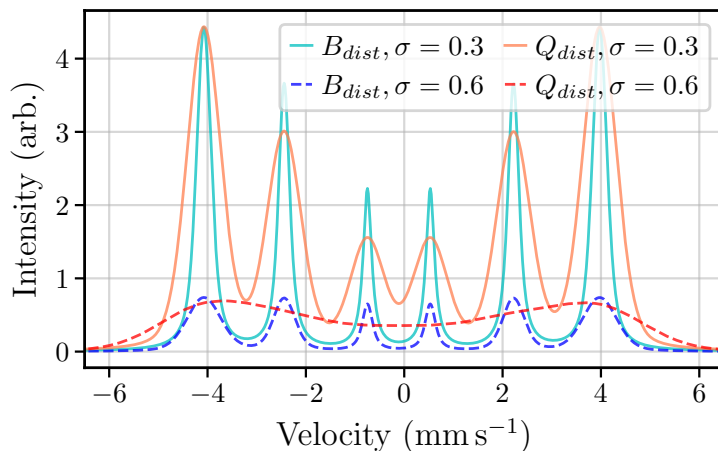
Figure 4.3: A comparison of the B_{hf}-distribution and Q-distribution models for two different values of the broadening parameter σ which controls the width of the normal distribution from which the parameter values are chosen.

$x = 2$, so the relative peak areas of the sextet are always 3:2:1:1:2:3 regardless of sample orientation.

For the region between perfect crystallinity and fully amorphous structure: single crystals with substantial structural and chemical disorder, it does not make sense to use a single value for the hyperfine parameters since the ^{57}Fe nuclei will exist is a variety of distinct environments. In this case we use a "B_{hf}-broadened" or "Q-broadened" model, where the spectrum is represented as a sum of contributions with the hyperfine parameter in question chosen from a continuous distribution for each contribution. The width of the distribution depends on the degree of disorder [11]. The B_{hf}-broadened model yields a broadening proportional to the velocity (since the hyperfine field increases the splitting of all sub-levels), while the broadening due to a distribution of Q values is constant, allowing one to visually decide which approach is more suitable (or indeed use both). A comparison of the two sources of broadening is shown in Figure 4.3: The velocity dependence of the B_{hf}-distribution is very clear in the highly broadened spectrum in Figure 4.3. In the results section, real data which is well-explained by this model will be shown. A final note is that the distribution need not be Gaussian: a weighted distribution based on a space-filling model, such as the radial distribution functions that describe the variation of interatomic spacings in amorphous materials [12, §19], could be used [13]. The distribution of interatomic spacings is of particular interest in amorphous magnetic materials due to the distance-dependence of the exchange interaction.

4.3 Methods

4.3.1 Backscatter Mössbauer Spectroscopy

In traditional MöS [1], the transmission of the emitted 14.4 keV γ-rays through an absorber is measured and the resonant dips with changing velocity constitute the Mössbauer spectrum. This linear geometry of traditional MöS is an adaptable one, where collimators, filters etc. can be inserted in the beam path. By contrast, in our novel system, described in detail in this section, data is collected in the backscatter geometry [14], with the source and the detector on the same side of the absorber, see Figure 4.4.
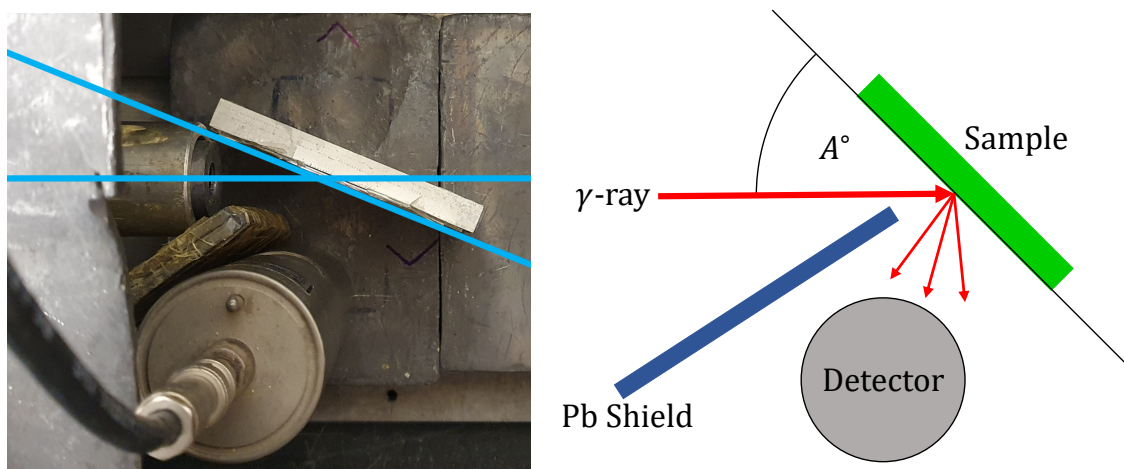
Figure 4.4: Backscatter geometry with γ-ray to sample-surface angle shown. Minimal (graded) Pb shielding is used to allow for the reduction of the sample-detector distance.

The absolute signal intensity collected in the backscatter geometry is reduced relative to that measured in the transmission geometry because the emitted fluorescence from the absorber is generally close to isotropic in 3D space while the detector window only covers a small solid angle so only a relatively small fraction of Mössbauer photons re-emitted by the sample are captured. Additionally, not all excited ^{57}Fe nuclei decay by radiative emission: one $E = 14.4\,\text{keV}$ photon is re-emitted for roughly every 10 absorbed, see Figure 4.5. As an example, when natural α-Fe is probed in the transmission geometry at normal incidence, a maximum relative intensity of the Mössbauer signal of about 27% can be readily achieved. This value may be compared to a maximum conversion of about 20% in the backscatter geometry with angle of incidence with respect to the surface normal $A_\gamma \approx 45°$. However,

the backscatter geometry enables us to exploit the entire energy range of the fluorescence spectrum, including the re-emitted 14.4 keV γ-rays (BSMS: back-scatter MöS), the characteristic X-rays (CXMS: conversion X-ray MöS) and the internal-conversion electrons (CEMS: conversion electron MöS). The different decay products of $^{57}\mathrm{Fe}^*$ are illustrated in Figure 4.5, while the energy level transitions were tabulated in Table 4.1. In our system, data is simultaneously recorded with one proportional detector over an energy range that includes the X-ray and γ-ray energies and extends up to roughly 150 keV. One advantage of this technique is the ability to correct for the background signal using photons that have been detected with off-resonance energies. In a typical acquisition scenario, the off-resonance photons can be a few times more numerous than their resonant counterparts (in un-enriched and dilute specimens), allowing for a substantially more accurate subtraction of the background as a function of velocity. The shape of the background depends primarily on the variation of steric angles from which the source and detector "see" the sample surface as the drive oscillates. A second advantage is the depth sensitivity provided by the different mean free paths of the resonant γ-rays and characteristic X-rays: Fleischer et al. [15] found that the maximum experimentally resolvable depth of resonant photons emitted from an Fe foil was below 50 µm for the 14.4 keV γ-rays and was roughly 20 µm for the 6.4 keV X-rays, corresponding to 3-5 times the photon absorption length at each specific energy. As this depth sensitivity cannot be accurately computed analytically, for any realistic sample containing multiple fluorescent and scattering species, comprehensive Monte Carlo simulations should be performed for each specific material and measurement geometry that is being investigated. The resolution varies substantially as a function of the angle of incidence of the primary photons and can reach individual micrometers. When compared with CEMS and its depth- elective version (DCEMS) (which can be performed with the same acquisition electronics we use in our setup but a different detector), depth sensitivity can be as high as 10s of nanometres. While these two electron-detecting techniques have profound requirements for surface roughness, CXMS and BSMS have no substantial requirements for sample surface preparation. Often macroscopically rough and completely untreated surfaces can be measured successfully, as well as surfaces covered by passivation layers or with polymer protection films. Finally, in contrast to transmission MöS, thick (e.g. $(t >= 0.1\,\mathrm{mm})$ for α-Fe) undiluted samples can be probed (to a certain

depth) because the source γ-rays do not need to pass through the absorber.
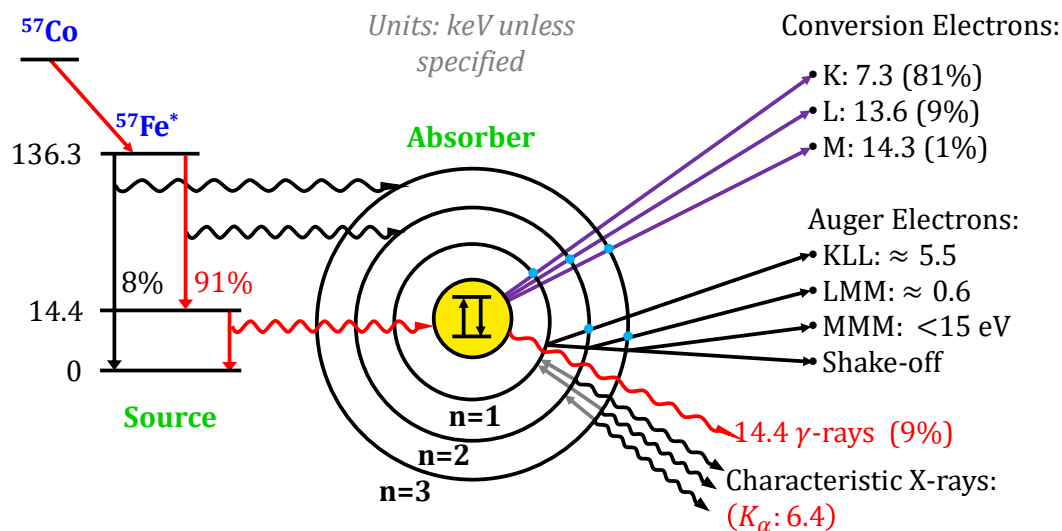
Figure 4.5: γ-ray production with absorber excitation and decay illustrated, adapted from De Grave *et al.* [16].

4.3.2 Data Acquisition
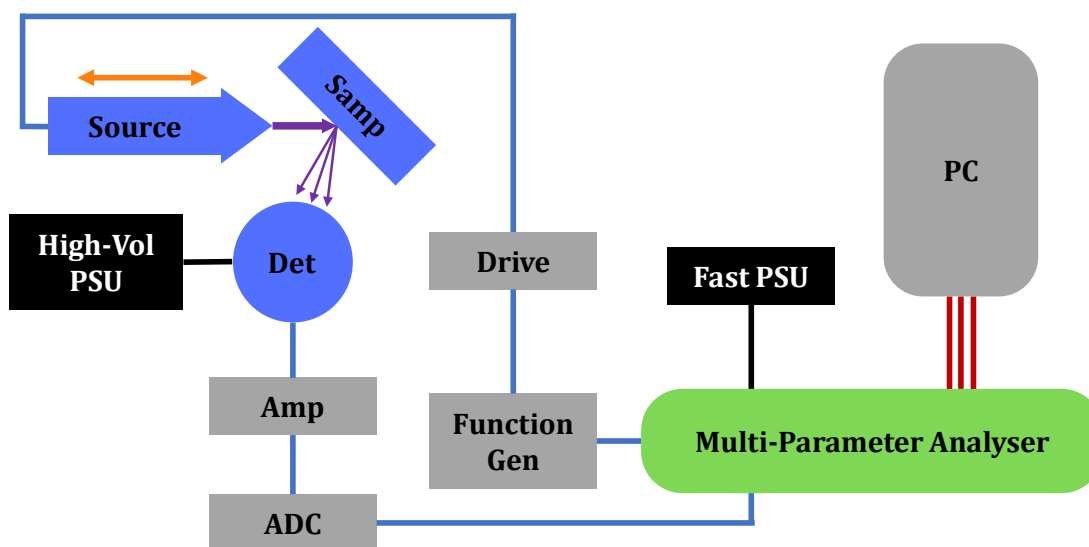
Figure 4.6: Block diagram for our backscatter setup.

In this section, the setup apparatus for data acquisition will be briefly described. A block diagram for the system is shown in Figure 4.6.

The source of the γ-rays used to probe the first energy-level transition of ^{57}Fe is ^{57}Co embedded in a Rh matrix. This matrix is engineered to maximise the phonon-free fraction

of emissions and minimise the magnetic field and electric field gradient at the source nucleus [17]. ^{57}Co decays to ^{57}Fe* by electron capture with a half-life of $\tau_{1/2} = 272$ days and ^{57}Fe* then de-excites via emission of the aforementioned 14.4 keV γ-ray, exhibiting the Mössbauer effect [5]. The activity of the radioactive source in our apparatus was $A \approx 2$ GBq when purchased, but after roughly five years this has fallen to $A \approx 0.02$ GBq, meaning significantly more time is required to obtain sufficient statistics, until the source is replaced[2].

The Mössbauer drive system consists of a FG (function generator) and a reciprocating linear motor on which the source is mounted. The FG produces a $f \approx 25$ Hz triangular wave signal that drives the transducer with constant acceleration within the linear permanent magnet motor, and a positional feedback loop corrects discrepancies, see Figure 4.9(c). The FG has "start" and "channel" digital signals which reset or increment a counter in the MPA, respectively. The generator can use up to 4096 channels, without impacting on the MPA's dead time, but we typically use 512 channels, as high-resolution velocity acquisition is rarely worth the memory space and processing time [18]. The source oscillates at around $10 \, \text{mm s}^{-1}$ for Fe MöS (the maximum hyperfine field splitting for Fe is around $9 \, \text{mm s}^{-1}$).

The absorber must be placed as close as possible to the source and detector to maximise the solid angle of the absorber's isotropic emissions incident on the detector window, Figure 4.4. This proximity has bearing on the necessary background and geometry corrections, as will be discussed in subsection 4.3.3. Thin Pb shielding is used between the source and detector, with suitably thick, chevroned Pb bricks surrounding the entire apparatus.

The detector is a Xe/CO_2 proportional counter [19, §6] operated at a high voltage between 1.5 kV and 2.0 kV, depending on whether maximum efficiency or resolution is desired. The anode is a gold-coated tungsten wire. The Townsend Avalanche of electrons [19, §6.I.A], following an initial ionisation by a photon, provides a built-in amplification which allows the detection of individual photons. The magnitude of the current pulse produced thus produced is proportional to the energy of the ionising photons. This detector type has a relative energy resolution of $10\% - 15\%$ [20], as confirmed by fitting the fluorescence

---

[2]Replacing the source has been difficult in recent years. Essentially all MöS sources were manufactured in Russia, who stopped exporting radioactive materials prior to the Ukraine war. Additionally, old contacts and communication pathways have moved on and broken down, respectively, over the course of the COVID pandemic.

spectrum of a calibration sample, see Figure 4.7(a): the various peaks come from the Fe in the source/sample, the Xe gas and Au/W wire in the detector and the Pb shielding around the setup. The Fitting to the fluorescence spectrum can also yield the calibration
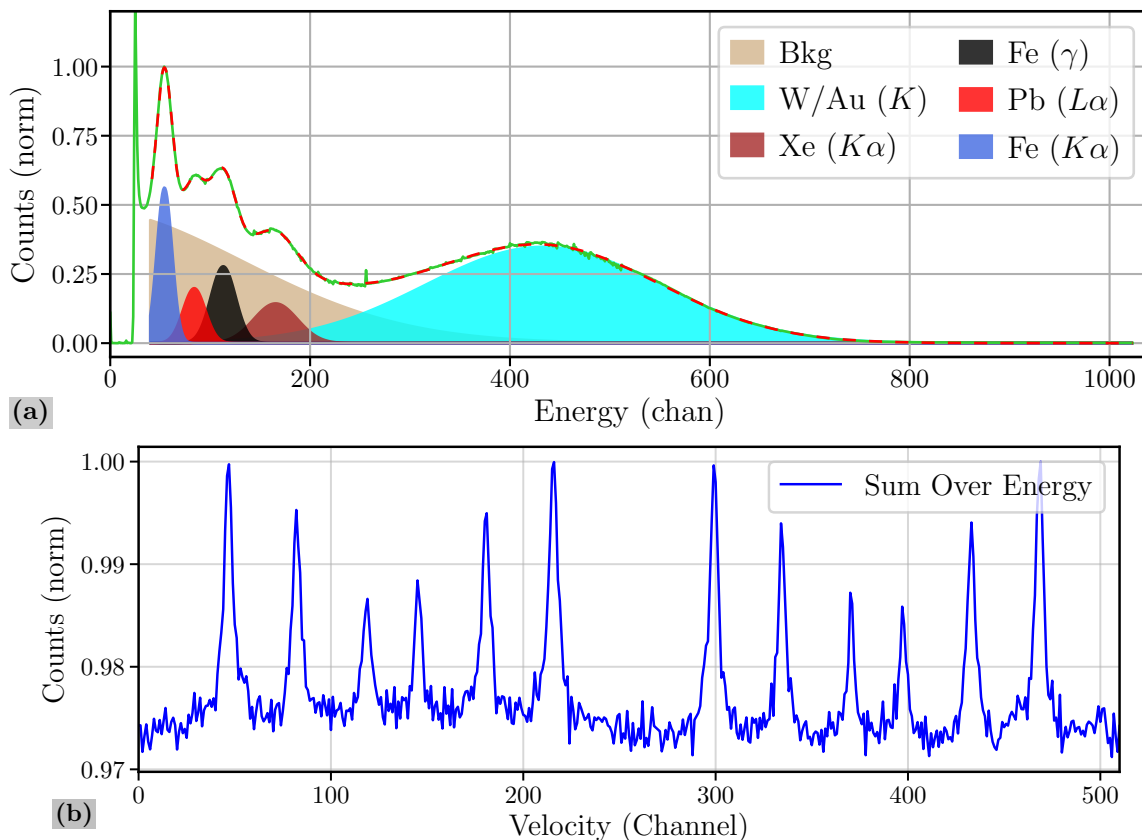
Figure 4.7: **(a)** The data summed over the velocity axis, aka the fluorescence spectrum, with contributions fit using Gaussian profiles. Before the geometry was optimised to remove Pb. **(b)** The data summed over the energy axis, clearly showing the resonance. The velocity axis is mirrored as both the upstroke and downstroke of the triangular velocity are included, this is addressed in the next section.

factor for the energy channels, by fitting the peak positions obtained in Figure 4.7 to the theoretical positions as defined in the X-ray data booklet [21, §1.2]. There can be further benefits to fluorescence fitting if a sample contains other elements with X-ray edges in the same energy region, more on that in the data analysis subsection 4.3.3

The current pulses from the detector are first amplified by a charge-sensitive pre-amplifier with a gain of 30 dB and further amplified by a variable-gain shaping-amplifier (with a typical gain of between 10 dB and 20 dB and shaping time between 0.1 μs and 1 μs). These pulses are then digitised by a fast analogue-to-digital converter (ADC) with a maximum resolution of 8192 channels (13 binary bits), but resolution this high is not
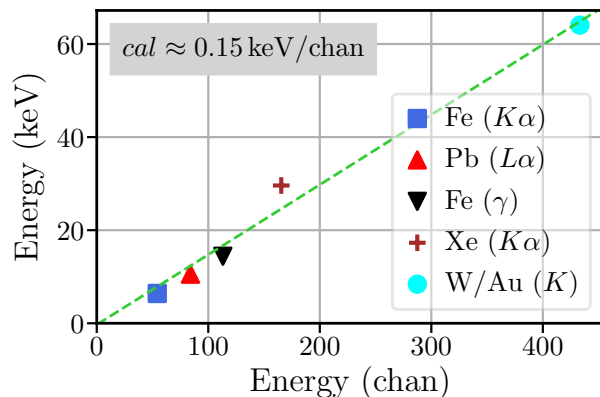
Figure 4.8: Energy calibration using the theoretical values for the K and L X-ray edges of the various elements that contribute to the detector signal. The average value is used for W/Au since at high energy the absolute energy resolution is poor and there is no benefit to separating the peaks.

necessary given the energy resolution of the detector and we typically use only the most significant 10 bits (1024 channels) to reduce the dead time from the $\Sigma\Delta$-integration in the analogue-to-digital conversion process. The ADC provides analogue upper and lower discrimination thresholds on the energy, which is key to minimising the dead time by filtering out the cascade of low-energy excitations and high-energy cosmic or ^{40}K-related photons. The digitised pulse height, proportional to photon energy, is then passed on to the MPA.

The custom-built MPA is at the heart of the setup and consists of a timer-counter chip and an array of high-speed digital latches arranged into 8-bit blocks. The digital latches are edge-triggered D-type flip-flops (Texas Instruments SN74HC574N) with maximum switching time $t \approx 50\,\text{ns}$: these ICs contain 8 independent flip-flops which are individually addressed in our circuit, hence the 8-bit block arrangement. The aforementioned FG signals control the counter, with the 512-channel velocity signal stored in 9 bits. The 10-bit signal from the ADC, encoding the photon energy, is similarly stored. The MPA interfaces with the PC via three IEEE-1284 standard cables [22], each nominally capable of 8-bit parallel data transmission (up to five of these can be accommodated in principle, providing 40-bit maximal depth). Through low-level (Assembly) coding, one can utilise an additional three or four bits per connector that are typically reserved for legacy hardware reasons by default (providing 60-bit maximal depth).

The system is controlled by a computer with an Intel Pentium 4 processor (2.8 GHz)
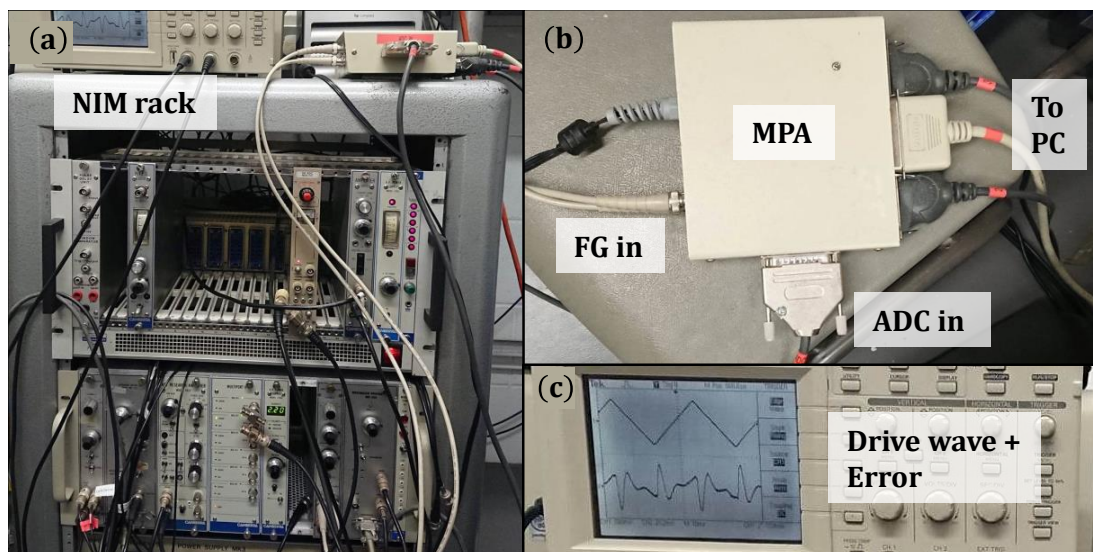
Figure 4.9: The electronics: NIM rack with drive units, amplifiers and ADCs for two setups; overhead view of the MPA showing the connections and an oscilloscope showing the triangular wave and drive error.

running Windows 98: the last Windows version to allow seamless hardware port access... The MPA is controlled by custom Assembly and C code running on system interrupts (which precede the operating system interrupts), this feature is not readily achievable on modern operating systems. The data is read from the MPA using the IEEE-1284 connectors plugged into three (again, up to five) "Extended Capability Ports" on the PC, which offer bi-directional parallel data transfer and direct memory access. The data for each detector event is read directly into the CPU's L1-cache (a small, very low-latency and high-speed memory built into the CPU) before being buffered in DRAM and finally written to the hard drive. A rough outline of the data flow is shown in Figure 4.10. The described combination of equipment allows for a tested maximum acquisition speed of order 10^6 cps with 4K velocity and 8K energy resolution, respectively.

The front-end interface is written in LabView$^{\text{TM}}$ and runs concurrently and in parallel to the data acquisition. The data contains the time of detection, the drive velocity at the time of detection and the photon energy, for each photon that enters the detector. The data is read from the hard drive and each detection event is binned by its energy and velocity, resulting in a (typically) 1024×512 matrix, or histogram. The raw data (Figure 4.11), as well as the energy and velocity averages (Figure 4.7) are displayed in real time to ensure that the discrimination thresholds are set optimally, to determine when
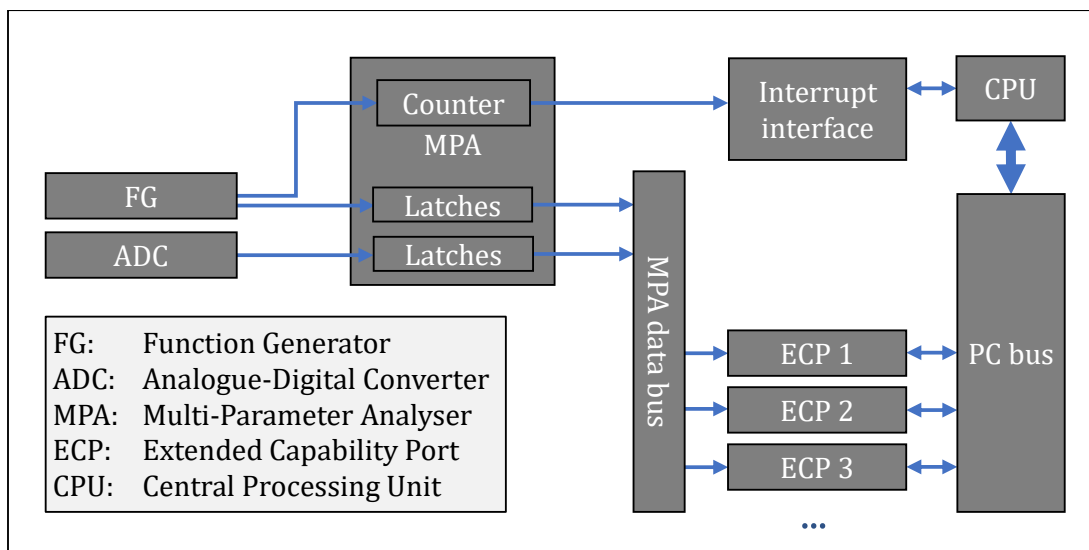
Figure 4.10: A bus diagram showing the path of the data takes after it is digitised.

sufficient data have been collected and to allow a user determination of the signal-to-noise ratio (SNR) as data acquisition progresses.
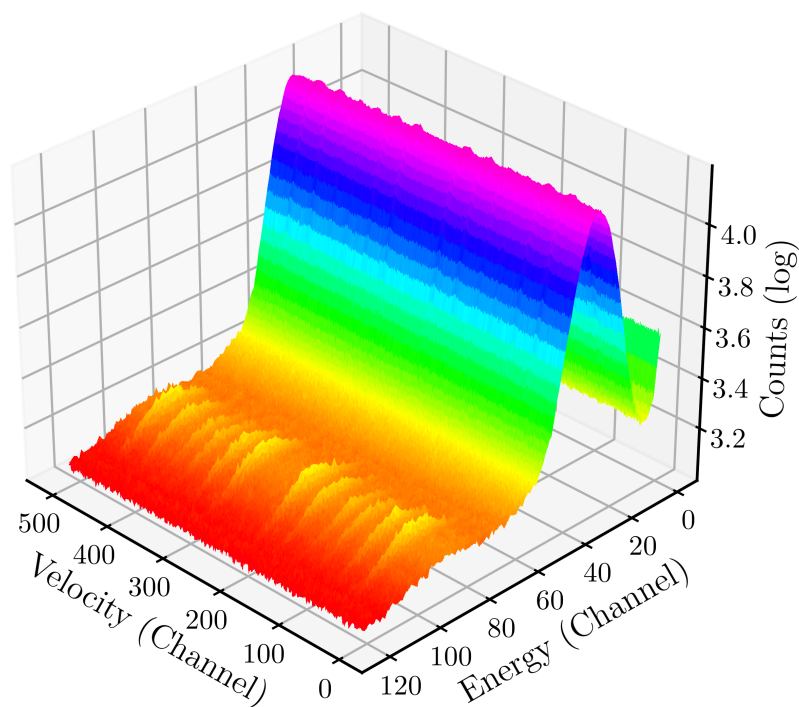
Figure 4.11: The 3D view of the raw data from a calibration sample, showing the low-energy region (150/1024 channels). The X-ray and γ-ray peaks are clearly visible at approximately energy channel 20 and 90 respectively. The velocity resonances are also clearly visible at the top of these peaks, particularly the at γ-ray energy.

4.3.3 Data Pre-Processing

Within each energy channel, the middle 20 velocity values are used to normalise the data. These central values correspond to the minimum velocity of the source (bottom of the triangular wave), where the Doppler-shifted energies are far from the resonant energies, which are observed at intermediate velocities. This normalisation thereby emphasises the resonant MöS signal. The minimum velocity region is illustrated in Figure 4.12(a). The data after normalisation is shown in Figure 4.12(b). To isolate the resonant signals of the characteristic X-rays and γ-rays from the non-resonant background, the energy discrimination bands are manually optimised post-acquisition such that the SNR for the individual spectra are maximised: these bands are illustrated in Figure 4.12(b). As a general rule of thumb, the bands extend ± 10 energy channels either side of the resonant peaks at 6.4 keV and 14.4 keV, but can depend on the sample peculiarities. In particular, Cr, Mn, Co, Ni and Cu emit K_α X-rays with energies in the range $5 \rightarrow 8$ keV, while the rare-Earth elements emit L edge X-rays in the similar energy range $5 \rightarrow 9$ keV. Therefore, specimens under examination which contain any of the aforementioned elements may benefit from more aggressive energy discrimination. In addition, the L_α absorption edge of Pb is at 10.5 keV, a value that lies between the two resonant energies. It is therefore imperative to optimise the geometry of the setup such that the Pb shielding does not overly contaminate the resultant spectrum. Lastly, as the detector contains Xe gas with an anode wire of Au and W, fluorescence from these elements will also be produced, but at higher energies than are relevant for MöS, see Figure 4.7(a). The steps for normalising and discrimination are illustrated in Figure 4.12.

A background contribution is present in the overall signal, that varies quasi-sinusoidally with velocity. This background signal is due to the relative motion of the source: when the source is closer to the absorber, more photons hit the absorber and at steeper angles. The result of this varying geometry can be seen in the sinusoidal variation of the background with velocity in Figure 4.12(c): the isolated background signal is fit with a second-order sinusoid and subtracted from the resonant data. The trend is also visible as the background in Figure 4.7(b). This very natural and effective method removing the background signal would not be possible without recording the entire continuous energy range (as opposed to narrow energy bands) and isolating relevant energy regions.
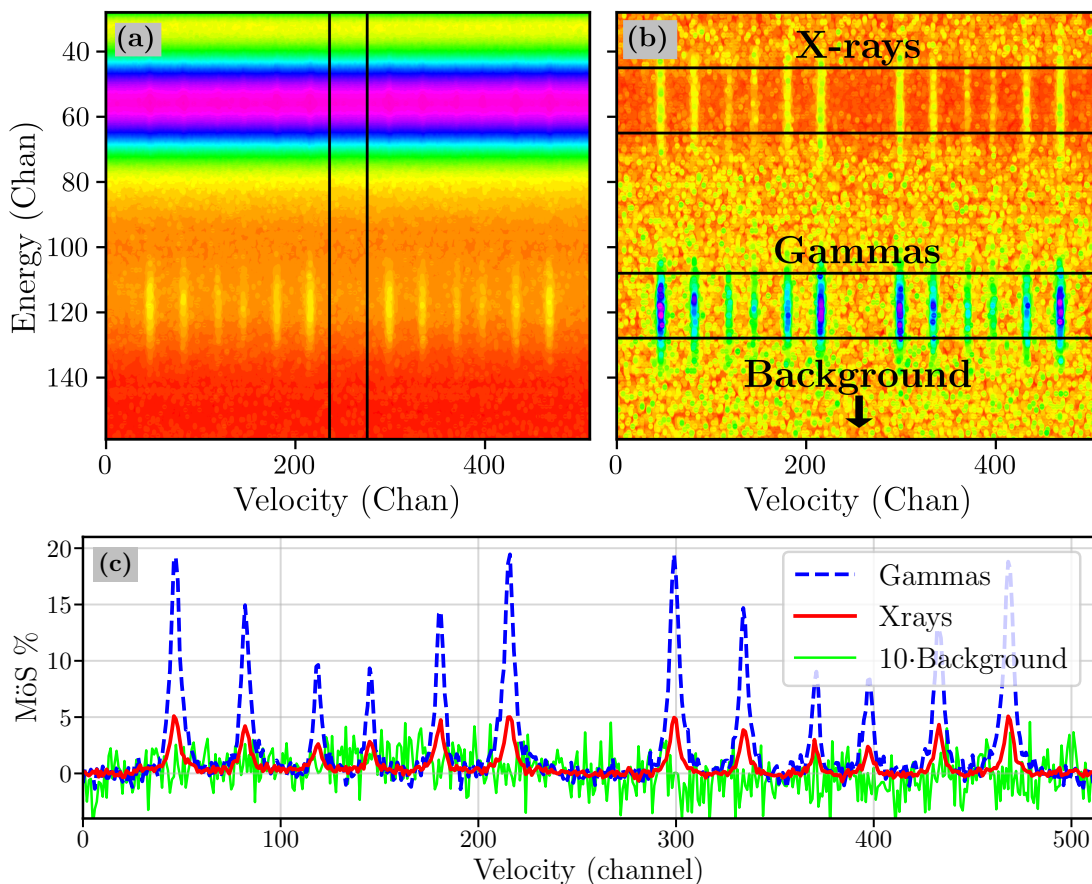
Figure 4.12: **(a)** The raw data in the low-energy region with the minimum velocity, off-resonance region denoted. **(b)** The normalised data with the X-ray, γ-ray and background energy regions denoted. **(c)** The three spectra obtained from this process.

 The velocity channels are converted to units of $mm\,s^{-1}$ using data obtained from a calibration sample of natural α-Fe. The theoretical peak positions for α-Fe are well known; fitting two straight lines to the measured peak positions as a function of the predicted positions yields the conversion, see Figure 4.13. Unique slopes must be used for the positive and negative acceleration components of the source motion since physically different bipolar transistors control aspects and they will have some manufacturing tolerances. In this manner the centre point, or folding axis, of the velocity axis is determined with resolution better than one discrete channel and the positive and negative acceleration spectra can be averaged without spuriously broadening the peaks due to misalignment. The calibration is repeated whenever the source environment is altered in any way.
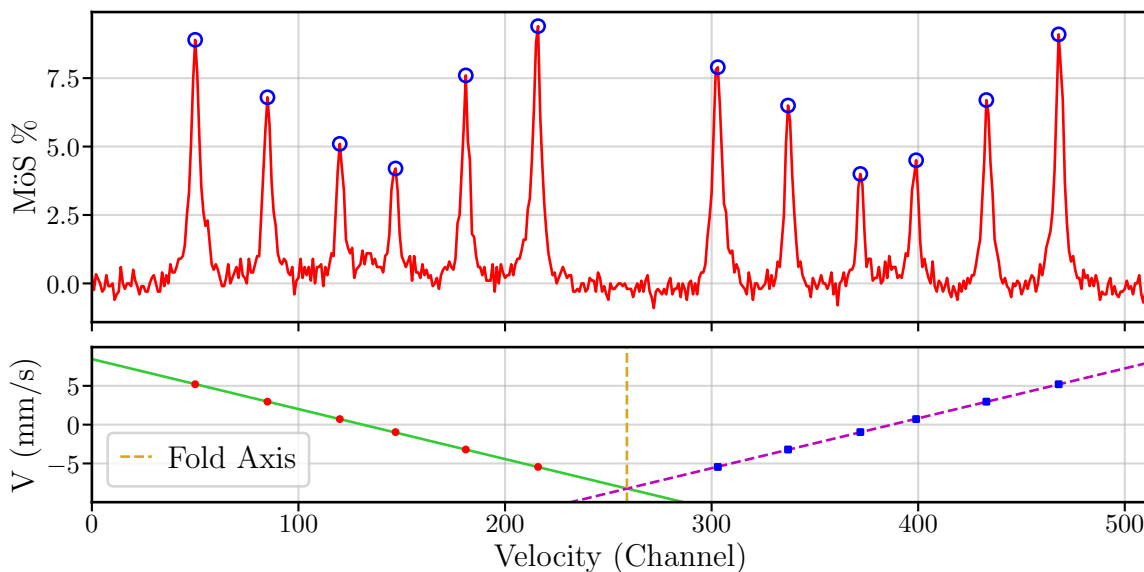
Figure 4.13: Velocity unit conversion and folding point determination using a reference sample of natural α-Fe.

4.3.4 Fitting to Theory

When the data has been fully pre-processed, the constituent X-ray and γ-ray spectra are considered individually and the appropriate fitting model is chosen from those described in subsection 4.2.4. The model is fit to the data using a non-linear least-squares regression algorithm for the input parameters. The experimentalist's algorithm of choice can be used, but we prefer a basic iterative grid-search: The initial guess values, along with the upper and lower limits for each parameters, are chosen based on the expected literature or simulations for the type of material being studied. The parameters are first refined by eye. The algorithm cycles through the parameters one-by-one. For each parameter, the sum of squared residuals (S_r^2) between the data and the model is calculated for n uniformly spaced values of the parameter, between the specified limits. The value which yields the best fit (minimises S_r^2) is kept before moving to the next parameter. This process repeats until the fit converges (i.e., until the best-fit values for the parameters do not change between iterations) or the maximum number of allowed iterations is reached. The limits for the parameters can then moved to better bracket the expected best-fit value and narrowed in parameter space so there is a smaller interval between tested values for each parameter. This type of algorithm is not guaranteed to converge to the global minimum of S_r^2 and is not particularly fast compared to, for example, gradient descent algorithms [23, §10].

207

However, the strict control over the parameter limits and order of regression is well-suited to the non-empirical nature of modelling MöS, and can help ensure convergence to a minimum which is physically sensible.

4.4 Examples of Application

In this section, the earlier-described Mössbauer data collection and analysis approach has been applied to three unique forms of magnetic material: an amorphous CoFeB-based ribbon, NdFeB thick films and a slab of a stony iron-nickel meteorite. These samples have been chosen as they are examples of form factors which are either better suited to BSMS and CXMS or simply impossible to measure in the transmission geometry. When measuring in the backscatter geometry, only one side off a planar sample is accessible at a time and it is important to know to what depth the sample is probed. The $50\,\mu m$ and $20\,\mu m$ values mentioned in subsection 4.3.1 were estimated by Fleischer et al. [15] as the maximum escape depths for 14.4 keV and 6.4 keV photons, with good SNR and distinct shapes of the Mössbauer spectra, originating from an Fe foil surface layer and an Fe-containing substrate layer respectively, at normal incidence, i.e. the signal from the substrate could no longer be resolved with a $50\,\mu m$ Fe foil deposited on top. Although the materials investigated here all have a similar density and mass-energy absorption length to pure Fe, the presence of additional fluorescence contributions, in conjunction with disorder in the local Fe environments, degrades the signal. Thus the resolvable depth of information collected from these samples is assumed to be roughly 50% less than that estimated by Fleischer. For the average depth probed (or most probable escape depth for a particular photon), we assume the values to be halved again so the depths probed by the γ-rays and X-rays are approximately $13\,\mu m$ and $5\,\mu m$ at normal incidence. These values can then naively be reduced by the cosine of the angle of incidence with respect to the surface normal. More accurate estimates can, in principal, be obtained via Monte Carlo simulations of the photon absorption and detection processes for arbitrary angle of incidence. Here we have not performed these as no publicly available code exists and the examples referenced by Fleischer et al. [15] are only for normal incidence and importantly are tailored to their experimental setup which utilises two fixed-position narrow-band

detectors, in contrast to our single moveable broadband detector. Independent simulations would need to be performed for various incidence angles and any other changed variable in our more versatile setup.

4.4.1 Amorphous CoFeB-Based Ribbons

Power conversion electronics typically involve magnetic-core inductors that are operated at high frequencies up to $500\,\mathrm{kHz}$. In order to minimise losses, ultra-soft magnetic materials with minimal coercivity but appreciable saturation magnetisation are desired. One such class of materials recently shown to satisfy these conditions is melt-spun amorphous CoFeB-based alloys [13]. The investigation of an example composition of this material using the backscatter MöS technique is presented here.

4.4.1.1 Sample Description

The sample studied was a melt-spun ribbon of dimensions $12\,\mathrm{\mu m}$ thick by approximately $2\,\mathrm{mm}$ wide, with the nominal chemical composition $Co_{75.5}Fe_{4.5}B_{20}$. The ribbon was produced by repeated arc-melting of the constituents followed by injection of the molten precursor onto a rapidly rotating Cu wheel (outer rim velocity $\approx 80\,ms^{-1}$) for ultra-fast cooling. As the wheel side (WS) of the resultant amorphous ribbon, which is in contact with the Cu wheel, cools via conduction much more rapidly than the free side (FS) cools in contact with the quenching atmosphere, the FS can, in principal, more readily facilitate partial crystallisation of the alloy. In preparation for MöS, a mosaic sample was assembled out of $l \approx 2\,\mathrm{cm}$ long segments of ribbon, that were taped together using transparent adhesive tape, as in Figure 4.14. The sample was placed in the beam path such that the long axes of the ribbon segments were oriented perpendicular to the incoming photons and the short axes were oriented in the source-sample-detector plane.

Backscatter Mössbauer data was collected from both sides of the ribbon and processed as described in section 4.3. We also performed transmission MöS on the same sample for comparison.
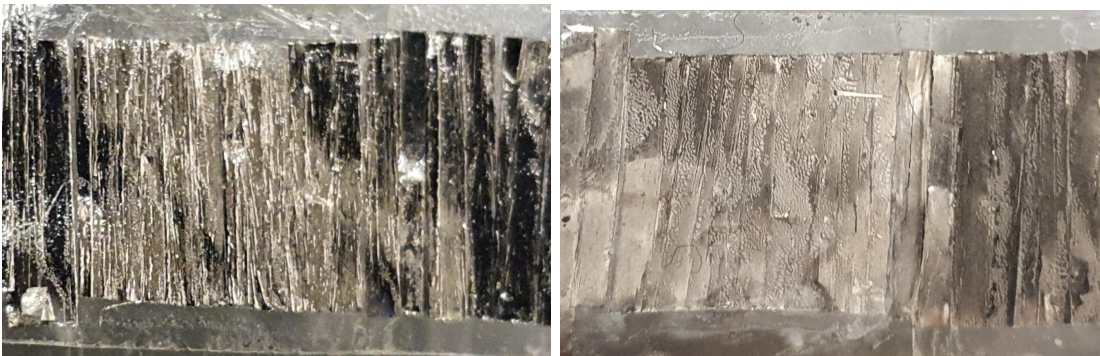
Figure 4.14: The mosaic sample arranged from strips of the $Co_{75.5}Fe_{4.5}B_{20}$ribbons, showing the WS and FS. With respect to these pictures, the incoming photons from the source travel to the right and into the page, while those travelling to the right and out of the page will be captured by the detector. This information is important to relate the measured values of Θ to actual magnetic orientation in the sample.

4.4.1.2 Results

The X-ray and γ-ray spectra obtained from both sides of the ribbon arrangement are shown in Figure 4.15. The poor SNR is expected due to the small proportion of Fe in the composition, in tandem with the other factors mentioned in subsection 4.3.1. The Mössbauer peaks are very broad due to the amorphous nature of the alloys and the data is well-fitted using a B_{hf}-broadened model. The average value for the hyperfine field was $B_{hf} = 26.3\,\mathrm{T}$ with $\sigma B_{hf} = 0.8\,\mathrm{T}$. This low value of B_{hf}, compared to the canonical value of $B_{hf} \approx 33\,\mathrm{T}$ for α-Fe, reflects the structural and chemical disorder of the sites occupied by the Fe nuclei in these types of ribbon.

The spectra collected from the WS and the FS of the ribbon segments were practically indistinguishable, suggesting that the amorphous crystal structure of the ribbon was uniform throughout the volume despite the different cooling rates of the opposing sides, this uniformity is likely due to the small thickness of the ribbon.

The magnetisation orientation ($\vec{m}$) of the ribbon was anticipated to be in-plane (IP) due to shape anisotropy, exacerbated by the high moment and ultra-low coercivity. This assumption was tested using the collected MöS data. As described in subsection 4.2.4 , the angle Θ between the momentum direction of the incoming photons $\vec{k}_\gamma$ and the sample magnetisation $\vec{m}$, is obtained from the relative peak areas within a sextet. Angles of $\Theta_x = 57° \pm 2°$ and $\Theta_\gamma = 71° \pm 5°$ were obtained from application of the fitting procedure for the X-ray and γ-ray spectra, respectively. The angle of incidence between $\vec{k}_\gamma$ and the surface
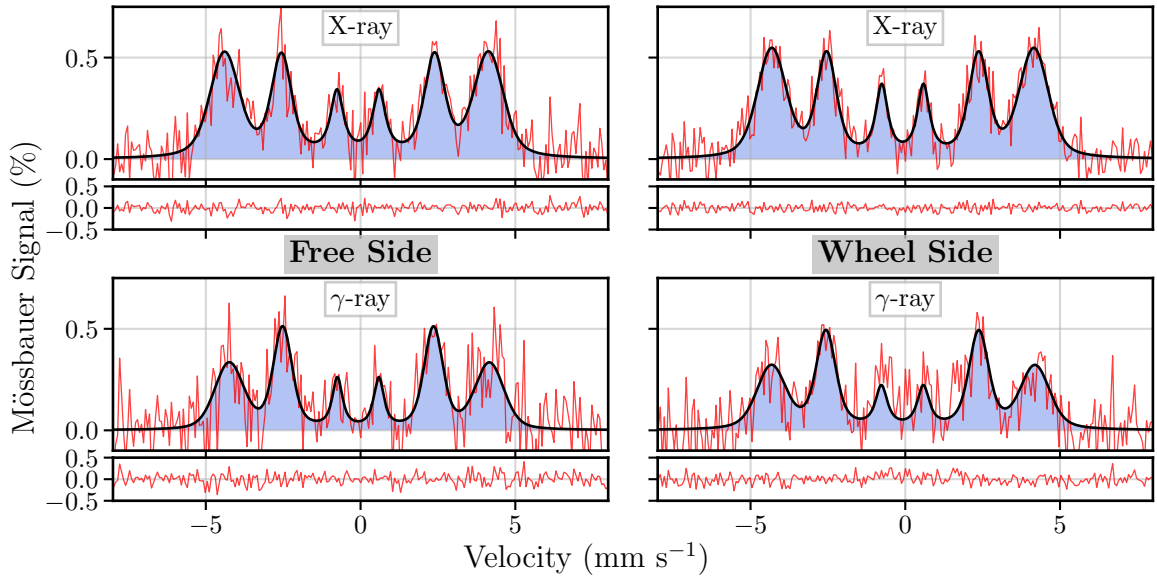
Figure 4.15: Mössbauer spectra from both sides of the amorphous $Co_{75.5}Fe_{4.5}B_{20}$ ribbon. Note the velocity dependent broadening of the peaks, indicating a distribution of B_{hf} values. The spectra from the two sides of the ribbon are practically indistinguishable but the different relative intensities of the peaks for the different energy photons indicates a different magnetisation direction in the areas probed by these photons. The random noise appearance of the residuals indicates the data is well-explained by the model.

normal was determined as $A_\gamma \approx 65°$ for these measurements. Assuming that the magnetic moment $\vec{m}$ is oriented IP and along the ribbon's long axis (vertical in Figure 4.14), Θ would be equal to $90°$ given the orientation of the ribbon segments in the experiment; in this case the absorption peak intensity ratios would be $3 : 4 : 1$. However, the angle $\Theta_\gamma = 71° \pm 5°$ determined from the γ-ray spectrum implies that $\vec{m}$ has a component, approximately 20% of the total magnitude of the magnetisation, that is aligned along the short (IP) axis of the ribbon segments (horizontal in Figure 4.14). The ribbon segments were confirmed to be magnetised IP by measuring a transmission spectrum with the photons from the source incident normally on the surface; a value of Θ close to $90°$ was obtained. The SNR for the transmission data (Figure 4.16) is slightly improved compared to the backscatter data at γ-ray energy (Figure 4.15). However, the additional information (depth sensitivity and background correction) obtained in the backscatter geometry renders it still superior in this case.

This conclusion, that the ribbon is magnetised IP with finite components along both IP axes, is good news for the proposed application of this type of ribbon, as a finite
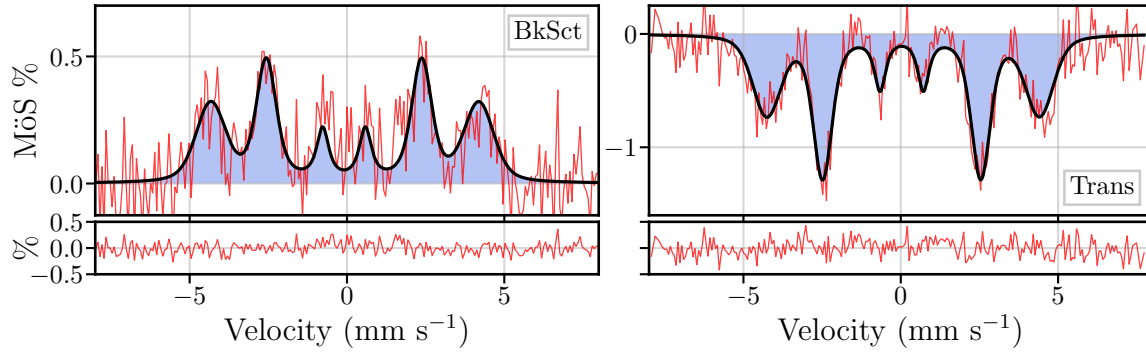
Figure 4.16: Normal incidence transmission MöS data from the $Co_{75.5}Fe_{4.5}B_{20}$ sample, with the WS γ-ray spectrum for comparison.

component of $\vec{m}$ oriented away from the easy axis is anticipated to mitigate power losses during rotation of magnetisation in power conversion applications.

The smaller value of $\Theta_x = 57° \pm 2°$, obtained from fitting the X-ray spectrum compared to that derived from analysis of the γ-ray spectrum, points to spatially inhomogeneous magnetisation in the ribbon, recall that the X-rays and γ-rays probe different effective depths of the order of $5\,\mu m$ and $10\,\mu m$ respectively (refer back to section 4.4). This result is consistent with the existence of a larger component of $\vec{m}$ along the short IP axis near to the surface of the ribbon compared to that of the bulk, or perhaps reveals some component of $\vec{m}$ in an out-of-plane (OOP) orientation near the surface. The presence of flux-closure domains near the ribbon surface, perhaps associated with the highly amorphous surface state or with strain, may underlie this observed change in the direction of $\vec{m}$ revealed by the X-ray spectrum as compared to the information provided the γ-ray spectrum.

4.4.2 Nd-Fe-B Thick-Film Micro-Magnets

$Nd_2Fe_{14}B$-based magnets have the largest energy product among all modern commercial magnets [24, §13.2], resulting in their widespread use in a variety of applications. The $Nd_2Fe_{14}B$ phase has a large, complex unit cell with six distinct Fe-occupied sites:

Fe Site	k_1	k_2	j_1	j_2	c	e
Occupancy	16	16	8	8	4	4

The desired "2-14" phase of NdFeB alloys is generally obtained in bulk via sintering of powder samples with the correct stoichiometric ratio. The hyperfine parameters for

Fe nuclei in $Nd_2Fe_{14}B$ have been determined on a bulk, melt-spun sample in the past using traditional transmission MöS [25], see Figure 4.17. These values can be compared to Nd-Fe-B samples to determine if the correct phase has been obtained.
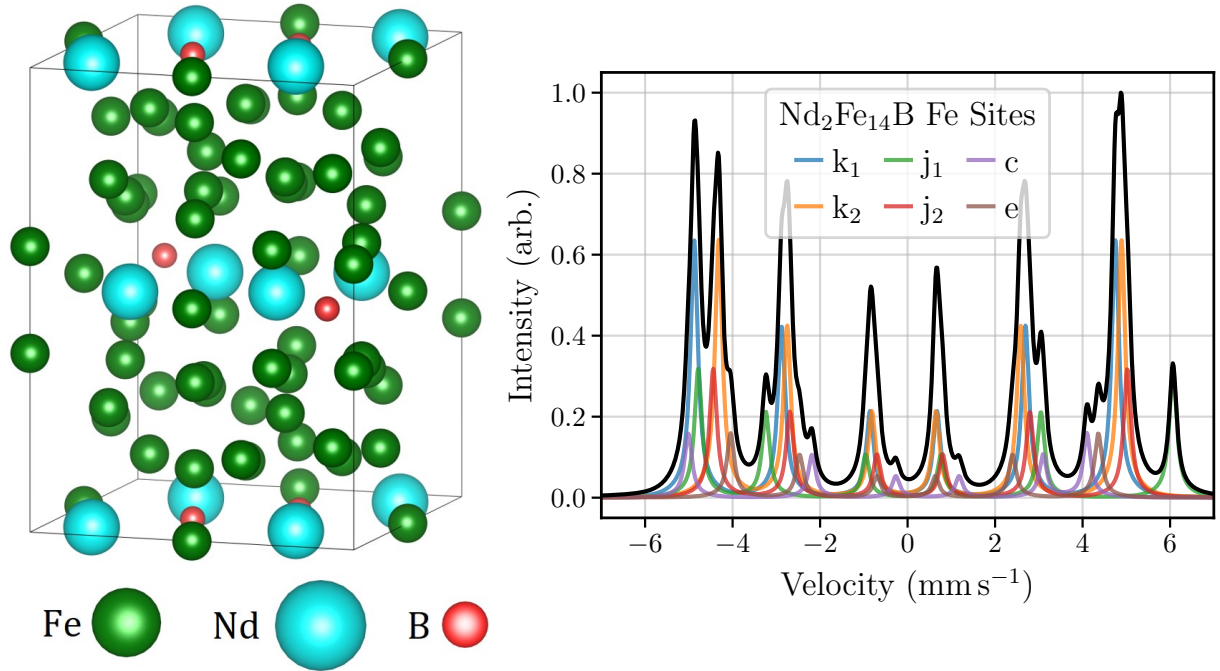
Figure 4.17: $Nd_2Fe_{14}B$ unit cell, and the Mössbauer spectrum for $Nd_2Fe_{14}B$ plotted using the hyperfine values measured by Pinkerton et al. [25] from a melt-spun bulk alloy using the transmission geometry [25].

Thin films of $Nd_2Fe_{14}B$ can display similar superlative properties to the bulk, but lack the magnetic volume and the ability to project substantial stray fields when patterned for use in, for example, NEMS/MEMS devices. **Thick** films (micrometric as opposed to nanometric) of $Nd_2Fe_{14}B$ could potentially bridge this gap and are currently investigated for use in the aforementioned devices [26]. Thick films are very well-suited to the depth-selective characterisation provided by simultaneous X-ray and γ-ray photon collection from our backscatter MöS technique.

4.4.2.1 Sample Description

Mössbauer spectra were recorded from five films of $5\,\mu m$ thickness in the virgin magnetic state. The films were deposited on Si substrates via triode sputtering in a method similar to that described by Frederico et al. [26], with a range of deposition and subsequent annealing temperatures. Buffer and capping layers of Ta with $100\,nm$ thickness were also

used. After the initial measurements, the most crystalline sample was field polarised in 5.5 T to observe if there was substantial difference from the virgin state. The sample conditions are tabulated in Table 4.2.

Sample	(a)	(b)	(c)	(d)	(e)	(f)
T_{dep}	RT	550°C	RT	500°C	550°C	550°C(P)
T_{anneal}	RT	RT	700°C	700°C	700°C	700°C(P)

Table 4.2: The deposition and annealing temperatures of the samples, with field-polarisation denoted by P, otherwise samples were measured in the virgin state.

Data was accumulated for approximately three weeks to obtain adequate statistics as the activity of the ^{57}Co source used was low, in addition to the relative thinness of the absorbing films. Due to the low SNR, we only consider the two most populous Fe sites when fitting the data obtained from the crystalline (annealed) samples. For those films that were not annealed, the structural and chemical order is poor and the B_{hf}-distribution model is used.

4.4.2.2 Results

The twelve spectra obtained from the six measured films are shown in Figure 4.18. For the regression, the literature values for the hyperfine parameters were used as a starting point. Firstly, the angle Θ, the hyperfine field B_{hf}, and the Voigtian broadening parameters were refined, before releasing all the parameters to get the best possible fit. The good quality of the fits in Figure 4.18 for the annealed samples, and the striking similarity of the data to the spectrum in Figure 4.17, confirms that those annealed films are crystallised in the $Nd_2Fe_{14}B$ phase. The difference in the relative peak heights to those of Pinkerton et al. are attributed to a different angle of incidence of the source γ-rays. Again, the residuals confirm the success of the model in explaining the data. The key parameters obtained from the regressions are shown in Figure 4.19. The hyperfine field monotonically increases with increasing deposition/annealing temperature, and also noticeably increases after field-polarisation. This is consistent with improved crystalline order with increasing temperature.

The angle of incidence of the source γ-rays with respect to the surface normal was $A_\gamma \approx 67°$ for these measurements. It is useful here to introduce a "tilt" angle $A_{\mathrm{tilt}} =$
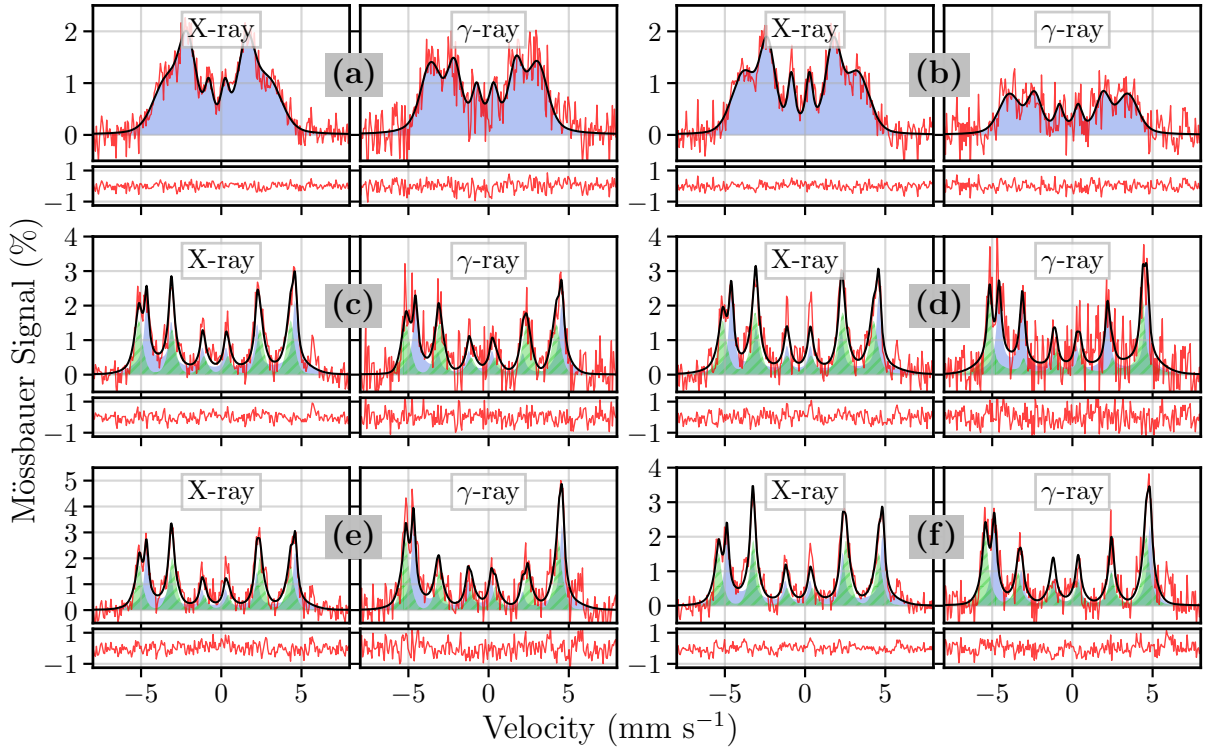
Figure 4.18: X-ray and γ-ray spectra from the films labelled as in Table 4.2. The difference annealing makes to the crystal structure is obvious (top row vs lower rows), as is the difference in peak ratios between the X-ray and γ-ray spectra, signifying the existence of surface domains.

A_γ - Θ, where again A_γ is the angle between k_γ and the surface normal, and Θ is the angle between k_γ and the magnetisation direction. The tilt angle A_{tilt} therefore contains information about the canting of the magnetisation away from the surface normal, a useful figure of merit when considering perpendicular magnetic anisotropy (PMA) materials. The measured values for B_{hf} and A_{tilt} for the X-ray and γ-ray spectra for each sample are shown in Figure 4.19. A_{tilt} was found to be near zero for all X-ray spectra, consistent with magnetisation that was oriented fully perpendicular near the surface of the films, regardless of whether they had been annealed or not. In contrast, analyses of the γ-ray spectra, originating from deeper within the film, revealed a tilt angle of $10° \pm 4°$ for the as-deposited films and a tilt angle greater than $20°$, within experimental error, for the annealed films. This result implies that some component of the magnetisation within the volume of the film was oriented IP, and this IP component is larger in the annealed film than it is in the as-deposited film. This interpretation was again reinforced by analysis of a conventional transmission spectrum recorded with incoming γ-rays normally
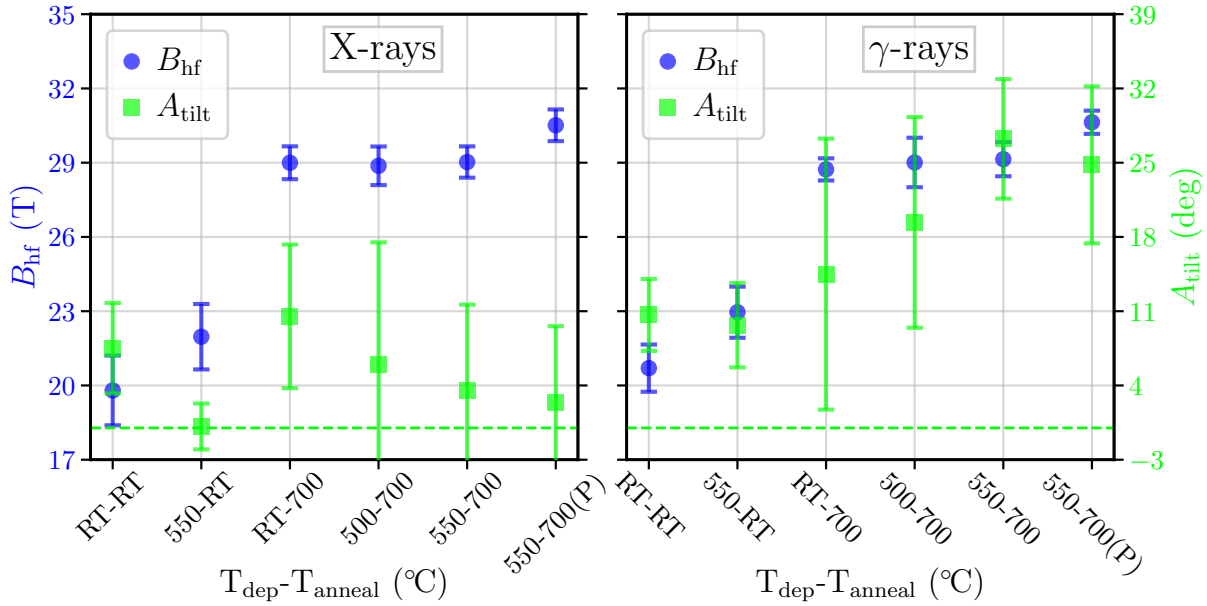
Figure 4.19: The magnitude of the hyperfine field (or central value of the distribution for the B_{hf}-broadened model) and the magnetic moment orientation (the weighted average is used for the two-phase model) are plotted. The x-axis shows increasing T_{dep} and T_{an}, with field-polarised data appended.

incident on the as-deposited film. In this case a value of $\Theta = 19° \pm 5°$ was obtained from the fit, consistent with up to roughly 20% of the film volume possessing an IP magnetic polarisation, leaving the majority of the film with an OOP magnetic polarisation. The attainment of a finite tilt angle for the magnetisation in the bulk of the film (large penetration depth derived from the γ-ray spectrum) but not near the film surface (shallow penetration derived from the X-ray spectrum) might be explained by the presence of flux-closure domains with an IP remnant magnetisation that formed near the substrate interface. In contrast to the CFB ribbons of the previous section, the bulk magnetisation here was primarily out-of-plane, so the peaks in the sextet are not well-resolved at normal incidence, made worse by the B_{hf}-broadening of this sample. Measuring at oblique angles solves this problem but the SNR is significantly reduced in transmission geometry at these angles, see Figure 4.20. In this case, the backscatter geometry offers **better** SNR, at angles where the peaks can be resolved, in addition to the aforementioned benefits.

Notably, OOP remnant magnetisation was detected in all samples, supporting the existence of a significant uniaxial anisotropy even in as-deposited films, i.e. prior to the establishment of long-range crystalline and atomic order. This result was evidenced by the similar values of Θ obtained from the regressions of the data from all films. Further,
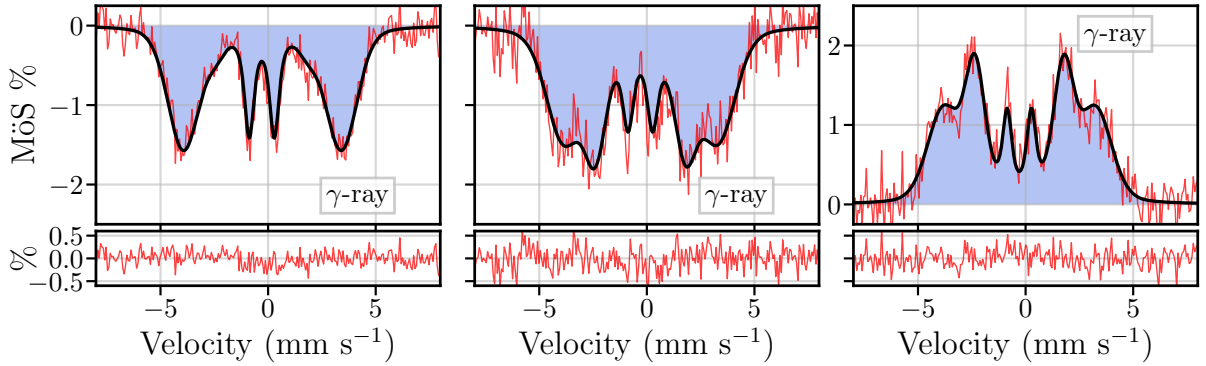
Figure 4.20: MöS spectra on a disordered NdFeB thick film measured in **(a)** Transmission at normal incidence, **(b)** Transmission at an oblique angle and **(c)** Backscatter at an oblique angle.

this result (that all films were observed to be magnetised OOP) is in agreement with magnetometry data obtained from Nd-Fe-B films that were sputter-deposited at a temperature that was just below the crystallisation temperature of the $Nd_2Fe_{14}B$ phase and were then subsequently annealed [27].

4.4.3 Meteoritic FeNi Phase Analysis

Magnetocrystalline anisotropy is a key property of technologically useful magnetic materials. To this end, FeNi is a promising candidate material which exhibits significant uniaxial anisotropy without rare-Earth or heavy-metal elements, when it is crystallised in the tetragonal $L1_0$ phase (space group 123, $P4/mmm$) [28], known as tetrataenite. However, the disordered-fcc $A1$ parent phase (space group 225, $Fm\bar{3}m$) is very close in energy to that of the $L1_0$ phase and the kinetics of formation of the desired phase is very slow [29]. The chemical ordering within the fcc unit cell for the two phases is illustrated see Figure 4.21. FeNi in the $L1_0$ phase can be synthetically produced [30, 31, 32] but a large-scale method has not yet been demonstrated.

An interesting source of $L1_0$-type FeNi is extraterrestrial bodies, specifically very slow-cooled iron-nickel meteorites. The extremely long-term cooling that such meteorites undergo in the vacuum of space provides sufficient time (tens of thousands of years at the optimal temperatures) to crystallise in the $L1_0$ phase [33]. There is also interest in such meteorites due to their ability to "record" the magnetic fields of the early solar system due to the fact that they have been effectively field-cooled in said magnetic fields. To
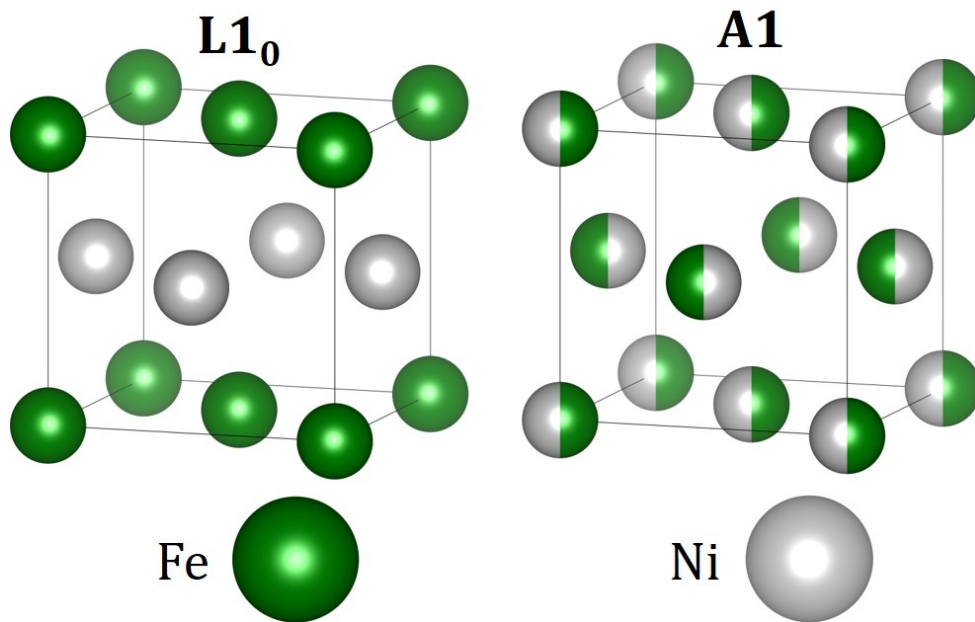
Figure 4.21: The atomically ordered ($L1_0$) and atomically disordered (A1) crystalline phases of equiatomic FeNi.

investigate this material, we obtained a sample extracted from the nickel-rich iron meteorite NWA 6259 [34] and employed our backscatter MöS technique to non-destructively investigate the Fe-containing crystal phases present within it.

4.4.3.1 Sample Description

The meteoritic sample studied had dimensions of $70\,\mathrm{mm} \times 35\,\mathrm{mm}$ at its widest points and a thickness of $6\,\mathrm{mm}$, too thick to conduct transmission MöS. The specimen had been cut with a diamond saw and mechanically polished on one side. It was mounted in the usual fashion for backscatter measurements with the polished side facing the incoming γ-rays from the MöS source. The polished face was at all times protected by a layer of transparent adhesive tape to protect the surface from oxidation and picking up dirt or grime from being handled. A picture of the sample is shown in Figure 4.22.

4.4.3.2 Results

FeNi has a simple (compared to $Nd_2Fe_{14}B$) and well-studied structure and its theoretical hyperfine parameters are known [35] and were used as a starting point for the regression of MöS data. In addition to the $L1_0$ tetrataenite phase and the $A1$ disordered phase,

Figure 4.22: The polished sample from the meteorite. The circular indentations and other straight-edged marks are from cuts taken from this piece for other measurements before we obtained the sample.
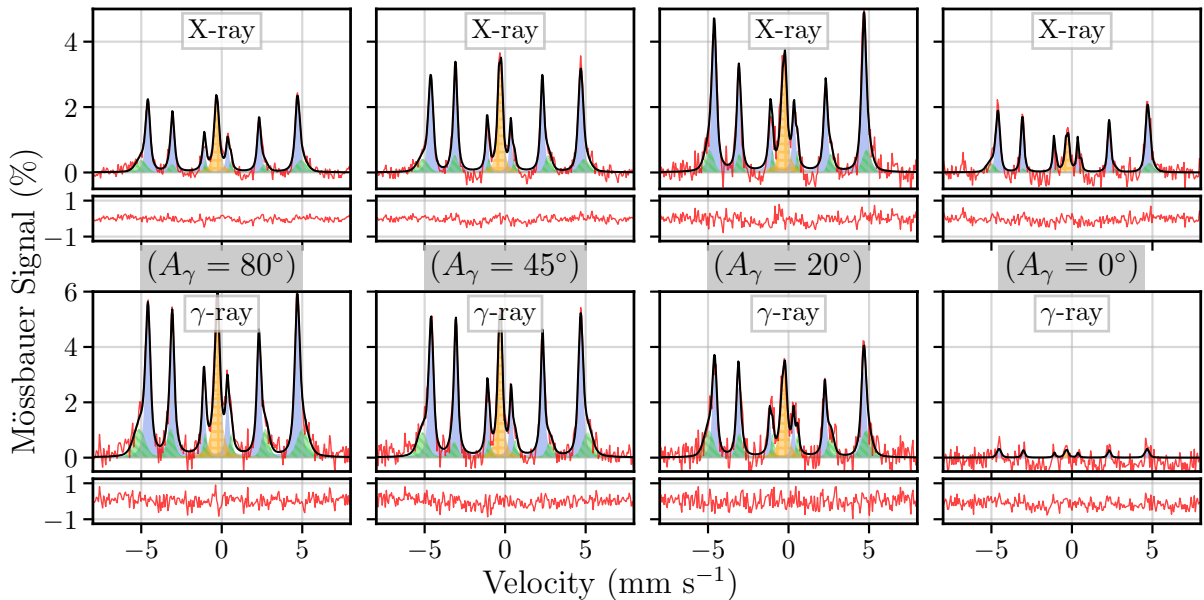
Figure 4.23: The data obtained from the MöS measurements on the meteoritic sample performed at difference incidence angles. The angle between the photon momentum vector and the surface normal A_γ is denoted. The trend in total Mössbauer intensity for the spectrum can be explained by the changing sensitivity as a function of angle, shown in Figure 4.24(a).

a contribution from a paramagnetic (at room temperature) phase, denoted "PM", was included. As a paramagnetic phase, this contributes a large singlet (actually a tight doublet but the two peaks are strongly overlapping) to the spectrum, and is included to explain the data. This phase is thought to be an intermediate structure which populates regions between fcc crystalline grains [29, 36], see Figure 4.23. For the analysis of the volume

fractions of the different crystal phases, we initially considered only the X-ray spectrum, which has better SNR than that provided by the γ-ray spectrum. The relative areas of the three contributions to the spectrum, equivalent to the relative abundances of the three crystal phases in the probed volume of the sample were determined as: $66\% \pm 5\%$ $L1_0$, $17\% \pm 10\%$ $A1$ and $17\% \pm 5\%$ PM. This value for volume fraction of the $L1_0$ phase is among the highest reported for FeNi alloys and is the highest reported from natural (non-synthetic) samples [32]. The angle between the incoming photons' momentum vector and the sample hyperfine field, averaged for the two magnetic phases, was found to be $\Theta = 49° \pm 5°$ for this measurement (Figure 4.23), which was recorded with an incidence angle of $A_\gamma \approx 20°$, implying that the magnetisation is somewhat tilted in-plane (at least $20°$) close to the surface in the region probed by the X-rays.

The fits of the model to the X-ray and γ-ray MöS spectra collected from the NWA 6259 specimen gave slightly different values for the relative phase contributions, consistent with a depth dependence of the composition. To investigate this possibility more systematically, measurements were repeated with different incidence angles of the incoming photons, with the results shown in Figure 4.21.
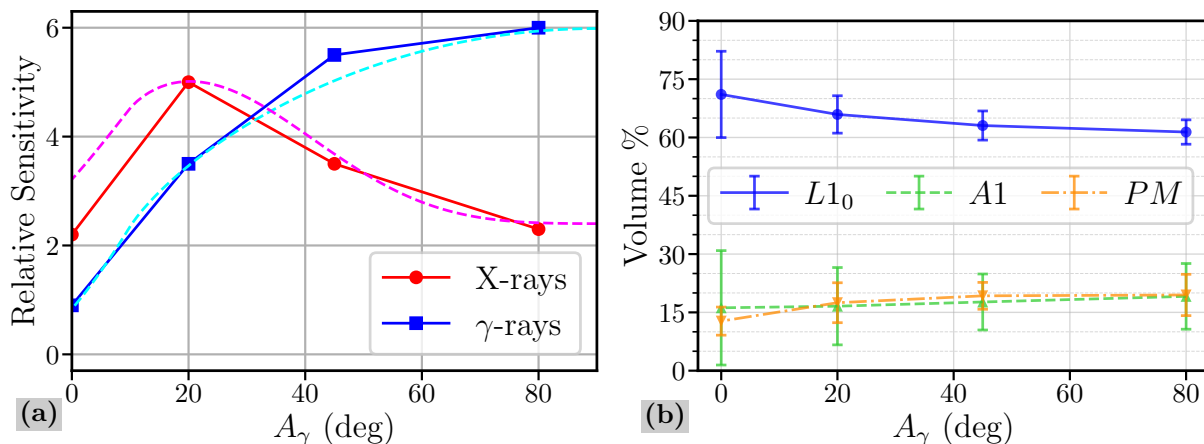
Figure 4.24: **(a)** Calculated (dashed lines) and experimentally measured (points, from Figure 4.23 angular dependence of relative MöS sensitivity of X-rays and γ-rays, Equation 4.9 was used to calculate the dashed lines, see section 4.B. **(b)** The angular dependence of the phase contributions.

The volume fraction of the $L1_0$ phase was found to decrease significantly as the incidence angle A_γ was increased, while the volume fractions of the PM and $A1$ phases both increased, shown in Figure 4.24. At small values of A_γ, the source γ-rays arrive at an

orientation that is nearly perpendicular to the sample surface, thus penetrating further into the material and providing lower surface sensitivity. From the results shown in Figure 4.24, it can be concluded that the $L1_0$ phase is less prevalent near the surface region compared to its concentration in the bulk, while the opposite is true for the PM phase, with the $A1$ phase exhibiting near constant prevalence as a function of depth within the specimen. This observed gradient in the contributions of the constituent phases may have been caused by the mechanical and thermal stresses near the surface arising from the specimen preparation procedures of cutting and polishing. These stresses are considered to have compromised the $L1_0$ atomic order near the surface, with the PM phase being preferentially formed over the $A1$ phase. This observation implies that a distinctly different crystal structure has been formed.

4.5 Summary

Backscatter Mössbauer spectroscopy with simultaneous recording of the entire fluorescence spectrum shows immense promise as a tool to investigate a wide range of material properties, such local atomic order, magnetic orientation and the presence of different Fe-containing phases. This technique provides an intrinsic depth sensitivity by virtue of the two different mean free paths of the resonant photon energies: the 14.4 keV re-emitted γ-rays and the 6.4 keV conversion X-rays. The applicability of backscatter MöS to samples with varying thicknesses and degrees of crystalline order has been confirmed, and advantages over transmission MöS have been established, in cases where the transmission and backscatter geometries are both feasible. Essentially any iron-containing sample can be non-destructively investigated with this approach, making this technique very attractive as a probe in modern magnetic materials science as well as in the earth and planetary sciences. Our experimental setup has been largely custom-built and programmed in-house at a fraction of the cost of a single commercial multi-parameter analyser. It has been shown that this multi-parallel-acquisition MöS technique provides a viable alternative to other spectroscopic techniques to investigate a number of key material properties, for a variety of sample geometries.

The here-described electronics and software can and have also been utilised to perform

conversion electron MöS (CEMS) (see, for example, the supplementary material of Borisov et al. [37]), where the electrons themselves are detected rather than the photons, yielding a truly surface sensitive technique. The high speed and low dead time of the acquisition electronics are of even higher importance in this case due to the much larger number of electrons in the detector cascade.

4.6   Future Work

A very-rarely used methodology to decrease linewidths below the natural Lorentzian ones is time-differential MöS, where the 122.1 keV γ-rays emitted by the source, see Figure 4.1, are detected using a scintillation detector, signalling the occupation of the 14.4 keV energy level in the source ^{57}Fe nuclei. Subsequent detections of the resonant fluorescence photons from the sample can then be assigned a time delay value, since the occupation of the 14.4 keV energy levels in the source. When processing the data, detected photons can be discriminated based on their time delay, thus improving the SNR [38]. We have recently added additional flip-flop latches to the our MPA to provide the additional bandwidth necessary to incorporate this extra data while maintaining the established acquisition speeds and dead time.

4.A   Full General Hamiltonian Model

To describe the energy sub-levels of two states and their respective transition probabilities, it is useful to construct a full Hamiltonian model of the states. In the case of ^{57}Fe MöS, the two states are the ground and first excited states of the ^{57}Fe nucleus. The relevant terms for describing Mössbauer spectra relate to the hyperfine interactions, namely the Coulomb, magnetic Zeeman and electric field gradient interactions at the emitting/absorbing nuclei; or the electric monopole, magnetic dipole and electric quadrupole terms.

$$\mathcal{H} = \mathcal{H_C} + \mathcal{H_M} + \mathcal{H_Q}$$

The former results in the Isomer Shift and equally shifts all peaks in the spectrum, making it simply an additive term in the model. The other, important terms can be written, after

[10]:

$$\mathcal{H}_{\mathcal{Q}} = \frac{eQV_{zz}}{4I\left(2I-1\right)} \left[3\mathbf{I}_z^2 - I(I+1) + \eta\left(\mathbf{I}_x^2 - \mathbf{I}_y^2\right)\right]$$

$$\mathcal{H}_{\mathcal{M}} = -\gamma\mu_N B_{hf}\left(\mathbf{I}_z\cos(\theta) + \sin(\theta)\left[\mathbf{I}_x\cos(\phi) + \mathbf{I}_y\sin(\phi)\right]\right)$$

Where the angles θ and ϕ are the polar and azimuthal angles describing the orientation of the magnetic field with respect to the electric field gradient $\vec{V}$, the chosen quantisation axis. I is the nuclear spin, Q is the electric quadrupole moment, η is the electric field gradient asymmetry and $\mathbf{I}_{x,y,z}$ are the angular momentum operator matrices.
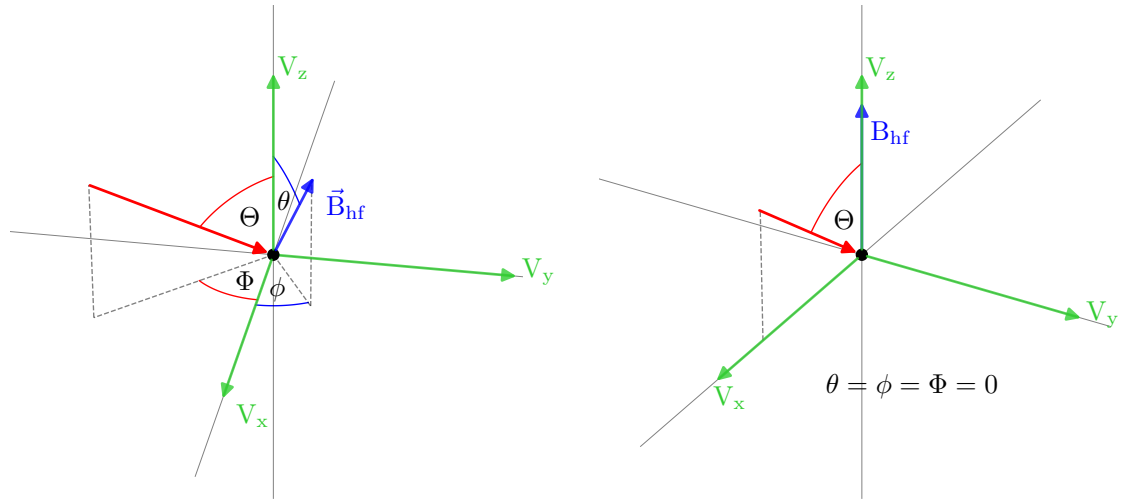
Figure 4.25: Diagram showing the meaning of the angles in the model for the general case, and the simple case which is usually adequate to describe the data for ^{57}Fe MöS.

The ground state of ^{57}Fe has spin $I = 1/2$ and therefore a spherically symmetric nucleus and no electric quadrupole moment, only the magnetic dipole term contributes. Substituting for simplification $A = \frac{eQV_{zz}}{4I(2I-1)}$, $\alpha = \gamma_{\frac{3}{2}}\mu_N B_{hf}$, $\beta = \gamma_{\frac{1}{2}}\mu_N B_{hf}$ and writing in matrix form after e.g. Edmonds [39] or Sakurai [40]:

$$H_{1/2}(\beta,\theta,\phi) = \begin{bmatrix} -\frac{\beta}{2}\cos(\theta) & -\frac{\beta}{2}e^{-i\phi}\sin(\theta) \\ -\frac{\beta}{2}e^{i\phi}\sin(\theta) & \frac{\beta}{2}\cos(\theta) \end{bmatrix} \tag{4.2}$$

$$H_{3/2}(A, \alpha, \theta, \varphi, \eta) =$$

$$\begin{bmatrix} 3A - \frac{3\alpha}{2}\cos(\theta) & -\frac{\sqrt{3}\alpha}{2}e^{-i\phi}\sin(\theta) & \sqrt{3}A\eta & 0 \\ -\frac{\sqrt{3}\alpha}{2}e^{i\phi}\sin(\theta) & -3A - \frac{\alpha}{2}\cos(\theta) & -\alpha e^{-i\phi}\sqrt{\sin(\theta)} & \sqrt{3}A\eta \\ \sqrt{3}A\eta & -\alpha e^{i\phi}\sqrt{\sin(\theta)} & -3A + \frac{\alpha}{2}\cos(\theta) & -\frac{\sqrt{3}\alpha}{2}e^{-i\phi}\sin(\theta) \\ 0 & \sqrt{3}A\eta & -\frac{\sqrt{3}\alpha}{2}e^{i\phi}\sin(\theta) & 3A + \frac{3\alpha}{2}\cos(\theta) \end{bmatrix} \quad (4.3)$$

Where the Euler formula, $e^{ix} = \cos(x) + i\sin(x)$ is utilised.

The peak positions in a Mössbauer spectrum correspond to the differences in energy between the hyperfine split ground and exited states, which are simply the differences in the eigenvalues $E_s(m)$ of the Hamiltonians $\mathcal{H}_s$

$$\Delta E = -\delta_{IS} + \sum_{m_g=-\frac{1}{2}}^{\frac{1}{2}} \sum_{m_e=-\frac{3}{2}}^{\frac{3}{2}} [E_e(m_e) - E_g(m_g)] \quad (4.4)$$

4.A.1   Line Intensity as Absorbed Power from Multi-pole Field

Following the method of [7], the measured intensity of each peak in the Mössbauer spectrum is related to the normalised power absorbed by each transition, equal to the square modulus of the electromagnetic field vector of the source γ-rays $|\mathbf{E}|^2 = \mathbf{E} \cdot \mathbf{E}^*$. The electromagnetic multi-pole field can be expanded in terms of the spherical harmonics, after [8]:

$$\mathbf{E}(\Theta, \Phi) = \sum_l \sum_{\Delta m} (-i)^{l+1} \left[a_E(l, \Delta m) \left(\mathbf{X}_l^{\Delta m} \times \mathbf{r} \right) + a_M(l, \Delta m) \mathbf{X}_l^{\Delta m} \right] \quad (4.5)$$

As mentioned in subsection 4.2.1, the transition we are interested in is purely M1 so the first term in Equation 4.5 can be neglected, $l = 1$ and $\Delta m = 0, \pm 1$ so:

$$\mathbf{E}(\Theta, \Phi) = -\sum_{\Delta m=-1}^{1} \left[a_M(l, \Delta m) \mathbf{X}_1^{\Delta m} \right]$$

where the vector spherical harmonics are given by

$$\mathbf{X}_1^{\Delta m} = \frac{1}{\sqrt{2}} \hat{\mathbf{L}} Y_1^{\Delta m}(\Theta, \Phi)$$

with the angular momentum operator and quantum-mechanical spherical harmonic oper-

ator given by [8]:

$$\hat{\mathbf{L}} = \frac{1}{i}(\hat{r} \times \hat{\nabla}) = i\left(\hat{\Theta}\frac{1}{\sin(\Theta)}\frac{\partial}{\partial\Phi} - \hat{\Phi}\frac{\partial}{\partial\Theta}\right)$$

$$Y_1^{\Delta m}(\Theta, \Phi) = (-1)^{\Delta m}\sqrt{\frac{3}{4\pi}\frac{(1-\Delta m)!}{(1+\Delta m)!}}P_1^{\Delta m}(\cos(\Theta))e^{i\Delta m\Phi}$$

Lastly, $P_1^{\Delta m}$ are the associated Legendre polynomials whose three relevant terms are

$$P_1^1(x) = -\sqrt{1-x^2} \qquad P_1^0(x) = x \qquad P_1^{-1}(x) = \frac{1}{2}\sqrt{1-x^2}$$

Substituting all of the above expressions back into Equation 4.A.1, shortening $a_M(l, \Delta m)$ to $a_{\Delta m}$, and simplifying (first on paper then confirming via computer using the Python package SymPy [41]), we obtain:

$$\mathbf{E}(\Theta, \Phi) = \frac{1}{4}\sqrt{\frac{3}{\pi}}\left[\left(a_1e^{i\phi} + a_{-1}e^{-i\phi}\right)\hat{\Theta}\right.$$
$$\left. + \left(a_1i\cos(\Theta)e^{i\Phi} - a_0i\sqrt{2}\sin(\Theta) - a_{-1}i\cos(\Theta)e^{-i\Phi}\right)\hat{\Theta}\right]$$

Noting that the cross terms are zero $\hat{\Theta}\cdot\hat{\Phi} = 0$ (orthogonal unit vectors), the absorbed power is then:

$$|\mathbf{E}|^2 = \frac{3}{16\pi}|\hat{\Theta}|^2\left[|a_1|^2 + a_1a_{-1}^*e^{-2i\Phi} + a_{-1}a_1^*e^{-2i\Phi} + |a_{-1}|^2\right]$$
$$+ \frac{3}{16\pi}|\hat{\Phi}|^2\left[|a_1|^2\cos^2(\Theta) - a_1a_0^*\sqrt{2}\cos(\Theta)\sin(\Theta)e^{i\Phi} - a_1a_{-1}^*\cos^2(\Theta)e^{2i\Phi}\right.$$
$$- a_0a_1^*\sqrt{2}\cos(\Theta)\sin(\Theta)e^{-i\Phi} + 2|a_0|^2\sin^2(\Theta) + a_0a_{-1}^*\sqrt{2}\cos(\Theta)\sin(\Theta)e^{i\Phi}$$
$$\left. + a_{-1}a_1^*\cos^2(\Theta)e^{-2i\Phi} + a_{-1}a_0^*\sqrt{2}\cos(\Theta)\sin(\Theta)e^{-i\Phi} + |a_{-1}|^2\cos^2(\Theta)\right]$$

If we now note that $|\hat{\Theta}|^2, |\hat{\Phi}|^2 = 1$ (unit vector magnitude is one) and also assume the property of the magnetic dipole field coefficients $a_1a_2^* = a_2a_1^*$, we can simplify the expression to:

$$|\mathbf{E}|^2 = \frac{3}{16\pi}\left[|a_1|^2\left(1 + \cos^2(\Theta)\right) + 2|a_0|^2\sin^2(\Theta) + |a_{-1}|^2\left(1 + \cos^2(\Theta)\right)\right.$$
$$+ 2a_1a_{-1}^*\left(2\cos(2\Phi) - \cos^2(\Theta)e^{2i\Phi}\right) - a_1a_0^*\sqrt{2}\sin(2\Theta)\cos(\Phi)$$
$$\left. + a_0a_{-1}^*\sqrt{2}\sin(2\Theta)\cos(\Phi)\right]$$

where we make use of the Euler formula $e^{ix} + e^{-ix} = 2\cos(x)$ and the trigonometric formula $2\sin(2x) = \sin(x)\cos(x)$. This can further be compacted to:

$$|\mathbf{E}|^2 = \frac{3}{16\pi}\left[\left(|a_1|^2 + |a_{-1}|^2\right)\left(1 + \cos^2(\Theta)\right) + 2\sin^2(\Theta)\left(|a_0|^2 + a_1 a_{-1}^* \cos(2\Phi)\right)\right.$$
$$\left. - \sqrt{2}(a_1 a_0^* + a_0 a_{-1}^*)\sin(2\Theta)\cos(\Phi)\right] \quad (4.6)$$

This formula gives the normalised power absorbed by each transition when we sub in the respective values for the a coefficients and the polar angles of the source γ-rays Θ and Φ. The more simplified the better because having fewer computations involved makes it faster to compute, which is very important for regression.

4.A.2   The Field Components a

After [9], the coefficients multiplying the spherical harmonics are written

$$a(l, \Delta m) = \sum_{\Delta m = m_e - m_g} \left(\vec{V}_e[m_e] \cdot \vec{V}_g^*[m_g] \cdot \langle I_g l m_g m \,|\, I_e m_e\rangle\right)$$

where the sum is over values for m_e and m_g which yield the correct Δm. The three terms are the components of the eigenvectors of the excited and ground state Hamiltonians $H_I|V_I\rangle = E_I|V_I\rangle$, and the Clebsch-Gordan coefficients which couple them, respectively. Again, we only consider the M1 transition, so $l = 1$ and $\Delta m = 0, \pm 1$. The Clebsch-Gordan coefficients can be converted to a usable form using the relations in [39] or [42]

$$\langle I_g 1 m_g \Delta m \,|\, I_e m_e\rangle = \left\langle \frac{1}{2} 1 m_g \Delta m \,\middle|\, \frac{3}{2} m_e\right\rangle = (-1)^{m_g + \frac{1}{2}}\sqrt{\frac{4}{3}}\left\langle \frac{3}{2}\frac{1}{2} m_e - m_g \,\middle|\, 1\Delta m\right\rangle$$

and can then be read from one of the many published tables, for example, [43].
The a coefficients are finally (noting the sign of m_g in the table):

$$a_1 = \sqrt{\frac{1}{3}}\,\vec{V}_e\!\left[\frac{1}{2}\right]\vec{V}_g^*\!\left[-\frac{1}{2}\right] + \vec{V}_e\!\left[\frac{3}{2}\right]\vec{V}_g^*\!\left[\frac{1}{2}\right]$$
$$a_0 = \sqrt{\frac{2}{3}}\,\vec{V}_e\!\left[-\frac{1}{2}\right]\vec{V}_g^*\!\left[-\frac{1}{2}\right] + \sqrt{\frac{2}{3}}\,\vec{V}_e\!\left[\frac{1}{2}\right]\vec{V}_g^*\!\left[\frac{1}{2}\right] \qquad (4.7)$$
$$a_{-1} = \vec{V}_e\!\left[-\frac{3}{2}\right]\vec{V}_g^*\!\left[-\frac{1}{2}\right] + \sqrt{\frac{1}{3}}\,\vec{V}_e\!\left[-\frac{1}{2}\right]\vec{V}_g^*\!\left[\frac{1}{2}\right]$$

Table 4.3: Normalised Clebsch-Gordan coefficients for the $I = \frac{3}{2} \to \frac{1}{2}$ M1 transition in ^{57}Fe, with Θ dependence for each transition appended.

m_e	$-m_g$	Δm	CG	$3(CG)^2$	$I(\Theta)$
$+\frac{3}{2}$	$+\frac{1}{2}$	$+1$	1	3	$1 + \cos^2(\Theta)$
$+\frac{1}{2}$	$+\frac{1}{2}$	0	$\sqrt{\frac{2}{3}}$	2	$2\sin^2(\Theta)$
$-\frac{1}{2}$	$+\frac{1}{2}$	-1	$\sqrt{\frac{1}{3}}$	1	$1 + \cos^2(\Theta)$
$+\frac{1}{2}$	$-\frac{1}{2}$	$+1$	$\sqrt{\frac{1}{3}}$	1	$1 + \cos^2(\Theta)$
$-\frac{1}{2}$	$-\frac{1}{2}$	0	$\sqrt{\frac{2}{3}}$	2	$2\sin^2(\Theta)$
$-\frac{3}{2}$	$-\frac{1}{2}$	-1	1	3	$1 + \cos^2(\Theta)$

Each of the components of $\vec{V}_e$ and $\vec{V}_g$ are vectors of length four and two respectively. The products as written thus have eight components corresponding to all possible transitions. The components corresponding to $\Delta m = 2$ of course always being zero because we have only considered terms in the expansion with $\Delta m = 0, \pm 1$.

The procedure to obtain the intensities for each line is to:

- Calculate the eigenvalues of the Hamiltonians and find the differences between sublevels to get the line positions.

- Calculate the eigenvectors and sub into the equations for a in Equation 4.7.

- Sub the expressions for a into the expression for the absorbed power Equation 4.6 to get the intensity for each line.

- Define a sum of six peak profiles whose positions and intensities have just been calculated and whose breadth depends on the local crystalline and atomic order. We generally use pseudo-Voigt profiles but have the capacity to utilise time-differential or dynamic lineshapes.

- Add a background and scaling factor.

The final model has the form

$$I = A \cdot f(v, \Gamma, \sigma, \mu, \delta, Q, B_{\mathrm{hf}}, \theta, \phi, \eta, \Theta, \Phi) + C$$

where the broadening terms Γ, σ and μ are the Lorentzian width, Gaussian width and mixing ratio of the peaks. The other terms are all defined above.

If, as is usually the case in the higher symmetry crystal singonies, the quadrupole field angles and azimuthal emission angle can be ignored such that $\theta, \phi, \eta, \Phi = 0$, the intensities only depend on the Clebsch-Gordan coefficients and polar emission angle Θ as tabulated in Table 4.3. For magnetically isotropic samples, we integrate over all directions so Θ also drops out and the Clebsch-Gordan coefficients alone describe the relative peak intensity, resulting in the famous $3 : 2 : 1$ ratio from outer to inner peaks.

It is essential to consider different magnetic orientations when interpreting Mössbauer spectra obtained with different angles of incidence of the source photons. Three characteristic cases are: uniaxial magnetisation (assumed out-of-plane), planar uniform magnetisation, and 3D isotropic magnetisation. In the latter case, the peak ratios are always $3 : 2 : 1$ as mentioned. For uniaxial magnetisation, the angular dependence in Table 4.3 gives the intensity variation. For samples that are isotropically magnetised in-plane (negative uniaxial anisotropy) all magnetic moment vectors will be perpendicular to an incoming γ-ray at normal incidence, but for oblique angles of incidence, we must integrate over the distribution of magnetic moment directions:

$$I_{IPavr} = \frac{2}{\pi} \int_0^{2\pi} \frac{1 - (\cos(x)\sin(\Theta))^2}{1 + (\cos(x)\sin(\Theta))^2} \mathrm{dx} \tag{4.8}$$

The calculated intensities are plotted against the angle of incidence measured from the sample surface normal in Figure 4.26. The "magic angles" $\Theta = 54.74°^3$ and $\Theta_{planar} = 61.9°$ denote the angles where the peak intensity ratios are $3 : 2 : 1$ for uniaxial out-of-plane and planar uniform magnetisation.

---

[3]This magic angle, equal to $\arccos(1/\sqrt{3})$, often arises in nuclear angular momentum coupling scenarios, for example the "magic angle spinning" technique in NMR spectroscopy [44].
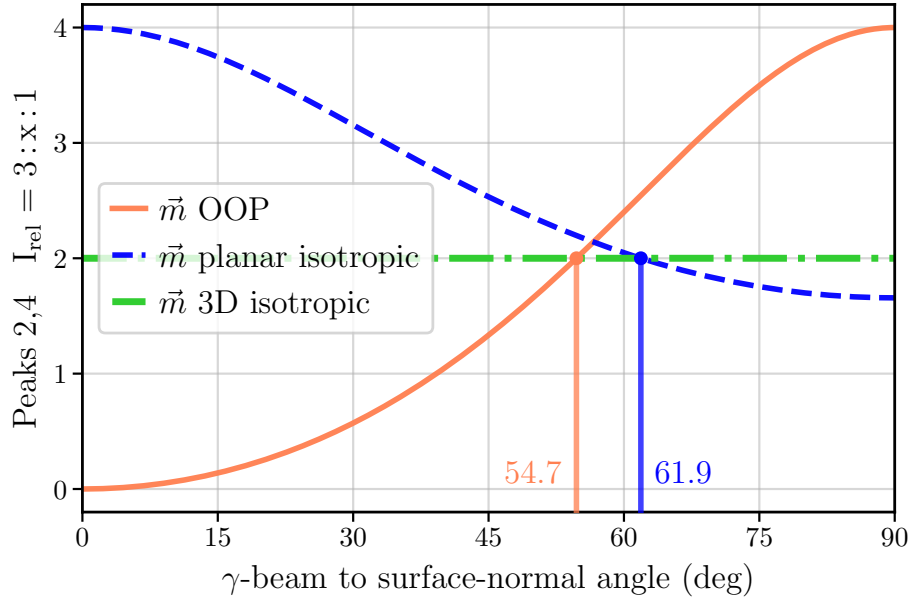
Figure 4.26: I_{rel} of peaks 2,5 as the angle between the source γ-rays and the surface normal increases, for various magnetic orientations.

4.B Angular Dependence of MöS Sensitivity

The MöS sensitivity as a function of angle can be approximated by integrals of sinusoidal functions over a suitable conical spread of incident photon angles δ:

$$
S_x(\theta) = 0.4 + \int_{-2\delta}^{2\delta} \sin^4(\theta - \theta') \ \sqrt{\cos(\theta - \theta')} \, D(\theta') \ \mathrm{d}\theta'
$$

$$
S_\gamma(\theta) = \int_{-2\delta}^{2\delta} \sqrt{\cos(\theta - \theta')} \, D(\theta') \ \mathrm{d}\theta'
$$

$$
\text{where} \quad D(\theta) = \begin{cases} \frac{1}{2\delta} & |\theta| \leq \delta \\ 0 & \text{otherwise} \end{cases}
$$

(4.9)

This was shown in Figure 4.24 and explains the trend in total Mössbauer peak area as a function of the angle of incidence seen in Figure 4.23.

References

[1] N. N. Greenwood and T. C. Gibb, *Mössbauer spectroscopy.* Chapman and Hall Ltd, London, 1972. [Cited on pages 190, 191, 193, and 197]

[2] G. Smirnov, U. Van Bürck, A. Chumakov, A. Baron, and R. Rüffer, "Synchrotron Mössbauer source," *Physical Review B*, vol. 55, no. 9, p. 5811, 1997. [Cited on page 190]

[3] J. O'Brien, H. A. Baghbaderani, F. O. Keller, N. Dempsey, L. H. Lewis, and P. Stamenov, "Hardware, methodology and applications of 2^+D backscatter Mössbauer spectroscopy with simultaneous X–ray and γ–ray detection," *Measurement Science and Technology*, vol. 35, no. 2, p. 025503, 2023. [Cited on page 190]

[4] R. L. Mössbauer, "Nuclear resonance fluorescence of γ–rays in ^{191}Ir," *Zeitschrift für Physik*, vol. 151, no. 2, pp. 124–143, 1958. in German. [Cited on page 191]

[5] M. Bhat, "Nuclear data sheets for a=57," *Nuclear Data Sheets*, vol. 85, no. 3, pp. 415–536, 1998. [Cited on pages xxvi, 191, 192, and 200]

[6] M. D. Dyar, D. G. Agresti, M. W. Schaefer, C. A. Grant, and E. C. Sklute, "Mössbauer spectroscopy of earth and planetary materials," *Annu. Rev. Earth Planet. Sci.*, vol. 34, pp. 83–125, 2006. [Cited on pages xxvi and 193]

[7] C. Voyer and D. Ryan, "A complete solution to the Mössbauer problem, all in one place," *Hyperfine interactions*, vol. 170, no. 1, pp. 91–104, 2006. [Cited on pages 195 and 224]

[8] J. D. Jackson, *Classical electrodynamics.* Wiley, 1999. [Cited on pages 195, 224, and 225]

[9] R. Housley, R. Grant, and U. Gonser, "Coherence and polarization effects in Mössbauer absorption by single crystals," *Physical Review*, vol. 178, no. 2, p. 514, 1969. [Cited on pages 195 and 226]

[10] W. Kündig, "Evaluation of Mössbauer spectra for ^{57}Fe," *Nuclear Instruments and Methods*, vol. 48, no. 2, pp. 219–228, 1967. [Cited on pages 195 and 223]

[11] P. Mangin, G. Marchal, M. Piecuch, and C. Janot, "Mössbauer spectra analysis in amorphous system studies," *Journal of Physics E: Scientific Instruments*, vol. 9, no. 12, p. 1101, 1976. [Cited on page 196]

[12] C. Kittel and P. McEuen, *Introduction to solid state physics.* John Wiley & Sons, 2018. [Cited on page 196]

[13] H. A. Baghbaderani, A. Masood, K. L. Alvarez, D. Lordan, M. Venkatesan, C. Ó. Mathúna, P. McCloskey, and P. Stamenov, "Composition engineering of ultra–soft magnetic Co–based alloys," *Journal of Alloys and Compounds*, vol. 924, p. 166366, 2022. [Cited on pages 196 and 209]

[14] F. Wagner, "Applications of Mössbauer scattering techniques," *Le Journal de Physique Colloques*, vol. 37, no. C6, pp. C6–673, 1976. [Cited on page 197]

[15] I. Fleischer, G. Klingelhoefer, C. Schröder, R. V. Morris, M. Hahn, D. Rodionov, R. Gellert, and P. de Souza, "Depth selective Mössbauer spectroscopy: analysis and simulation of 6.4 keV and 14.4 keV spectra obtained from rocks at Gusev crater, Mars, and layered laboratory samples," *Journal of Geophysical Research: Planets*, vol. 113, no. E6, 2008. [Cited on pages 198 and 208]

[16] E. De Grave, R. Vandenberghe, and C. Dauwe, "ILEEMS: methodology and applications to iron oxides," *Hyperfine Interactions*, vol. 161, no. 1, pp. 147–160, 2005. [Cited on pages xxvi and 199]

[17] G. Longworth and B. Window, "The preparation of narrow–line Mössbauer sources of ^{57}Co in metallic matrices," *Journal of Physics D: Applied Physics*, vol. 4, no. 6, p. 835, 1971. [Cited on page 200]

[18] M. Oshtrakh and V. Semionkin, "Mössbauer spectroscopy with a high velocity resolution: advances in biomedical, pharmaceutical, cosmochemical and nanotechnological research," *Spectrochimica Acta Part A: Molecular and Biomolecular Spectroscopy*, vol. 100, pp. 78–87, 2013. [Cited on page 200]

[19] G. F. Knoll, *Radiation detection and measurement.* John Wiley & Sons, 2010. [Cited on page 200]

[20] P. Rachinhas, T. Dias, A. Stauffer, F. Santos, and C. Conde, "Energy resolution of xenon proportional counters: Monte–Carlo simulation and experimental results," *IEEE Transactions on Nuclear Science*, vol. 43, no. 4, pp. 2399–2405, 1996. [Cited on page 200]

[21] J. Kortright and A. C. Thompson, *X–ray data booklet, 3rd ed.* Lawrence Berkeley National Laboratory, University of California Berkeley, CA, 2009. [Cited on page 201]

[22] H. Frock, "IEEE 1284: updating the PC parallel port," *National In—struments App ̃ ca6on note*, vol. 62, 1995. [Cited on page 202]

[23] S. A. Teukolsky, B. P. Flannery, W. Press, and W. Vetterling, "Numerical recipes in C," *SMR*, vol. 693, no. 1, pp. 59–70, 1992. [Cited on page 207]

[24] J. M. D. Coey, *Magnetism and magnetic materials*. Cambridge university press, 2010. [Cited on pages x, xii, 7, 9, 10, 12, 15, 32, 38, 40, 41, 42, 49, 56, 66, and 212]

[25] F. Pinkerton and W. R. Dunham, "Mössbauer effect studies of $Nd_2Fe_{14}B$ and related melt–spun permanent magnet alloys," *Applied physics letters*, vol. 45, no. 11, pp. 1248–1250, 1984. [Cited on pages xxviii and 213]

[26] F. O. Keller, R. Haettel, T. Devillers, and N. M. Dempsey, "Batch fabrication of 50 μm–thick anisotropic Nd–Fe–B micro–magnets," *IEEE Transactions on Magnetics*, vol. 58, no. 2, pp. 1–5, 2021. [Cited on page 213]

[27] B. A. Kapitanov, N. V. Kornilov, Y. L. Linetsky, and V. Y. Tsvetkov, "Sputtered permanent Nd–Fe–B magnets," *Journal of Magnetism and Magnetic Materials*, vol. 127, no. 3, pp. 289–297, 1993. [Cited on page 217]

[28] L. H. Lewis, A. Mubarok, E. Poirier, N. Bordeaux, P. Manchanda, A. Kashyap, R. Skomski, J. Goldstein, F. Pinkerton, R. Mishra, *et al.*, "Inspired by nature: investigating tetrataenite for permanent magnet applications," *Journal of Physics: Condensed Matter*, vol. 26, no. 6, p. 064213, 2014. [Cited on page 217]

[29] G. Cacciamani, A. Dinsdale, M. Palumbo, and A. Pasturel, "The Fe–Ni system: thermodynamic modelling assisted by atomistic calculations," *Intermetallics*, vol. 18, no. 6, pp. 1148–1162, 2010. [Cited on pages 217 and 219]

[30] L. Néel, J. Pauleve, R. Pauthenet, J. Laugier, and D. Dautreppe, "Magnetic properties of an iron—nickel single crystal ordered by neutron bombardment," *Journal of Applied Physics*, vol. 35, no. 3, pp. 873–876, 1964. [Cited on page 217]

[31] T. Shima, M. Okamura, S. Mitani, and K. Takanashi, "Structure and magnetic properties for $L1_0$–ordered FeNi films prepared by alternate monatomic layer deposition," *Journal of Magnetism and Magnetic Materials*, vol. 310, no. 2, pp. 2213–2214, 2007. [Cited on page 217]

[32] Y. P. Ivanov, B. Sarac, S. V. Ketov, J. Eckert, and A. L. Greer, "Direct formation of hard–magnetic tetrataenite in bulk alloy castings," *Advanced Science*, p. 2204315, 2022. [Cited on pages 217 and 220]

[33] R. Scorzelli, "A study of phase stability in invar Fe–Ni alloys obtained by non–conventional methods," *Hyperfine Interactions*, vol. 110, no. 1, pp. 143–150, 1997. [Cited on page 217]

[34] J. Gattacceca, F. M. McCubbin, A. Bouvier, and J. N. Grossman, "The meteoritical bulletin, no. 108," *Meteoritics & Planetary Science*, vol. 55, no. 5, pp. 1146–1150, 2020. [Cited on page 218]

[35] J. Albertsen, N. Roy-Poulsen, and L. Vistisen, "Ordered FeNi, tetrataenite, and the cooling rate of iron meteorites below 320 ℃," *Meteoritics*, vol. 15, p. 258, 1980. [Cited on page 218]

[36] D. Rancourt and R. Scorzelli, "Low–spin γ–Fe–Ni (γLS) proposed as a new mineral in Fe–Ni–bearing meteorites: epitaxial intergrowth of γLS and tetrataenite as a possible equilibrium state at $\sim$ 20–40 at% Ni," *Journal of Magnetism and Magnetic Materials*, vol. 150, no. 1, pp. 30–36, 1995. [Cited on page 219]

[37] K. Borisov, J. Ehrler, C. Fowley, B. Eggert, H. Wende, S. Cornelius, K. Potzger, J. Lindner, J. Fassbender, R. Bali, *et al.*, "Spin–polarisation and magnetotransport properties of systematically disordered $Fe_{60}Al_{40}$ thin films," *Physical Review B*, vol. 104, no. 13, p. 134417, 2021. [Cited on page 222]

[38] G. R. Hoy, D. W. Hamill, and P. P. Wintersteiner, "Coincidence Mössbauer spectroscopy," in *Proceedings of the Sixth Symposium on Mössbauer Effect Methodology New York City, January 25, 1970*, pp. 109–121, Springer, 1971. [Cited on page 222]

[39] A. R. Edmonds, *Angular momentum in quantum mechanics*. Princeton university press, 1957. [Cited on pages 223 and 226]

[40] J. J. Sakurai and E. D. Commins, *Modern quantum mechanics, revised edition*. American Association of Physics Teachers, 1995. [Cited on page 223]

[41] A. Meurer, C. P. Smith, M. Paprocki, O. Čertík, S. B. Kirpichev, M. Rocklin, A. Kumar, S. Ivanov, J. K. Moore, S. Singh, *et al.*, "SymPy: symbolic computing in Python," *PeerJ Computer Science*, vol. 3, p. e103, 2017. [Cited on page 225]

[42] E. U. Condon, E. Condon, and G. H. Shortley, *The theory of atomic spectra*. Cambridge University Press, 1935. [Cited on page 226]

[43] Particle Data Group and others, "Review of particle physics," *Progress of Theoretical and Experimental Physics*, vol. 2022, no. 8, p. 083C01, 2022. [Cited on page 226]

[44] E. Andrew, "Magic angle spinning," *International Reviews in Physical Chemistry*, vol. 1, no. 2, pp. 195–224, 1981. [Cited on page 228]

Conclusions

We wished to establish a complete physical picture of a spintronics material, primarily for THz oscillation applications. In this picture, the computational model is the paint brush while the experimental investigations provide the paint.

I developed models of increasing complexity to describe the complex dynamics of a compensated ferrimagnetic half-metals, similar to Mn_2Ru_xGa. This culminated in the current model, which is still in early stage, which takes inspiration from Ehrenfest dynamics, wherein the conduction electrons are treated fully quantum-mechanically while the localised atomic spins and nuclei are treated classically. This model, in principle, allows for the simulation of phenomena such as electron-magnon scattering and a provides a well-motivated basis for studying the interplay of electron transport and magnetic dynamics. The results presented included magnon, phonon and plasmon spectra. There is still much of the phase space to be explored, especially regarding the interactions of these quasi-particles.

To continue providing paint for the picture, I took over the mantle of probing the crystal structure of Mn_2Ru_xGa and potential new materials. This is particularly important as we installed a new UHV thin-film deposition platform just as I started my Ph.D. studies, the films deposited there had distinct properties to those that came before, often being significantly better ordered. Some of the key experimental results were the investigation of epitaxy in high-quality Mn_2Ru_xGa films and how that affects the strain-profile in the film, and neutron diffraction measurements which indicated the ground state magnetic orientation of the high-quality Mn_2Ru_xGa was not necessarily the same as the older examples.

Another brush was the Mössbauer spectroscopy setup that I helped to develop with my supervisor. This is not a new technique but our novel energy-dispersive (multi-dimensional) approach allows for a lot of extra information to be obtained "for free", so to speak. Being limited to Fe-containing and preferably $t > 100\,nm$ materials, the technique is not so relevant for Mn_2Ru_xGa, but is useful for investigating other potential new ZMHM materials. Examples of three very morphologically distinct materials were

shown, indicating the versatility of our setup to probe the local chemical and magnetic order of suitable materials.

At this stage the physical picture is sufficiently complete that we can interpret a number of experimental quasi-static properties, such as the magnetisation, conductivity and Hall effect, as a function of applied magnetic field (magnitude and direction), and fit and determine the values of the relevant effective Hamiltonian parameters. Looking from the opposite angle: the results of complex DFT-style computations can also be mapped onto the effective Hamiltonian parameters, to aid in our modelling and understanding of the electron, spin and nuclear quasi-particle dispersions, as well as the ultrafast demagnetisation and precessional dynamics (as evidenced in the AOS of this class of materials).